

Plasmaphysik

Dissertationsthema

**GYROKINETIC SIMULATION  
OF  
MULTIMODE PLASMA TURBULENCE**

Inaugural-Dissertation  
zur Erlangung des Doktorgrades  
der Naturwissenschaften im Fachbereich Physik  
der Mathematisch-Naturwissenschaftlichen Fakultät  
der Westfälischen Wilhelms-Universität Münster

vorgelegt von  
Florian Merz  
aus Rottweil

2008

---

Dekan: Prof. Dr. Johannes Wessels  
Erster Gutachter: Prof. Dr. Frank Jenko  
Zweiter Gutachter: Prof. Dr. Rudolf Friedrich  
Tag der mündlichen Prüfung: 12.11.2008  
Tag der Promotion: 06.02.2009



# Abstract

Anomalous transport in magnetically confined fusion plasmas is one of the principal obstacles on the way towards power plants based on fusion energy. It is induced by turbulence on scales that are comparable to the gyroradius of the charged plasma particles, and leads to a degradation of confinement, which makes it very difficult to reach the conditions that are necessary for a self-sustained fusion reaction in the plasma. An important goal of fusion research is therefore to identify and understand the processes that determine the level of anomalous transport, allowing for a prediction or even reduction of this nonlinear effect.

In the present thesis, a numerical approach to plasma microturbulence is pursued. The gyrokinetic equations, which describe magnetized plasmas at fusion relevant conditions, are presented in a form that is suitable for a numerical treatment. The equations are formulated for general magnetic geometries and include a linearized Landau-Boltzmann collision operator, the influence of the pressure gradient, and other physical effects, extending and generalizing previous presentations of this kind.

Some of the numerical issues concerning the implementation of these equations in the massively parallel plasma turbulence code GENE are discussed, focusing on the significant modifications and improvements that were introduced as part of this PhD project. The modifications include new time stepping schemes and other optimizations that allow for faster computations, improvements of the parallelization that enables the efficient use of thousands of processors, and anti-aliasing procedures that make the simulations more reliable and robust. An important new feature that is also discussed is an interface to an iterative eigenvalue solver, which can be used to efficiently access arbitrary parts of the eigenvalue spectrum of the linear gyrokinetic operator.

This eigenvalue solver is used to study higher dimensional parameter dependencies of transitions between well known plasma microinstabilities, which leads to the discovery of non-Hermitian degeneracies in linear gyrokinetics. The implications of this finding and analogies to other fields like quantum mechanics are discussed.

Nonlinear investigations of pure trapped electron mode (TEM) driven turbulence show that zonal flows, which are crucial for the saturation of the well studied ion temperature gradient (ITG) mode driven turbulence, are often not essential in the TEM case. A detailed investigation of the statistical properties of the  $\vec{E} \times \vec{B}$  nonlinearity suggests that the latter can be approximated by a simple diffusion term, confirming numerically, for the first time, longstanding predictions based on renormalized turbulence theories. These findings are used to justify a quasilinear transport model that has been applied successfully to pure TEM turbulence in previous works.

The transitions between TEM and ITG turbulence are studied systematically, revealing a coexistence of the two kinds of turbulence for a wide range of parameters. Surprisingly, it is found that a single wavenumber may be associated with different frequencies belonging to dif-

ferent modes. Two different mechanisms that lead to the experimentally relevant condition of zero particle transport are identified. A simple quasilinear model, which is shown to describe some basic features of the transition, is presented. The model allows for high dimensional parameter scans and can be used to understand the parameter dependencies of the experimentally relevant hypersurface of zero particle transport. As an example, the dependence of the TEM-ITG system on the collision frequency is studied.

Finally, some of the first simulations of ITG turbulence in the W7-X stellarator in realistic geometry are presented, both in the adiabatic electron approximation and for fully gyrokinetic electrons and ions, demonstrating the advances in computational gyrokinetics. Several features like the gradient dependence of the ion heat transport are discussed, suggesting a significant potential of non-axisymmetric devices for a systematic control of turbulent transport.

# Zusammenfassung

Der anomale Transport in magnetisch eingeschlossenen Hochtemperaturplasmen ist eines der größten Hindernisse für die Verwirklichung von Fusionskraftwerken. Er wird durch Turbulenz auf Skalen vergleichbar zum Gyroradius der geladenen Plasmateilchen verursacht und führt zu einer Verschlechterung des Einschlusserhaltens, was das Erreichen der Zündbedingung, die für eine selbsterhaltende thermonukleare Reaktion im Plasma notwendig ist, deutlich erschwert. Ein wichtiges Ziel der Fusionsforschung ist es daher, die physikalischen Prozesse, die das Transportniveau bestimmen, zu identifizieren und zu verstehen und somit eine Vorhersage oder sogar Beeinflussung anomalen Transports zu ermöglichen.

In der vorliegenden Arbeit wird hierzu ein numerischer Ansatz verfolgt. Die gyrokinetischen Gleichungen, die magnetisierte Plasmen bei fusionsrelevanten Parametern beschreiben, werden für die numerische Behandlung vorbereitet. In der hier gezeigten Form sind sie für allgemeine magnetische Geometrien gültig und beinhalten einen linearisierten Landau-Boltzmann-Stossoperator, den Einfluss des Druckgradienten und andere physikalische Effekte und erweitern und verallgemeinern somit frühere Darstellungen.

Es werden einige Aspekte bezüglich der numerischen Implementierung dieser Gleichungen in den massiv parallelen Plasmaturbulenz-Code GENE diskutiert, wobei der Schwerpunkt auf den deutlichen Modifikationen und Verbesserungen liegt, die im Laufe dieser Doktorarbeit in den Code eingeflossen sind. Beispielsweise wurden die Recheneffizienz u.a. durch neue Zeitschrittverfahren deutlich optimiert, die Parallelisierung verbessert und Antialiasing-Verfahren eingeführt, die die Simulationen verlässlicher und robuster machen. Eine wichtige Neuerung stellt auch die Schnittstelle zu einem iterativen Eigenwertlöser dar, der die Untersuchung beliebiger Bereiche des Eigenwertspektrums des linearen gyrokinetischen Operators erlaubt.

Dieser Eigenwertlöser wird benutzt, um die Parameterabhängigkeit von Übergängen zwischen den bekannten Mikroinstabilitäten zu untersuchen. Diese Untersuchung führt zur Entdeckung nichthermitescher Entartungen in der linearen Gyrokinetik; die daraus resultierenden Implikationen und Analogien mit anderen Fachgebieten wie der Quantenmechanik werden diskutiert.

Nichtlineare Untersuchungen reiner Trapped Electron Mode (TEM) Turbulenz zeigen, dass zonale Strömungen, die für die Sättigung der gut untersuchten Ion Temperature Gradient Mode (ITG) Turbulenz entscheidend sind, im TEM-Fall oft nicht wichtig sind. Eine genaue Untersuchung der statistischen Eigenschaften der  $\vec{E} \times \vec{B}$ -Nichtlinearität ergibt, dass diese durch einen einfachen Diffusionsterm approximiert werden kann, was theoretische Vorhersagen im Rahmen von renormierten Turbulenztheorien zum ersten Mal numerisch bestätigt. Dieses Ergebnis liefert nachträglich auch die Grundlage für ein quasilineares Transportmodell, das in früheren Arbeiten bereits erfolgreich angewandt wurde.

Weiterhin werden die Übergänge zwischen TEM- und ITG-Turbulenz ausführlich unter-

sucht. Über einen weiten Parameterbereich zeigt sich eine Koexistenz der beiden Turbulenzarten, in manchen Fällen erstaunlicherweise sogar bei der gleichen Wellenzahl. Zwei Mechanismen, die zur experimentell relevanten Bedingung von verschwindendem Teichentransport führen, werden identifiziert. Ein einfaches quasilineares Modell wird vorgestellt, das einige der grundlegenden Merkmale des Übergangs beschreiben kann. Das Modell erlaubt hochdimensionale Untersuchungen des gyrokinetischen Parameterraums und kann für Untersuchungen der Parameterabhängigkeit der Hyperfläche mit verschwindendem Teilchenfluss benutzt werden. Dies wird am Beispiel der Abhängigkeit des TEM-ITG-Systems von der Stoßfrequenz demonstriert.

Zuletzt wird noch ITG-Turbulenz im Stellarator W7-X untersucht. Es werden sowohl Simulationen in der Näherung adiabatischer Elektronen als auch mit einer vollen gyrokinetischen Behandlung beider Spezies präsentiert, was die Fortschritte in der numerischen Beschreibung von Plasmaturbulenz verdeutlicht. Es werden einige Aspekte der Turbulenz in W7-X wie z.B. die Abhängigkeit des Ionen-Wärmetransports vom Temperaturgradienten diskutiert und das Potential verschiedener nicht-axialsymmetrischen Magnetfeldkonfigurationen aufgezeigt.

# Contents

<b>1. Introduction</b>	<b>1</b>
<b>2. Gyrokinetics</b>	<b>5</b>
2.1. Basic description of a plasma . . . . .	6
2.2. Geometry and coordinates . . . . .	8
2.2.1. Flux tube approximation . . . . .	9
2.2.2. Guiding-center coordinates . . . . .	12
2.3. General gyrokinetic equations . . . . .	13
2.4. The $\delta f$ splitting . . . . .	15
2.4.1. Equation for the distribution function . . . . .	16
2.4.2. Field equations . . . . .	17
2.4.3. Collision operator . . . . .	17
2.5. Choice of $F_{0j}$ . . . . .	18
2.5.1. Equation for the distribution function . . . . .	19
2.5.2. Field equations . . . . .	19
2.5.3. Collision operator . . . . .	22
2.6. Expansion of the vector expressions . . . . .	24
2.6.1. Equation for the distribution function . . . . .	24
2.6.2. Field equations . . . . .	25
2.6.3. Collision operator . . . . .	27
2.7. Normalization . . . . .	28
2.7.1. Equation for the distribution function . . . . .	30
2.7.2. Field equations . . . . .	33
2.7.3. Collision operator . . . . .	35
2.8. Summary of the equations being solved in GENE . . . . .	36
2.9. Special simplifications . . . . .	37
2.9.1. $\hat{s} - \alpha$ geometry . . . . .	37
2.9.2. Adiabatic electrons . . . . .	38
2.9.3. Adiabatic ions . . . . .	39
2.9.4. Pitch-angle scattering . . . . .	39
2.10. Observables . . . . .	40
2.11. Summary . . . . .	42
<b>3. The GENE code</b>	<b>43</b>
3.1. Discretization of the operators . . . . .	44
3.1.1. Perpendicular direction . . . . .	44
3.1.2. Parallel direction . . . . .	44

3.1.3. Velocity space . . . . .	45
3.2. Anti-aliasing . . . . .	46
3.3. Eigenvalue solver . . . . .	47
3.4. Initial value solver . . . . .	49
3.4.1. Implicit time stepping scheme . . . . .	51
3.4.2. Explicit time stepping schemes . . . . .	51
3.5. Nonlinear simulations . . . . .	54
3.6. Parallelization . . . . .	55
3.7. Summary . . . . .	57
<b>4. Fundamental features of linear gyrokinetics</b>	<b>59</b>
4.1. Structure of the linear gyrokinetic equation . . . . .	59
4.2. Settings for the numerical investigations . . . . .	62
4.3. Mode transitions . . . . .	62
4.4. Exceptional points . . . . .	63
4.5. Mode correlations . . . . .	67
4.6. Theory and occurrence of non-Hermitian degeneracies . . . . .	68
4.7. Summary . . . . .	69
<b>5. Trapped electron mode turbulence</b>	<b>71</b>
5.1. Simulation parameters . . . . .	71
5.2. Zonal flows in TEM turbulence . . . . .	72
5.3. Similarities between linear and nonlinear simulations . . . . .	73
5.4. Statistical properties of the nonlinearity . . . . .	74
5.5. Quasilinear transport model for TEM turbulence . . . . .	77
5.6. Summary . . . . .	78
<b>6. TEM/ITG turbulence in tokamaks</b>	<b>79</b>
6.1. Setup for the simulations . . . . .	80
6.2. Nonlinear results and comparison to linear behaviour . . . . .	80
6.3. Construction of a quasilinear model for the flux ratios . . . . .	86
6.4. Application and test of the quasilinear model . . . . .	88
6.5. TEM-ITG transitions in the presence of collisions . . . . .	92
6.6. Summary . . . . .	94
<b>7. ITG turbulence in stellarators</b>	<b>97</b>
7.1. Flux tube approximation for stellarators . . . . .	98
7.2. Adiabatic ITG turbulence in a standard equilibrium . . . . .	99
7.3. Adiabatic ITG turbulence in the high mirror configuration . . . . .	101
7.4. Stellarator turbulence with kinetic electrons . . . . .	106
7.5. Summary . . . . .	109

*Contents*

<b>8. Conclusions</b>	<b>111</b>
8.1. Summary . . . . .	111
8.2. Outlook . . . . .	113
<b>A. Integrals for the field equations</b>	<b>115</b>
<b>B. Finite difference methods</b>	<b>119</b>
<b>C. Runge-Kutta methods</b>	<b>123</b>
<b>Bibliography</b>	<b>125</b>
<b>Acknowledgement</b>	<b>133</b>

# 1. Introduction

In the past, economic growth and the associated increase of the standard of living have always been linked to an increasing energy consumption. And although the governments of the developed countries are now trying to improve the energy efficiency and to decouple the economic growth from the energy consumption, it is clear that the rapid development of big economies in Asia and Latin America will lead to a massive increase of the world primary energy demand in the next decades. Depending on the scenario, the International Energy Agency predicts a growth of 1.2% to 1.6% per year until 2030 [1].

The biggest contribution to the world energy production is by far the burning of fossil fuels like oil, coal, and gas. In 2005, 12.7% of the total primary energy used in the world [2] came from renewable sources including hydropower and burning of combustible renewables and waste, 6.3% came from nuclear fission, and the rest, i.e. more than 80%, came from the burning of fossil fuels (the numbers for the developed OECD countries are 6.2% renewables, 11% fission and 82.8% fossil fuels). Despite the efforts to promote renewable energies in recent years, the 2007 numbers for Germany are very similar to the numbers for the average of the OECD countries stated above [3].

It is clear that the availability of fossil fuels is limited, so that they can not be part of a sustainable energy supply and have to be replaced in the long term. Additionally, the burning of fossil fuels constitutes the biggest source of anthropogenic green house gases, which cause the global warming that is presently observed, as is now generally accepted [4]. Together with geopolitical reasons, these points make clear that the use of fossil fuels has to be reduced dramatically.

A widely used source of energy that does not produce green house gas emissions is nuclear fission. There has been a renewed interest in this technology lately, but with the intrinsic possibility of catastrophic accidents, the potential misuse for nuclear weapon production, and the unsolved question of how to ultimately dispose the long-lived nuclear waste that is created, fission has significant drawbacks, which in several European countries have lead to the political decision to abandon fission energy.

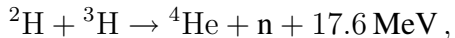
With the exceptions of geothermal and tidal power stations, which have no significant contribution to the world energy production, the renewable energy sources used and promoted today are different forms of solar energy, i.e. they result from nuclear fusion reactions in the sun. The thermal energy that is created in the sun is radiated through space, transmitted through the earth's atmosphere, and then converted either directly in solarthermal or photovoltaic power plants or used in indirect forms such as biomass or wind.

While the efficiency of the different technologies to exploit solar energy is currently improved through many technical innovations and the different forms of solar power will certainly play an important role in the future energy supply, there has also been a constant effort over the last decades to enable a direct use of fusion power in a power plant on earth. The

## 1. Introduction

benefits of such an energy source would be manifold. As in conventional power plants using fission or fossil fuels, the power output could be controlled directly and would not dependent on atmospheric conditions (weather, concentration of aerosols etc.). In contrast to conventional power plants, fusion power plants would not produce green house gases or big amounts of long-lived radioactive waste; catastrophic runaway chain reactions or the use of the technology for weapon production would be ruled out. Furthermore, the fuel for the reaction is readily available in all countries and in virtually unlimited quantities, so that nuclear fusion would be a reliable, safe, and abundant source of energy.

The conditions that are necessary to sustain a fusion reaction are very difficult to achieve on earth. Because of its favourable cross section [5], the fusion reaction that is intended for a fusion power plant is



i.e. the fusion of tritium and deuterium, the heavy isotopes of hydrogen. Deuterium is widely available from water, since it constitutes 0.015% of all hydrogen atoms. Tritium is radioactive with a relatively short half-life of 12.3 years, so that its natural occurrence is negligible and it has to be produced. Fortunately, the tritium-deuterium fusion reaction creates a neutron, which can be used to breed new tritium out of lithium directly in the wall of the reaction vessel.

The most important parameters that control the fusion reaction rate are the density  $n$  and the temperature  $T$  of the tritium-deuterium mixture, which is in the plasma state for fusion relevant conditions. To achieve a self-sustained fusion reaction ("ignition"), furthermore a sufficiently large energy confinement time  $\tau_E$  is necessary.

The condition for an ignited tritium-deuterium plasma can be approximated in the experimentally relevant parameter range by the condition

$$nT\tau_E > 3 \times 10^{21} \text{ keV s m}^{-3},$$

which combines the above parameters [5]. In stars like the sun, which sustain a different fusion reaction, plasma confinement is achieved through gravitation. The enormous mass and extent of the stars lead to a high plasma density and long energy confinement time in the core, so that plasma temperatures can be moderate. These conditions are impossible to achieve on earth, since gravitational effects are negligible in laboratory scale plasmas. The most promising approach to obtain the confinement times that are necessary to sustain a controlled fusion reaction at technically achievable densities and temperatures is magnetic confinement, which is characterized by rather low densities ( $10^{19} \text{ m}^{-3}$  to  $10^{20} \text{ m}^{-3}$ ), high temperatures (above 10 keV) and confinement times of a few seconds.

In this approach, a strong magnetic field confines the motion of the plasma particles perpendicular to the magnetic field lines to gyroorbits. Parallel to the field lines, the particles move more or less freely (up to magnetic mirror effects); to avoid losses at the ends of the magnetic field, the field lines are usually bent to a torus. As it turns out, plasmas in purely toroidal magnetic fields are subject to drifts [5] that prevent a stable confinement. This problem is solved by a twisting of the magnetic field lines, i.e. the creation of an additional poloidal component of the magnetic field. The pitch of the field line, i.e. the ratio of toroidal and poloidal revolutions of a field line, is given by the so-called safety factor  $q$ . If this  $q$  is not a rational number,

the field line covers a so-called flux surface; the field lines at different radial positions inside the toroidal plasma vessel define nested flux surfaces.

The two most important concepts for magnetic confinement fusion essentially differ in the way the twisting of the field lines is achieved. In a tokamak (left plot of Fig. 1.1), a set of external field coils produces a purely toroidal magnetic field. Additionally, a strong toroidal electric current is induced in the plasma, which creates the necessary poloidal magnetic field component. Most fusion experiments in the world, including the International Thermonuclear Experimental Reactor (ITER), now under construction at Cadarache, France, follow this concept. In a stellarator (right plot of Fig. 1.1), the twisted magnetic field that is needed for confinement is completely generated by the external field coils, with no need for a plasma current.

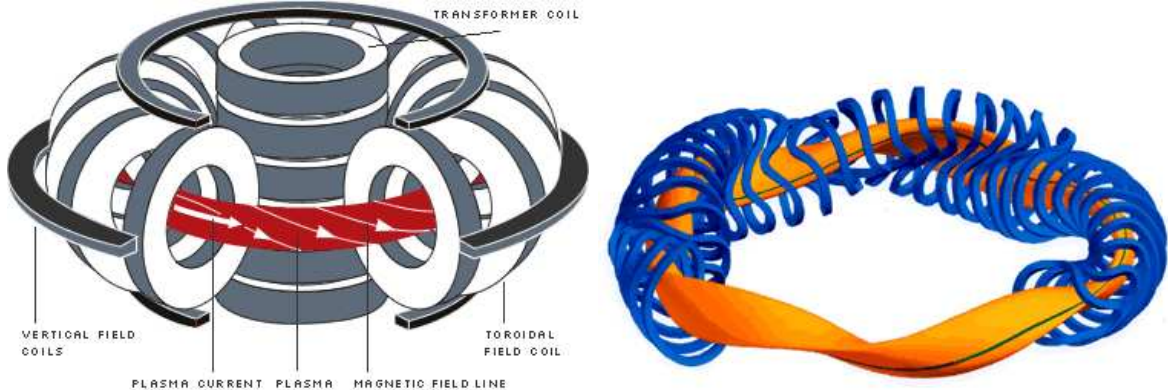


Figure 1.1.: Left: Schematic view of the coil system and magnetic field of a tokamak. Right: Field coils and a flux surface of the optimized stellarator W7-X. Source: IPP.

Due to the extreme conditions that are necessary to ignitite a fusion plasma, many engineering problems related to the construction of a fusion power plant have to be solved, e.g. concerning corrosion and tritium inventory of wall materials, structural issues due to the high magnetic fields, or the construction of superconducting field coils, the associated cooling systems and high power plasma heating systems. But also the fusion plasma itself poses many challenges, e.g. macroscopic drifts or instabilities of the plasma column caused by the interaction of the plasma and self-generated electromagnetic fields, which have to be controlled in order to avoid an unintentional termination of the plasma discharge.

Macroscopic plasma stability provided, the energy confinement time is set by the transport processes in the plasma. While a single charged particle would remain close to a given flux surface forever, collective effects in the plasma lead to a degradation of the confinement. There are two such effects: The first are particle collisions, which lead to a repositioning of the particle orbits (the so-called neoclassical transport); the second are self-generated gyroradius-scale electric and magnetic field fluctuations leading to a turbulent drift of the plasma (anomalous transport). In tokamaks (and probably also in optimized stellarators), the core transport is generally dominated by the latter, i.e. the anomalous contribution.

Because of its relevance for the energy confinement time, plasma microturbulence constitutes one of the key open issues in magnetic confinement fusion research. The identification and analysis of the processes that determine the anomalous transport will hopefully lead to a

## 1. Introduction

level of understanding that allows for reliable predictions and, eventually, the control of this phenomenon, which is one of the main obstacles on the way to a working fusion device.

Turbulence in general is considered to be one of the most important unsolved problems in physics. The most common system to study turbulence is the dynamics of fluids as described by the Navier-Stokes equation, which has been known since the first half of the 19th century. Although it has been an important topic in physics and mathematics for a long time, only very few theoretical approaches and results exist, demonstrating the complexity of the problem. With this background, it is not surprising that the much newer field of plasma microturbulence, which is described by considerably more complicated equations, has similar problems.

Despite significant progress in this area over the last years, fundamental questions remain, e.g., concerning the properties of the linear plasma microinstabilities or their nonlinear saturation mechanisms in some idealized limits, and even more so for realistic situations with several coexisting microinstabilities or additional physical effects, where several phenomena compete. Because of the complexity of the equations that describe the plasma in reactor-relevant geometries, even the linear instabilities can not be computed analytically. However, the microinstabilities and also the turbulent system can be studied by means of numerical simulations, which make all plasma properties accessible with a spatial resolution that can never be achieved in experiments. Furthermore, numerical simulations offer the possibility for parametric studies that would be very difficult or even impossible to do in an experimental setup. Direct simulations of plasma turbulence are numerically very demanding and a lot of work has to be invested in the development and the parallelization and optimization of such a simulation code. Still, depending on the problem under consideration, a single simulation requires computation times of thousands to several ten thousand CPU hours, so that these investigations have only become feasible with the advent of big parallel supercomputers in the last years.

The present work is structured as follows. After a short introduction concerning the description of magnetized plasmas, the general gyrokinetic equations will be presented. These equations will then be prepared for a numerical treatment by adapting them to the  $\delta f$  flux tube approach and normalizing them in a very general fashion. In Chapter 3, the GENE code, which solves the gyrokinetic equations numerically will be discussed, with a special emphasis on the aspects that have been added or improved considerably in the course of this PhD project. The GENE code will be used for the investigations of all following chapters, starting with investigations of linear phenomena in Chapter 4, where the nontrivial structure of the eigenvalue surfaces in parameter space will be discussed.

The remaining chapters then deal with plasma microturbulence and the induced anomalous transport. In Chapter 5, the saturation of pure trapped electron mode (TEM) turbulence will be discussed, based on a study of the statistical properties of the  $\vec{E} \times \vec{B}$  nonlinearity. In the following chapter, the idealization of a vanishing ion temperature gradient will be dropped and the coexistence of TEM and ion temperature gradient (ITG) mode turbulence will be studied, merging the pure TEM turbulence of Chapter 5 and pure ITG turbulence often found in the literature to a more complex but more realistic scenario. In Chapter 7, some of the first results for ITG turbulence in the W7-X stellarator will be presented, first in the adiabatic electron limit and then with a full gyrokinetic treatment of both electrons and ions, demonstrating the progress in the description of systems with complicated realistic geometries. In the last chapter, the key results of this thesis will be summarized and a short outlook will be given.

## 2. Gyrokinetics

Plasmas in magnetic confinement fusion experiments are very hot and dilute. Collisions therefore only play a subdominant role. This implies that the usage of standard fluid descriptions is not justified, and kinetic effects have to be taken into account. Although so-called gyrofluid models, which try to incorporate kinetic effects in a fluid context, can be useful for some applications, the most accurate and straightforward approach for the description of plasma microturbulence, which is the subject of this thesis, is to retain the velocity space dependence of the distribution function in the evolution equation of the plasma.

The core temperatures of fusion plasmas are of the order of 100 million Kelvin, corresponding to a thermal energy of approximately 15 keV. This is still small compared to the rest mass of the electrons of about 500 keV, so that relativistic effects can be safely neglected. Furthermore, the main constituents, deuterium, tritium and helium, and remaining impurities up to the atomic number of argon are fully ionized at these temperatures, so that neutral particles and the associated ionization/neutralization processes can be neglected as well.

Thus, in order to describe the processes occurring in the core region of a fusion experiment, the classical, non-relativistic motion of electrons and (at least one) fully ionized ion species in the presence of an external magnetic field has to be considered, the charge of the plasma constituents leading to collective effects like the self-generation of additional electromagnetic fields or single-particle effects like scattering. The equations for the time evolution of the six-dimensional particle distribution functions in space and velocity space and Maxwell's equations, which relate the velocity space moments of the distribution functions to the (self-generated) electromagnetic fields, form a closed system of equations.

The computational effort to numerically solve this system of equations would still be totally out of scope for present day supercomputers, since it describes phenomena covering a huge range of spatial and temporal scales, from light waves to macroscopic plasma instabilities. It is therefore essential to confine the equations to the space and time scales that are really of interest for the microturbulence considered here.

The strong magnetic fields of approximately three to five Tesla used in magnetic confinement fusion lead to a fast gyration of the charged particles around the magnetic field lines. This fast gyromotion is of no practical interest, since only the comparatively slow drift of the gyrocenters results in a net cross-field transport of particles or heat that deteriorates confinement. In coordinates that are aligned with the magnetic field, this fast gyromotion can be removed analytically from the (collisionless) Vlasov equation, which is then formulated in terms of the distribution functions of the gyrocenters rather than the corresponding particles. The electromagnetic fields can be dealt with in two different ways. The simplest approximation is to use the value at the position of the gyrocenter, which is known as the drift kinetic approach. A more sophisticated approach is to average the fields over the gyroangle. The resulting equations are known as the gyrokinetic equations, which are today the standard paradigm for the

## 2. Gyrokinetics

description of plasma microturbulence. For an overview and a modern formulation of the derivation, see [6].

Although they provide a significant reduction of the problem, the nonlinear gyrokinetic equations are still challenging to solve numerically. To minimize the computational effort, the distribution function is usually split into a static, Maxwellian background plus fluctuations. This greatly improves the possibilities for a numerical solution of the equations, but separating the background distribution function from the fluctuations also removes important features like the plasma current, so that the equations for the fluctuations do not describe the evolution of e.g. the magnetic flux surfaces. This evolution is well described by MHD, and since the time scales for the evolution of the equilibrium are much larger than the corresponding micro-turbulent time scales, the MHD equilibrium is usually assumed to be static over the simulation time. This leads to a hierarchy of models. First, an MHD equilibrium is reconstructed from experimental data or projections, then the obtained data for temperature and density profiles, equilibrium magnetic field  $B_0$ , etc., are used as input for the gyrokinetic description.

### 2.1. Basic description of a plasma

A single particle of charge  $q$  and mass  $m$  moving in electric and magnetic fields is subject to Coulomb and Lorentz forces. In Hamiltonian mechanics, the time evolution of the canonical variables  $\vec{x}$  and  $\vec{p}$  (different from the kinetic momentum  $\vec{p} - q\vec{A}$  in the presence of a magnetic vector potential) is given by the Poisson bracket  $\dot{\vec{x}} = \{\vec{x}, H\}$  and analogous for  $\vec{p}$ , with the Hamiltonian

$$H = \frac{p^2}{2m} + q\phi(\vec{x})$$

( $\phi$  is an external electrostatic potential).

A formal description of the whole plasma [7], which consists of a macroscopic number  $N$  of particles obeying the equations of motion for the single particle, taking into account the electromagnetic forces on each particle resulting from the distribution and motion of all other particles, is given by the Liouville equation for the  $N$ -particle distribution function  $\rho(\vec{x}_1, \dots, \vec{x}_N, \vec{p}_1, \dots, \vec{p}_N, t)$  of the canonical variables  $\vec{x}$  and  $\vec{p}$ ,

$$\frac{d\rho}{dt} = \left( \frac{\partial}{\partial t} + \sum_j \{\vec{q}_j, H\} \cdot \frac{\partial}{\partial \vec{q}_j} + \sum_j \{\vec{p}_j, H\} \cdot \frac{\partial}{\partial \vec{p}_j} \right) \rho = 0, \quad j = 1, \dots, N$$

where  $\{\}$  is the Poisson bracket and the Hamiltonian is given by

$$H = \sum_j \left[ \frac{p_j^2}{2m_j} + q_j \phi(\vec{x}_j) \right] + \sum_{i < j} \frac{q_i q_j}{|\vec{x}_i - \vec{x}_j|}. \quad (2.1)$$

This equation is of course useless for practical purposes; it has to be reduced to an equation for a one particle distribution function  $F(\vec{x}, \vec{v}, t)$ . This leads to the BBGKY (Bogoliubov, Born, Green, Kirkwood, Yvon) hierarchy, where the equation for the one-particle distribution

## 2.1. Basic description of a plasma

function contains the two particle distribution function, the equation for the two-particle distribution function contains the three-particle distribution function etc. Truncating the hierarchy by neglecting all particle correlations leads to the Vlasov equation,

$$\frac{dF(\vec{x}, \vec{v}, t)}{dt} = \left( \frac{\partial}{\partial t} + \dot{\vec{x}} \cdot \frac{\partial}{\partial \vec{x}} + \dot{\vec{v}} \cdot \frac{\partial}{\partial \vec{v}} \right) F(\vec{x}, \vec{v}, t) = 0 \quad (2.2)$$

(with the appropriate expressions for  $\dot{\vec{x}}, \dot{\vec{v}}$ ). In this case, the discreteness of the plasma is fully neglected and the only remaining interaction of the plasma particles (stemming from the last term of the Hamiltonian 2.1 and now hidden in  $\dot{\vec{x}}, \dot{\vec{v}}$ ), is the interaction with the collectively generated electric and magnetic fields, which are given by velocity space moments of the (continuous) distribution functions of the different species.

Closing the BBGKY hierarchy at higher order adds terms to the Vlasov equation which describe collisions between the discrete constituents of the plasma. These contributions can be considered subdominant for the very hot and dilute plasmas occurring in magnetic confinement fusion and are therefore often neglected; however, they constitute an important element in the context of comprehensive, predictive transport simulations. To obtain a manageable expression for the collision operator, three-particle and higher order correlations are neglected, which is justified given the low densities. The approximation that will be used in the following is the Landau-Boltzmann operator, which is derived by neglecting the three particle effects altogether and truncating the BBGKY hierarchy at the second order (see, e.g. [8]). With this assumption of purely binary collisions, the full collision operator entering the time evolution of species  $j$  (often called test particle species in this context) is given by the sum of the contributions  $C(F_j, F_{j'})$  arising from collisions with all species  $j'$  (field particles) in the system:

$$C_j(F) = \sum_{j'} C(F_j, F_{j'}). \quad (2.3)$$

Because the interaction between individual plasma particles is caused by long-range, plasma-shielded Coulomb forces, the effect of these binary collisions are predominantly small-angle (i.e. Fokker-Planck) deflections. In the derivation of an explicit form of the operator (also see [8]), an integral over the Coulomb potential has to be evaluated

$$\gamma_{jj'} = 2\pi q_j^2 q_{j'}^2 \int_0^\infty dr \frac{1}{r}.$$

This integral suffers from logarithmic divergences at very large and very small separations. The first occurs because shielding effects due to a third particle have been neglected, the second because the assumption of weak coupling (i.e. small deflection angles) breaks down at small separations, so that both divergences can be avoided by a physically motivated limitation of the integral bounds. Because it is difficult to find an algebraic expression for this so-called Coulomb logarithm  $\ln \Lambda_c$ , usually approximate numerical values are used. These are tabulated e.g. in [9], and the above expression becomes  $\gamma_{jj'} = 2\pi q_j^2 q_{j'}^2 \ln \Lambda_c$ .

## 2. Gyrokinetics

With this, the Landau-Boltzmann collision operator for the distribution function  $F_j$  of species  $j$  scattering off  $F_{j'}$  is [8, 10]

$$C(F_j, F_{j'}) = \frac{\partial}{\partial \vec{v}} \cdot \frac{\gamma_{jj'}}{m_j} \int d^3 v' \mathbf{U} \cdot \left( \frac{F_{j'}}{m_j} \frac{\partial}{\partial \vec{v}} F_j - \frac{F_j}{m'_j} \frac{\partial}{\partial \vec{v}'} F_{j'} \right),$$

with the abbreviations

$$\mathbf{U} = \frac{u^2 - \vec{u}\vec{u}}{u^3}, \quad \vec{u} = \vec{v} - \vec{v}'.$$

Because  $C$  is written as the velocity space divergence of a velocity space flux, particle number conservation is obvious, it also conserves energy and momentum. For an easier evaluation, the contributions to the collision operator can also be written as

$$C(F_j, F_{j'}) = \frac{\partial}{\partial \vec{v}} \cdot (\mathbf{D} \cdot \frac{\partial}{\partial \vec{v}} - \vec{R}) F_j \quad (2.4)$$

where the diffusion tensor  $\mathbf{D}$  and the dynamical friction  $\vec{R}$  are functions of the Rosenbluth potentials  $G$  and  $H$

$$\begin{aligned} \mathbf{D} &= \frac{\gamma_{jj'}}{m_j^2} \frac{\partial^2 G_{j'}}{\partial \vec{v} \partial \vec{v}} & \vec{R} &= \frac{2\gamma_{jj'}}{m_j m_{j'}} \frac{\partial H_{j'}}{\partial \vec{v}} \\ G_{j'}(\vec{v}) &= \int d^3 v' F_{j'} u & H_{j'}(\vec{v}) &= \int d^3 v' F_{j'} \frac{1}{u}. \end{aligned} \quad (2.5)$$

## 2.2. Geometry and coordinates

It is important to realize that the dynamics and the associated structures of magnetized plasmas described by the gyrokinetic equations are strongly anisotropic. The Lorentz force does not alter the particle dynamics parallel to the magnetic field, i.e. up to magnetic mirror forces, the particles move freely with their thermal velocity. In contrast to that, the mobility of the gyrocenters perpendicular to the magnetic field is strongly reduced; only the relatively slow  $\nabla B$ , curvature, and  $\vec{E} \times \vec{B}$  drifts remain. This leads to a strong anisotropy of the structures occurring in a fusion plasma – the parallel correlation length (typically of several ten meters) being much larger than the perpendicular one (typically of the order of a few centimeters). As in many other physical systems, the choice of an appropriate coordinate system that takes into account this anisotropy is crucial for an efficient description. In the present case, the coordinate system should be aligned with the background magnetic field. By this means, the anisotropy can be exploited to perform analytic approximations (like the gyroaveraging that will be described below), but also simplifications concerning a numerical solution of the resulting evolution equations. By choosing different numerical schemes and resolutions for the physically different directions; the number of grid points in the parallel direction can be reduced by 2-3 orders of magnitude and the constraints on the time step for explicit schemes are relaxed significantly (see Sec. 3.4.2). The construction of these field aligned coordinate systems can be quite involved, since the coordinate systems here have to be curvilinear with a defining metric  $g$  that depends on the position in the torus. A good overview of field aligned coordinate systems used in fusion research can be found in [11].

### 2.2.1. Flux tube approximation

Even with field aligned coordinates, it is virtually impossible to perform a plasma micro-turbulence simulation with the grid size required to resolve a full torus (a so-called global simulation) on a present day supercomputer; systematic studies, which require the comparison of several simulations, are therefore only possible if the simulation domain is reduced significantly.

A concept that is widely used in this context is the flux tube approach [12, 13, 14]. In this approximation, that will be used throughout this work, a magnetic field line is followed an integer number of poloidal turns around the torus; for a tokamak with its axisymmetric and therefore two-dimensional equilibrium, all variations on a flux surface are sampled after one turn already. A curved and sheared box around this central field line is then taken as simulation domain, and the equilibrium quantities are Taylor expanded to first order in the perpendicular coordinates around the central field line. The values and first derivatives, together with the metric coefficients that describe the shaping of the box, are then considered to be constant over the perpendicular extent of the simulation domain; only parallel variations are taken into account. This local approximation is justified if the radial extent of the box is small compared to the machine size.

The temperature, density, and pressure of the equilibrium are constant on a flux surface, their parallel dependence can therefore be neglected and they are completely determined by two scalars in this approximation, namely their value on the field line and their radial gradient.

As mentioned above, the magnetic geometry is not calculated self-consistently with the turbulent fluctuations, but taken as input from an analytical or numerical solution of the Grad-Shafranov equation [15, 16, 5]. A description of the procedure to numerically extract the relevant quantities from numerical MHD equilibria is given in [17]; this procedure is implemented in the TRACER code, which interfaces with GENE and can be used to extract the geometric information from MHD reconstructions of assumed or experimentally measured profiles, from present and future experiments like ASDEX Upgrade, JET, NCSX, W7-X, or NSTX. A widely used, although strictly speaking inconsistent analytical model is the  $s - \alpha$  equilibrium that will be discussed in detail in Sec. 2.9.1.

Since in the flux tube approximation, the simulation domain does not cover the full extent of the system, its boundaries do not correspond to physical boundaries. It is therefore very important to define suitable boundary conditions that keep the effects of this artificial reduction as small as possible. To be able to write the radial gradients in a simple form and to easily compute the important radial fluxes, the  $x$  direction is chosen to be a flux surface label, i.e. to be perpendicular to the flux surface that contains the central field line. The  $z$  direction is the parallel direction and  $y$  labels the field lines on a flux surface.

In the perpendicular  $x$  and  $y$ , i.e. radial and binormal directions, periodic boundary conditions

$$F(x + L_x, y, z) = F(x, y, z), \quad F(x, y + L_y, z) = F(x, y, z)$$

(and analogous for the electromagnetic fields) are assumed,  $L_x$  and  $L_y$  are the lengths of the simulation domain in the corresponding directions. These boundary conditions are consistent with the local approximation introduced above and automatically ensure that heat and particles, which leave the simulation domain due to the various drifts, are replenished at the

## 2. Gyrokinetics

opposite side of the simulation domain. Moreover, this assumption prevents the accumulation of heat or particles at certain radial positions, so that the average radial gradients are not changed in the simulation.

Note that the perpendicular box lengths  $L_x, L_y$  have to be big enough to accommodate all structures created in the simulation. More specifically, the box lengths have to be bigger than the correlation lengths of the turbulent fields in the corresponding directions, otherwise the boundary condition can lead to unphysical effects like very high values of transport due to end-to-end radial streamers of the electrostatic potential. With these periodic boundary conditions, it is possible to choose a Fourier representation for the  $x$  and  $y$  directions, which gives a relatively simple representation of the gyroaveraging procedure (see below).

To sample the whole flux surface of a two dimensional (tokamak) equilibrium, the simulation domain follows the field line one poloidal turn around the torus, the poloidal angle can therefore be used to parametrize the parallel direction  $z$ . Since the microinstabilities and the associated turbulent fluctuations usually peak at the low field (outboard) side, the matching of the two ends of the flux tube is normally done at the high field (i.e. inboard) side to reduce numerical effects of the boundary condition. In general, the two ends of the simulation domain, which are at the same poloidal position do not coincide toroidally, but because of the axisymmetry in the case of tokamaks or because of discrete toroidal symmetries combined with a suitable value of  $q_0$  and potentially more poloidal turns in the case of stellarators, (pseudo-) periodic boundary conditions are assumed.

One important complication arises from the finite radial extent of the simulation domain in the presence of finite magnetic shear  $\hat{s} = \frac{x_0}{q_0} \frac{\partial q_0}{\partial x}$  ( $x_0$  is the radial coordinate of the central flux surface): Starting at the outboard side ( $z = 0$ ) with a rectangular perpendicular cross section, the simulation domain gets distorted in opposite binormal directions for ( $z \rightarrow -\pi$ ) and ( $z \rightarrow \pi$ ). The two perpendicular surfaces with  $z = \pm\pi$  then have to be matched. From symmetry considerations, there are the following constraints on the metric:

$$g^{xx}(\pi) = g^{xx}(-\pi) \quad g^{yz}(\pi) = g^{yz}(-\pi) \quad g^{zz}(\pi) = g^{zz}(-\pi) \quad J(\pi) = J(-\pi).$$

The metric elements  $g^{xy}$  and  $g^{yy}$  do not have to be periodic, but because of the relation for  $J$  (and  $g^{xz} = 0$  for tokamaks), the Jacobian of the  $(x, y)$  submatrix,  $g^{xx}g^{yy} - (g^{xy})^2$ , has to be periodic.

The shearing of the simulation domain corresponds to an  $x$ -dependent shift in the  $y$  direction. Differences of the metric elements at ends of the flux tube can therefore only occur due to a coordinate transformation  $y' = y + S(x)$ . The shift  $S(x)$  is (in line with the local approximation defined above) Taylor expanded to first order,  $S(x) = S_0 + \eta(x - x_0)$ , with  $x \in [0, L_x]$ . Strictly speaking, the constant part of the shift,  $S_0$  which accounts for the fact that the ends of the central field line of the flux tube are in general at different toroidal positions, only disappears if  $S_0$  is a multiple of  $L_y$  and the periodicity is exploited, but for tokamaks it can be neglected due to the axisymmetry and for stellarators if special conditions are met (see Sec. 7.1), which is always assumed in the following. The remaining part of the shift, which describes a linear radial shearing of the simulation domain, can not be neglected, the

## 2.2. Geometry and coordinates

associated transformation can be expressed as a matrix in the  $(x, y, z)$  coordinates,

$$\hat{S} = \begin{bmatrix} 1 & -\eta & 0 \\ 0 & 1 & 0 \\ 0 & 0 & 1 \end{bmatrix}. \quad (2.6)$$

With the general form of the metric tensor,

$$g = \begin{bmatrix} g^{xx} & g^{xy} & 0 \\ g^{xy} & g^{yy} & g^{yz} \\ 0 & g^{yz} & g^{zz} \end{bmatrix}, \quad (2.7)$$

matching the ends of the flux tube means

$$g(-\pi) \stackrel{!}{=} \hat{S}(\eta)^T \cdot g(\pi) \cdot \hat{S}(\eta), \quad (2.8)$$

which can be used to determine the relation between the shift parameter  $\eta$  and the elements of the metric tensor. The condition for the  $(x, y)$  components reads

$$g^{xy}(\pi) = g^{xy}(-\pi) + \eta g^{xx}(-\pi),$$

so that

$$\eta = \frac{g^{xy}(\pi) - g^{xy}(-\pi)}{g^{xx}(\pi)}.$$

With the above periodicity constraints, this simultaneously satisfies the  $(y, y)$  component of the equation. Note that this shift parameter is the local shear integrated over one poloidal turn, or  $2\pi$  times the global shear [18].

With the definition

$$\begin{aligned} f(k_x, k_y) &= \frac{1}{L_x L_y} \int_0^{L_x} \int_0^{L_y} dx dy e^{-i(k_x x + k_y y)} f(x, y), \\ f(x, y) &= \sum_{k_x, k_y} e^{i(k_x x + k_y y)} f(k_x, k_y), \end{aligned}$$

the boundary condition in direct space can be transformed to Fourier space (the  $x$ -dependent, because shifted  $y$  bounds of the simulation domain are  $y_1 = -\eta(x - x_0)$  and  $y_2 = L_y - \eta(x - x_0)$ )

$$\begin{aligned} F(x, y, \pi) &= F(x, y - \eta(x - x_0), -\pi) \\ \int_0^{L_x} \int_0^{L_y} F(x, y, \pi) e^{-ik_x x} e^{-ik_y y} dx dy &= \int_0^{L_x} \int_{y_1}^{y_2} F(x, y - \eta(x - x_0), -\pi) e^{-ik_x x} e^{-ik_y y} dx dy \\ \int_0^{L_x} \int_0^{L_y} F(x, y, \pi) e^{-ik_x x} e^{-ik_y y} dx dy &= \int_0^{L_x} \int_0^{L_y} F(x, y', -\pi) e^{-i(k_x + \eta k_y)x} e^{-ik_y y'} e^{ik_y \eta x_0} dx dy', \end{aligned}$$

implying that the  $k_y$  shift in direct space corresponds to a  $k_x$  shift in Fourier space:

$$F(k_x, k_y, \pi) = F(k_x + \eta k_y, k_y, -\pi) e^{ik_y \eta x_0}. \quad (2.9)$$

## 2. Gyrokinetics

The finiteness of the box in the  $x$  and  $y$  directions leads to a discretization of the wavevector,

$$k_x = m k_x^{\min}, \quad k_y = n k_y^{\min}$$

with

$$k_x^{\min} = 2\pi/L_x, \quad k_y^{\min} = 2\pi/L_y, \quad m, n \in \mathbb{Z}.$$

This constrains condition 2.9, since the combination  $m k_x^{\min} + \eta n k_y^{\min}$  also has to be a multiple of  $k_x^{\min}$ . This means that  $n \eta k_y^{\min} / k_x^{\min}$  must be integer for all  $y$  mode numbers  $n$ , so that the condition

$$N = \frac{\eta k_y^{\min}}{k_x^{\min}} = \frac{\eta L_x}{L_y}, \quad N \in \mathbb{Z}$$

has to be fulfilled. This also implies that the phase factor in Eq. (2.9) is

$$e^{ik_y \eta x_0} = e^{inN k_x^{\min} L_x / 2} = e^{i\pi n N} = (-1)^{nN}$$

which combined gives the final parallel boundary condition

$$F(k_x, k_y, \pi) = (-1)^{nN} F(k'_x, k_y, -\pi), \quad \text{with } k'_x = (m + nN) k_x^{\min}. \quad (2.10)$$

This completes the definition of the local flux tube approximation, which will be used throughout this work.

### 2.2.2. Guiding-center coordinates

In strongly magnetized plasmas, the dynamics perpendicular to the magnetic field is dominated by a fast gyromotion. To separate this very fast gyration from the more relevant drifts, the field-aligned guiding-center coordinates  $\vec{X}$  and suitable velocity space coordinates are introduced. The transformation between guiding center and particle coordinates involves the vectorial gyroradius  $\vec{r}$ ,

$$\vec{x} = \vec{X} + \vec{r}(\theta), \quad (2.11)$$

which can be parametrized as

$$\vec{r}(\theta) = (\cos \theta \vec{e}_x + \sin \theta \vec{e}_y) \rho_j$$

for perpendicular (x,y) coordinates, where

$$\rho_j = \frac{v_{\perp}}{|\Omega_j|} = \frac{c}{|q_j|} \sqrt{\frac{2m_j \mu}{B_0}} \quad \text{and} \quad \Omega_j = \frac{q_j B_0}{m_j c}$$

are the gyroradius and Larmor frequency of species  $j$ . Since  $\vec{r}$  is perpendicular to the magnetic field, the parallel direction  $z$  is not transformed ( $z = Z$ ).

### 2.3. General gyrokinetic equations

A natural choice for the velocity space coordinates is, besides the gyroangle  $\theta$ , the velocity  $v_{\parallel}$  parallel to the magnetic field and the magnetic moment

$$\mu = \frac{m_j v_{\perp}^2}{2B_0},$$

which turns out to be the first adiabatic invariant of the (collisionless) Vlasov equation. The perpendicular velocity vector is given by

$$\vec{v}_{\perp}(\theta) = v_{\perp} \frac{\partial}{\partial \theta} (\cos \theta \vec{e}_x + \sin \theta \vec{e}_y) = v_{\perp} (-\sin \theta \vec{e}_x + \cos \theta \vec{e}_y),$$

which completely defines the relation between the different velocity space coordinates,

$$\begin{aligned} v_{\parallel} &= v_z & v_x &= -\sqrt{\frac{2B_0 \mu}{m_j}} \sin \theta \\ \mu &= \frac{m_j v_{\perp}^2}{2B_0} = \frac{m_j (v_x^2 + v_y^2)}{2B_0} & v_y &= \sqrt{\frac{2B_0 \mu}{m_j}} \cos \theta \\ \theta &= \arctan \left( -\frac{v_x}{v_y} \right) & v_z &= v_{\parallel}. \end{aligned}$$

As is obvious from Eq. (2.11), the complete phase space transformation matrix for  $\vec{z} = (\vec{x}, v_x, v_y, v_z) \rightarrow \vec{Z} = (\vec{X}, v_{\parallel}, \mu, \theta)$  has nonvanishing  $(x, \theta)$  and  $(y, \theta)$  entries, which means that the transformation mixes spatial and velocity space coordinates. However, the gyrocenter transformation does not affect the parallel direction, so that the  $z, v_{\parallel}$  submatrix of the transformation is the unit matrix. Dropping the trivial  $z$  direction, the Jacobi matrix for the transformation reads

$$\mathbf{G} = \begin{bmatrix} \frac{\partial X}{\partial v_x} & \frac{\partial Y}{\partial v_x} & \frac{\partial v_{\parallel}}{\partial v_x} & \frac{\partial \mu}{\partial v_x} & \frac{\partial \theta}{\partial v_x} \\ \frac{\partial X}{\partial v_y} & \frac{\partial Y}{\partial v_y} & \frac{\partial v_{\parallel}}{\partial v_y} & \frac{\partial \mu}{\partial v_y} & \frac{\partial \theta}{\partial v_y} \\ \frac{\partial X}{\partial v_z} & \frac{\partial Y}{\partial v_z} & \frac{\partial v_{\parallel}}{\partial v_z} & \frac{\partial \mu}{\partial v_z} & \frac{\partial \theta}{\partial v_z} \end{bmatrix} = \frac{1}{v_{\perp}} \begin{bmatrix} 0 & \rho_j & 0 & -2\mu \sin \theta & -\cos \theta \\ -\rho_j & 0 & 0 & 2\mu \cos \theta & -\sin \theta \\ 0 & 0 & v_{\perp} & 0 & 0 \end{bmatrix}. \quad (2.12)$$

If the coordinates of the  $(x, y)$  plane are not orthogonal, this has to be taken into account by applying an additional coordinate transformation related to the metric defined in the last section. The velocity space Jacobian  $J_v = B_0/m_j$ , which appears in the new velocity space integration element  $d^3v \rightarrow J_v dv_{\parallel} d\mu d\theta$ , is not affected by this additional transformation.

After the transformation to guiding-center coordinates, the gyromotion is separated from the remaining dynamics and described solely by the  $\theta$  coordinate. Since this gyromotion, as mentioned above, is not relevant for transport processes and other quantities of interest, it can now be removed by an average over the  $\theta$  coordinate.

## 2.3. General gyrokinetic equations

In the plasmas of magnetic confinement fusion experiments, the motion of the particles perpendicular to the strong background magnetic field can be viewed as a superposition of a fast

## 2. Gyrokinetics

gyration and a slow drift of the gyrocenters. In a Hamiltonian description of the single particle motion, this splitting into gyration and drift can be achieved by a pseudocanonical coordinate transformation, such that the gyroangle, which is one of the new, noncanonical variables, does only appear in higher order corrections to the equations of motion of the other five variables, if these are expanded in the gyrokinetic ordering parameter  $\epsilon = \rho_{\text{ref}}/L_{\text{ref}}$ , which corresponds to the (small) ratio of a typical gyroradius to a typical scale of the nonuniformities of the equilibrium magnetic field. This leads to an (approximate) decoupling of the variables and the very fast time evolution of the gyroangle, which is irrelevant for many questions concerning cross-field transport in plasmas, can be neglected. The Lie perturbation methods that are used in this procedure have been introduced to plasma physics by Littlejohn [19, 20, 21], and the gyrokinetic equations in the present form have been derived in [22, 23, 24].

The derivation of the equations is not repeated here, instead, the collisionless gyrokinetic equations in Gaussian cgs units are taken from [25], which is based on the references given above. A modern and pedagogical introduction to gyrokinetics can be found in [6, 26]. The equation for the gyrocenter distribution function  $F_j(\vec{X}, v_{\parallel}, \mu)$  of a species  $j$  is

$$\frac{\partial F_j}{\partial t} + \left( v_{\parallel} \vec{b}_0 + \frac{B_0}{B_{0\parallel}^*} (\vec{v}_{E \times B} + \vec{v}_{\nabla B_0} + \vec{v}_c) \right) \cdot \left( \vec{\nabla} F_j + \frac{1}{m_j v_{\parallel}} \left( q_j \vec{E}_1 - \mu \vec{\nabla} (B_0 + \bar{B}_{1\parallel}) \right) \frac{\partial F_j}{\partial v_{\parallel}} \right) = \langle C_j(F) \rangle, \quad (2.13)$$

where bars denote gyroaveraging and the gyroaveraged collision operator  $\langle C_j(F) \rangle$ , that has been added with respect to [25], is discussed below.

The expressions for the drifts are

$$\begin{aligned} \vec{v}_{E \times B} &= \frac{c}{B_0} \vec{b}_0 \times \vec{\nabla} \chi_j \\ \vec{v}_{\nabla B_0} &= \frac{\mu}{m_j \Omega_j} \vec{b}_0 \times \vec{\nabla} B_0 \\ \vec{v}_c &= \frac{v_{\parallel}^2}{\Omega_j} (\vec{\nabla} \times \vec{b}_0)_{\perp} = \frac{v_{\parallel}^2}{\Omega_j B_0} (\vec{b}_0 \times \vec{\nabla} B_0) + \frac{4\pi v_{\parallel}^2}{\Omega_j B_0^2} (\vec{b}_0 \times \vec{\nabla} p_0) \\ &= \frac{v_{\parallel}^2}{\Omega_j B_0} \left( \vec{b}_0 \times \left( \vec{\nabla} B_0 + \frac{4\pi}{B_0} \vec{\nabla} p_0 \right) \right) \end{aligned} \quad (2.14)$$

with the abbreviations  $\chi_j = \bar{\phi} - \frac{1}{c} v_{\parallel} \bar{A}_{1\parallel} + \frac{1}{q_j} \mu \bar{B}_{1\parallel}$  and  $B_{0\parallel}^* = \vec{b}_0 \cdot (\vec{\nabla} \times (\vec{A}_0 + \frac{m_j c}{q_j} v_{\parallel} \vec{b}_0))$ ; note that in the derivation of the expression for  $\vec{v}_c$ , the MHD equilibrium condition  $\vec{\nabla} p = \frac{1}{c} \vec{j}_{\perp} \times \vec{B}_0$  has been used.

The perturbed fields are given by the pre-Maxwell equations:

$$\begin{aligned} \vec{\nabla} \cdot \vec{E}_1 &= -\nabla^2 \phi = 4\pi \rho & \vec{\nabla} \times \vec{E}_1 &= -\frac{1}{c} \frac{\partial}{\partial t} \vec{B}_1 \\ \vec{\nabla} \times \vec{B}_1 &= \frac{4\pi}{c} \vec{j} & \vec{\nabla} \cdot \vec{B}_1 &= 0. \end{aligned} \quad (2.15)$$

## 2.4. The $\delta f$ splitting

Note that the constant parallel current density of the equilibrium that was used to define the geometry should not be contained in  $\vec{j}$ .

This system of equations is closed by the expressions for the charge and current densities,

$$\begin{aligned}\rho(\vec{x}) &= \sum_j q_j \int F_j^*(\vec{x}, \vec{v}) d^3 v & j_{\parallel}(\vec{x}) &= \sum_j q_j \int v_{\parallel} F_j^*(\vec{x}, \vec{v}) d^3 v \\ \vec{j}_{\perp}(\vec{x}) &= \sum_j q_j \int \vec{v}_{\perp} F_j^*(\vec{x}, \vec{v}) d^3 v,\end{aligned}$$

where  $F^*(\vec{x}, \vec{v})$  is the distribution function at the particle position. These velocity space moments can be computed from the distribution function of the gyrocenters in the respective coordinates,  $F(X, v_{\parallel}, \mu, \theta)$ , by applying the transformation

$$\begin{aligned}M(\vec{x}) &= \sum_j q_j \int K(\vec{v}) F_j^*(\vec{x}, \vec{v}) d^3 v \quad (\text{with } K(\vec{v}) = (1, v_{\parallel}, v_{\perp}) \text{ for } M = (\rho, j_{\parallel}, j_{\perp})) \\ &\rightarrow \sum_j q_j \int K(v_{\parallel}, \mu, \theta) \delta(\vec{X} + \vec{r} - \vec{x}) T^* F_j(\vec{X}, v_{\parallel}, \mu, \theta) d^3 X J_v dv_{\parallel} d\mu d\theta,\end{aligned}\quad (2.16)$$

that involves the pull-back operator  $T^*$ , which Lie-transforms the scalar fields back to particle phase space.

The collision operator  $C_j(F)$  given by Eqs. (2.3) and (2.4) was intended for non-magnetized plasmas, but its application to magnetized plasmas is justified if the characteristic gyroradii of the different species are larger than the Debye length [27], which is always given for the high temperature fusion plasmas considered here. While the Lie transformation has been used to remove the fast gyroangle dependence of the left hand side of the evolution equation (2.13), the gyroangle dependence of the collision operator is retained and has to be removed by gyroaveraging, denoted by the brackets. Because the approximations that will be applied to the system in the next sections will simplify expression (2.4) for the collision operator considerably, the transformation to gyrocenter variables and the gyroaveraging is postponed to a later section of this chapter.

## 2.4. The $\delta f$ splitting

In order to reduce the computational effort and to separate the macroscopic evolution of the plasma from the microturbulence, the full distribution function of the gyrocenters is split into a static background distribution function  $F_0$  (with the key properties of the MHD equilibrium) plus a perturbation  $f$  (named  $\delta f$  in previous presentations; here, the  $\delta$  is dropped for clarity). Formally, the background distribution function is of order one, the perturbed distribution function of order  $\epsilon = \rho_{\text{ref}}/L_{\text{ref}}$ .

Note that in the definition of the field aligned coordinates, the equilibrium magnetic field  $B_0$  has been used, which (at least in the case of tokamaks) is not identical to the field from the external coils but has a significant contribution from the plasma current of the equilibrium. By using field aligned coordinates, the equilibrium current has already been taken into account. It

## 2. Gyrokinetics

therefore has to be removed from the distribution function to obtain a consistent description; this is also achieved with the  $\delta f$  splitting.

The effect of the  $\delta f$  splitting on the equation for the distribution function, the field equations and the collision operator will be discussed in the following subsections.

### 2.4.1. Equation for the distribution function

The splitting  $F = F_{0j} + f_j$  applied to Eq. (2.13) gives

$$\begin{aligned} \langle C_j(F) \rangle &= \frac{\partial F_{0j}}{\partial t} + \frac{\partial f_j}{\partial t} + \left( v_{\parallel} \vec{b}_0 + \frac{B_0}{B_{0\parallel}^*} (\vec{v}_{\nabla B_0} + \vec{v}_c) + \frac{B_0}{B_{0\parallel}^*} \vec{v}_{E \times B} \right) \\ &\quad \cdot \left( \vec{\nabla} F_{0j} - \frac{\mu}{m_j v_{\parallel}} \frac{\partial F_{0j}}{\partial v_{\parallel}} \vec{\nabla} B_0 + \frac{1}{m_j v_{\parallel}} \left( q_j \vec{E}_1 - \mu \vec{\nabla} \bar{B}_{1\parallel} \right) \frac{\partial F_{0j}}{\partial v_{\parallel}} \right) \\ &\quad + \left( v_{\parallel} \vec{b}_0 + \frac{B_0}{B_{0\parallel}^*} (\vec{v}_{E \times B} + \vec{v}_{\nabla B_0} + \vec{v}_c) \right) \\ &\quad \cdot \left( \vec{\nabla} f_j + \frac{1}{m_j v_{\parallel}} \left( q_j \vec{E}_1 - \mu \vec{\nabla} (B_0 + \bar{B}_{1\parallel}) \right) \frac{\partial f_j}{\partial v_{\parallel}} \right). \end{aligned}$$

Collecting the terms that are of zeroth order in  $\epsilon$  gives

$$\frac{\partial F_{0j}}{\partial t} + v_{\parallel} \vec{b}_0 \cdot \left( \vec{\nabla} F_{0j} - \frac{\mu}{m_j v_{\parallel}} \frac{\partial F_{0j}}{\partial v_{\parallel}} \vec{\nabla} B_0 \right) = \langle C_j(F_0) \rangle. \quad (2.17)$$

Note that the  $\frac{B_0}{B_{0\parallel}^*} (\vec{v}_{\nabla B_0} + \vec{v}_c) \cdot \left( \vec{\nabla} F_{0j} - \frac{\mu}{m_j v_{\parallel}} \frac{\partial F_{0j}}{\partial v_{\parallel}} \vec{\nabla} B_0 \right)$  terms are of first order, even though they do not contain  $f_j$ . This is because the gradients of the equilibrium quantities  $F_{0j}, B_0$  are proportional to  $1/L_{\text{ref}}$ , the drift velocities to  $\rho_{\text{ref}}$ , and the terms under consideration therefore to  $\epsilon = \rho_{\text{ref}}/L_{\text{ref}}$ . The equation for the perturbation, including these terms reads

$$\begin{aligned} \langle C_j(f) \rangle &= \frac{\partial f_j}{\partial t} + \frac{B_0}{B_{0\parallel}^*} (\vec{v}_{E \times B} + \vec{v}_{\nabla B_0} + \vec{v}_c) \cdot \left( \vec{\nabla} F_{0j} - \frac{\mu}{m_j v_{\parallel}} \frac{\partial F_{0j}}{\partial v_{\parallel}} \vec{\nabla} B_0 \right) \\ &\quad + \left( v_{\parallel} \vec{b}_0 + \frac{B_0}{B_{0\parallel}^*} (\vec{v}_{E \times B} + \vec{v}_{\nabla B_0} + \vec{v}_c) \right) \\ &\quad \cdot \left( \frac{1}{m_j v_{\parallel}} \left( q_j \vec{E}_1 - \mu \vec{\nabla} \bar{B}_{1\parallel} \right) \frac{\partial F_{0j}}{\partial v_{\parallel}} + \vec{\nabla} f_j + \frac{1}{m_j v_{\parallel}} \left( q_j \vec{E}_1 - \mu \vec{\nabla} (B_0 + \bar{B}_{1\parallel}) \right) \frac{\partial f_j}{\partial v_{\parallel}} \right) \\ &= \frac{\partial g_j}{\partial t} + \frac{B_0}{B_{0\parallel}^*} (\vec{v}_{E \times B} + \vec{v}_{\nabla B_0} + \vec{v}_c) \cdot \left( \vec{\nabla} F_{0j} - \frac{\mu}{m_j v_{\parallel}} \frac{\partial F_{0j}}{\partial v_{\parallel}} \vec{\nabla} B_0 \right) \\ &\quad + v_{\parallel} \vec{b}_0 \cdot \vec{\Gamma}_j + \frac{B_0}{B_{0\parallel}^*} (\vec{v}_{E \times B} + \vec{v}_{\nabla B_0} + \vec{v}_c) \cdot \vec{\Gamma}_j - \frac{\mu}{m} \vec{b}_0 \cdot \vec{\nabla} B_0 \frac{\partial f_j}{\partial v_{\parallel}}. \end{aligned} \quad (2.18)$$

In the last step, trilinear terms in  $f_j$ , which are of third order in  $\epsilon$ , the subdominant  $v_{\parallel}$  nonlinearity (see [28, 29]) and the nonlinear part of the collision operator (see below) have been

neglected. With the same argument as above, the term  $\vec{v}_c \cdot \vec{\nabla} B_0 \frac{\partial f_j}{\partial v_{\parallel}}$ , although linear in  $f_j$ , is quadratic in  $\epsilon$  and therefore also neglected. The only nonlinear (and second order) term that is considered is the  $\vec{E} \times \vec{B}$  nonlinearity, which is the dominant term of this kind. Furthermore, the abbreviations

$$\begin{aligned} g_j &= f_j - \frac{q_j}{m_j c} \frac{\partial F_{0j}}{\partial v_{\parallel}} \bar{A}_{1\parallel} \\ \vec{\Gamma}_j &= \vec{\nabla} f_j - \frac{1}{m_j v_{\parallel}} \frac{\partial F_{0j}}{\partial v_{\parallel}} \left( q_j \vec{\nabla} \bar{\Phi} + \mu \vec{\nabla} \bar{B}_{1\parallel} \right) \\ &= \vec{\nabla} g_j - \frac{q_j}{m_j v_{\parallel}} \frac{\partial F_{0j}}{\partial v_{\parallel}} \vec{\nabla} \chi_j + \frac{q_j}{m_j c} \bar{A}_{1\parallel} \vec{\nabla} \frac{\partial F_{0j}}{\partial v_{\parallel}}, \end{aligned}$$

have been introduced, both of them are linear in the distribution function  $f_j$ .

## 2.4.2. Field equations

The equilibrium magnetic field  $\vec{B}_0$ , which was used to define the coordinate system, is not just the field from the toroidal field coils, but already contains the poloidal contribution from the (background) plasma current  $j_{0\parallel}$ , which means that the  $\delta f$  splitting of the fields has already been used implicitly to define the geometry. Maxwell's equations (2.15) have been formulated for the perturbed fields only. For the electric field, it is assumed that the equilibrium contribution vanishes, in the equation for the perturbed magnetic field,  $\vec{j}$  does not contain the equilibrium current.

Besides this, the field equations are affected through the closing equations (2.16), where a pull-back operator to first order in the gyrokinetic expansion

$$T^* F_j = F_{0j} + f_j + \frac{q_j}{m_j c} \tilde{A}_{1\parallel} \frac{\partial F_{0j}}{\partial v_{\parallel}} + \frac{1}{B_0} (q_j \tilde{\phi}_1 - \frac{q_j v_{\parallel}}{c} \tilde{A}_{1\parallel} - \mu \bar{B}_{1\parallel}) \frac{\partial F_0}{\partial \mu} \quad (2.19)$$

(taken from [25]) can be used and higher order terms can be neglected.

## 2.4.3. Collision operator

It is easy to see that the  $\delta f$ -splitting  $F = F_0 + \delta f$  divides the contributions (2.4) and therefore the collision operator (2.3) into four different parts:

$$\langle C_j(F) \rangle = \sum_{j'} \langle C(F_{0j}, F_{0j'}) \rangle + \sum_{j'} \langle C(f_j, F_{0j'}) \rangle + \sum_{j'} \langle C(F_{0j}, f_{j'}) \rangle + \sum_{j'} \langle C(f_j, f_{j'}) \rangle \quad (2.20)$$

The first term (denoted  $\langle C_j(F_0) \rangle$  above) describes the collisional interactions between the different background distribution functions. The second and third terms are the constituents of the linearized collision operator for the perturbed distribution function,

$$\langle C_j(f) \rangle = \sum_{j'} \langle C(f_j, F_{0j'}) \rangle + \sum_{j'} \langle C(F_{0j}, f_{j'}) \rangle.$$

## 2. Gyrokinetics

Its first term describes the effect of  $f_j$  scattering off the background distribution function  $F_{0j'}$  and will be calculated in the following. The complementary second term, describing particles of the background distribution function scattering off particles of the perturbed distribution function, provides for conservation of energy and parallel momentum, which has to be obeyed by any operator describing elastic collisions. The last term is quadratic in  $\epsilon$ , it describes scattering between two perturbed distribution functions and is neglected.

### 2.5. Choice of $F_{0j}$

For the background distribution function, a local (and unshifted) Maxwell distribution is chosen, i.e.

$$F_{0j} = \left( \frac{m_j}{2\pi T_{0j}} \right)^{\frac{3}{2}} n_{0j} e^{-\frac{m_j v_{\parallel}^2/2 + \mu B_0}{T_{0j}}}.$$

The derivatives of this background distribution can be computed analytically:

$$\begin{aligned} \vec{\nabla} F_{0j} &= \left[ \vec{\nabla} \left( \frac{m_j}{2\pi T_{0j}} \right)^{\frac{3}{2}} \right] n_{0j} e^{-\frac{m_j v_{\parallel}^2/2 + \mu B_0}{T_{0j}}} + \left( \frac{m_j}{2\pi T_{0j}} \right)^{\frac{3}{2}} [\vec{\nabla} n_{0j}] e^{-\frac{m_j v_{\parallel}^2/2 + \mu B_0}{T_{0j}}} \\ &\quad + \left( \frac{m_j}{2\pi T_{0j}} \right)^{\frac{3}{2}} n_{0j} e^{-\frac{m_j v_{\parallel}^2/2 + \mu B_0}{T_{0j}}} \left[ -\vec{\nabla} \frac{m_j v_{\parallel}^2/2 + \mu B_0}{T_{0j}} \right] \\ &= -\frac{3}{2T_{0j}} F_{0j} \vec{\nabla} T_{0j} + \frac{1}{n_{0j}} F_{0j} \vec{\nabla} n_{0j} + F_{0j} \left( \frac{m_j v_{\parallel}^2}{2T_{0j}^2} \vec{\nabla} T_{0j} - \frac{\mu}{T_{0j}} \vec{\nabla} B_0 + \frac{\mu B_0}{T_{0j}^2} \vec{\nabla} T_{0j} \right) \\ &= F_{0j} \left( \frac{1}{n_{0j}} \vec{\nabla} n_{0j} + \left( \frac{m_j v_{\parallel}^2}{2T_{0j}} + \frac{\mu B_0}{T_{0j}} - \frac{3}{2} \right) \frac{1}{T_{0j}} \vec{\nabla} T_{0j} - \frac{\mu}{T_{0j}} \vec{\nabla} B_0 \right) \\ \partial_{v_{\parallel}} F_{0j} &= -\frac{m_j v_{\parallel}}{T_{0j}} F_{0j} \\ \partial_{\mu} F_{0j} &= -\frac{B_0}{T_{0j}} F_{0j}. \end{aligned}$$

This transforms the term

$$\begin{aligned} \left( \vec{\nabla} F_{0j} - \frac{\mu}{m_j v_{\parallel}} \frac{\partial F_{0j}}{\partial v_{\parallel}} \vec{\nabla} B_0 \right) &= \vec{\nabla} F_{0j} + \frac{\mu}{T_{0j}} F_{0j} \vec{\nabla} B_0 \\ &= F_{0j} \left( \frac{1}{n_{0j}} \vec{\nabla} n_{0j} + \left( \frac{m_j v_{\parallel}^2}{2T_{0j}} + \frac{\mu B_0}{T_{0j}} - \frac{3}{2} \right) \frac{1}{T_{0j}} \vec{\nabla} T_{0j} \right), \quad (2.21) \end{aligned}$$

so that the zeroth order equation (2.17) now reads

$$\frac{\partial F_{0j}}{\partial t} + v_{\parallel} F_{0j} \vec{b}_0 \cdot \left( \frac{1}{n_{0j}} \vec{\nabla} n_{0j} + \left( \frac{m_j v_{\parallel}^2}{2T_{0j}} + \frac{\mu B_0}{T_{0j}} - \frac{3}{2} \right) \frac{1}{T_{0j}} \vec{\nabla} T_{0j} \right) = \langle C_j(F_0) \rangle. \quad (2.22)$$

The density and temperatures are constant on a flux surface,  $\vec{b}_0 \cdot \vec{\nabla} n_{0j} = \vec{b}_0 \cdot \vec{\nabla} T_{0j} = 0$ , and the collisions between the background distribution functions can be neglected (see below) so that all terms of Eq. (2.22) are zero and the equation is indeed fulfilled.

The integrals

$$\begin{aligned} \int F_{0j} d^3v &= \int \left( \frac{m_j}{2\pi T_{0j}} \right)^{3/2} n_{0j} e^{-\frac{m_j v^2}{2T_{0j}}} d^3v = n_{0j} \\ \int F_{0j} dv_{\parallel} d\mu &= \frac{n_{0j} m_j}{2\pi B} \end{aligned} \quad (2.23)$$

will also be useful in the following.

### 2.5.1. Equation for the distribution function

This choice of  $F_0$  changes Eq. (2.18) for the distribution function through relation (2.21),

$$\begin{aligned} \langle C_j(f) \rangle &= \frac{\partial g_j}{\partial t} + \frac{B_0}{B_{0\parallel}^*} F_{0j} (\vec{v}_{E \times B} + \vec{v}_{\nabla B_0} + \vec{v}_c) \cdot \left( \frac{1}{n_{0j}} \vec{\nabla} n_{0j} + \left( \frac{m_j v_{\parallel}^2}{2T_{0j}} + \frac{\mu B_0}{T_{0j}} - \frac{3}{2} \right) \frac{1}{T_{0j}} \vec{\nabla} T_{0j} \right) \\ &\quad + v_{\parallel} \vec{b}_0 \cdot \vec{\Gamma}_j + \frac{B_0}{B_{0\parallel}^*} (\vec{v}_{E \times B} + \vec{v}_{\nabla B_0} + \vec{v}_c) \cdot \vec{\Gamma}_j - \frac{\mu}{m} \vec{b}_0 \cdot \vec{\nabla} B_0 \frac{\partial f_j}{\partial v_{\parallel}}, \end{aligned}$$

and introduces the gradients of the background distribution function, which will later on constitute the drive of the plasma microturbulence.

### 2.5.2. Field equations

With this choice for the background distribution function, the  $\tilde{A}_{1\parallel}$  terms in Eq. (2.19) cancel. This gives the relation

$$T^* F_j = F_{0j}(\vec{X}) + f_j(\vec{X}) + \frac{\mu}{T_{0j}} \bar{B}_{1\parallel}(\vec{X}) F_{0j}(\vec{X}) - \frac{q_j}{T_{0j}} (\phi(\vec{X} + \vec{r}) - \bar{\phi}(\vec{X})) F_{0j}(\vec{X})$$

which can be used to calculate the moments (2.16):

$$\begin{aligned} M(\vec{x}) &= \sum_j q_j \int K(v_{\parallel}, \mu, \theta) \delta(\vec{X} + \vec{r} - \vec{x}) (F_{0j}(\vec{X}) + f_j(\vec{X})) d^3X J_v dv_{\parallel} d\mu d\theta \\ &\quad - \sum_j q_j \int K(v_{\parallel}, \mu, \theta) \delta(\vec{X} + \vec{r} - \vec{x}) \frac{q_j}{T_{0j}} \phi(\vec{X} + \vec{r}) F_{0j}(\vec{X}) d^3X J_v dv_{\parallel} d\mu d\theta \\ &\quad + \sum_j q_j \int K(v_{\parallel}, \mu, \theta) \delta(\vec{X} + \vec{r} - \vec{x}) \left( \frac{\mu}{T_{0j}} \bar{B}_{1\parallel} + \frac{q_j}{T_{0j}} \bar{\phi}(\vec{X}) \right) F_{0j}(\vec{X}) d^3X J_v dv_{\parallel} d\mu d\theta \end{aligned}$$

## 2. Gyrokinetics

$$\begin{aligned}
&= \sum_j (q_j - \frac{q_j^2}{T_{0j}} \phi(\vec{x})) \int 2\pi J_v \langle K(v_\parallel, \mu, \theta) \rangle F_{0j} dv_\parallel d\mu \\
&\quad + \sum_j q_j \int 2\pi J_v \langle K(v_\parallel, \mu, \theta) f_j(\vec{x} - \vec{r}) \rangle dv_\parallel d\mu \\
&\quad + \sum_j \frac{q_j^2}{T_{0j}} \int 2\pi J_v \langle K(v_\parallel, \mu, \theta) \bar{\phi}(\vec{x} - \vec{r}) \rangle F_{0j} dv_\parallel d\mu \\
&\quad + \sum_j \frac{q_j}{T_{0j}} \int 2\pi J_v \langle K(v_\parallel, \mu, \theta) \mu \bar{B}_{1\parallel}(\vec{x} - \vec{r}) \rangle F_{0j} dv_\parallel d\mu .
\end{aligned}$$

The background distribution function only varies on macroscopic length scales which are bigger than the gyroradii. As a constant, it can therefore be extracted from the gyroaveraging bracket,  $\langle (\dots) F_{0j}(\vec{x} - \vec{r}) \rangle = \langle (\dots) \rangle F_{0j}$ .

The different contributions now have to be evaluated with the appropriate  $K$  for the different moments. The details of the more involved calculations can be found in Appendix A. The moments that are needed for the calculation of the density  $n$  are

$$\begin{aligned}
\int 2\pi J_v F_{0j} dv_\parallel d\mu &= n_{j0} \\
\int 2\pi J_v \langle f_j(\vec{x} - \vec{r}) \rangle dv_\parallel d\mu &= \frac{2\pi B_0}{m_j} \sum_{k_x, k_y} e^{i\vec{k}_\perp \cdot \vec{x}_\perp} \int J_0(\lambda_j) f_j(\vec{k}_\perp) dv_\parallel d\mu \\
\int 2\pi J_v \langle \bar{\phi}(\vec{x} - \vec{r}) \rangle F_{0j} dv_\parallel d\mu &= n_{0j} \sum_{k_x, k_y} e^{i\vec{k}_\perp \cdot \vec{x}_\perp} \phi(k_x, k_y) \Gamma_0(b_j) \\
\int 2\pi J_v \langle \mu \bar{B}_{1\parallel}(\vec{x} - \vec{r}) \rangle F_{0j} dv_\parallel d\mu &= \frac{T_{0j}}{B_0} n_{0j} \sum_{k_x, k_y} e^{i\vec{k}_\perp \cdot \vec{x}_\perp} B_{1\parallel}(k_x, k_y) \Delta(b_j) .
\end{aligned}$$

In these expressions,  $\vec{x}_\perp = (x, y)$  and the perpendicular wave vector  $k_\perp = (k_x, k_y)$  have been introduced. The moments needed for the calculation of the parallel current density  $j_\parallel$  are

$$\begin{aligned}
\int 2\pi J_v v_\parallel F_{0j} dv_\parallel d\mu &= 0 \\
\int 2\pi J_v v_\parallel \langle f_j(\vec{x} - \vec{r}) \rangle dv_\parallel d\mu &= \frac{2\pi B_0}{m_j} \sum_{k_x, k_y} e^{i\vec{k}_\perp \cdot \vec{x}_\perp} \int v_\parallel J_0(\lambda_j) f_j(\vec{k}) dv_\parallel d\mu \\
\int 2\pi J_v v_\parallel \langle \bar{\phi}(\vec{x} - \vec{r}) \rangle F_{0j} dv_\parallel d\mu &= 0 \\
\int 2\pi J_v v_\parallel \langle \mu \bar{B}_{1\parallel}(\vec{x} - \vec{r}) \rangle F_{0j} dv_\parallel d\mu &= 0 .
\end{aligned}$$

The major simplifications here are due to the fact that  $F_{0j}$  is an even function of  $v_\parallel$  while the electromagnetic fields and the gyroaveraging do not depend on  $v_\parallel$  at all, so that the integrals of the form  $a(\mu) \int v_\parallel F_{0j} dv_\parallel$  vanish.

## 2.5. Choice of $F_{0j}$

The moments needed for the perpendicular current density  $\vec{j}_\perp$  are

$$\begin{aligned} \int 2\pi J_v \langle \vec{v}_\perp \rangle F_{0j} dv_\parallel d\mu &= 0 \\ \int 2\pi J_v \langle \vec{v}_\perp f_j(\vec{x} - \vec{r}) \rangle dv_\parallel d\mu &= \frac{\pi(2B_0)^{3/2}}{m^{3/2}} \sum_{k_x, k_y} e^{i\vec{k}_\perp \cdot \vec{x}_\perp} i \frac{k_y \vec{e}_x - k_x \vec{e}_y}{k_\perp} \\ &\quad \cdot \int \sqrt{\mu} J_1(\lambda_j) f_j(k_x, k_y) dv_\parallel d\mu \\ \int 2\pi J_v \langle \vec{v}_\perp \bar{\phi}(\vec{x} - \vec{r}) \rangle F_{0j} dv_\parallel d\mu &= \frac{v_{Tj}^2 n_{0j}}{2\Omega_j} \sum_{k_x, k_y} e^{i\vec{k}_\perp \cdot \vec{x}_\perp} \phi(k_x, k_y) i(k_y \vec{e}_x - k_x \vec{e}_y) \Delta(b_j) \\ \int 2\pi J_v \mu \langle \vec{v}_\perp \bar{B}_{1\parallel}(\vec{x} - \vec{r}) \rangle F_{0j} dv_\parallel d\mu &= \frac{v_{Tj}^2 n_{0j} T_{0j}}{B_0 \Omega} \sum_{k_x, k_y} e^{i\vec{k}_\perp \cdot \vec{x}_\perp} B_{1\parallel}(k_x, k_y) i(k_y \vec{e}_x - k_x \vec{e}_y) \Delta(b_j). \end{aligned}$$

The abbreviations that have been used in these expressions (also introduced in Appendix A) are

$$\Delta(x) = \frac{\hat{I}_0(x) - \hat{I}_1(x)}{e^x} \quad \lambda_j = \sqrt{\frac{2B_0\mu}{m_j} \frac{k_\perp}{\Omega_j}} \quad b_j = \frac{v_{Tj}^2 k_\perp^2}{2\Omega_j^2}$$

( $\hat{I}_0$ ,  $\hat{I}_1$  are modified Bessel functions).

With these moments, it is now possible to give an explicit expression for the charge density

$$\begin{aligned} \rho(\vec{x}) &= \sum_j q_j n_{j0} - \sum_j \frac{q_j^2}{T_{0j}} \phi(\vec{x}) n_{j0} + \sum_{k_x, k_y} e^{i\vec{k}_\perp \cdot \vec{x}_\perp} \left[ \sum_j q_j \frac{2\pi B_0}{m_j} \int J_0(\lambda_j) f_j(\vec{k}_\perp) dv_\parallel d\mu \right. \\ &\quad \left. + \sum_j \frac{q_j^2}{T_{0j}} n_{0j} \phi(k_x, k_y) \Gamma_0(b_j) + \sum_j \frac{q_j}{B_0} n_{0j} B_{1\parallel}(k_x, k_y) \Delta(b_j) \right]. \end{aligned}$$

The charge density due to the equilibrium is assumed to be zero (quasineutrality), so that the first term vanishes,  $\sum_j q_j n_{j0} = 0$ . In the simpler Fourier space representation for the  $(x, y)$  plane (the  $z$  direction remains in direct space), the charge density therefore reads

$$\begin{aligned} \rho(\vec{k}) &= \sum_j q_j \frac{2\pi B_0}{m_j} \int J_0(\lambda_j) f_j(k_x, k_y) dv_\parallel d\mu + \sum_j \frac{q_j^2}{T_{0j}} n_{0j} (\Gamma_0(b_j) - 1) \phi(k_x, k_y) \\ &\quad + \sum_j \frac{q_j}{B_0} n_{0j} \Delta(b_j) B_{1\parallel}(k_x, k_y). \end{aligned}$$

The parallel current density in Fourier space is

$$j_\parallel(\vec{k}) = \sum_j q_j \frac{2\pi B_0}{m_j} \int v_\parallel J_0(\lambda_j) f_j(\vec{k}) dv_\parallel d\mu,$$

## 2. Gyrokinetics

the perpendicular current density is

$$\vec{j}_\perp(\vec{k}) = i(k_y \vec{e}_x - k_x \vec{e}_y) \left( \sum_j \frac{\pi q_j}{k_\perp} \left( \frac{2B_0}{m} \right)^{3/2} \int \sqrt{\mu} J_1(\lambda_j) f_j(k_x, k_y) dv_\parallel d\mu \right. \\ \left. + \sum_j \frac{q_j^2 n_{0j}}{m_j \Omega_j} \Delta(b_j) \phi(k_x, k_y) + \sum_j \frac{q_j v_T^2 n_{0j}}{B_0 \Omega} \Delta(b_j) B_{1\parallel}(k_x, k_y) \right).$$

Since the Vlasov equation is formulated in terms of the modified distribution function  $g$ , the charge and current densities are also rewritten as functions of  $g$ ,

$$\rho(\vec{k}) = \sum_j q_j \frac{2\pi B_0}{m_j} \int J_0(\lambda_j) g_j(k_x, k_y) dv_\parallel d\mu + \sum_j \frac{q_j^2}{T_{0j}} n_{0j} (\Gamma_0(b_j) - 1) \phi(k_x, k_y) \\ + \sum_j \frac{q_j}{B_0} n_{0j} \Delta(b_j) B_{1\parallel}(k_x, k_y) \\ j_\parallel(\vec{k}) = \sum_j q_j \frac{2\pi B_0}{m_j} \int v_\parallel J_0(\lambda_j) g_j(\vec{k}) dv_\parallel d\mu - A_{1\parallel}(\vec{k}) \sum_j q_j^2 \frac{2\pi B_0}{m_j c T_{0j}} \int v_\parallel^2 J_0^2(\lambda_j) F_{0j} dv_\parallel d\mu \\ \vec{j}_\perp(\vec{k}) = i(k_y \vec{e}_x - k_x \vec{e}_y) \left( \sum_j \frac{\pi q_j}{k_\perp} \left( \frac{2B_0}{m} \right)^{3/2} \int \sqrt{\mu} J_1(\lambda_j) g_j(k_x, k_y) dv_\parallel d\mu \right. \\ \left. + \sum_j \frac{q_j^2 n_{0j}}{m_j \Omega_j} \Delta(b_j) \phi(k_x, k_y) + \sum_j \frac{q_j v_T^2 n_{0j}}{B_0 \Omega} \Delta(b_j) B_{1\parallel}(k_x, k_y) \right). \quad (2.24)$$

Because of the  $v_\parallel$  symmetry of  $F_0$ , the additional terms in  $\rho$  and  $\vec{j}_\perp$  vanish and only  $j_\parallel$  is modified. The remaining  $F_0$  integral could be solved analytically, but since the moment of  $g$  will be computed numerically it is preferable treat this integral equivalently to ensure numerical cancellation.

### 2.5.3. Collision operator

The above choice for  $F_0$  also leads to significant analytical simplifications of the collision operator. The  $\langle C_j(F_0) \rangle$  term describes temperature equalization of the different background distribution functions, its contributions  $\langle C(F_{0j}, F_{0j'}) \rangle$  vanish identically for  $T_{0j} = T_{0j'}$ . For self-collisions, this is always fulfilled, but even for slightly different temperatures, this process is slower than the microturbulence time scales of interest and  $\langle C_j(F_0) \rangle$  can be neglected.

The terms entering  $\langle C(f_j, F_{0j'}) \rangle$  are simplified by analytically evaluating the Rosenbluth potentials. This has been done e.g. in [10] and yields

$$\mathbf{D}_{jj'} = \frac{\gamma_{jj'} n_{j'} T_{j'}}{m_j^2 m_{j'}} \frac{1}{v^3} \left[ \mathbf{1}_{\vec{v}} F_1(x) + 3 \frac{\vec{v} \vec{v}}{v^2} F_2(x) \right] \\ \vec{R}_{jj'} = \frac{\gamma_{jj'} n_{j'}}{m_j m_{j'}} \frac{\vec{v}}{v^3} F_3(x)$$

for the collisional diffusion and dynamical friction terms of Eq. 2.5. The abbreviations

$$\begin{aligned} F_1(x) &= x \frac{\text{derf}(x)}{\text{dx}} + (2x^2 - 1)\text{erf}(x) \\ F_2(x) &= (1 - \frac{2}{3}x^2)\text{erf}(x) - x \frac{\text{derf}(x)}{\text{dx}} \\ F_3(x) &= F_1(x) + 3F_2(x) = 2\text{erf}(x) - 2x \frac{\text{derf}(x)}{\text{dx}}, \end{aligned}$$

which contain the error function  $\text{erf}(x)$ , the normalized velocity  $x = v/v_{Tj'}$ , the prefactor  $\gamma_{jj'} = 2\pi q_j^2 q_{j'}^2 \ln \Lambda_c$  in Gaussian units and the unit matrix in velocity space,  $\mathbf{1}_{\vec{v}}$  have been introduced. Together, this gives

$$\langle C(f_j, F_{0j'}) \rangle = \frac{\gamma_{jj'} n_{j'}}{m_j m_{j'}} \left\langle \frac{\partial}{\partial \vec{v}} \cdot \left( \frac{T_{j'}}{m_j} \frac{1}{v^3} \left[ \mathbf{1}_{\vec{v}} F_1(x) + 3 \frac{\vec{v} \vec{v}}{v^2} F_2(x) \right] \cdot \frac{\partial}{\partial \vec{v}} - \frac{\vec{v}}{v^3} F_3(x) \right) f_j \right\rangle \quad (2.25)$$

The exact computation of the remaining  $\langle C(F_{0j}, f_{j'}) \rangle$  contributions to the linearized collision operator would be very expensive due to the  $\vec{v}$ -space convolution, which cannot be performed analytically in this case. Since the background distribution function is kept fixed in the  $\delta f$  approach anyway, an exact computation of this term can be avoided and it can be replaced by much simpler model terms

$$A_{j'j} = a_{j'j} F_{0j'} + b_{j'j} v_{\parallel} F_{0j'} + c_{j'j} v^2 F_{0j'}.$$

These terms are added to the evolution equation for species  $j'$  and account for the transfer of energy and momentum between species while observing particle conservation for each species individually. The conditions for  $A_{j'j}$  to restore the conservation properties read

$$\begin{aligned} \int d^3v A_{j'j} &= \int d^3v \langle C(f_j, F_{0j'}) \rangle = 0 \\ \int d^3v m_{j'} v_{\parallel} A_{j'j} &= -m_j K_{j'j}^{v_{\parallel}} = - \int d^3v m_j v_{\parallel} \langle C(f_j, F_{0j'}) \rangle \\ \int d^3v \frac{m_{j'}}{2} v^2 A_{j'j} &= -\frac{m_j}{2} K_{j'j}^E = - \int d^3v \frac{m_j}{2} v^2 \langle C(f_j, F_{0j'}) \rangle. \end{aligned} \quad (2.26)$$

With the abbreviations

$$B_{1j'} = \int d^3v F_{0j'} \quad B_{2j'} = \int d^3v v^2 F_{0j'} \quad B_{3j'} = \int d^3v v^4 F_{0j'} \quad B_{4j'} = \int d^3v v_{\parallel}^2 F_{0j'},$$

the model parameters of  $A_{j'j}$  can be determined,

$$a_{j'j} = \frac{m_j}{m_{j'}} \frac{B_{2j'} K_{j'j}^E}{B_{1j'} B_{3j'} - B_{2j'}^2} \quad b_{j'j} = -\frac{m_j}{m_{j'}} \frac{K_{j'j}^{v_{\parallel}}}{B_{4j'}} \quad c_{j'j} = -\frac{m_j}{m_{j'}} \frac{B_{1j'} K_{j'j}^E}{B_{1j'} B_{3j'} - B_{2j'}^2}.$$

Note that the energy contained in the electrostatic potential is conserved automatically if the densities of the different species are conserved. However, since the currents are not conserved by the collision operator (only the overall parallel momentum), the corresponding magnetic field fluctuations for  $\beta \neq 0$  are in general slightly modified.

## 2.6. Expansion of the vector expressions

In order to arrive at a form that is suitable for a numerical implementation, all vector expressions that appear in the equations for the (scalar) distribution function and electromagnetic fields, i.e. the dot and vector products, have to be expanded. The coordinates are field aligned, and the covariant entries of  $\vec{B}_0$  are chosen to be  $B_0^i = B^\phi \delta^{i3}$  (see [17]).

### 2.6.1. Equation for the distribution function

The (scalar) vector expressions that appear in the gyrokinetic Vlasov equation can be expressed in terms of the components

$$\begin{aligned} (\vec{b}_0 \times \vec{\nabla} A) \cdot \vec{C} &= J \epsilon_{ijk} g^{lj} g^{km} b_0^i (\partial_l A) C_m \stackrel{b_0^i \propto \delta^{i3}}{=} J b^3 (g^{1i} g^{2j} - g^{2i} g^{1j}) (\partial_i A) C_j \\ &= J b^3 (\gamma_1 ((\partial_1 A) C_2 - (\partial_2 A) C_1) \\ &\quad + (\gamma_2 \partial_1 A + \gamma_3 \partial_2 A) C_3 - (\partial_3 A) (\gamma_2 C_1 + \gamma_3 C_2)) \\ \vec{b}_0 \cdot \vec{\nabla} A &= b_0^i \partial_i A = b^3 \partial_3 A, \end{aligned} \tag{2.27}$$

where the abbreviations

$$\gamma_1 = g^{11} g^{22} - g^{21} g^{12} \quad \gamma_2 = g^{11} g^{23} - g^{21} g^{13} \quad \gamma_3 = g^{12} g^{23} - g^{22} g^{13}$$

for the geometric factors have been introduced. Since the parallel correlation lengths of the fluctuations are much larger than the perpendicular ones in a strongly magnetized plasma, parallel derivatives of the perturbed quantities can be neglected over perpendicular ones. Furthermore, the perpendicular derivatives of the equilibrium quantities can be neglected compared to the perpendicular derivatives of the fluctuating quantities. The vector expressions appearing in the Vlasov equation can therefore be written as

$$\begin{aligned} \vec{v}_{E \times B} \cdot \vec{\nabla} \{n, T\} &= J b^3 \frac{c}{B_0} (g^{1i} g^{2j} - g^{2i} g^{1j}) (\partial_i \chi) (\partial_j \{n, T\}) \\ &= - J b^3 \frac{c}{B_0} \gamma_1 \partial_y \chi \partial_x \{n, T\} \\ \vec{v}_{E \times B} \cdot \vec{\Gamma}_j &= J b^3 \frac{c}{B_0} (g^{1i} g^{2k} - g^{2i} g^{1k}) (\partial_i \chi) \Gamma_{jk} \\ &= J b^3 \frac{c}{B_0} \gamma_1 (\partial_x \chi \Gamma_{jy} - \partial_y \chi \Gamma_{jx}) \\ (\vec{v}_{\nabla B_0} + \vec{v}_c) \cdot \vec{\Gamma}_j &= J b^3 (g^{1i} g^{2k} - g^{2i} g^{1k}) \left( \left( \frac{\mu}{m_j \Omega_j} + \frac{v_\parallel^2}{\Omega_j B_0} \right) \partial_i B_0 + \frac{4\pi v_\parallel^2}{\Omega_j B_0^2} \partial_i p_0 \right) \Gamma_{jk} \\ &= J b^3 \left( \frac{\mu}{m_j \Omega_j} + \frac{v_\parallel^2}{\Omega_j B_0} \right) (\gamma_1 ((\partial_x B_0) \Gamma_{jy} - (\partial_y B_0) \Gamma_{jx}) \\ &\quad - \partial_z B_0 (\gamma_2 \Gamma_{jx} + \gamma_3 \Gamma_{jy})) + J b^3 \gamma_1 \frac{4\pi v_\parallel^2}{\Omega_j B_0^2} \partial_x p_0 \Gamma_{jy} \end{aligned}$$

## 2.6. Expansion of the vector expressions

$$\begin{aligned}
(\vec{v}_c + \vec{v}_{\nabla B_0}) \cdot \vec{\nabla} \{n, T\} &= Jb^3 \left( \frac{v_{\parallel}^2}{\Omega_j B_0} + \frac{\mu}{m_j \Omega_j} \right) (g^{1i} g^{2j} - g^{2i} g^{1j}) (\partial_i B_0) \partial_j \{n, T\} \\
&\quad + Jb^3 \frac{4\pi v_{\parallel}^2}{\Omega_j B_0^2} (g^{1i} g^{2j} - g^{2i} g^{1j}) \partial_i p_0 \partial_j \{n, T\} \\
&= - Jb^3 \left( \frac{v_{\parallel}^2}{\Omega_j B_0} + \frac{\mu}{m_j \Omega_j} \right) (\gamma_1 \partial_y B_0 + \gamma_2 \partial_z B_0) \partial_x \{n, T\} \\
\vec{b}_0 \cdot \vec{\Gamma}_j &= b^3 \Gamma_{jz} \\
\vec{b}_0 \cdot \vec{\nabla} B_0 &= b^3 \partial_z B_0.
\end{aligned}$$

The gyrokinetic equation for the distribution function

$$\begin{aligned}
\langle C_j(f) \rangle &= \frac{\partial g_j}{\partial t} - \frac{Jb^3 \gamma_1}{B_0} \frac{B_0}{B_{0\parallel}^*} F_{0j} c \partial_y \chi \left( \frac{1}{n_{0j}} \partial_x n_{0j} + \left( \frac{m_j v_{\parallel}^2}{2T_{0j}} + \frac{\mu B_0}{T_{0j}} - \frac{3}{2} \right) \frac{1}{T_{0j}} \partial_x T_{0j} \right) \\
&\quad - \frac{Jb^3 \gamma_1}{B_0} \frac{B_0}{B_{0\parallel}^*} F_{0j} \left( \frac{v_{\parallel}^2}{\Omega_j} + \frac{\mu B_0}{m_j \Omega_j} \right) \left( \partial_y B_0 + \frac{\gamma_2}{\gamma_1} \partial_z B_0 \right) \\
&\quad \cdot \left( \frac{1}{n_{0j}} \partial_x n_{0j} + \left( \frac{m_j v_{\parallel}^2}{2T_{0j}} + \frac{\mu B_0}{T_{0j}} - \frac{3}{2} \right) \frac{1}{T_{0j}} \partial_x T_{0j} \right) + v_{\parallel} b^3 \Gamma_{jz} \\
&\quad + \frac{Jb^3 \gamma_1}{B_0} \frac{B_0}{B_{0\parallel}^*} c (\partial_x \chi \Gamma_{jy} - \partial_y \chi \Gamma_{jx}) + \frac{Jb^3 \gamma_1}{B_0} \frac{B_0}{B_{0\parallel}^*} \left( \frac{\mu B_0}{m_j \Omega_j} + \frac{v_{\parallel}^2}{\Omega_j} \right) \\
&\quad \cdot \left( \left( \partial_x B_0 - \frac{\gamma_3}{\gamma_1} \partial_z B_0 \right) \Gamma_{jy} - \left( \partial_y B_0 + \frac{\gamma_2}{\gamma_1} \partial_z B_0 \right) \Gamma_{jx} \right) \\
&\quad + \frac{Jb^3 \gamma_1}{B_0} \frac{B_0}{B_{0\parallel}^*} \frac{4\pi v_{\parallel}^2}{\Omega_j B_0} \partial_x p_0 \Gamma_{jy} - \frac{\mu}{m} b^3 \partial_z B_0 \frac{\partial f_j}{\partial v_{\parallel}}
\end{aligned}$$

is now free of vector expressions.

### 2.6.2. Field equations

In the equation for the electrostatic potential, only the scalar product

$$k_{\perp}^2 = \vec{k}_{\perp} \cdot \vec{k}_{\perp} = g^{xx} k_x^2 + 2g^{xy} k_x k_y + g^{yy} k_y^2$$

has to be expanded. Gauss' law from Eq. (2.15) with the corresponding expression for the moment (2.24) gives

$$\begin{aligned}
k_{\perp}^2 \phi &= 4\pi \rho = \sum_j q_j \frac{8\pi^2 B_0}{m_j} \int J_0(\lambda_j) f dv_{\parallel} d\mu + \sum_j \frac{4\pi q_j^2}{T_{0j}} n_{0j} (\Gamma_0(b_j) - 1) \phi \\
&\quad + \sum_j \frac{4\pi q_j}{B_0} n_{0j} \Delta(b_j) B_{1\parallel},
\end{aligned}$$

## 2. Gyrokinetics

which can be rearranged to

$$\begin{aligned} \left( \frac{k_\perp^2}{4\pi} - \sum_j \frac{q_j^2}{T_{0j}} n_{0j} (\Gamma_0(b_j) - 1) \right) \phi - \left( \sum_j \frac{q_j}{B_0} n_{0j} \Delta(b_j) \right) B_{1\parallel} \\ = \sum_j q_j \frac{2\pi B_0}{m_j} \int J_0(\lambda_j) f dv_\parallel d\mu, \end{aligned} \quad (2.28)$$

showing that the equation for the electrostatic potential is coupled to the equation for  $B_{1\parallel}$ . To obtain an equation for  $B_{1\parallel}$ , Ampère's law Eq. (2.15) has to be split into a parallel and perpendicular component. Because parallel derivatives of fluctuation quantities are neglected, the left hand side of its perpendicular part,

$$(\vec{\nabla} \times \vec{B}_1)_\perp = \frac{4\pi}{c} \vec{j}_\perp,$$

can be simplified to

$$(\vec{\nabla} \times \vec{B}_1)_\perp = i[(k_y B_{1\parallel} - k_z B_{1x}) \vec{e}_x + (k_z B_{1x} - k_x B_{1\parallel}) \vec{e}_y] = i[k_y B_{1\parallel} \vec{e}_x - k_x B_{1\parallel} \vec{e}_y]$$

in Fourier space. With this simplification and the moment from Eq. (2.24), the perpendicular part of Ampère's law is

$$\begin{aligned} i[k_y \vec{e}_x - k_x \vec{e}_y] B_{1\parallel} &= \frac{4\pi}{c} i(k_y \vec{e}_x - k_x \vec{e}_y) \left( \sum_j \frac{\pi q_j}{k_\perp} \left( \frac{2B_0}{m} \right)^{3/2} \int \sqrt{\mu} J_1(\lambda_j) f dv_\parallel d\mu \right. \\ &\quad \left. + \sum_j \frac{q_j^2 n_{0j}}{m_j \Omega_j} \Delta(b_j) \phi + \sum_j \frac{q_j v_T^2 n_{0j}}{B_0 \Omega} \Delta(b_j) B_{1\parallel} \right). \end{aligned}$$

Further simplification gives

$$\begin{aligned} \left( - \sum_j \frac{q_j n_{0j}}{B_0} \Delta(b_j) \right) \phi + \left( \frac{1}{4\pi} - \sum_j \frac{v_T^2 m_j n_{0j}}{B_0^2} \Delta(b_j) \right) B_{1\parallel} \\ = \sum_j \frac{\pi q_j (2B_0)^{3/2}}{cm^{3/2} k_\perp} \int \sqrt{\mu} J_1(\lambda_j) f dv_\parallel d\mu, \end{aligned} \quad (2.29)$$

which together with Eq. (2.28) forms a solvable linear system of equations.

The parallel component of Ampère's law in the Coulomb gauge (i.e.  $\vec{\nabla} \cdot \vec{A}_1 = 0$ ) can be transformed into an equation for  $A_{1\parallel}$ ,

$$-\nabla^2 A_{1\parallel} = k_\perp^2 A_{1\parallel} = \frac{4\pi}{c} j_\parallel,$$

which (with  $j_\parallel$  inserted) gives

$$A_{1\parallel} = \frac{\sum_j \frac{8\pi^2 q_j B_0}{cm_j} \int v_\parallel J_0(\lambda_j) g_j(\vec{k}) dv_\parallel d\mu}{k_\perp^2 + \sum_j \frac{8\pi^2 q_j^2 B_0}{m_j c^2 T_{0j}} \int v_\parallel^2 J_0^2(\lambda_j) F_{0j} dv_\parallel d\mu}.$$

### 2.6.3. Collision operator

In order to obtain an explicit expression for the gyroaveraged collision operator in the coordinates used here, the derivatives occurring in expression (2.25) have to be transformed according to the coordinate transformation (2.12). As described above, for the linearized Landau-Boltzmann operator considered here, only the scattering of the perturbed distribution function off the Maxwellian background distribution functions is considered. The  $F_{0j}$  do not change on gyroradius scales, so that it is plausible that it does not matter whether  $f_j$  is evaluated at the particle position (as it initially occurs in the collision operator) or the gyrocenter position (which is much easier for calculations and will be used below). This turns out to be correct; a more sophisticated derivation of the gyroaveraged Landau-Boltzmann operator using a non-canonical Poisson bracket formalism and a subsequent expansion in  $\epsilon_\nu = \rho/\lambda_\nu$  (the ratio of gyroradius and the collisional mean free path) gives the same result, if isotropic field particles (i.e. background distribution function) are assumed and higher order corrections are neglected (see [27]). The coordinate transformation of the derivatives involves the expressions

$$\begin{aligned} \mathbf{G}^T \cdot \mathbf{1}_{\vec{v}} \cdot \mathbf{G} &= \frac{1}{v_\perp^2} \begin{bmatrix} 0 & -\rho_j & 0 \\ \rho_j & 0 & 0 \\ 0 & 0 & v_\perp \\ -2\mu \sin \theta & 2\mu \cos \theta & 0 \\ -\cos \theta & -\sin \theta & 0 \end{bmatrix} \cdot \mathbf{1}_{\vec{v}} \cdot \begin{bmatrix} 0 & \rho_j & 0 & -2\mu \sin \theta & -\cos \theta \\ -\rho_j & 0 & 0 & 2\mu \cos \theta & -\sin \theta \\ 0 & 0 & v_\perp & 0 & 0 \end{bmatrix} \\ &= \frac{1}{v_\perp^2} \begin{bmatrix} \rho_j^2 & 0 & 0 & -2\mu \rho_j \cos \theta & \rho_j \sin \theta \\ 0 & \rho_j^2 & 0 & -2\mu \rho_j \sin \theta & -\rho_j \cos \theta \\ 0 & 0 & v_\perp^2 & 0 & 0 \\ -2\mu \rho_j \cos \theta & -2\mu \rho_j \sin \theta & 0 & 4\mu^2 & 0 \\ \rho_j \sin \theta & -\rho_j \cos \theta & 0 & 0 & 1 \end{bmatrix}, \\ \mathbf{G}^T \cdot \vec{v} \cdot \mathbf{G} &= \mathbf{G}^T \cdot \begin{bmatrix} \sin^2 \theta & -\sin \theta \cos \theta & -\sin \theta \frac{v_\parallel}{v_\perp} \\ -\sin \theta \cos \theta & \cos^2 \theta & \cos \theta \frac{v_\parallel}{v_\perp} \\ -\sin \theta \frac{v_\parallel}{v_\perp} & \cos \theta \frac{v_\parallel}{v_\perp} & \frac{v_\parallel^2}{v_\perp^2} \end{bmatrix} \cdot \mathbf{G} \\ &= \begin{bmatrix} \rho_j^2 \cos^2 \theta & \rho_j^2 \sin \theta \cos \theta & -\rho_j \cos \theta v_\parallel & -2\rho_j \mu \cos \theta & 0 \\ \rho_j^2 \sin \theta \cos \theta & \rho_j^2 \sin^2 \theta & -\rho_j \sin \theta v_\parallel & -2\mu \rho_j \sin \theta & 0 \\ -\rho_j \cos \theta v_\parallel & -\rho_j \sin \theta v_\parallel & v_\parallel^2 & 2\mu v_\parallel & 0 \\ -2\mu \rho_j \cos \theta & -2\mu \rho_j \sin \theta & 2\mu v_\parallel & 4\mu^2 & 0 \\ 0 & 0 & 0 & 0 & 0 \end{bmatrix} \end{aligned}$$

and

$$\mathbf{G}^T \cdot \vec{v} = \begin{bmatrix} 0 & -\rho_j & 0 \\ \rho_j & 0 & 0 \\ 0 & 0 & v_\perp \\ -2\mu \sin \theta & 2\mu \cos \theta & 0 \\ -\cos \theta & -\sin \theta & 0 \end{bmatrix} \cdot \begin{bmatrix} -\sin \theta \\ \cos \theta \\ \frac{v_\parallel}{v_\perp} \end{bmatrix} = \begin{bmatrix} -\rho_j \cos \theta \\ -\rho_j \sin \theta \\ v_\parallel \\ 2\mu \\ 0 \end{bmatrix}.$$

## 2. Gyrokinetics

As indicated above, the coordinate transformation has reintroduced the dependence on the gyroangle  $\theta$ , which has to be removed explicitly. Taking  $f_j$  at the gyrocenter position and therefore out of the gyroaveraging bracket, the gyroaveraging  $\langle \cdot \rangle = \frac{1}{2\pi} \int_0^{2\pi} d\theta$  gives

$$\begin{aligned}\langle \mathbf{D}_{jj'} \rangle &= \frac{\gamma_{jj'} n_{j'} T_{j'}}{m_j^2 m_{j'}} \frac{1}{v^3} \left[ F_1 \begin{bmatrix} \frac{1}{\Omega_j^2} & 0 & 0 & 0 & 0 \\ 0 & \frac{1}{\Omega_j^2} & 0 & 0 & 0 \\ 0 & 0 & 1 & 0 & 0 \\ 0 & 0 & 0 & \frac{2m_j}{B_0} \mu & 0 \\ 0 & 0 & 0 & 0 & \frac{1}{v_\perp^2} \end{bmatrix} + 3 \frac{F_2}{v^2} \begin{bmatrix} \frac{\rho_j^2}{2} & 0 & 0 & 0 & 0 \\ 0 & \frac{\rho_j^2}{2} & 0 & 0 & 0 \\ 0 & 0 & v_\parallel^2 & 2\mu v_\parallel & 0 \\ 0 & 0 & 2\mu v_\parallel & 4\mu^2 & 0 \\ 0 & 0 & 0 & 0 & 0 \end{bmatrix} \right] \\ \langle \vec{R}_{jj'} \rangle &= \frac{\gamma_{jj'} n_{j'}}{m_j m_{j'}} \frac{1}{v^3} F_3(x) \begin{bmatrix} 0 \\ 0 \\ v_\parallel \\ 2\mu \\ 0 \end{bmatrix}\end{aligned}$$

for the collisional diffusion and dynamical friction. As intended, all terms coupling the dynamics of the gyroangle to the rest of the dynamics cancel, so that the  $\theta$  dimension can be neglected from now on. Furthermore, spatial part of  $\langle \vec{R} \rangle$  vanishes while the spatial part of  $\langle \mathbf{D} \rangle$  is completely decoupled from the velocity space and proportional to the unit matrix. This contribution  $\langle C_{jj'}^\perp \rangle$  to the collision operator describes perpendicular spatial diffusion due to the repositioning of the gyrocenter after a collision,

$$\langle C_{jj'}^\perp \rangle = \frac{\gamma_{jj'} n_{j'} T_{j'}}{m_j^2 m_{j'} \Omega_j^2} \frac{1}{v^5} \left( v^2 F_1 + \frac{3B_0\mu}{m_j} F_2 \right) \nabla_\perp^2 f_j,$$

and has also been described in [27, 30, 31]. The contribution in the  $\vec{V} = (v_\parallel, \mu)$  direction is

$$\langle C_{jj'}^\parallel \rangle = \frac{\partial}{\partial \vec{V}} \cdot \frac{\gamma_{jj'} n_{j'}}{m_j m_{j'}} \left( \frac{T_{j'}}{m_j v^5} \begin{bmatrix} \frac{2B_0\mu}{m_j} F_1 + v_\parallel^2 F_3 & 6\mu v_\parallel F_2 \\ 6\mu v_\parallel F_2 & \frac{2m_j}{B_0} v_\parallel^2 \mu F_1 + 4\mu^2 F_3 \end{bmatrix} \cdot \frac{\partial}{\partial \vec{V}} - \frac{F_3(x)}{v^3} \begin{bmatrix} v_\parallel \\ 2\mu \end{bmatrix} \right) f_j.$$

The dot products in the last expression are not expanded, since this conservation form can be used directly for the implementation of a finite volume scheme. As mentioned in Sec. 2.2.2, the guiding center transformation used here is based on orthogonal  $x$  and  $y$  coordinates. In general, an additional, purely spatial transformation in these coordinates is necessary, but because of the simple form of the spatial part of the collision operator, this reduces to the introduction of the metric in the computation of the perpendicular Laplacian.

## 2.7. Normalization

Finally, the equations have to be normalized. To this end, dimensional reference quantities are extracted from all physical parameters, like for example the mass,  $m_j = m_{\text{ref}} \hat{m}_j$ , so that  $\hat{m}_j = m_j / m_{\text{ref}}$  is dimensionless. In order for the constant prefactors  $\frac{Jb^3 \gamma_1}{B_0} = \frac{1}{JB^\phi}$  to vanish,

## 2.7. Normalization

the magnetic field  $B_0$  is normalized to  $B_{\text{ref}} = JB^\phi$  (see [17] on this issue). This implies that in contrast to all other reference quantities,  $B_0$  cannot be chosen arbitrarily and leads to the relations

$$\begin{aligned} \frac{Jb^3\gamma_1}{B_0} &= \frac{1}{JB^\phi} = \frac{1}{B_{\text{ref}}} \\ b^3 &= \frac{B^\phi}{B} = \frac{B^\phi}{\hat{B}_0 B_{\text{ref}}} = \frac{1}{J\hat{B}_0} = \frac{1}{L_{\text{ref}}\hat{J}\hat{B}_0}. \end{aligned} \quad (2.30)$$

In the following, all dimensional quantities that appear in the equations of the last section are normalized. The hats are dropped immediately; with the exception of the elementary charge  $e$ , which is used to normalize  $q_j$ , on the right hand side of the arrows only the reference quantities are dimensional, all other quantities, in particular the coordinates and all quantities with a species label, are then dimensionless. The external gradients and curvatures are normalized to the macroscopic normalization length  $L_{\text{ref}}$ .

$$\begin{array}{lll} x \rightarrow \rho_{\text{ref}}x & y \rightarrow \rho_{\text{ref}}y & k_x \rightarrow \frac{1}{\rho_{\text{ref}}}k_x \\ k_y \rightarrow \frac{1}{\rho_{\text{ref}}}k_y & J \rightarrow L_{\text{ref}}J & b^3 \rightarrow \frac{1}{L_{\text{ref}}JB_0} \\ z \rightarrow z & \gamma_1 \rightarrow \gamma_1 & v_{\parallel} \rightarrow c_{\text{ref}}v_{Tj}v_{\parallel} \\ \mu \rightarrow \frac{T_{\text{ref}}}{B_{\text{ref}}}T_{0j}\mu & B_0 \rightarrow B_{\text{ref}}B_0 & t \rightarrow \frac{L_{\text{ref}}}{c_{\text{ref}}}t \\ m_j \rightarrow m_{\text{ref}}m_j & T_{0j} \rightarrow T_{\text{ref}}T_{0j} & n_{0j} \rightarrow n_{\text{ref}}n_{0j} \\ q_j \rightarrow eq_j & \Omega_j \rightarrow \Omega_{\text{ref}}\Omega_j & \gamma_2 \rightarrow \frac{1}{L_{\text{ref}}}\gamma_2 \\ \gamma_3 \rightarrow \frac{1}{L_{\text{ref}}}\gamma_3 & B_{0\parallel}^* \rightarrow B_{\text{ref}}B_{0\parallel}^* & \end{array} \quad (2.31)$$

The normalization affects also composed quantities,

$$\begin{array}{lll} c_{\text{ref}} = \sqrt{T_{\text{ref}}/m_{\text{ref}}} & \rho_{\text{ref}} = c_{\text{ref}}/\Omega_{\text{ref}} & \Omega_{\text{ref}} = \frac{eB_{\text{ref}}}{m_{\text{ref}}c} \\ \Omega_j = \frac{q_j B_0}{m_j} & v_{Tj} = \sqrt{\frac{2T_{0j}}{m_j}}. & \end{array} \quad (2.32)$$

Note that this normalization is very general and allows for an arbitrary number of species. If only one ion species plus electrons are considered, normalization quantities with index  $s$  ( $\rho_s$ ,  $c_s$ ) are often used in the literature, these are equal to  $\rho_{\text{ref}}$ ,  $c_{\text{ref}}$  for  $T_{\text{ref}} = T_e$ ,  $m_{\text{ref}} = m_i$ .

After this normalization of the basic parameters, the distribution functions and electromag-

## 2. Gyrokinetics

netic fields are normalized as well,

$$\begin{aligned}
g_j &\rightarrow \frac{\rho_{\text{ref}}}{L_{\text{ref}}} \frac{n_{\text{ref}}}{c_{\text{ref}}^3} \frac{n_{0j}}{v_{Tj}^3} g_j & F_{0j} &\rightarrow \frac{n_{\text{ref}}}{c_{\text{ref}}^3} \frac{n_{0j}}{v_{Tj}^3} F_0 \\
\Phi &\rightarrow \frac{\rho_{\text{ref}}}{L_{\text{ref}}} \frac{T_{\text{ref}}}{e} \Phi & A_{\parallel} &\rightarrow \frac{\rho_{\text{ref}}}{L_{\text{ref}}} B_{\text{ref}} \rho_{\text{ref}} A_{\parallel} \\
(\Gamma_{jx}, \Gamma_{jy}, \Gamma_{jz}) &\rightarrow \frac{n_{\text{ref}}}{c_{\text{ref}}^3 L_{\text{ref}}} \frac{n_{0j}}{v_{Tj}^3} (\Gamma_{jx}, \Gamma_{jy}, \rho_{\text{ref}} \Gamma_{jz}) & B_{\parallel} &\rightarrow \frac{\rho_{\text{ref}}}{L_{\text{ref}}} B_{\text{ref}} B_{\parallel}. \tag{2.33}
\end{aligned}$$

The dependent quantity  $f_j$  is normalized as  $g_j$ ,  $\chi_j$  as  $\phi$ . Together, this implies that the collision operator (and the conservation term  $A_{jj'}$ ) is normalized as

$$\langle C(f) \rangle \rightarrow \frac{\rho_{\text{ref}}}{L_{\text{ref}}^2} \frac{n_{\text{ref}}}{c_{\text{ref}}^2} \frac{n_{0j}}{v_{Tj}^3} \langle C(f) \rangle. \tag{2.34}$$

and gives the normalized relations

$$\begin{aligned}
F_{0j} = F_0 &= \pi^{-3/2} e^{-(v_{\parallel}^2 + \mu B_0)} & f_j &= g_j - \frac{2q_j}{m_j v_{Tj}} v_{\parallel} \bar{A}_{1\parallel} F_{0j} \\
\chi_j &= \bar{\phi}_j - v_{Tj} v_{\parallel} \bar{A}_{1\parallel j} + \frac{T_{0j}}{q_j} \mu \bar{B}_{1\parallel} & \vec{\Gamma}_j &= \vec{\nabla} f_j + F_{0j} \left[ \sigma_j \vec{\nabla} \bar{\phi}_j + \mu \vec{\nabla} \bar{B}_{1\parallel} \right] \\
\Gamma_{x,y} &= \partial_{x,y} g + \frac{q_j}{T_{0j}} F_0 \partial_{x,y} \chi & \Gamma_z &= \partial_z g + \frac{q_j}{T_{0j}} F_0 \partial_z \chi + \frac{v_{Tj} q_j}{T_{0j}} v_{\parallel} \mu F_0 A_{\parallel} \partial_z B_0
\end{aligned}$$

( $\mathcal{O}(\rho_{\text{ref}}/L_{\text{ref}})$  corrections are neglected).

### 2.7.1. Equation for the distribution function

Applying the normalization (2.31) to the equation for the distribution function gives

$$\begin{aligned}
\langle C_j(f) \rangle &= \frac{c_{\text{ref}}}{L_{\text{ref}}} \frac{\partial g_j}{\partial t} + \frac{B_0}{B_{0\parallel}^*} \frac{e}{m_{\text{ref}} c_{\text{ref}} L_{\text{ref}}} F_{0j} \partial_y \chi \left( \omega_n + (v_{\parallel}^2 + \mu B_0 - \frac{3}{2}) \omega_{Tj} \right) \\
&\quad - \frac{B_0}{B_{0\parallel}^*} \frac{c_{\text{ref}} \rho_{\text{ref}}}{L_{\text{ref}}^2} F_{0j} \frac{T_{0j}(2v_{\parallel}^2 + \mu B_0)}{q_j B_0} K_x \left( \omega_n + (v_{\parallel}^2 + \mu B_0 - \frac{3}{2}) \omega_{Tj} \right) \\
&\quad + \frac{c_{\text{ref}}}{L_{\text{ref}}} \frac{v_{Tj}}{JB_0} v_{\parallel} \Gamma_{jz} + \frac{B_0}{B_{0\parallel}^*} \frac{e}{m_{\text{ref}} c_{\text{ref}}} (\partial_x \chi \Gamma_{jy} - \partial_y \chi \Gamma_{jx}) \\
&\quad + \frac{B_0}{B_{0\parallel}^*} \frac{c_{\text{ref}} \rho_{\text{ref}}}{L_{\text{ref}}} \frac{T_{0j}(2v_{\parallel}^2 + \mu B_0)}{q_j B_0} (K_y \Gamma_{jy} + K_x \Gamma_{jx}) \\
&\quad - \frac{B_0}{B_{0\parallel}^*} \frac{c_{\text{ref}} \rho_{\text{ref}}}{L_{\text{ref}}} \frac{8\pi n_{\text{ref}} T_{\text{ref}}}{B_{\text{ref}}^2} \frac{T_{0j}}{q_j B_0^2} v_{\parallel}^2 \omega_p \Gamma_{jy} - \frac{c_{\text{ref}}}{L_{\text{ref}}} \frac{v_{Tj}}{2JB_0} \mu \partial_z B_0 \frac{\partial f_j}{\partial v_{\parallel}},
\end{aligned}$$

where the following abbreviations have been introduced,

$$\begin{aligned}\omega_n &= -\frac{L_{\text{ref}}}{n_{0j}} \partial_x n_{0j} & \omega_{Tj} &= -\frac{L_{\text{ref}}}{T_{0j}} \partial_x T_{0j} & \omega_p &= -\frac{L_{\text{ref}}}{n_{\text{ref}} T_{\text{ref}}} \partial_x p_0 \\ K_x &= -\frac{L_{\text{ref}}}{B_{\text{ref}}} (\partial_y B_0 + \frac{\gamma_2}{\gamma_1} \partial_z B_0) & K_y &= \frac{L_{\text{ref}}}{B_{\text{ref}}} (\partial_x B_0 - \frac{\gamma_3}{\gamma_1} \partial_z B_0)\end{aligned}$$

( $x$ ,  $y$ ,  $\gamma_2$ ,  $\gamma_3$ ,  $B_0$  and  $p_0$  are dimensional in these definitions). This equation can be simplified using relations (2.32),

$$\begin{aligned}\frac{L_{\text{ref}}}{c_{\text{ref}}} \langle C_j(f) \rangle &= \frac{\partial g_j}{\partial t} + \frac{B_0}{B_{0\parallel}^*} \frac{e}{T_{\text{ref}}} F_{0j} \partial_y \chi - \frac{v_{Tj}}{2JB_0} \mu \partial_z B_0 \frac{\partial f_j}{\partial v_\parallel} \\ &\quad + \frac{B_0}{B_{0\parallel}^*} \frac{eL_{\text{ref}}}{T_{\text{ref}}} (\partial_x \chi \Gamma_{jy} - \partial_y \chi \Gamma_{jx}) \left( \omega_n + (v_\parallel^2 + \mu B_0 - \frac{3}{2}) \omega_{Tj} \right) \\ &\quad - \frac{B_0}{B_{0\parallel}^*} \frac{\rho_{\text{ref}}}{L_{\text{ref}}} F_{0j} \frac{T_{0j}(2v_\parallel^2 + \mu B_0)}{q_j B_0} K_x \left( \omega_n + (v_\parallel^2 + \mu B_0 - \frac{3}{2}) \omega_{Tj} \right) + \frac{v_{Tj}}{JB_0} v_\parallel \Gamma_{jz} \\ &\quad + \frac{B_0}{B_{0\parallel}^*} \frac{\rho_{\text{ref}} T_{0j}(2v_\parallel^2 + \mu B_0)}{q_j B_0} (K_y \Gamma_{jy} + K_x \Gamma_{jx}) - \frac{B_0}{B_{0\parallel}^*} \frac{\rho_{\text{ref}} \beta T_{0j}}{q_j B_0^2} v_\parallel^2 \omega_p \Gamma_{jy}\end{aligned}$$

where the important parameter  $\beta$ , which describes the ratio of kinetic to magnetic pressure, has been introduced

$$\beta = \frac{8\pi n_{\text{ref}} T_{\text{ref}}}{B_{\text{ref}}^2}.$$

The  $B_0/B_{0\parallel}^*$  prefactors can be simplified by observing that with

$$\vec{b}_0 \cdot (\vec{\nabla} \times \vec{B}_0) = \vec{b}_0 \cdot (\vec{\nabla} B_0 \times \vec{b}_0 + B_0 \vec{\nabla} \times \vec{b}_0) = \vec{b}_0 \cdot B_0 \vec{\nabla} \times \vec{b}_0$$

and Ampère's law, the normalized expression for  $B_{0\parallel}^*$  can be written as

$$B_{0\parallel}^* = B_0 \left( 1 + \beta \frac{m_j v_{Tj}}{2q_j B_0^2} v_\parallel j_{0\parallel} \right)$$

with the equilibrium parallel current density  $j_{0\parallel}$ , which has been normalized to  $ec_{\text{ref}} n_{\text{ref}}$ . With this normalization,  $j_{0\parallel}$  is of order unity for tokamak experiments (and close to zero for stellarators), so that for small  $\beta$ , the approximation  $B_0/B_{0\parallel}^* \approx 1$  can be made. The additional normalization of the fields and distribution functions according to Eqs. (2.33) and (2.34) gives

$$\begin{aligned}\frac{\partial g_j}{\partial t} &= - \left( \omega_n + (v_\parallel^2 + \mu B_0 - \frac{3}{2}) \omega_{Tj} \right) F_{0j} \partial_y \chi - \frac{v_{Tj}}{JB_0} v_\parallel \Gamma_{jz} + (\partial_y \chi \partial_x g_j - \partial_x \chi \partial_y g_j) \\ &\quad - \frac{T_{0j}(2v_\parallel^2 + \mu B_0)}{q_j B_0} (K_y \Gamma_{jy} + K_x \Gamma_{jx}) + \frac{\beta T_{0j}}{q_j B_0^2} v_\parallel^2 \omega_p \Gamma_{jy} + \frac{v_{Tj}}{2JB_0} \mu \partial_z B_0 \frac{\partial f_j}{\partial v_\parallel} \\ &\quad + \frac{T_{0j}(2v_\parallel^2 + \mu B_0)}{q_j B_0} K_x \left( \omega_n + (v_\parallel^2 + \mu B_0 - \frac{3}{2}) \omega_{Tj} \right) F_{0j} + \langle C_j(f) \rangle,\end{aligned}$$

## 2. Gyrokinetics

where the nonlinearity has been simplified by inserting the expressions for  $\Gamma_{jx}$ ,  $\Gamma_{jy}$ , and observing that the  $\partial_x \chi \partial_y \chi$  terms drop out due to symmetry.

Since the field equations have been formulated in Fourier space because of the much simpler gyroaveraging procedure, it is convenient to also transform the Vlasov equation in  $x$  and  $y$  directions. For all linear terms, this is trivial because the prefactors contain no additional perpendicular dependence due to the local approximation, the only term which does not transform trivially is the nonlinearity. The transformation gives

$$\begin{aligned}
N(k) &= \frac{1}{L_x L_y} \int_0^{L_x, L_y} d^2 x e^{-i\vec{k}\vec{x}} (\partial_y \chi(x) \partial_x g_j(x) - \partial_x \chi(x) \partial_y g_j(x)) \\
&= \frac{1}{L_x L_y} \int_0^{L_x, L_y} d^2 x e^{-i\vec{x}\vec{k}} \left( \left( \sum_{\vec{k}'} e^{i\vec{x}\vec{k}'} i k'_y \chi(k') \right) \left( \sum_{\vec{k}''} e^{i\vec{x}\vec{k}''} i k''_x g_j(k'') \right) \right. \\
&\quad \left. - \left( \sum_{\vec{k}'} e^{i\vec{x}\vec{k}'} i k'_x \chi(k') \right) \left( \sum_{\vec{k}''} e^{i\vec{x}\vec{k}''} i k''_y g_j(k'') \right) \right) \\
&= -\frac{1}{L_x L_y} \int_0^{L_x, L_y} d^2 x \sum_{\vec{k}'} \sum_{\vec{k}''} e^{-i\vec{x}(\vec{k}-\vec{k}'-\vec{k}'')} (k'_y \chi(k') k''_x g_j(k'') - k'_x \chi(k') k''_y g_j(k'')) \\
&= -\sum_{\vec{k}'} \sum_{\vec{k}''} \delta_{\vec{k}-\vec{k}'-\vec{k}''} (k'_y k''_x - k'_x k''_y) \chi(k') g_j(k'') \\
&= \sum_{\vec{k}'} (k'_x k_y - k_x k'_y) \chi(k') g_j(k-k'),
\end{aligned} \tag{2.35}$$

so that the final equation in Fourier space (with the perpendicular derivatives in  $\Gamma_{jx}$ ,  $\Gamma_{jy}$  replaced by  $i k_x$ ,  $i k_y$ ) is

$$\begin{aligned}
\frac{\partial g_j}{\partial t} &= - \left( \omega_n + (v_\parallel^2 + \mu B_0 - \frac{3}{2}) \omega_{Tj} \right) F_{0j} i k_y \chi + \frac{v_{Tj}}{2 J B_0} \mu \partial_z B_0 \frac{\partial f_j}{\partial v_\parallel} + \frac{\beta T_{0j}}{q_j B_0^2} v_\parallel^2 \omega_p \Gamma_{jy} \\
&\quad + \sum_{\vec{k}'} (k'_x k_y - k_x k'_y) \chi(k') g_j(k-k') - \frac{T_{0j}(2v_\parallel^2 + \mu B_0)}{q_j B_0} (K_y \Gamma_{jy} + K_x \Gamma_{jx}) \\
&\quad - \frac{v_{Tj}}{J B_0} v_\parallel \Gamma_{jz} + \frac{T_{0j}(2v_\parallel^2 + \mu B_0)}{q_j B_0} K_x \left( \omega_n + (v_\parallel^2 + \mu B_0 - \frac{3}{2}) \omega_{Tj} \right) \delta_{k_x,0} \delta_{k_y,0} F_{0j} \\
&\quad + \langle C_j(f) \rangle.
\end{aligned}$$

## 2.7.2. Field equations

The normalization (2.31) turns the field equations into

$$\begin{aligned} \left( \frac{k_\perp^2}{4\pi\rho_{\text{ref}}^2} - \sum_j \frac{e^2 q_j^2}{T_{\text{ref}} T_{0j}} n_{\text{ref}} n_{0j} (\Gamma_0(b_j) - 1) \right) \phi - \left( \sum_j \frac{eq_j}{B_{\text{ref}} B_0} n_{\text{ref}} n_{0j} \Delta(b_j) \right) B_{1\parallel} \\ = \sum_j \pi eq_j B_0 c_{\text{ref}}^3 v_{Tj}^3 \int J_0(\lambda_j) g_j dv_{\parallel} d\mu \end{aligned}$$

$$\begin{aligned} \left( - \sum_j \frac{eq_j n_{\text{ref}} n_{0j}}{B_{\text{ref}} B_0} \Delta(b_j) \right) \phi + \left( \frac{1}{4\pi} - \sum_j \frac{c_{\text{ref}}^2 v_{Tj}^2 m_{\text{ref}} m_j n_{\text{ref}} n_{0j}}{B_{\text{ref}}^2 B_0^2} \Delta(b_j) \right) B_{1\parallel} \\ = \sum_j \frac{\pi eq_j B_0^{3/2} \rho_{\text{ref}}}{ck_\perp} c_{\text{ref}}^4 v_{Tj}^4 \int \sqrt{\mu} J_1(\lambda_j) g_j dv_{\parallel} d\mu \end{aligned}$$

$$A_{1\parallel} = \frac{\sum_j \frac{e}{c} 4\pi^2 q_j B_0 c_{\text{ref}}^4 v_{Tj}^4 \int v_{\parallel} J_0(\lambda_j) g_j(\vec{k}) dv_{\parallel} d\mu}{\frac{k_\perp^2}{\rho_{\text{ref}}^2} + \sum_j \frac{8\pi^2 e^2 q_j^2 B_0}{m_{\text{ref}} m_j c^2} v_{Tj}^3 c_{\text{ref}}^3 \int v_{\parallel}^2 J_0^2(\lambda_j) F_{0j} dv_{\parallel} d\mu},$$

with the (dimensionless) arguments of the Bessel functions now being

$$\begin{aligned} b_j &= \frac{k_\perp^2 c_{\text{ref}}^2 v_{Tj}^2}{\rho_{\text{ref}}^2 2\Omega_j^2 \Omega_{\text{ref}}^2} = \frac{T_{0j} m_j}{q_j^2 B_0^2} k_\perp^2 \\ \lambda_j &= \sqrt{\frac{2B_0 T_{\text{ref}} T_{0j} \mu}{m_{\text{ref}} m_j}} \frac{k_\perp}{\rho_{\text{ref}} \Omega_j \Omega_{\text{ref}}} = \frac{v_{Tj}}{\Omega_j} k_\perp \sqrt{B_0 \mu}. \end{aligned}$$

The normalization of the fields and distribution functions gives

$$\begin{aligned} \left( k_\perp^2 \lambda_D^2 + \sum_j \frac{q_j^2}{T_{0j}} n_{0j} (1 - \Gamma_0(b_j)) \right) \Phi - \left( \sum_j \frac{q_j n_{0j}}{B_0} \Delta(b_j) \right) B_{1\parallel} \\ = \sum_j n_{0j} \pi q_j B_0 \int J_0(\lambda_j) g_j dv_{\parallel} d\mu \end{aligned}$$

$$\begin{aligned} \left( - \sum_j \frac{q_j n_{0j}}{B_0} \Delta(b_j) \right) \Phi + \left( \frac{2}{\beta} - \sum_j \frac{2T_{0j} n_{0j}}{B_0^2} \Delta(b_j) \right) B_{1\parallel} \\ = \sum_j n_{0j} \frac{\pi v_{Tj} q_j B_0^{3/2}}{k_\perp} \int \sqrt{\mu} J_1(\lambda_j) g_j dv_{\parallel} d\mu \end{aligned}$$

## 2. Gyrokinetics

$$A_{1\parallel} = \frac{\sum_j \frac{\beta}{2} q_j n_{j0} v_{Tj} \pi B_0 \int v_{\parallel} J_0(\lambda_j) g_j(\vec{k}) dv_{\parallel} d\mu}{k_{\perp}^2 + \sum_j \frac{\beta q_j^2}{m_j} n_{0j} \pi B_0 \int v_{\parallel}^2 J_0^2(\lambda_j) F_{0j} dv_{\parallel} d\mu}$$

with the Debye length

$$\lambda_D = \sqrt{\frac{T_{\text{ref}}}{4\pi\rho_{\text{ref}}^2 e^2 n_{\text{ref}}}} = \sqrt{\frac{B_{\text{ref}}^2}{4\pi c^2 n_{\text{ref}} m_{\text{ref}}}}.$$

In order to solve the system of equations for  $\phi$  and  $B_{\parallel}$ , the abbreviations

$$\begin{aligned} C_1 &= k_{\perp}^2 \lambda_D^2 + \sum_j \frac{q_j^2}{T_{0j}} n_{0j} (1 - \Gamma_0(b_j)), & C_2 &= - \sum_j \frac{q_j n_{0j}}{B_0} \Delta(b_j), \\ C_3 &= \frac{2}{\beta} - \sum_j \frac{2T_{0j} n_{0j}}{B_0^2} \Delta(b_j) \end{aligned}$$

and

$$M_{00} = \sum_j n_{0j} \pi q_j B_0 \int J_0(\lambda_j) g_j dv_{\parallel} d\mu, \quad M_{01} = \sum_j n_{0j} \frac{\pi v_{Tj} q_j B_0^{3/2}}{k_{\perp}} \int \sqrt{\mu} J_1(\lambda_j) g_j dv_{\parallel} d\mu$$

for the velocity space moments of the distribution function are introduced. With these, the linear system of equations can be written as

$$\begin{bmatrix} C_1 & C_2 \\ C_2 & C_3 \end{bmatrix} \cdot \begin{bmatrix} \phi \\ B_{\parallel} \end{bmatrix} = \begin{bmatrix} M_{00} \\ M_{01} \end{bmatrix}$$

and solved explicitly,

$$\begin{bmatrix} \phi \\ B_{\parallel} \end{bmatrix} = \frac{1}{\det C} \begin{bmatrix} C_3 & -C_2 \\ -C_2 & C_1 \end{bmatrix} \cdot \begin{bmatrix} M_{00} \\ M_{01} \end{bmatrix} = \frac{1}{C_1 C_3 - C_2^2} \begin{bmatrix} C_3 M_{00} - C_2 M_{01} \\ C_1 M_{01} - C_2 M_{00} \end{bmatrix}.$$

For  $\beta \rightarrow 0$ , the determinant diverges because of  $C_3 \rightarrow \infty$ . In this limit,

$$\begin{aligned} \phi &= \frac{C_3 M_{00} - C_2 M_{01}}{C_1 C_3 - C_2^2} \rightarrow \frac{M_{00}}{C_1} \\ B_{\parallel} &= \frac{C_1 M_{01} - C_2 M_{00}}{C_1 C_3 - C_2^2} \rightarrow 0, \end{aligned}$$

which means that for small  $\beta$ , the  $B_{\parallel}$  contributions can be neglected compared to the contributions of the electrostatic potential.

In this limit, the equation for  $\phi$  reads

$$\phi = \frac{\sum_j n_{0j} \pi q_j B_0 \int J_0(\lambda_j) g_j dv_{\parallel} d\mu}{k_{\perp}^2 \lambda_D^2 + \sum_j \frac{q_j^2}{T_{0j}} n_{0j} (1 - \Gamma_0(b_j))},$$

which is the relation that will be used in the rest of this thesis.

### 2.7.3. Collision operator

Normalization (2.31) of the collisional spatial diffusion term gives

$$\langle C_{jj'}^\perp \rangle = \frac{c_{\text{ref}}}{L_{\text{ref}}} \frac{\pi e^4 \ln \Lambda_c n_{\text{ref}} L_{\text{ref}} n_{j'} q_j^2 T_{j'} m_j^{3/2}}{\sqrt{2}^3 T_{\text{ref}}^2 m_{j'} B_0^2 T_{0j}^{3/2}} \frac{1}{v^5} (2v^2 F_1 + 3B_0 \mu F_2) \nabla_\perp^2 f_j,$$

the velocity space  $\vec{V} = (v_\parallel, \mu)$  contribution is

$$\begin{aligned} \langle C_{jj'}^V \rangle &= \frac{c_{\text{ref}}}{L_{\text{ref}}} \frac{\partial}{\partial \vec{V}} \cdot \frac{2\pi q_j^2 q_{j'}^2 e^4 \ln \Lambda_c n_{\text{ref}} L_{\text{ref}} n_{j'} \sqrt{m_j}}{\sqrt{2}^3 T_{\text{ref}}^2 m_{j'} T_{0j}^{3/2}} \\ &\quad \left( \frac{T_{j'}}{2T_{0j} v^5} \begin{bmatrix} B_0 \mu F_1 + v_\parallel^2 F_3 & 6\mu v_\parallel F_2 \\ 6\mu v_\parallel F_2 & \frac{4}{B_0} v_\parallel^2 \mu F_1 + 4\mu^2 F_3 \end{bmatrix} \cdot \frac{\partial}{\partial \vec{V}} - \frac{F_3}{v^3} \begin{bmatrix} v_\parallel \\ 2\mu \end{bmatrix} \right) f_j. \end{aligned}$$

The (dimensionless) arguments of the  $F_i$  are now  $F_i(\frac{v_{Tj}}{v_{Tj'}} v)$ . Introducing the dimensionless collision frequency

$$\nu_c = \frac{\pi \ln \Lambda_c e^4 n_{\text{ref}} L_{\text{ref}}}{\sqrt{2}^3 T_{\text{ref}}^2},$$

normalizing the distribution functions and taking into account the factors in (2.34), the normalized collision operator is

$$\begin{aligned} \langle C_{jj'}^\perp \rangle &= -\frac{\nu_c n_{j'} q_j^2 T_{j'} m_j^{3/2}}{m_{j'} B_0^2 T_{0j}^{3/2}} \frac{1}{v^5} (2v^2 F_1 + 3B_0 \mu F_2) k_\perp^2 f_j \\ \langle C_{jj'}^V \rangle &= \frac{\partial}{\partial \vec{V}} \cdot \frac{\nu_c q_j^2 q_{j'}^2 n_{j'} \sqrt{m_j}}{m_{j'} T_{0j}^{3/2}} \\ &\quad \left( \frac{T_{j'}}{T_{0j} v^5} \begin{bmatrix} B_0 \mu F_1 + v_\parallel^2 F_3 & 6\mu v_\parallel F_2 \\ 6\mu v_\parallel F_2 & \frac{4}{B_0} v_\parallel^2 \mu F_1 + 4\mu^2 F_3 \end{bmatrix} \cdot \frac{\partial}{\partial \vec{V}} - \frac{2F_3}{v^3} \begin{bmatrix} v_\parallel \\ 2\mu \end{bmatrix} \right) f_j \end{aligned} \quad (2.36)$$

With the normalized abbreviations

$$\begin{aligned} B_{1j} &= \int dv_\parallel d\mu F_{0j}, & B_{2j} &= \int dv_\parallel d\mu v^2 F_{0j}, \\ B_{3j} &= \int dv_\parallel d\mu v^4 F_{0j}, & B_{4j} &= \int dv_\parallel d\mu v_\parallel^2 F_{0j}, \end{aligned}$$

the normalized conservation term that is added to the equation for species  $j$  reads

$$\begin{aligned} A_{jj'} &= \frac{T_{0j} n_{0j'}}{T_{0j} n_{0j}} \frac{B_{2j} - v^2 B_{1j}}{B_{1j} B_{3j} - (B_{2j})^2} \left( \int dv_\parallel d\mu v^2 \langle C(f_{j'}, F_{0j}) \rangle \right) F_{0j} \\ &\quad - \frac{m_{j'} v_{Tj'} n_{0j'}}{m_j v_{Tj} n_{0j}} \frac{1}{B_{4j}} \left( \int dv_\parallel d\mu v_\parallel \langle C(f_{j'}, F_{0j}) \rangle \right) v_\parallel F_{0j}, \end{aligned} \quad (2.37)$$

completing the final expression for the collision operator.

## 2. Gyrokinetics

### 2.8. Summary of the equations being solved in GENE

The final equations can be summarized schematically as

$$\frac{\partial g}{\partial t} = Z + \mathcal{L}[g] + \mathcal{N}[g], \quad (2.38)$$

where  $g$  is the combined modified distribution function of all species.

The constant part  $Z$

$$Z = \frac{T_{0j}(2v_{\parallel}^2 + \mu B_0)}{q_j B_0} K_x \left( \omega_n + (v_{\parallel}^2 + \mu B_0 - \frac{3}{2})\omega_{Tj} \right) \delta_{k_x,0} \delta_{k_y,0} F_{0j}$$

arises due to the fact that in the presence of curvature and density or temperature gradients,  $F_0$  (i.e.,  $f = 0$ ) is not a solution of the gyrokinetic equations. It only affects the  $k_{\perp} = 0$  mode and decouples linearly and nonlinearly from the rest of the system. The linear operator is given by

$$\begin{aligned} \mathcal{L}[g] = & - \left( \omega_n + (v_{\parallel}^2 + \mu B_0 - \frac{3}{2})\omega_{Tj} \right) F_{0j} i k_y \chi + \frac{\beta T_{0j}}{q_j B_0^2} v_{\parallel}^2 \omega_p \Gamma_{jy} - \frac{v_{Tj}}{J B_0} v_{\parallel} \Gamma_{jz} \\ & - \frac{T_{0j}(2v_{\parallel}^2 + \mu B_0)}{q_j B_0} (K_y \Gamma_{jy} + K_x \Gamma_{jx}) + \frac{v_{Tj}}{2 J B_0} \mu \partial_z B_0 \frac{\partial f_j}{\partial v_{\parallel}} + \langle C_j(f) \rangle, \end{aligned} \quad (2.39)$$

consisting of the drive term, the pressure term, a term describing the parallel dynamics, the curvature terms, the trapping term and collisions. The auxiliary fields are

$$\begin{aligned} F_{0j} = F_0 &= \pi^{-3/2} e^{-(v_{\parallel}^2 + \mu B_0)} & f_j = g_j - \frac{2q_j}{m_j v_{Tj}} v_{\parallel} \bar{A}_{1\parallel} F_{0j} \\ \chi_j &= \bar{\phi}_j - v_{Tj} v_{\parallel} \bar{A}_{1\parallel j} & \Gamma_{x,y} = i k_{x,y} g + \frac{q_j}{T_{0j}} F_0 i k_{x,y} \chi \\ \Gamma_z &= \partial_z g + \frac{q_j}{T_{0j}} F_0 \partial_z \chi + \frac{v_{Tj} q_j}{T_{0j}} v_{\parallel} \mu F_0 A_{\parallel} \partial_z B_0, \end{aligned}$$

and the electromagnetic fields, which are also linear in the distribution function are

$$\begin{aligned} \phi &= \frac{\sum_j n_{0j} \pi q_j B_0 \int J_0(\lambda_j) g_j dv_{\parallel} d\mu}{k_{\perp}^2 \lambda_D^2 + \sum_j \frac{q_j^2}{T_{0j}} n_{0j} (1 - \Gamma_0(b_j))} \\ A_{1\parallel} &= \frac{\sum_j \frac{\beta}{2} q_j n_{j0} v_{Tj} \pi B_0 \int v_{\parallel} J_0(\lambda_j) g_j(\vec{k}) dv_{\parallel} d\mu}{k_{\perp}^2 + \sum_j \frac{\beta q_j^2}{m_j} n_{0j} \pi B_0 \int v_{\parallel}^2 J_0^2(\lambda_j) F_{0j} dv_{\parallel} d\mu}. \end{aligned}$$

The collision term is given by

$$\langle C_j(f) \rangle = \sum_{j'} \left( \langle C_{jj'}^{\perp} \rangle + \langle C_{jj'}^{\vec{V}} \rangle + A_{jj'} \right),$$

where the expressions for  $\langle C_{jj'}^{\perp} \rangle$ ,  $\langle C_{jj'}^{\vec{V}} \rangle$  and  $A_{jj'}$  are given by Eqs. (2.36) and (2.37).

The  $\vec{E} \times \vec{B}$  nonlinearity in this representation is

$$N[g] = \sum_{\vec{k}'_\perp} (k'_x k_y - k_x k'_y) \chi(\vec{k}'_\perp) g_j(\vec{k}_\perp - \vec{k}'_\perp), \quad (2.40)$$

although for the numerical treatment, the more complicated expression (2.35) will be used.

Besides the parallel  $B_0$  variation, the most important equilibrium quantities entering the gyrokinetic equations are the gradients and curvature terms,

$$\begin{aligned} \omega_n &= -\frac{L_{\text{ref}}}{n_{0j}} \partial_x n_{0j} & \omega_{Tj} &= -\frac{L_{\text{ref}}}{T_{0j}} \partial_x T_{0j} & \omega_p &= -\frac{L_{\text{ref}}}{n_{\text{ref}} T_{\text{ref}}} \partial_x p_0 \\ K_x &= -\frac{L_{\text{ref}}}{B_{\text{ref}}} (\partial_y B_0 + \frac{\gamma_2}{\gamma_1} \partial_z B_0) & K_y &= \frac{L_{\text{ref}}}{B_{\text{ref}}} (\partial_x B_0 - \frac{\gamma_3}{\gamma_1} \partial_z B_0) \end{aligned}$$

(with dimensional  $x, y, \gamma_2, \gamma_3, p$ ). The pressure gradient  $\omega_p$  can be extracted from an MHD equilibrium or estimated from the gradients via

$$\omega_p = -\frac{L_{\text{ref}}}{n_{\text{ref}} T_{\text{ref}}} \partial_x p = \sum_s n_s T_s (\omega_n + \omega_{Ts}).$$

In these normalized equations, the physical values of the equilibrium quantities do not enter. However, in the normalization process, three dimensionless parameters relating different normalization scales have been introduced,

$$\beta = \frac{8\pi n_{\text{ref}} T_{\text{ref}}}{B_{\text{ref}}^2} \quad \nu_c = \frac{\pi \ln \Lambda_c e^4 n_{\text{ref}} L_{\text{ref}}}{\sqrt{2}^3 T_{\text{ref}}^2} \quad \lambda_D = \sqrt{\frac{B_{\text{ref}}^2}{4\pi c^2 n_{\text{ref}} m_{\text{ref}}}},$$

effectively reducing the number of freely scalable parameters.

The linearized gyrokinetic equation

$$\frac{\partial g}{\partial t} = \mathcal{L}[g] \quad (2.41)$$

is used for investigations concerning linear stability and e.g. attempts to find quasilinear models of the turbulent behaviour in certain regimes.

## 2.9. Special simplifications

### 2.9.1. $\hat{s} - \alpha$ geometry

If the geometric coefficients are not extracted from a numerical MHD-equilibrium, a model geometry can be used. The widely used  $\hat{s} - \alpha$  model equilibrium [32] describes (Shafranov shifted) circular flux surfaces and is a good approximation to a real solution of the MHD equations close to the magnetic axis, i.e. for a inverse local aspect ratio  $\epsilon_t = r/R \rightarrow 0$ , with  $R$  and  $r$  the major and minor radius of the central field line in torus coordinates.

## 2. Gyrokinetics

The Shafranov shift  $\alpha_{\text{MHD}}$  is given by

$$\alpha_{\text{MHD}} = \frac{q_0^2}{R} \beta \omega_p = \frac{q_0^2}{R} \beta \sum_j (\omega_{Tj} + \omega_n) T_{0j} n_{0j},$$

where  $R$  (and  $r$  in the following expressions) are normalized to  $L_{\text{ref}}$ .

In the  $\hat{s}-\alpha$  model, the (normalized) metric and equilibrium magnetic field are approximated by

$$g^{ij} = \begin{bmatrix} 1 & \hat{s}z - \alpha_{\text{MHD}} \sin z & 0 \\ \hat{s}z - \alpha_{\text{MHD}} \sin z & 1 + (\hat{s}z - \alpha_{\text{MHD}} \sin z)^2 & 1/r \\ 0 & 1/r & 1/r^2 \end{bmatrix}$$

$$B_0 = \frac{1}{1 + \epsilon_t \cos z} \quad \partial_z B_0 = B_0^2 \epsilon_t \sin z \quad J = \frac{1}{B_0}$$

and the curvature terms are assumed to be

$$K_x = -\frac{L_{\text{ref}}}{R} \sin z \quad K_y = -\frac{L_{\text{ref}}}{R} (\cos z + \sin z (\hat{s}z - \alpha_{\text{MHD}} \sin z)).$$

These assumptions are strictly speaking inconsistent, the most obvious symptom of this is that a computation of the Jacobian from the metric yields  $J = 0$ , which means that  $g$  as given above is actually singular. Furthermore, the relations (2.30) for the geometric prefactors  $\frac{Jb^3\gamma_1}{B_0}$  and  $b^3$  are still used, although they are not consistent with the above assumptions. For a more detailed discussion about the limitations of this approximation, see [33].

Interfaces between gyrokinetic codes and MHD codes have become popular only in the last few years and are not available for all codes. Despite its inconsistencies, the  $\hat{s} - \alpha$  model is therefore still widely used for benchmarks between codes ([34, 35]) or fundamental investigations, where effects of the exact details of the magnetic equilibrium are not of interest.

### 2.9.2. Adiabatic electrons

Most results on ion-temperature gradient mode (ITG) turbulence documented in the literature were obtained with the adiabatic electron approximation. In this approximation, the electron distribution function is not advanced explicitly. The adiabaticity relation for the electrons on a flux surface,

$$\frac{n_{1e}}{n_{0e}} = \frac{-q_e(\phi - \langle \phi \rangle_{\text{FS}})}{T_e},$$

relates the perturbed electron density to deviations of  $\phi$  from the flux surface average  $\langle \phi \rangle_{\text{FS}}$ . To calculate  $\langle \phi \rangle_{\text{FS}}$ , it is assumed that the electrons contribution vanishes, so that

$$\langle \phi \rangle_{\text{FS}} = \frac{\sum_i \pi q_i n_{0i} B_0 \langle \int J_0(\lambda_i) g_i dv_{||} d\mu \rangle_{\text{FS}}}{\sum_i \frac{q_i^2 n_{0i}}{T_i} \left[ 1 - \langle \Gamma_0 \left( \frac{T_i m_i k_{\perp}^2}{q_i^2 B_0^2} \right) \rangle_{\text{FS}} \right]}$$

(with  $i$  only ion indices) can be calculated. Because of  $\Gamma_0(b_e) \approx 1$  (which is consistent with  $m_e/m_i \rightarrow 0$ ),  $n_{1e}$  is equal to the first velocity space moment of  $g_e$  and the expression for the electron charge density is

$$q_e n_{1e} = q_e n_{0e} \pi B_0 \int J_0(\lambda_e) g_e d\mu dv_{\parallel} = \frac{q_e^2 n_{0e} \langle \phi \rangle_{FS}}{T_e} - \frac{q_e^2 n_{0e} \phi}{T_e},$$

which is used to replace the electron contribution in the equation for  $\phi$ ,

$$\phi = \frac{\sum_i \pi q_i n_{0i} B_0 \int \bar{g}_i d\mu dv_{\parallel} + \frac{q_e^2 n_{0e}}{T_e} \langle \phi \rangle}{\frac{q_e^2 n_{0e}}{T_e} + \sum_i \frac{q_i^2 n_{0i}}{T_i} \left[ 1 - \Gamma_0 \left( \frac{T_i m_i k_{\perp}^2}{q_i^2 B_0^2} \right) \right]}.$$

The Debye length is neglected in this approximation.

### 2.9.3. Adiabatic ions

For basic investigations of electron temperature gradient (ETG) mode turbulence, a similar assumption can be made for the ion distribution function.

$$\frac{n_{1i}}{n_{0i}} = \frac{\pi n_{0i} B_0 \int J_0(\lambda_i) g_i d\mu dv_{\parallel}}{n_{0i}} - \frac{q_i}{T_i} \phi(\vec{x}) (1 - \Gamma_0(b_i)) = \frac{-q_i \phi}{T_i}$$

In electron units,  $b_i$  is large and  $\Gamma_0(b_i) \approx 0$  can be assumed, leading to

$$\pi q_i n_{0i} B_0 \int J_0(\lambda_i) g_i d\mu dv_{\parallel} = 0.$$

Inserting this result into the equation for  $\phi$ , the approximation

$$\phi = \frac{\pi q_e n_{0e} B_0 \int J_0(\lambda_e) g_e d\mu dv_{\parallel}}{\lambda_D^2 k_{\perp}^2 + \frac{q_e^2 n_{0e}}{T_i} + \frac{q_e^2 n_{0e}}{T_e} [1 - \Gamma_0 \left( \frac{T_e m_e k_{\perp}^2}{q_e^2 B_0^2} \right)]}$$

is obtained.

### 2.9.4. Pitch-angle scattering

The Lorentz collision operator is obtained from Eq. (2.36) with  $s, j' = e, i$  in the limit  $v_{Ti} \rightarrow 0$ . In this approximation, the functions  $F$  of Eq. (2.25) entering the collision operator simplify,

$$\begin{aligned} F_1 \left( \frac{v_{Ts}}{v_{Tj'}} v \right) &\rightarrow 2 \left( \frac{v_{Ts}}{v_{Tj'}} v \right)^2 \\ F_2 \left( \frac{v_{Ts}}{v_{Tj'}} v \right) &\rightarrow -\frac{2}{3} \left( \frac{v_{Ts}}{v_{Tj'}} v \right)^2 \\ F_3 \left( \frac{v_{Ts}}{v_{Tj'}} v \right) &\rightarrow 0, \end{aligned}$$

## 2. Gyrokinetics

and the collision operator for electrons scattering off ions can be written as

$$\begin{aligned}\langle C_{ei}^\perp \rangle &= -\frac{\nu_c n_i q_i^2 m_e^{1/2}}{B_0^2 T_e^{1/2}} \frac{1}{v^3} (4v^2 - 2B_0\mu) k_\perp^2 f_e \\ \langle C_{ei}^\vec{V} \rangle &= \frac{\partial}{\partial \vec{V}} \cdot \frac{\nu_c q_e^2 q_i^2 n_i}{\sqrt{m_e} T_e^{3/2}} \frac{1}{v^3} \begin{bmatrix} 2B_0\mu & -4\mu v_\parallel \\ -4\mu v_\parallel & \frac{8}{B_0} v_\parallel^2 \mu \end{bmatrix} \cdot \frac{\partial}{\partial \vec{V}} f_e.\end{aligned}\quad (2.42)$$

The  $\langle C_{ei}^\perp \rangle$  part is usually neglected. If the pitch angle  $\xi = v_\parallel/v$  and kinetic energy  $\mathcal{E}$  are used as velocity space coordinates, the  $(\mathcal{E}, \mathcal{E})$  and  $(\xi, \mathcal{E})$  entries of the matrix in the collision operator vanish, because in the limit of infinitely heavy ions considered here, the energy transfer of electron-ion collisions is exactly zero. The resulting operator therefore only describes diffusion and advection in  $\xi$  and its affect on the distribution function is called pitch-angle scattering.

Pitch-angle scattering is a good approximation for electron-ion collisions. Because of the simplicity of the resulting operator in  $(\xi, \mathcal{E})$  coordinates, the energy and mixed contributions to the electron-electron collisions, which are approximately as important as electron-ion collisions, is also often neglected. However, this (and similar approximations on the ion-ion collision operator) cannot be justified with physical arguments. In the  $(v_\parallel, \mu)$  coordinates used here, the pitch-angle approximation brings no benefit concerning the simplicity of the collision operator and is only used for benchmarks with other codes.

## 2.10. Observables

Since the time evolution of the five-dimensional distribution function  $g_j(k_x, k_y, z, v_\parallel, \mu)$  is difficult to analyze and impossible to compare to experimental results, it is important to reduce the amount of information to manageable levels. Of special relevance are the radial temperature and heat fluxes due to the microturbulence, i.e. the anomalous transport. These fluxes and most other practical quantities in this context are spatial averages of products of two fields  $A$  and  $B$ . In direct space, the spatial average of a product  $AB$  is

$$\langle A(\vec{X})B(\vec{X}) \rangle = \frac{\int_0^{L_x} \int_0^{L_y} \int_{-\pi}^{\pi} J A(\vec{X})B(\vec{X}) dx dy dz}{\int_0^{L_x} \int_0^{L_y} \int_{-\pi}^{\pi} J dx dy dz} = \frac{\int_0^{L_x} \int_0^{L_y} \int_{-\pi}^{\pi} J A(\vec{X})B(\vec{X}) dx dy dz}{L_x L_y \int_{-\pi}^{\pi} J dz}$$

Expressing this with  $A$  and  $B$  in Fourier representation gives

$$\begin{aligned}\langle A(\vec{X})B(\vec{X}) \rangle &= \frac{\int_0^{L_x} \int_0^{L_y} \int_{-\pi}^{\pi} J \sum_{\vec{k}, \vec{k}'} e^{i\vec{X} \cdot (\vec{k} + \vec{k}')} A(\vec{k}, z) B(\vec{k}', z) dx dy dz}{L_x L_y \int_{-\pi}^{\pi} J dz} \\ &= \frac{\int_{-\pi}^{\pi} J \sum_{\vec{k}, \vec{k}'} \delta_{\vec{k} - \vec{k}'} A(\vec{k}, z) B(\vec{k}', z) dz}{\int_{-\pi}^{\pi} J dz} = \frac{\int_{-\pi}^{\pi} J \sum_{\vec{k}} A(\vec{k}, z) B(-\vec{k}, z) dz}{\int_{-\pi}^{\pi} J dz} \\ &= \frac{\int_{-\pi}^{\pi} \sum_{\vec{k}} J A(\vec{k}, z) B^*(\vec{k}, z) dz}{\int_{-\pi}^{\pi} J dz},\end{aligned}$$

where in the last step the condition  $B(-\vec{k}) = B^*(\vec{k})$  has been used, which has to be fulfilled if  $B$  is a real quantity in direct space. The products of interest are physical quantities and therefore usually dimensional, for comparisons with experiments, the normalization of these composed quantities has to be reconstructed carefully.

The dimensional radial  $\vec{E} \times \vec{B}$  velocity, which enters the computation of the radial fluxes, can be computed from Eqs. (2.14) and (2.27),

$$\begin{aligned}\vec{v}_{E \times B} \cdot \vec{e}_x &= \frac{c}{B_0} (\vec{b}_0 \times \vec{\nabla} \chi)^1 = \frac{c}{B_0} g^{1k} g^{jm} \epsilon_{3jk} J b^3 \partial_m \chi \\ &= -\frac{c J b^3 \gamma_1}{B_0} i k_y \chi\end{aligned}$$

where the parallel derivatives have again been neglected. The normalization according to (2.31) and (2.33) gives

$$\vec{v}_{E \times B} \cdot \vec{e}_x = -\frac{\rho_{\text{ref}} c_{\text{ref}}}{L_{\text{ref}}} i k_y \chi.$$

Without FLR corrections, the density and heat density fluctuations are given by

$$n_{1j} = \int dv_{\parallel} d\mu d\theta J_v f_j, \quad p_{1j} = \int dv_{\parallel} d\mu d\theta J_v \frac{1}{2} m_j v^2 f_j.$$

The normalization gives

$$n_{1j} = \frac{\rho_{\text{ref}} n_{\text{ref}}}{L_{\text{ref}}} n_{0j} \pi B_0 \int dv_{\parallel} d\mu f_j, \quad p_{1j} = \frac{\rho_{\text{ref}} n_{\text{ref}} T_{\text{ref}}}{L_{\text{ref}}} n_{0j} T_{0j} \pi B_0 \int dv_{\parallel} d\mu v^2 f_j.$$

The spatially averaged radial particle transport  $\Gamma = \langle n_{1j} \vec{v}_{E \times B} \cdot \vec{e}_x \rangle$  of species  $j$  in units of  $n_{\text{ref}} c_{\text{ref}} \rho_{\text{ref}}^2 / L_{\text{ref}}^2$  is therefore

$$\Gamma_j = -\frac{n_{0j}}{\int_{-\pi}^{\pi} J dz} \int_{-\pi}^{\pi} dz \sum_{\vec{k}} J i k_y \chi(\vec{k}) \left( \pi B_0 \int dv_{\parallel} d\mu f_j(\vec{k}) \right)^*.$$

Similarly, the heat transport  $Q_j = \langle p_{1j} \vec{v}_{E \times B} \cdot \vec{e}_x \rangle$  in units of  $n_{\text{ref}} T_{\text{ref}} c_{\text{ref}} \rho_{\text{ref}}^2 / L_{\text{ref}}^2$  is given by

$$Q_j = -\frac{n_{0j} T_{0j}}{\int_{-\pi}^{\pi} J dz} \int_{-\pi}^{\pi} dz \sum_{\vec{k}} J i k_y \chi(\vec{k}) \left( \pi B_0 \int dv_{\parallel} d\mu v^2 f_j(\vec{k}) \right)^*.$$

The radial transport due to  $\chi$  can be decomposed into a electrostatic ( $\phi$ ) and electromagnetic ( $A_{\parallel}$ ) contribution which can be analyzed separately.

Sometimes, the heat diffusivity  $\chi_j$  is considered instead of  $Q_j$ . It is connected to the heat flux via

$$Q_j = n_j T_j \chi_j \omega_{Tj}$$

and has the dimension  $c_{\text{ref}} \rho_{\text{ref}}^2 / L_{\text{ref}}$ .

## 2.11. Summary

In this chapter, a general form of the gyrokinetic equations has been taken from the literature and modified according to the local  $\delta f$  approximation, which is suitable for the numerical treatment of plasma microturbulence. Compared to previous presentations, several aspects have been compiled into a single coherent set of equations (concerning, e.g., the choice of velocity space coordinates and the normalization). The equations contain a linearized Landau-Boltzmann collision operator, are formulated for general magnetic geometry and include additional physical effects like the dependence on the pressure gradient; furthermore, the normalization is very general and allows for an arbitrary number of species. These equations will be the basis for a computational approach to plasma turbulence; some aspects of their numerical implementation into the GENE code will be discussed in the next chapter.

### 3. The GENE code

The GENE (Gyrokinetic Electromagnetic Numerical Experiment) project was first started by F. Jenko [36] and developed further by T. Dannert [37] in the following years. The core of GENE is a massively parallel simulation code, written in Fortran 90/95, which numerically solves Eq. (2.38) following a Eulerian approach, which means that the phase space is discretized using a fixed grid and the time evolution of the distribution function is then computed on this grid.

The present version, GENE11, has seen major developments as part of this PhD thesis. To take full advantage of the local approximation, which implies periodic boundary conditions for the directions perpendicular to the magnetic field, both  $x$  and  $y$  directions are now treated spectrally (as described in the previous chapter), in contrast to the direct space implementation for the  $x$  direction that was used before. This approach allows for an easy computation of the perpendicular derivatives and a careful anti-aliasing, which avoids numerical problems.

A collision operator has been implemented, further increasing the realism of the simulations; furthermore, an interface to an external eigenvalue solver has been developed, enabling the computation of arbitrary parts of the eigenvalue spectrum and making GENE the first gyrokinetic code to allow for a direct comparison between (linear) eigenvalue computations and nonlinear turbulence simulations, excluding errors from using different numerical representations of the linear operator in separate codes and thus allowing for more systematic studies. The normalization of the equations has been generalized, so that GENE can now handle an arbitrary number of species. The information about the eigenvalue spectrum has also been used to optimize the time stepping schemes, allowing for faster initial value computations; furthermore, the parallelization of the code has been improved in collaboration with Reinhard Tisma from the Garching Computing Center to be able to efficiently use even the biggest supercomputers. Optimizations like e.g. the option to use single or double precision for the computations and advanced time stepping schemes have been implemented, which can be used to save a lot of computation time.

Besides the performance, the portability has been improved, so that GENE is presently used on many different architectures, has been tested on some of the biggest present supercomputers (see, e.g. [38]) and has become a part of the DEISA benchmark suite. Together with a powerful IDL postprocessing tool, a PERL script for parameter scans and a preprocessing tool to extract the relevant geometric information from MHD equilibria, which all have been developed in the GENE working group, it has also been made available to other researchers in the fusion community.

In order to numerically solve the gyrokinetic equation (2.38) on a finite grid, all dimensions of this partial integro-differential equation have to be discretized. Following the method of lines, first the right hand side of Eq. (2.38) is discretized, i.e. the already discrete  $k_x$  and  $k_y$  dimensions are truncated at some  $k_x^{\max}$  and  $k_y^{\max}$ , the remaining continuous dimensions

### 3. The GENE code

$z$ ,  $v_{\parallel}$  and  $\mu$  are replaced by discrete, finite grids, turning the modified distribution function  $g$  into a finite dimensional state vector. The continuous operations contained in  $\mathcal{L}$  and  $\mathcal{N}$ , namely derivatives and integrations, are replaced by their discrete counterparts, turning the partial integro-differential equation into a system of ordinary differential equations in  $t$ , which can then be solved as initial value problem, or for linear computations also as an eigenvalue problem.

## 3.1. Discretization of the operators

### 3.1.1. Perpendicular direction

The  $x$  and  $y$  directions are treated spectrally, and the finite extent of the simulation domain already leads to a discretization in these directions. To treat the perpendicular dimensions numerically, only a high  $k$  cutoff has to be defined. The derivatives in these directions are represented by trivial multiplications with  $ik_x$  and  $ik_y$ , the only difficulty concerning the perpendicular direction of Eq. (2.38) is the  $\vec{E} \times \vec{B}$  nonlinearity, which in the Fourier space representation (2.40) corresponds to a convolution.

A direct evaluation of this term would be computationally too expensive,  $ik_{x,y}\chi(\vec{k})$  and  $ik_{x,y}g(\vec{k})$  are therefore transformed to real space and multiplied. The product is then transformed back to Fourier space, which corresponds to expression (2.35). This is still very costly, and in a typical turbulence simulation, the evaluation of the nonlinearity can amount to up to 70% of the overall computation time, but because of the efficient implementations of the Fast Fourier Transform (FFT) algorithm provided in numerical libraries like ESSL, MKL or FFTW, this is still way more efficient than a convolution.

### 3.1.2. Parallel direction

The parallel direction is discretized using  $n_z$  points with equidistant distribution in the poloidal angle. For the numerical integration along the  $z$  direction, which is necessary for the computation of volume averages, the trapezoid rule is used; the derivatives are approximated with finite differences, see Appendix B. Due to the parallel boundary condition (2.10), different  $k_x$  values are coupled via the parallel derivative, but if the shift is such that it connects to a  $k_x$  value which not included in the simulation, an artificial boundary condition has to be used. Usually, GENE uses a centered 4th order scheme for the derivative, which (as discussed in Appendix B) has a free parameter  $c$  for this external boundary condition. In contrast to e.g. upwind schemes, the centered schemes are not dissipative, but the fact that they primarily couple second neighbours and only loosely couple next neighbours can lead to a divergence of the two strongly coupled subsets of grid points (i.e. even and odd indices) in the presence of a strong parallel perturbation or discontinuity. Although the amplitudes at the external boundaries are quite small due to the ballooning structure of the unstable modes, the boundary condition represents such a discontinuity and can lead to zigzag perturbations, the amplitude depending on the value of the constant  $c$ . The optimal value for  $c$  depends on the physical parameters and resolution, an adaption to each individual situation is therefore impractical.

### 3.1. Discretization of the operators

Throughout this work, zero boundary conditions ( $c = 8$ ) are used, and the zigzag is controlled by adding (hyper-)diffusion terms, which remove these small scale artefacts and effectively couple the two subsets. In GENE, adjustable forth derivative damping terms are implemented to this end.

#### 3.1.3. Velocity space

For the velocity space, the numerical integration schemes that are used to calculate moments of the distribution function are a modified trapezoid rule in  $v_{\parallel}$  direction and Gauss-Legendre integration in  $\mu$  direction [39]. The parallel advection term is also represented with a finite difference scheme, with the comments from the last subsection and Appendix B concerning boundary conditions and hyperdiffusion also applying to the  $v_{\parallel}$  direction. Derivatives in the  $\mu$  direction are only needed for the collision operator (2.36), which is implemented using a finite volume scheme, so that only derivatives at the midpoints between the actual gridpoints are needed. In the  $\mu$  direction, a second order derivative is used, which implies that one additional boundary condition for the flux, namely that the flux over the boundary of the simulation domain vanishes, is enough to define the scheme. The collision operator consists of both advective and diffusive terms in velocity space, which avoids numerical problems both for the finite volume scheme and for an alternative pure finite difference approach, since the diffusive damping needed to avoid decoupling due to the first derivative is provided naturally and no hyperdiffusion in  $\mu$  direction is necessary. Collisions are a physical source of diffusion; for large enough  $\nu_c$ , the hyperdiffusion in the  $v_{\parallel}$  direction can therefore be switched off as well. Collisions also improve the convergence properties in velocity space. In the  $(v_{\parallel}, \mu)$

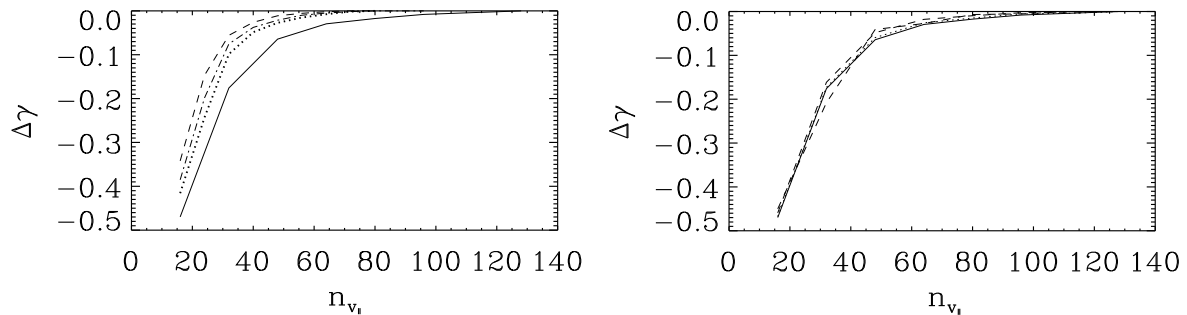


Figure 3.1.: Relative error of the growth rate for different numbers of  $v_{\parallel}$  points. Left plot: solid, dotted, dash-dotted and dashed lines correspond to  $\nu_c = 0.0, 5 \cdot 10^{-5}, 1 \cdot 10^{-4}$  and  $2 \cdot 10^{-4}$ . Right plot: different curves correspond to different resolutions in  $z$  and  $\mu$  directions with all other parameters constant.

coordinates used in GENE, particle trapping in an inhomogeneous  $B_0$  field occurs due to an advection in the  $v_{\parallel}$  direction which is caused by the magnetic mirror force. Although they are represented by the same distribution function, there is no mixing between trapped and passing particles in the absence of collisions. In cases where it is very important to have a good representation of this discontinuity due to the trapped-passing boundary, the resolution in  $v_{\parallel}$  has to be sufficiently high. If collisions are included, passing particles can become trapped

### 3. The GENE code

and vice versa, so that the trapped-passing boundary disintegrates with increasing collision frequency. This effect allows for a reduction of  $n_{v\parallel}$ , the number of points used in the  $v\parallel$  direction. This is shown in the left plot of Fig. 3.1, where the relative deviation of the linear growth rate  $(\gamma - \gamma_c)/\gamma_c$  with respect to the converged ( $n_{v\parallel} \rightarrow \infty$ ) value  $\gamma_c(v_c)$  is depicted as a function of  $n_{v\parallel}$  for some sensitive TEM test case. The right plot illustrates that although the value of the converged growth rate  $\gamma_c$  depends on the resolution in the  $z$  and  $\mu$  directions, the convergence properties in  $v\parallel$  direction are relatively independent of these parameters.

## 3.2. Anti-aliasing

The numerical discretization of a physically continuous dimension inevitably defines a largest scale, which is given by the extent of the simulation domain, and a smallest scale, which is implied by the finiteness of the number of grid points in that simulation domain. This smallest scale defines a lower limit on the structures that can be represented in the discretized system. If the system now exhibits a spectral evolution to higher wavenumbers, i.e. physical processes that create smaller and smaller structures, once the lower limit is reached the finite resolution leads to the erroneous creation of again larger structures due to the sampling theorem. While this effect is difficult to avoid in direct space and has to be reduced by artificial (hyper-)diffusion, aliasing can be neatly controlled in Fourier space by setting all modes with  $k > k^{max}$  to zero. In GENE11, there are two effects that lead to the creation of smaller scales in the perpendicular direction. One is a linear effect that is only active in the  $k_x$  direction, namely the parallel boundary condition, and the second is the nonlinearity, which leads to a spectral transfer in both  $k_x$  and  $k_y$ . For the parallel boundary condition, the connections of all  $k_x$  grid points that are considered in the simulation are done correctly according to Eq. (2.10); for the connections to grid points with higher absolute values of  $k_x$  than the chosen resolution, the boundary condition is set to zero. This is a reasonable assumption because the amplitudes of the unstable linear modes usually drop off at high  $k_x$  (see left plot of Fig. 3.2). To

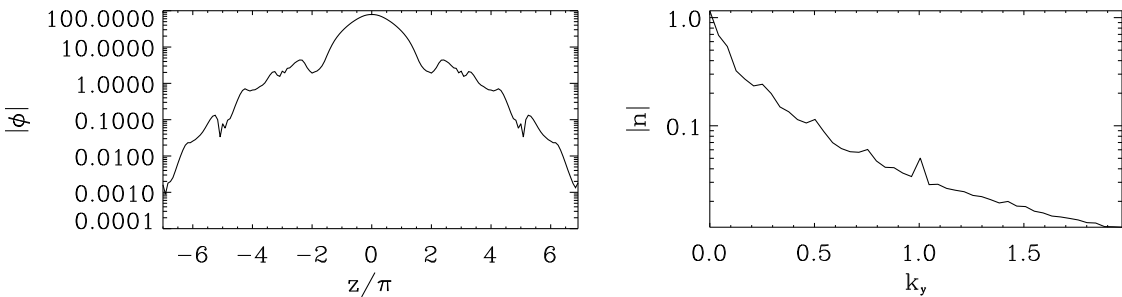


Figure 3.2.: Left: Typical ballooning structure of a linear mode with adiabatic electrons.  
Right: Typical nonlinear spectrum.

avoid aliasing effects in the  $x$  and  $y$  directions due to the nonlinearity, the well established 3/2 rule is employed, i.e. the numerical grid in these directions is expanded by small scale modes with amplitude zero before the Fourier transformation (this corresponds to a refinement of the grid), then the two quantities are multiplied in direct space, the result is transformed back

to Fourier space and the additional modes (which have been subject to aliasing effects) are removed again. In this way, all modes that remain in the computation are 'clean'. The assumption that all modes outside the simulation domain are zero is again justified by the fact that nonlinear simulations (for a reasonable choice for the simulation domain) always peak at a low  $k_{\perp}$  values, usually even lower than the linear spectra, and drop off to high  $k_{\perp}$  (see right plot of Fig. 3.2). With these measures, all aliasing effects have been removed spectrally and no numerical diffusion has to be added in the  $x$  and  $y$  directions, but as always, a negative influence of the unphysical boundary conditions has to be excluded by convergence tests.

### 3.3. Eigenvalue solver

To be able to analyze the eigenvalue spectrum of the linear gyrokinetic operator (2.39), an interface to the SLEPc extension [40, 41] of the PETSc package [42, 43, 44] has been developed. SLEPc is an iterative eigenvalue solver, which means that in contrast to direct methods, it does not manipulate the operator matrix, but repeatedly applies matrix-vector multiplications representing the evaluation of the right-hand side of Eq. (2.41) to a set of test vectors.

With this approach, the matrix does not even have to be calculated in explicit form, which would be very memory-intensive; a reasonably resolved state vector  $g$  necessary for a linear mode computation has of the order of 100,000 entries, so that an explicit representation of the linear operator matrix would have of the order of  $10^{10}$  complex entries, corresponding to approximately 150 GB of storage. In addition, a direct solver would be extremely slow, since it computes the full spectrum of the linear operator, which in general contains as many eigenvalues as the dimension of the state vector. Iterative methods are very effective compared to this if not all eigenvalues are needed but only a (small) subset, which is the case for linear gyrokinetics. Another advantage of the iterative matrix-free method is that the highly optimized and parallelized GENE routines for the right-hand side calculation of Eq. (2.41) that are usually used for initial value calculations (see next section) can be used without major modifications. If the eigenvalue problem is solved, the time evolution equation (2.41) can be solved trivially. The imaginary part of the eigenvalue then corresponds to the frequency of the mode, the real part to the growth rate. Eigenmodes with positive real part of the eigenvalue are therefore unstable and grow exponentially in time. Because of this equivalence, the terms growth rate (frequency) and real (imaginary) part of the eigenvalue will be used interchangeably in this thesis.

A typical eigenspectrum of the linear operator is shown in the left plot of Fig. 3.3, where for once *all* eigenvalues of a small test problem have been computed, using the SLEPc interface to the serial direct eigenvalue solver of the LAPACK package. There is only one eigenvalue with positive real part, i.e. one unstable eigenmode in this example. All other modes have eigenvalues with slightly negative real parts, i.e. are slightly damped due to hyperdiffusion in parallel and  $v_{\parallel}$  directions (see discussion in Sec. 4.1). The extent of the spectrum along the real and imaginary axes differs by almost two orders of magnitude, most modes being aligned with the imaginary axis. While the microinstabilities, i.e. unstable modes at scales comparable to the gyroradius that are considered in this work, typically have growth rates of  $0 < \gamma \lesssim 1$  in units of  $c_s/R$  and frequencies of the same order, the maximum frequencies of the stable

### 3. The GENE code

eigenmodes are in the hundreds. Since the most rapidly oscillating modes are very sensitive to the parallel dynamics, the anisotropy of the spectrum increases with parallel resolution and ion to electron mass ratio.

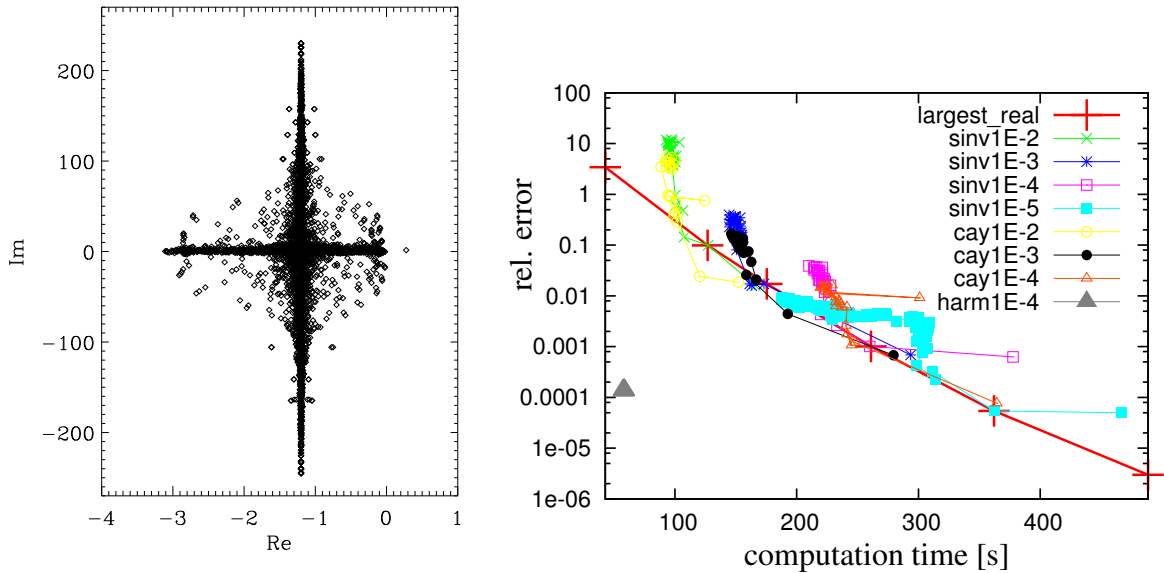


Figure 3.3.: Left: Typical full eigenvalue spectrum of the linear gyrokinetic operator with one unstable mode ( $\text{Re} > 0$ ). Right: Comparison of different iterative methods for the computation of the two most unstable eigenmodes in a realistic test case. Different points correspond to different shifts along the real axis, the values are between 10 and 250.

The standard algorithms available in SLEPc are most efficient in finding an arbitrary number of eigenvalues with the largest magnitudes. This is very useful for determining the maximal time step for an initial value computation (see Sec. 3.4.2 on explicit time stepping), but of physical interest are usually interior eigenvalues, namely the most unstable modes. These modes with positive real part turn out to have a very small imaginary part (frequency) compared to the many (marginally) stable modes in the system and can therefore only be accessed with the standard eigenvalue solvers after application of a so-called spectral transform. A spectral transform is a transformation of the operator  $\mathcal{L} \rightarrow \tilde{\mathcal{L}}$  which changes the spectrum  $\lambda_i$ , but leaves the corresponding eigenvectors intact. This implies that the transformation  $R$  necessary to diagonalize the linear operator has to stay the same, i.e. if  $R\mathcal{L}R^{-1} = \text{diag}(\lambda_i)$  then  $R\tilde{\mathcal{L}}R^{-1} = \text{diag}(\tilde{\lambda}_i)$ . A suitable transformation projects the eigenvalues of interest to large amplitudes while keeping the unwanted part of the spectrum at low amplitudes, so that the standard solvers can be applied. Once the desired eigenvectors are found, the spectrum can easily be transformed back to obtain the correct values for the original problem. Examples of spectral transforms are complex shifts (i.e. the addition of a complex number times the unit matrix)

$$R(\mathcal{L} + c\mathbf{1})R^{-1} = \text{diag}(\lambda_i) + c \quad (3.1)$$

and inversions of the operator. Of special relevance to the problems considered here is a combination of the two: The multiplication of Eq. (3.1) with  $R[\mathcal{L} + c\mathbf{1}]^{-1}R^{-1}$  gives

$$R[\mathcal{L} + c\mathbf{1}]^{-1}R^{-1} = \text{diag}(\tilde{\lambda}_i) = \frac{1}{\text{diag}(\lambda_i) + c}$$

which, together with an algorithm for finding the largest absolute value can be used to find eigenvalues close to  $-c$  in the complex plane. The inverted matrix is never computed explicitly, rather  $[\mathcal{L} + c\mathbf{1}]^{-1}g$ , which has to be evaluated in each iteration of SLEPc and for all test vectors, is computed with PETSc routines, which again employ matrix-free iterative methods to solve the linear system of equations associated with the inversion. While these inversions are very time-consuming, it is known that the efficiency of linear solvers can be increased drastically with a suitable preconditioner, unfortunately the preconditioners already implemented in PETSc are not suitable for the matrix-free integro-differential operator of GENE and the development of a specially designed preconditioner is rather difficult.

A very promising recent development of the SLEPc programmers, that has been quickened by a collaboration with the GENE group, are harmonic projection methods, which are able to access interior parts of the eigenspectrum without the costly inversions. At the time of writing, they were only available in a development version of SLEPc, but first tests showed a gain of a factor of 5 in the computation time compared to spectral transforms relying on inversions (see Fig. 3.3). Extensive tests of the different spectral transforms and their applicability to GENE problems can be found in [45, 46].

## 3.4. Initial value solver

While arbitrary parts of the spectrum of the linear gyrokinetic operator are only accessible with an eigenvalue solver, for some investigations it is only necessary to know the properties of the most unstable mode. An alternative to the eigenvalue solver is in this case the discretization of the time derivative of Eq. (2.41) and computation of the initial value problem, with a superposition of all linear modes as initial condition  $g(t = 0)$ . The evolution equation for the different eigenmodes  $g_i$ ,

$$\frac{\partial}{\partial t}g_i = \lambda_i g_i$$

describes an oscillation superposed by exponential growth, which is determined by the real part of the eigenvalue  $\lambda_i$ . After some time, the state vector  $g$  – which initially contained all modes – is dominated by the most unstable mode and the corresponding growth rate and frequency can be determined (see left plot of Fig. 3.4; the growth rate is proportional to the slope in this logarithmic plot). With a suitable time stepping scheme, this procedure is usually faster than the eigenvalue solver. For the case that all  $k_x$  grid points are coupled via the parallel boundary condition (2.10), a routine computing

$$\lambda_{\text{iv}}(k_y) = \frac{\sum_{k_x,z} w(k_x, k_y, z) \lambda(k_x, k_y, z)}{\sum_{k_x,z} w(k_x, k_y, z)} \quad \text{with} \quad \lambda(k_x, k_y, z) = \ln \left( \frac{\phi(t_n)}{\phi(t_{n-1})} \right) / \Delta t \quad (3.2)$$

### 3. The GENE code

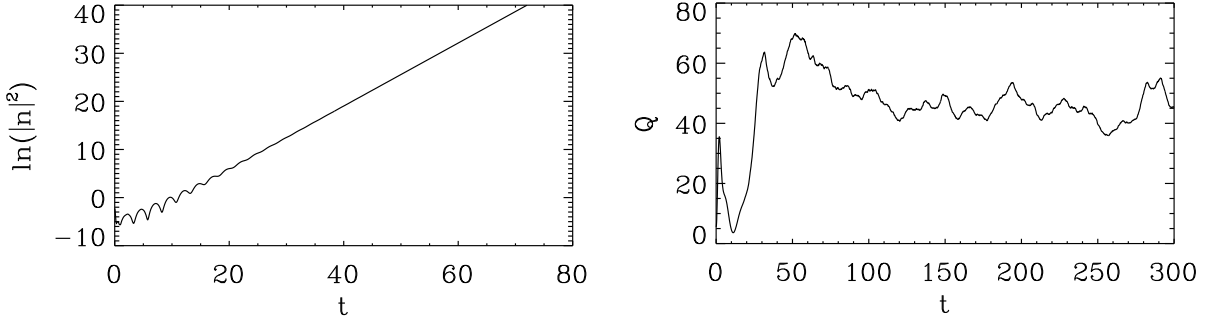


Figure 3.4.: Left: Linear initial value computation with competing eigenmodes for low  $t$ . Right: Nonlinear initial value computation with transient ( $t \lesssim 100$ ) and quasistationary phase ( $t \gtrsim 100$ ).

directly in GENE was implemented. The result  $\lambda_{\text{iv}} = \gamma_{\text{iv}} + i\omega_{\text{iv}}$  is the combined growth rate and frequency of the mode as represented by the time stepping scheme; a criterion that the computation is converged for a given  $k_y$  is that the scatter of  $\lambda(k_x, k_y, z)$  is below a certain, adjustable limit  $c_p$  connected to the precision of the value for  $\lambda$ :

$$\frac{\sum_{k_x,z} |\lambda(k_x, k_y, z) - \lambda_{\text{iv}}(k_y)|^2 w(k_x, k_y, z)}{\sum_{k_x,z} w(k_x, k_y, z)} < c_p \quad (3.3)$$

(for a pure eigenmode,  $\lambda(k_x, k_y, z) = \lambda_{\text{iv}}(k_y)$  for all  $k_x, z$ ). The weight  $w(k_x, k_y, z) = \phi(t_{n-1})$  proved to accelerate the computation. To reduce the computation time, the routine usually does not use each available time step but larger time intervals of approximately  $10/\Delta t$ .

Note that the discretization of the time derivative introduces an additional error, so that in general  $\lambda_{\text{iv}}$  obtained with an initial value computation is less accurate than the eigenvalue of the most unstable mode calculated with the eigenvalue solver  $\lambda_{\text{ev}}$ . For the implicit Euler scheme described below, these errors can be substantial and are corrected in GENE (see next section); for the higher-order explicit schemes with their limited time step, they can be neglected for the microinstabilities considered here, so that the distinction between  $\lambda_{\text{iv}}$  and  $\lambda_{\text{ev}}$  is dropped from now on.

With the routines computing (3.2) and (3.3), it was possible to achieve the same level of automatization for parameter scans with the initial value solver as with the eigenvalue solver. However, these routines are based on the assumption that the distribution function is (after some time) dominated by only one exponentially growing mode. If there is a second unstable mode in the system with a very similar growth rate (but different frequency), the beat of the two modes will avoid convergence until the two amplitudes are sufficiently different, so that the computation time goes to infinity for  $\gamma_2 \rightarrow \gamma_1$ . A case with two competing growth rates is shown in the left plot of Fig. 3.4, the beat is observable for  $t \lesssim 30$ .

For linear investigations, the initial value solver can be used to speed up the computations that could also be done with an eigenvalue solver, but way more important is that an efficient discretization of the time derivative also allows for a numerical solution of the nonlinear gyrokinetic equation (2.38). The right plot of Fig. 3.4 shows the time trace of the heat transport for some typical simulation, where after the initialization, a phase of linear growth is followed

by an overshoot, before finally a quasistationary state is reached. The transient phase depends on the initial conditions and is therefore not significant, of interest are only the statistical properties of the quasistationary phase (e.g. the average heat transport). With more effective time stepping schemes, less computational effort is wasted on the transient initial phase and the length and therefore the statistics of the quasistationary state can be improved.

### 3.4.1. Implicit time stepping scheme

A very simple discretization of the time derivative of Eq. (2.41) applicable to linear computations is the implicit Euler scheme,

$$\frac{g(t_{n+1}) - g(t_n)}{\Delta t} = \mathcal{L}g(t_{n+1}). \quad (3.4)$$

As in all implicit schemes, the right hand side of Eq. (3.4) is evaluated with the state vector at the incremented time index  $t_{n+1}$ , making the scheme A-stable, which means that the numerical representation of all modes with  $\text{Re}(\lambda) \leq 0$  is also stable, without any conditions on  $\Delta t$ . The drawback of implicit schemes is the matrix inversion, that is necessary to solve Eq. (3.4) for  $g(t_{n+1})$ :

$$g^{n+1} = [\mathbf{1} - \Delta t \mathcal{L}]^{-1} g^n. \quad (3.5)$$

The right hand side of this equation can be computed with the iterative solvers provided by PETSc, similar to the spectral transformations for the eigenvalue solver. As already mentioned, the implicit Euler scheme is numerically stable for all values of  $\Delta t$ . For larger values of  $\Delta t$ , fewer time steps are needed to bridge the transient phase and reach convergence as described by Eq. (3.3), but at the same time the off-diagonal elements of the operator to be inverted grow, which slows down the PETSc routines, so that the minimum of the over all computation time is at finite  $\Delta t$ , actually at similar values than for the explicit schemes described below. The comment concerning a suitable preconditioner in Sec. 3.3 also applies here.

Another subtlety with this method is that it is only accurate to first order in  $\Delta t$ , which combined with the unconditional stability can lead to huge dissipation and dispersion errors.

However, if the growth rate and frequency have been determined according to Eq. (3.2) without additional errors due to an insufficient sampling rate and the ordering of the eigenvalues according to their growth rates has been preserved, these errors can be corrected afterwards with

$$\lambda_{\text{corr}} = \frac{1 - e^{-\lambda_{\text{iv}} \Delta t}}{\Delta t},$$

so that this method is still suitable for linear initial value calculations.

### 3.4.2. Explicit time stepping schemes

Easier to evaluate are explicit time stepping schemes, since they do not involve matrix inversions. They are only conditionally stable, i.e. the numerical representation of the time

### 3. The GENE code

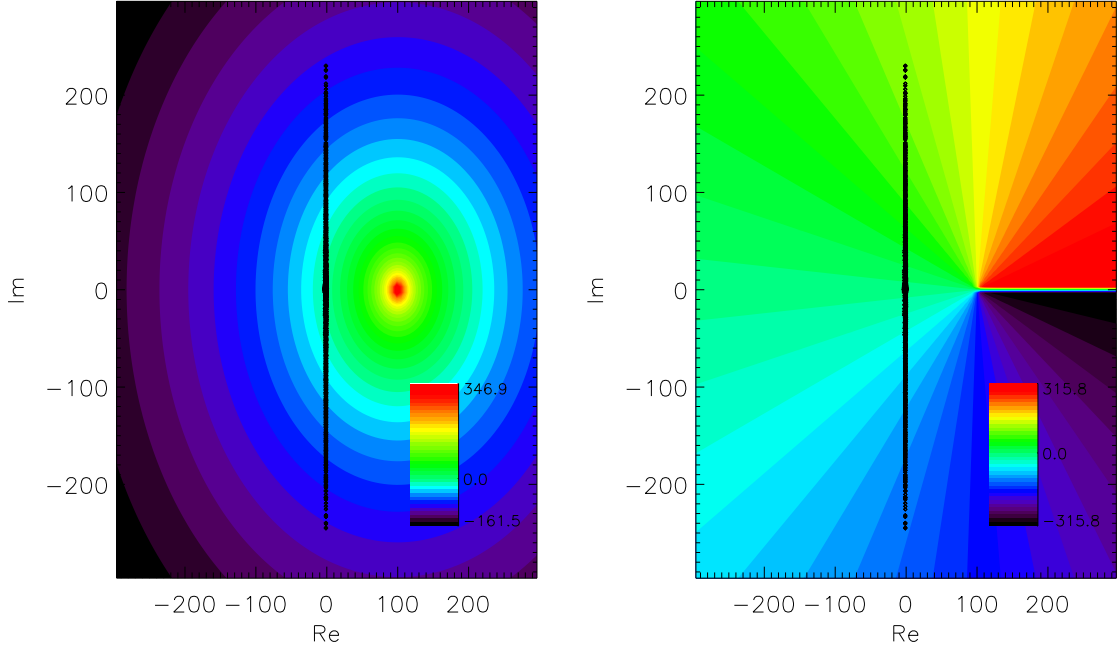


Figure 3.5.: Eigenvalues (black) and contour plots of  $\text{Re}(\lambda_{\text{iv}})$  (left) and  $\text{Im}(\lambda_{\text{iv}})$  (right) as seen by the implicit Euler scheme with  $\Delta t = 0.01$ .

evolution of an eigenmode with  $\text{Re}(\lambda)$  is stable if and only if the time step width  $\Delta t$  is below a certain limit. At least the nonlinearity in Eq. (2.38) has to be treated with an explicit time stepping scheme, since an inversion of the quadratic integro-differential operator representing the  $\vec{E} \times \vec{B}$  nonlinearity is not feasible; if the full system is treated with an explicit scheme, this allows for an easy adaption of  $\Delta t$  during the simulation, which is important for nonlinear simulations (see next section). The shape of the stability region depends on the choice of the time stepping scheme, its size can be increased by decreasing  $\Delta t$ . The white lines in Fig. 3.6 encircle the stability region of the various Runge-Kutta schemes implemented in GENE, i.e. they mark the values  $\lambda$  for which  $g$  in the test equation

$$\frac{\partial}{\partial t} g = \lambda g$$

is neutrally stable;  $\Delta t$  has been adapted in each case to keep all eigenvalues (black) within the stability region (white). The three explicit Runge-Kutta schemes are discussed in more detail in Appendix C. Each stage of a Runge-Kutta scheme involves one computation of the right hand side of Eq. (2.38), the numerical effort to advance the system by  $\Delta t$  with the different schemes is therefore proportional to the number of stages of the scheme.

The comparison of the three schemes presented here shows that while the number of stages for the 3rd, 4th and modified 4th order scheme are 3:4:6, the maximal  $\Delta t$  is 0.0071:0.0114:0.0198, so that the normalized efficiencies of the schemes are approximately 1.0:1.2:1.4, a ratio that is almost independent of the simulation parameters, since the shape of the eigen-spectrum is always mostly hyperbolic. This means that after a given CPU time, the physical

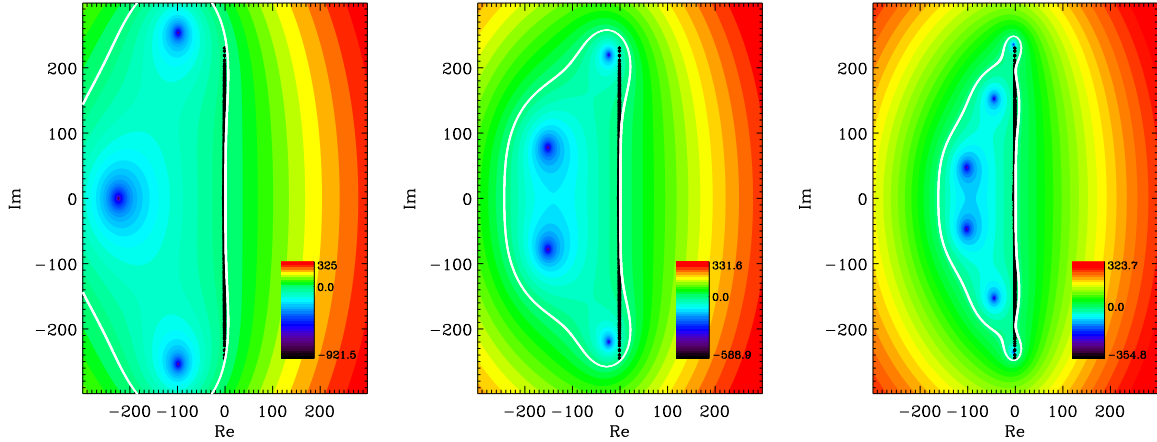


Figure 3.6.: Growth/damping rates (color) as seen by the time stepping scheme and stability region (white) in the complex plane for RK3, RK4 and RK4M, with  $\Delta t=0.0071$ , 0.0114 and 0.0198 respectively. The time step has been adapted to the eigenvalue spectrum for each case

time covered by a simulation using the modified 4th order scheme is 1.4 times longer than with the 3rd order scheme, which obviously speeds up convergence for linear runs, but also reduces the CPU time spent in the transient start-up phase of a nonlinear simulation.

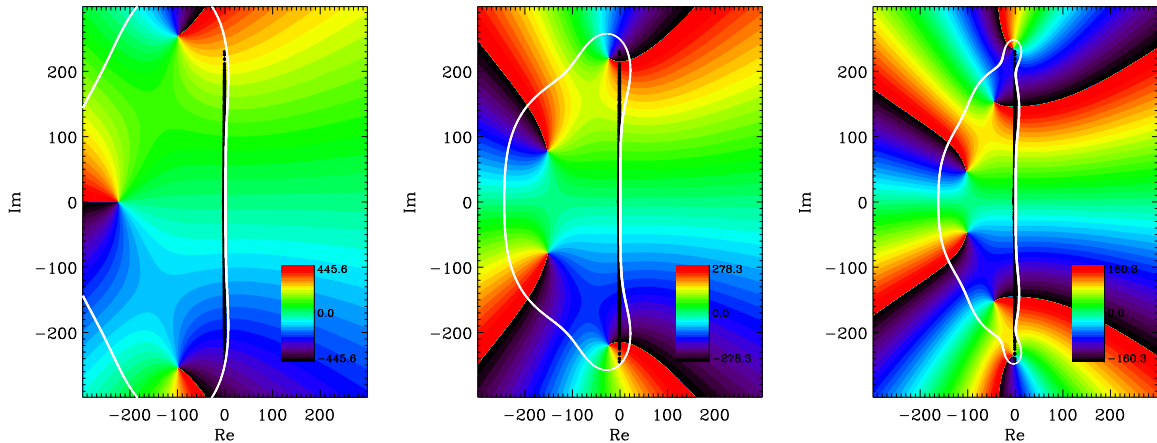


Figure 3.7.: The corresponding frequencies (color) as seen by the time stepping scheme and stability region (white) in the complex plane for RK3, RK4 and RK4M.

The figures 3.6 and 3.7 can also be used to discuss the numerical errors associated with the explicit time stepping schemes. The colour coding in Fig. 3.6 shows the growth rate as seen with the RK4 scheme. The error in the growth rate largely depends on the position of the eigenvalue in the complex plane. While a perfect representation of the time derivative would have growth rate isolines that are exactly parallel to the imaginary axis with values corresponding to the real axis, all numerical approximations show significant deviations from

### 3. The GENE code

this, especially for the stable (left) half plane. Modes with eigenvalues outside the stability region grow exponentially, which is correct for eigenvalues on the half plane with positive real part but clearly unphysical for modes on the left half of the complex plane. It is therefore essential to choose a  $\Delta t$  that ensures that all stable eigenvalues actually lie within the stability region. For the unstable half plane, the deviations decrease for lower imaginary parts, so that the physically relevant unstable modes, which always have low frequencies, are well represented. For all explicit schemes considered here, the purely oscillating modes on the imaginary axis are stabilized, especially for bigger imaginary parts. The high frequency modes close to the blue singularities (especially for RK4 and RK4M) are damped significantly by the numerical scheme. However, this is not too worrying, since the (shear Alfvén) modes with the highest frequencies have the lowest parallel wave lengths, so that the extent of the spectrum in the imaginary direction is connected to the parallel resolution. A damping of these modes is therefore equivalent to a slight reduction of the parallel resolution, which means that negative effects on the simulation can be excluded by the usual convergence tests and no additional constraint arises from using the faster RK4 or RK4M schemes.

Similar observations can be made for the dispersion errors shown in Fig. 3.7. A perfect representation of the time derivative would have isolines of the frequency parallel to the real axis with values corresponding to the imaginary axis. This is not given on the stable half plane, but even on the unstable half plane sign reversals of the frequency can occur for large imaginary parts. Again, the error decreases dramatically for lower imaginary parts and the physically relevant modes are well represented by all schemes.

This shows that the numerical errors due to the discrete time stepping of both the growth rate and the frequency are small in the region with low absolute growth rate and low frequency, which contains the physically relevant modes, especially the unstable ones that constitute the drive of the turbulent system.

## 3.5. Nonlinear simulations

Even if the linear time step has been computed correctly according to Sec. 3.4.2, the nonlinearity can lead to numerical instability in turbulence simulations. To avoid this,  $\Delta t$  has to be lowered if the time step limit due to the  $\vec{E} \times \vec{B}$  advection becomes stricter than the linear limit. To compute this additional limit at each time step  $t_n$  of a simulation, the nonlinearity is linearized by treating  $\phi(t_n)$  as a constant for the multiple stages of the time stepping scheme, so that in principle the eigenvalue solver could be used to compute the new maximal  $\Delta t$ . This would, however, be very costly, the maximal time step is therefore approximated as

$$\Delta t_{\max} = s_c * \min(\Delta t_{\text{lin}}, \Delta t_{\text{NL}}),$$

where  $\Delta t_{\text{NL}}$  is calculated with the assumption that only the  $\vec{E} \times \vec{B}$  advection (and no linear physics) is present. The assumption of a simple superposition of linear and nonlinear effects is of course only a crude approximation, for this reason the safety factor  $s_c$  has to be introduced. In addition it is known that simulations are less noisy if the time step is kept well below the maximal stability limit, the safety factor is therefore usually put to  $\approx 0.5$ .

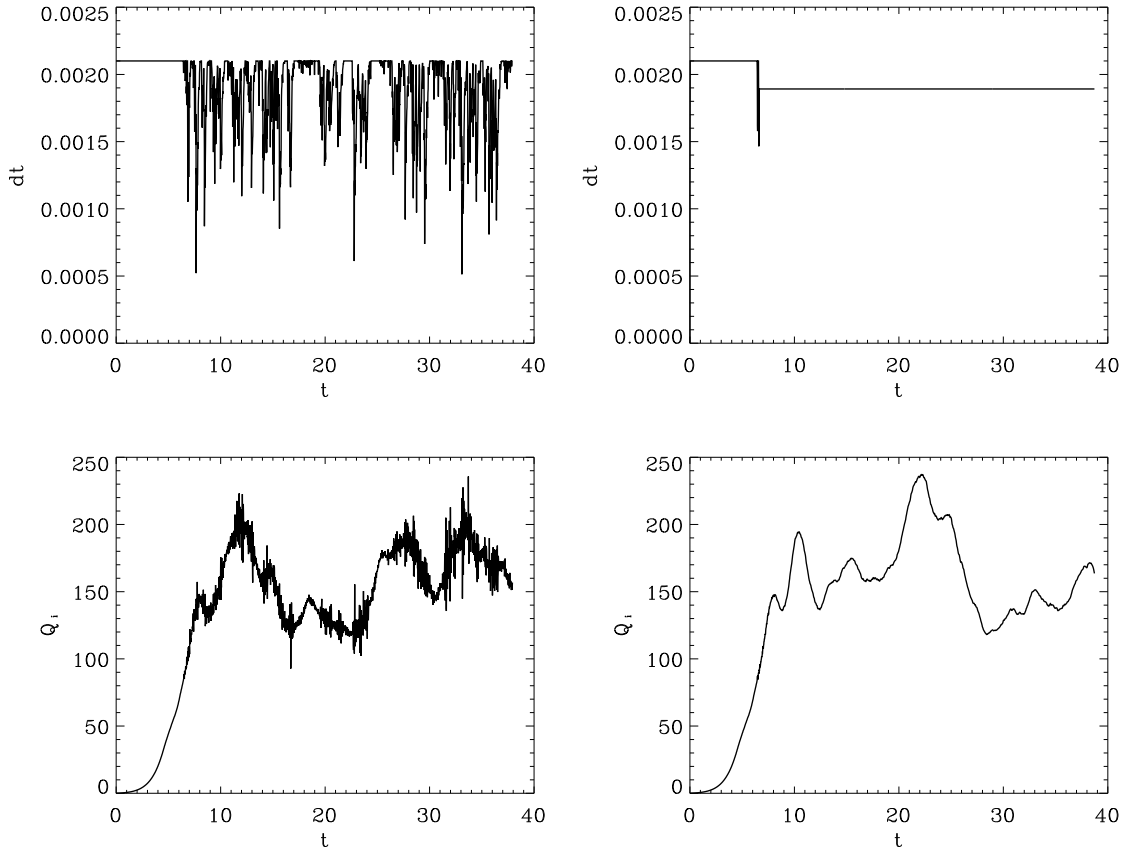


Figure 3.8.: Effect of the time step adaption on the nonlinear simulation. The left and right sides show the temporal change of  $\Delta t$  and the ion heat flux for two simulations with the same parameters, but different prescriptions for the nonlinear time step adaption.

If the  $\Delta t_{\max}$  defined above is determined by the nonlinearity, it changes with every time step. Rapid and significant variations of  $\Delta t$  can lead to numerical artefacts such as resonances in the simulation (see Fig. 3.8), it is therefore better to define a target corridor for  $\Delta t/\Delta t_{\max}$  and adapt  $\Delta t$  only if necessary. In gene,  $\Delta t$  is only adapted once it violates  $0.8 \leq \Delta t/\Delta t_{\max} \leq 1.2$ , which leads to much smoother simulations, as shown in Fig. 3.8.

## 3.6. Parallelization

For plasma turbulence simulations, the ability to use many processors in parallel is essential. One reason are the memory requirements: A typical nonlinear ion scale tokamak simulation needs around  $128 \times 64 \times 24 \times 48 \times 8 \times 2$  points for the distribution function in  $k_x, k_y, z, v_{\parallel}, \mu$  and species directions, this corresponds to a double complex array of 2.3 GB. To store auxiliary fields, e.g. from the time stepping scheme, GENE uses 4 of these high dimensional arrays,

### 3. The GENE code

some of which with additional ghost cells for boundary exchanges (see Appendix B), plus many lower dimensional arrays, so that the total memory requirements for this example would be around 12 GB; for simulations that include effects both on electron and ion gyroradius scales, or consider stellarator geometry, this number can be much higher. While this already shows that simulations of plasma turbulence would be impossible on a single processor, the even more important issue is time. A simulation with the above resolution usually takes (depending on the machine) of the order of 5,000 CPU hours, without massive parallelization, detailed investigations would therefore be impossible.

GENE can be run both on distributed and shared memory architectures. For distributed memory architectures, MPI parallelization and the so-called domain decomposition are of great importance. To make the computation of big problems possible on many processors with limited memory, the six dimensional modified distribution function  $g$  and all auxiliary arrays like  $f$ , the  $k$ 's of the Runge-Kutta schemes (see Appendix C), the electromagnetic fields and the multi-dimensional prefactors employed in the computation are cut into subarrays and then distributed to different processors. Every processor then only computes a small subvolume of the whole the problem, if information from neighbouring subvolumes of the distribution function is needed, e.g. for the calculation of derivatives in the various directions, this information has to be sent explicitly from one processor to the other. The finite difference schemes employed in GENE are local, i.e. to approximate the value of the derivative at one grid point, they only need the values of a limited number of neighbouring points. The usual method to provide these values if the direction is distributed on several processors is by so-called ghost cells, i.e. additional boundary cells where a copy of the corresponding values of the neighbouring cells from the neighbouring processor are stored. These ghost cells have to be updated prior to each evaluation of the derivative. Although this domain decomposition and the associated MPI communication calls make the code rather complex, MPI parallelization works both on shared and distributed memory architectures and is therefore more flexible than OpenMP parallelization, in addition it is crucial to reach high processor numbers. Gene is MPI-parallelized along the  $k_y, z, v_{\parallel}, \mu$  and species directions. In contrast to the  $k_y$  direction, the MPI-communication in the latter four dimensions, that includes for example exchanges of ghost cells for the finite difference schemes or global sums for the calculation of velocity space moments, is in general straightforward to implement.

The parallelization of the  $k_y$  direction is more complicated. For linear computations, it is trivial, because Eq. (2.41) decouples completely in  $k_y$  direction. For nonlinear computations however, the arrays needed for the computation of the nonlinearity have to be Fourier transformed in the  $k_x$  and  $k_y$  directions, but since the Fourier transform is a global operation, i.e. needs the values at all grid points, simple ghost cells in  $k_y$  direction are of no use. For the  $k_y$  Fourier transform, all data along the  $k_y$  direction has to be on the same processor, preferably contiguous in memory. This is achieved by first performing the Fourier transform in the (contiguous)  $x$  direction, e.g.  $A(k_x, k_{y1} : k_{y2}) \rightarrow A(x, k_{y1} : k_{y2})$  (the interval  $k_{y1} : k_{y2}$  are the  $k_y$  values stored on the given processor) and transposing the array on the processor  $A(x, k_{y1} : k_{y2}) \rightarrow A(k_{y1} : k_{y2}, x)$ , then exchanging the content of the different MPI processes along the  $k_y$  direction using MPI\_ALLTOALL communication to gather all  $k_y$  grid points belonging to a given interval of  $x$  grid points on one processor,  $A(k_{y1} : k_{y2}, x) \rightarrow A(k_y, x_1 : x_2)$ . Note that the array is now parallelized over the  $x$  direction instead of  $k_y$  and the Fourier trans-

form of the now contiguous  $k_y$  direction,  $A(k_y, x_1 : x_2) \rightarrow A(y, x_1 : x_2)$ , can be performed easily. With the arrays in this representation, the nonlinearity is then calculated and the result is transformed back performing the above steps in reversed order.

In addition to MPI, all numerically expensive loops are parallelized with OpenMP, so that on shared memory systems, the code scales well even without the use of MPI. It is also possible to use a hybrid MPI/OpenMP parallelization. Gene can run on many different architectures,

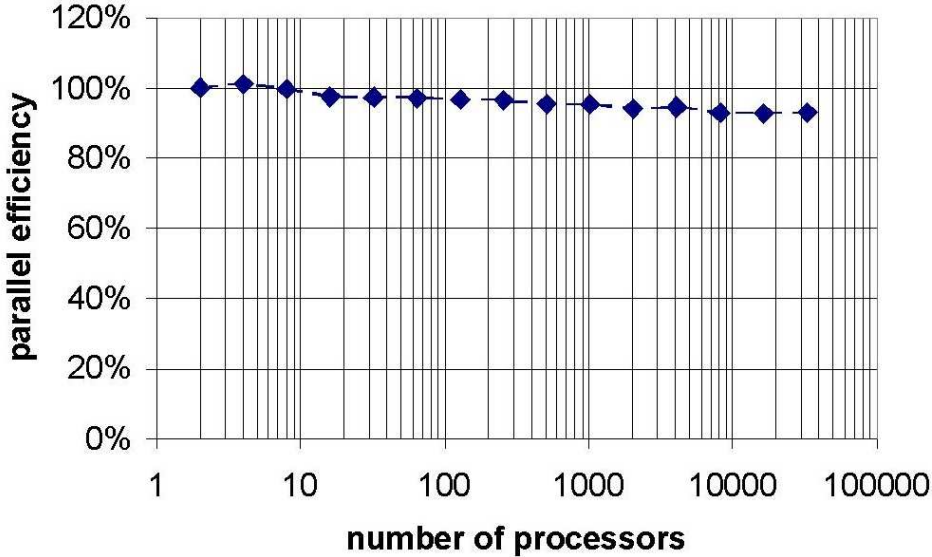


Figure 3.9.: Parallel efficiency (weak scaling) on BlueGene L of the IBM Watson Research center.

from a laptop computer for simple linear runs to Linux clusters to big supercomputers like IBM Power4/5/6, SGI Altix, Cray or IBM BlueGene systems. It has been tested extensively, and as can be seen in Fig. 3.9 and in more detail in [38], it can be used efficiently on up to at least 32768 processors.

## 3.7. Summary

In this chapter, the gyrokinetic plasma turbulence code GENE has been presented. The background of its implementation has been illustrated and some of the major advances have been discussed in more detail. The extensions and generalizations of the equations, that have been discussed in the previous chapter have been implemented in the code, including a transition from a direct space to a Fourier space representation of the radial coordinate. Considerable progress was achieved through improved numerical schemes, e.g. for the time stepping and anti-aliasing procedures, leading to faster and more robust computations.

Furthermore, completely new features like an interface to an eigenvalue solver have been implemented. Many of these developments, like the more sophisticated collision operator or the eigenvalue solver, are in this form presently only available in GENE and allow for

### *3. The GENE code*

completely new numerical investigations of plasma microturbulence and the underlying microinstabilities. This will be exploited in the remainder of this thesis.

## 4. Fundamental features of linear gyrokinetics

The magnetized plasmas that occur in the context of magnetic confinement fusion exhibit a large number of “microscopic” (i.e. gyroradius-scale) instabilities driven by the background density and temperature gradients. These microinstabilities constitute the drive for the turbulence that leads to the anomalous transport determining the energy confinement time. Before addressing the physically and technically very important plasma turbulence problem, it is crucial to understand the underlying linear physics.

The microinstabilities are usually classified according to some of their key characteristics like e.g. their diamagnetic drift direction, and studied in some ideal limit. On electron gyroradius scales, the most important instability in the core plasma of tokamaks and stellarators is the electron temperature gradient (ETG) mode. On ion gyroradius scales, the trapped electron mode (TEM) and/or the ion temperature gradient (ITG) mode are the most important ones. Although it has been known for a long time that under certain conditions, different types of modes can “mix” or “merge”, it was usually assumed that by continuously changing the plasma parameters, it is possible to trace a mode back to some region of parameter space in which its identity is clear without ambiguity.

After discussing some fundamental properties of the linear operator, it will be shown in this chapter that this idea in general does not work, since due to the non-Hermiticity of the linear gyrokinetic operator, non-Hermitian degeneracies occur that connect the different instabilities. The results of this chapter, which have been obtained in collaboration with M. Kammerer, have been published in [47].

### 4.1. Structure of the linear gyrokinetic equation

The linearized gyrokinetic equation,

$$\frac{\partial g}{\partial t} = \mathcal{L}[g], \quad (4.1)$$

describes the time evolution of the modified distribution function  $g$  by the complex integro-differential operator  $\mathcal{L}$  given by expression (2.39). Physically,  $g$  is a scalar field of the three spatial, two velocity space and the species coordinates, mathematically, it can be viewed as the complex state vector of the system. Discretization makes this state vector finite dimensional and turns the operator  $\mathcal{L}$  into a matrix. The properties of this matrix then fully define the system.

Eq. (4.1) is very similar to the Schrödinger equation in quantum mechanics,

$$i\hbar \frac{\partial}{\partial t} \psi = \hat{H} \psi,$$

#### 4. Fundamental features of linear gyrokinetics

where the time evolution of the wave function  $\psi$  is governed by the Hamiltonian  $\hat{H}$ . Because of the significance of the Schrödinger equation in physics, it is well studied and many results can be applied also to the linear gyrokinetic equation. Note however that due to the prefactor  $i\hbar$  that only occurs in the Schrödinger equation, the equivalent of a Hermitian Hamiltonian is an *anti*-Hermitian operator  $\mathcal{L}$ .

A key result from quantum mechanics is that a Hermitian Hamiltonian leads to a unitary time evolution operator, meaning that the norm of the state vector is invariant. This is a result of the fact that the eigenspectrum of a Hermitian operator is purely real and the eigenvectors belonging to different eigenvalues are orthogonal, which can be shown easily. Analogously, a purely anti-Hermitian operator  $\mathcal{L}$  would have a purely imaginary eigenvalue spectrum, i.e. all eigenmodes would be neutrally stable, which is, given the omnipresence of unstable modes in gyrokinetics, obviously not the case. Since it is the non-Hermiticity of  $\mathcal{L}$  that leads to the microinstabilities in the system, it is interesting to know the origin of this property.

The linear operator of Eq. (2.13) for the full distribution function  $F$  consists only of a  $z$  dependent perpendicular advection due to the  $\vec{\nabla}B$  and curvature drifts and a constant parallel advection due to the parallel velocity and is therefore anti-Hermitian. (As has been mentioned briefly in Appendix B, if the discretization schemes are chosen carefully, the Hermiticity properties of the underlying equations can be retained in the numerical representation. The first derivatives occurring in the equations can be discretized spectrally or by centered difference schemes with appropriate boundary conditions without loosing their anti-Hermiticity.)

The  $\delta f$  splitting described in Sec. 2.4 creates new linear terms out of the nonlinear terms of the initial equation. In the collisionless, electrostatic limit,  $\nu_c \rightarrow 0$ ,  $\beta \rightarrow 0$ , the linear operator (2.39) can be split into two parts

$$\frac{\partial f}{\partial t} = \mathcal{L}[f] = \mathcal{L}^f + \mathcal{L}^\phi$$

given by

$$\begin{aligned} \mathcal{L}^f &= \left( -\frac{v_{Tj}}{JB_0} v_\parallel \frac{\partial}{\partial z} - \frac{T_{0j}(2v_\parallel^2 + \mu B_0)}{q_j B_0} (K_y ik_y + K_x ik_x) + \frac{v_{Tj}}{2JB_0} \mu \partial_z B_0 \frac{\partial}{\partial v_\parallel} \right) f \\ \mathcal{L}^\phi &= - \left( \omega_n + (v_\parallel^2 + \mu B_0 - \frac{3}{2}) \omega_{Tj} \right) F_{0j} ik_y J_0 \phi - \frac{v_{Tj}}{JB_0} v_\parallel \frac{q_j}{T_{0j}} F_0 \frac{\partial}{\partial z} J_0 \phi \\ &\quad - \frac{T_{0j}(2v_\parallel^2 + \mu B_0)}{q_j B_0} (K_y ik_y + K_x ik_x) \frac{q_j}{T_{0j}} F_0 J_0 \phi \\ \phi &= \frac{\sum_j n_{0j} \pi q_j B_0 \int J_0(\lambda_j) f_j dv_\parallel d\mu}{k_\perp^2 \lambda_D^2 + \sum_j \frac{q_j^2}{T_{0j}} n_{0j} (1 - \Gamma_0(b_j))}. \end{aligned}$$

The  $\mathcal{L}^f$  part is a differential operator acting on the distribution function. This operator is block diagonal in the species label, i.e. it describes the motion of non-interacting particles in the background magnetic field. If the prefactor  $\frac{1}{JB_0}$  is independent of the parallel direction, as e.g. in the widely used  $s - \alpha$  geometry (see Sec. 2.9.1),  $\mathcal{L}^f$  is anti-Hermitian; this part of  $\mathcal{L}$  is the equivalent of the the linear operator in the full- $F$  equation.

#### 4.1. Structure of the linear gyrokinetic equation

The field part  $\mathcal{L}^\phi$  is much more complicated. The field operator  $\phi$  is a linear integral operator. Its matrix representation is therefore dense in the velocity and species coordinates (in contrast to the sparse matrix representation of the differential operators represented spectrally or with finite differences).  $\mathcal{L}^\phi$  can be expressed as a matrix multiplication of a differential operator (with similar properties as  $\mathcal{L}^f$ ) with the field operator. This combination is not (anti-)Hermitian, so that due to these terms, the eigenvalues of  $\mathcal{L}$  are, in general, not purely imaginary and the eigenvectors are not orthogonal.  $\mathcal{L}^\phi$  is thus the origin of the wealth of interesting phenomena occurring in linear gyrokinetics, including Landau damping, the various microinstabilities and the non-Hermitian degeneracies, that will be discussed in this chapter.

Note that  $\mathcal{L}^\phi$  couples  $f$  to the background distribution function  $F_0$  via the electrostatic field. All of the respective terms originate from the *nonlinear* part of the Vlasov equation for the *full* distribution function  $F$ , they have only become part of the linear operator because of the  $\delta f$  splitting. Without this coupling (or alternatively without  $\delta f$  splitting),  $\mathcal{L}^\phi$  would be zero,  $\mathcal{L}$  anti-Hermitian and all linear modes would be neutrally stable. This is similar to many other physical systems, where the basic physical processes are described by Hermitian Hamiltonians, but non-Hermiticity is introduced by boundary conditions or a simplified description of interactions by dissipation. In some sense, fixing one part of the full distribution function  $F$  to the stationary background distribution function  $F_0$ , coupled to the perturbed distribution function by  $\mathcal{L}^\phi$ , is also a kind of boundary condition.

For  $\nu_c > 0$ , the linearized collision operator contributes to the non-Hermiticity of the linear operator; like  $\mathcal{L}^\phi$ , it is only part of the linear operator because of the  $\delta f$  splitting. The same comments apply to the electromagnetic contributions for  $\beta > 0$ .

Note that numerical damping (introduced explicitly as in GENE, or implicitly, e.g., via upwind schemes) is another, artificial source of anti-Hermiticity. It has been checked however, that the phenomena that will be described in this chapter persist in the limit of no damping, even though the numerical values of growth rates and frequencies become less reliable in this limit.

Presently, not very much is known about non-Hermitian operators. However, sparked by a paper by Bender and Boettcher [48] in 1998, there has been an increasing activity in the research for non-Hermitian operators with real spectra. The strong interest mainly stems from the fact that they represent a completely new class of suitable candidates for quantum mechanical Hamiltonians. It has been shown that  $\mathcal{PT}$  symmetry in the context of quantum mechanics, or more general pseudo-Hermiticity [49, 50] leads to real spectra, but a simple, testable property of the operator matrix (such as the Hermiticity) that ensures that an arbitrary operator has a real spectrum is not known, so that in general, only a computation of all eigenvalues of the operator can tell if an operator is pseudo-Hermitian. For a recent review of the topic, see [51].

If the equilibrium density and temperature gradients are set to zero and the numerical damping is switched off, the eigenspectrum of  $\mathcal{L}$  seems to be purely imaginary up to numerical effects. These are expected to decrease with increasing resolution, but testing this is very difficult, since the memory requirements and computation time for a full eigenvalue decomposition increase dramatically with resolution (the iterative solvers described in 3.3 are not applicable for this task) and the LAPACK routine that was used for this computation is not parallelized. The conjecture that  $\mathcal{L}$  without drive is pseudo-(anti)-Hermitian is supported by a physical argument – microinstabilities "feed" on the energy contained in the background

## 4. Fundamental features of linear gyrokinetics

gradients, without these gradients, perturbations around  $F_0$  should therefore not grow.

### 4.2. Settings for the numerical investigations

As described in Sec. 3.3, GENE has been coupled to the SLEPc [40, 41] library, a fully parallel iterative solver for eigenvalue problems based on the PETSc package [42, 43, 44]. This allows – in contrast to initial value simulations – not only to compute the dominant microinstability for a given set of plasma parameters (i.e. the one with the largest growth rate), but also subdominant microinstabilities at the same perpendicular wavenumber. While GENE was not the first code able to perform gyrokinetic eigenvalue computations (compare, e.g., the FULL [52] and GOBLIN [53] codes), the possibility of easily handling extensive parameter scans allows for completely novel types of investigations.

Throughout this chapter, the  $\hat{s}$ - $\alpha$  model for the magnetic equilibrium (see Sec. 2.9.1) is used for simplicity, with  $\hat{s} = 0.8$ ,  $\alpha = 0$  and  $\epsilon_t = r/R = 0.16$ . Two particle species, electrons and (singly charged) ions are considered; the mass ratio is chosen to be  $m_e/m_i = 5.45 \cdot 10^{-5}$ . Unless stated otherwise, the binormal wavenumber is set to  $k_y\rho_s = 0.2$ , which is where nonlinear transport spectra typically tend to peak, and the radial box size is set to  $L_x = 1/(k_y\rho_s \hat{s}) = 6.25 \rho_s$ ; other nominal parameters are  $\beta \equiv 8\pi n_0 T_{\text{ref}} B_{\text{ref}}^{-2} = 2 \cdot 10^{-4}$ ,  $q_0 = 1.4$ , and a temperature ratio of unity, i.e.  $T_e = T_i = T_{\text{ref}}$ . The resulting eigenvalues – whose real and imaginary parts correspond, respectively, to the linear growth rates and real frequencies – are normalized with respect to  $c_s/R$ .

### 4.3. Mode transitions

To demonstrate the existence of two different scenarios related to mode transitions, an example with density gradients and both electron and ion temperature gradients switched on is shown in Fig. 4.1. To assure convergence also of the subdominant modes, a (relatively high) numerical resolution of 11  $k_x$  modes (corresponding to 11 poloidal turns), 20 parallel grid points, and  $64 \times 12$  points in  $v_{\parallel}\text{-}\mu$  (velocity) space has been used, the ion temperature gradient is held fixed at  $R/L_{T_i} = 6$ . The plots show the real and imaginary parts of the two unstable eigenvalues as a function of the electron temperature gradient for two different values of  $R/L_n$ . For  $R/L_n = 4.4$  (left plots), the most unstable mode for low values of  $R/L_{T_e}$  exhibits a drift velocity which points in the ion diamagnetic direction. It may therefore be identified as an ion temperature gradient (ITG) mode. Moreover, there exists a subdominant trapped electron mode (TEM) with its drift velocity pointing in the electron diamagnetic direction. Now, if  $R/L_{T_e}$  is increased to a value of about  $R/L_{T_e} = 6.4$ , the TEM takes over the role of the dominant mode, i.e., one finds a crossing of the linear growth rates. This is to be expected, since ITG modes and TEMs are, respectively, stabilized and driven by the electron temperature gradient, and mode crossings like this one have been observed frequently (see, e.g., Ref. [54]). What is interesting, however, is that this picture changes *qualitatively* if the same scan is performed for a slightly larger value of the density gradient  $R/L_n = 4.6$  (right plots of Fig. 4.1). Here, the two modes do not intersect in the whole  $R/L_{T_e}$  range, but it is hard to say from the

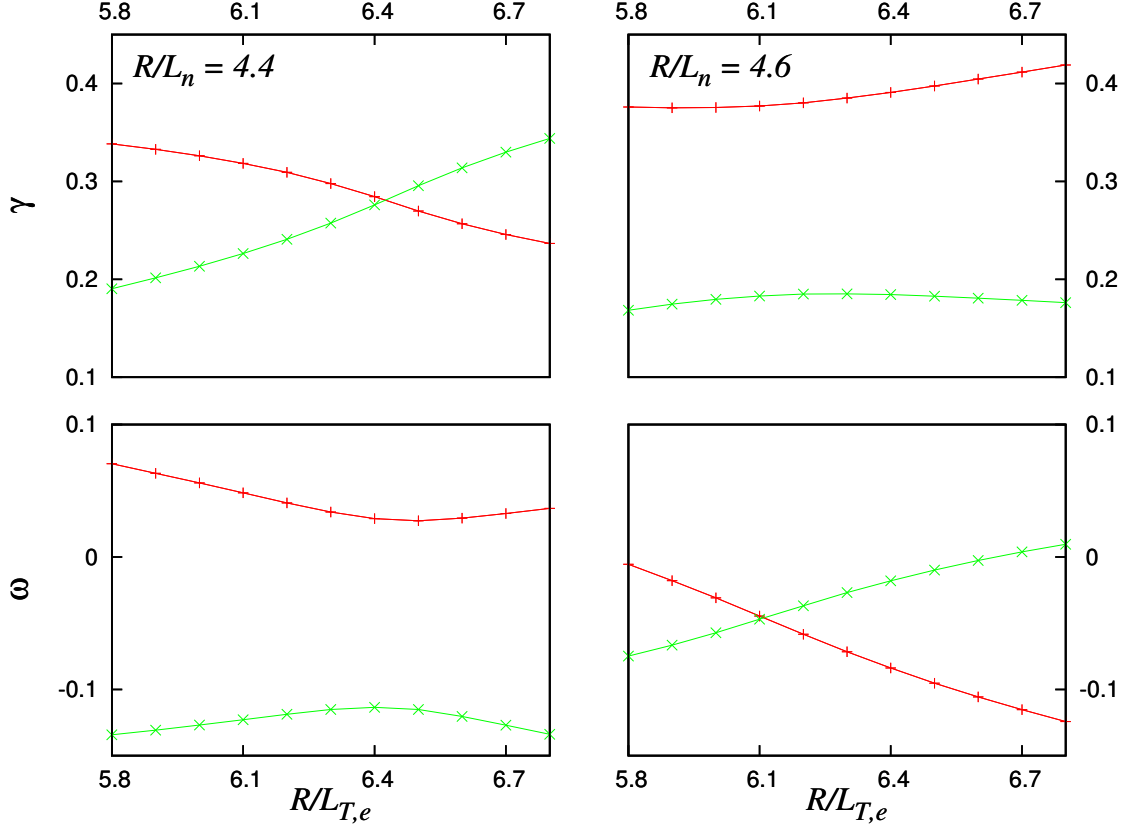


Figure 4.1.: Linear growth rates  $\gamma$  and real frequencies  $\omega$  (normalized with respect to  $c_s/R$ ) as a function of  $R/L_{T_e}$  for  $R/L_n = 4.4$  (left) and  $R/L_n = 4.6$  (right).

frequencies whether they should be called ITG modes, TEM, "hybrid ITG/TEM modes" (see, e.g., Ref. [54]) or "ubiquitous modes" (see Refs. [55, 56, 57]). Obviously, at some point in the range  $4.4 < R/L_n < 4.6$ , a transition takes place, which will be studied in more detail below.

## 4.4. Exceptional points

To reconcile the two scenarios described in the last section, the end points of the two scans shown in Fig. 4.1 are connected by a parameter scan in  $R/L_n$ , yielding a closed trajectory along a square in the  $R/L_{T_e}$ - $R/L_n$  plane around the nominal values,  $R/L_{T_e} = 6.3$  and  $R/L_n = 4.5$ . The result is shown in Fig. 4.2: The upper left plot depicts the exact path of the circular scan in parameter space, the lower plots show the linear growth rates and real frequencies of the two unstable modes. After one turn, the curves connect, as has to be expected. However, they connect in such a way that the roles of the dominant and subdominant mode are interchanged. This implies that through a continuous variation of plasma parameters, describing a closed path in the  $R/L_{T_e}$ - $R/L_n$  plane, one can transform an ITG mode into a TEM. After one turn, the formerly dominant mode has become the subdominant one and vice versa, and only after a second turn the curves "bite their own tails" again. This is also illustrated

#### 4. Fundamental features of linear gyrokinetics

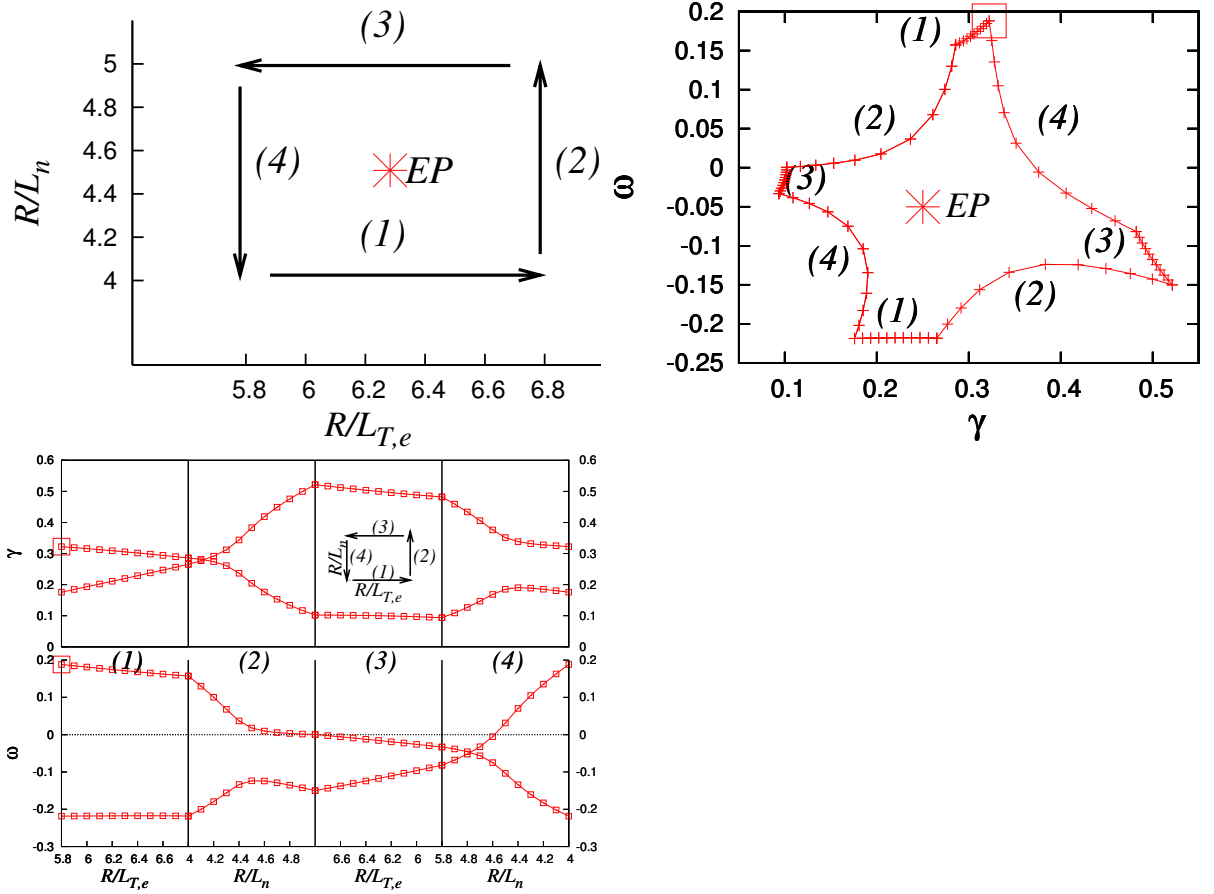


Figure 4.2.: Upper left: Picture of the closed path in the  $R/L_{T_e}$  and  $R/L_n$  parameter space that is used for the scan. Other plots: Linear growth rates  $\gamma$  and real frequencies  $\omega$  (normalized with respect to  $c_s/R$ ) for two unstable modes along this closed path. The big squares denote a corresponding eigenvalue in the two plots, the numbers denote the linear parameter interval of the corresponding scan.

in a somewhat different way in the upper right plot of Fig. 4.2, where all eigenvalues of the lower plot are depicted in the complex plane. Following the path in parameter space depicted by the numbers, it becomes obvious that the dominant and subdominant modes describe only half a circle in the complex plane respectively, and one full loop in the complex plane is only completed after two turns in the parameter plane. This nontrivial topology of the eigenvalue surface in the parameter space spanned by the density and electron temperature gradients is due to a so-called exceptional point (EP) at the nominal values defined above,  $R/L_{T_e} = 6.3$  and  $R/L_n = 4.5$ .

To illustrate the structure associated with such an EP, Fig. 4.3 shows the full surfaces described by  $\omega$  and  $\gamma$  in the  $R/L_{T_e}$ - $R/L_n$  plane, clearly exhibiting an anomaly in the center. The surfaces are topologically equivalent to the Riemann surface for the function  $f(z) = \sqrt{z}$  in the complex plane. Locally, the eigenvalue surface looks like two distinct surfaces, belonging to two different instabilities, the nontrivial structure (which is only observable globally)

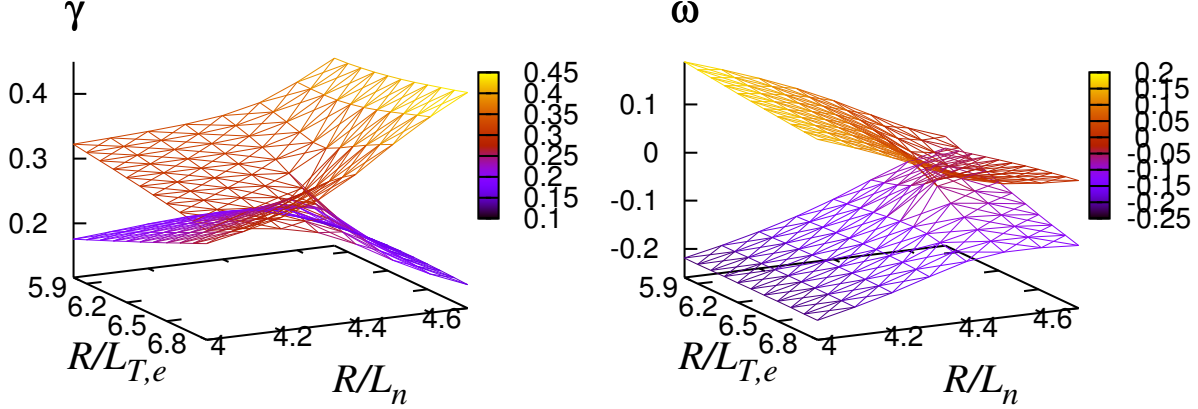


Figure 4.3.: Topological structure of the linear growth rates and real frequencies of two (ITG/TEM-like) microinstabilities in  $R/L_{T_e}$ - $R/L_n$  space, exhibiting an EP. Both structures are identical to that of a Riemann surface for the complex function  $f(z) = \sqrt{z}$ .

comes from the fact that the intersection line of the two presumed surfaces is not infinite but ends in an EP. Note that these intersection lines are different for the real and imaginary parts of the eigenvalues (i.e. the parameters where the two instabilities have equal growth rate or equal frequency are different), except for the exceptional point, which is the only point where both growth rates *and* frequencies coincide. From this, it is obvious that the scenario displayed in Fig. 4.2 will be identical for any closed path around the EP in our two-dimensional parameter space, while for closed paths which don't contain an EP, the connection of the two eigenvalues can not be observed and the two instabilities appear to be completely independent, each having the same values after one turn in parameter space already.

As will be shown in the following, EPs do not only occur in the transition between ITG modes and TEMs, but are a pretty ubiquitous phenomenon in linear gyrokinetics. An example is the pure TEM system with the nominal gradients  $R/L_n = 3.1$ ,  $R/L_{T_e} = 2$  and  $R/L_{T_i} = 0$  (such that ITG modes are stable) and  $T_e/T_i = 3$  (similar to the parameters used in Ref. [37]). The two instabilities, which both drift in the electron diamagnetic direction, are traditionally considered to be of the (distinct) density gradient driven and temperature gradient driven TEM variety. A parameter scan with the numerical resolution of 7  $k_x$  modes, 16 parallel grid points, and  $64 \times 16$  points in  $v_{\parallel}\mu$  (velocity) space reveals the same phenomenon as described above: If one follows the two eigenvalues on a closed circle in the  $R/L_n$ - $R/L_{T_e}$  plane around the nominal gradients, the two modes transform into each other, making it impossible to distinguish the two instabilities globally (see the left plot of Fig. 4.4).

The same holds for the TEM-ETG system displayed in the right plot of Fig. 4.4, which has been computed with  $5 \times 16 \times 40 \times 16$  points in  $k_x$ ,  $z$ ,  $v_{\parallel}$  and  $\mu$  directions at a slightly changed safety factor  $q_0 = 1.1$  and  $R/L_{T_e} = 4.65$ ,  $R/L_{T_e} = 0$ .

The last two examples that demonstrate the connection between seemingly different microinstabilities are systems of a so-called kinetic ballooning mode (KBM) on one hand and a TEM or ITG mode on the other. For this purpose, the surrounding of the two points in param-

#### 4. Fundamental features of linear gyrokinetics

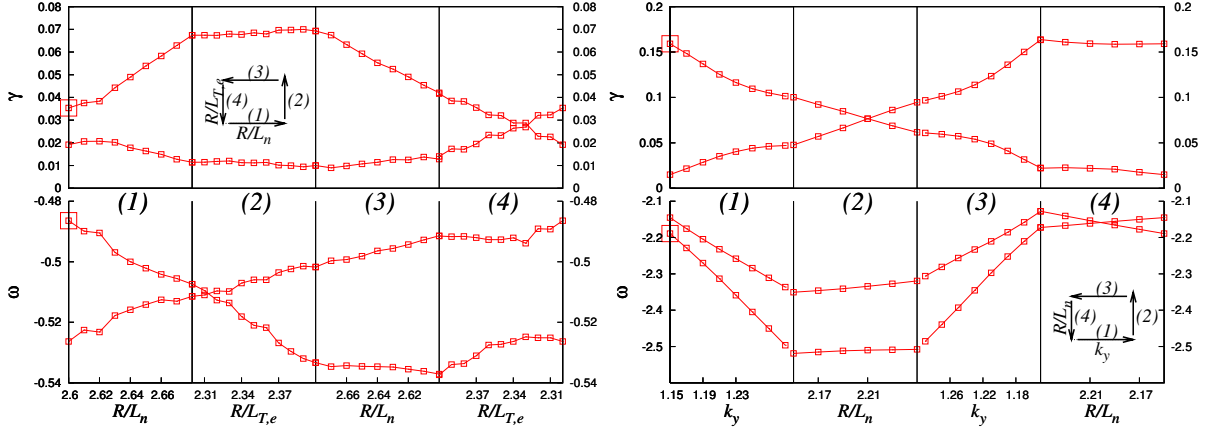


Figure 4.4.: Left: Linear growth rates  $\gamma$  and real frequencies  $\omega$  (normalized with respect to  $c_s/R$ ) for two unstable TEM-like modes along a closed path in a two-dimensional parameter space spanned by  $R/L_{T,e}$  and  $R/L_n$ . Right: The same for two TEM-ETG-like modes in the  $k_y - R/L_n$  plane.

eter space characterized by  $R/L_n = 6$ ,  $R/L_{T_i} = 0.5$ ,  $R/L_{T_e} = 6$ , and  $\beta = 0.018$  as well as by  $R/L_n = 6$ ,  $R/L_{T_i} = 0$ ,  $R/L_{T_e} = 5$ , and  $\beta = 0.022$  are considered. In the first case,  $\beta$  and  $R/L_{T_i}$  are varied; in the second case,  $\beta$  and  $R/L_{T_e}$ . The numerical resolution for these cases is 13  $k_x$  modes, 32 parallel grid points, and  $48 \times 12$  points in  $v_{\parallel}\text{-}\mu$  (velocity) space. The results are shown in Fig. 4.5, exhibiting the same effects as in the cases presented above.

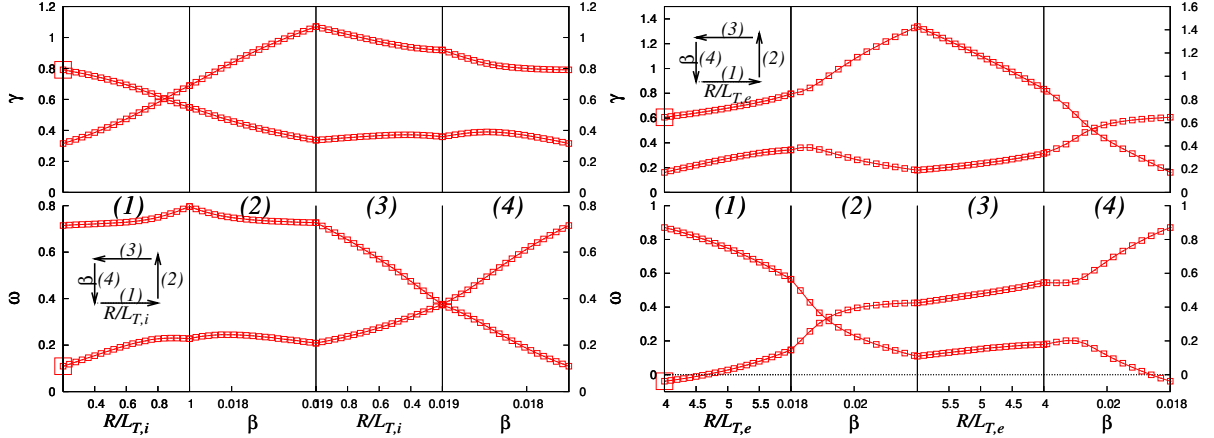


Figure 4.5.: Linear growth rates  $\gamma$  and frequencies  $\omega$  for two unstable ITG/KBM-like (left) and TEM/KBM-like (right) modes along a closed path in a two-dimensional parameter space spanned by  $\beta$  and  $R/L_{T_i}$  and  $R/L_{T_e}$  respectively.

## 4.5. Mode correlations

It is also interesting to investigate the behavior of the two eigenvectors in the surrounding of the EP. Fig. 4.6 displays the (absolute value of the) standard scalar product  $p \equiv |\vec{g}_1^* \cdot \vec{g}_2|$  between the complex-valued normalized eigenvectors  $\vec{g}_1$  and  $\vec{g}_2$  (i.e. the modified distribution functions of the two microinstabilities). This quantity can be considered as a measure of the correlation between two modes. As it turns out,  $p$  is unity at the EP, i.e. the two eigenvectors coincide in that point. Thus, at the EP, not only the two eigenvalues are identical, but the

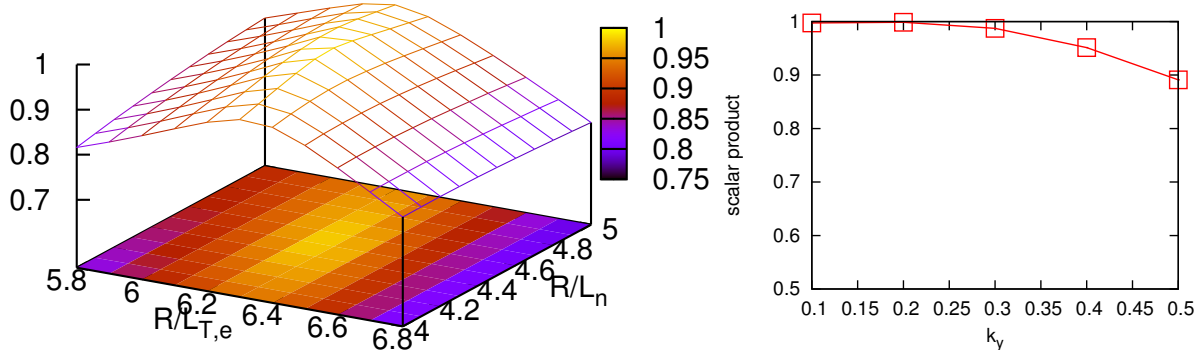


Figure 4.6.: Left: Dependence of the scalar product of two unstable TEM-like modes as a function of  $R/L_{T,e}$  and  $R/L_n$ . At the EP, one obtains unity, indicating that both modes coalesce. Right: Scalar product between an ITG-like mode and a KBM-like mode as a function of the binormal wavenumber  $k_y$  (normalized to  $\rho_s^{-1}$ ).

eigenstates as well, which is fundamentally different from the more familiar degeneracies in (Hermitian) quantum mechanics, where two different eigenstates happen to have the same eigenvalues. As one moves away from the EP,  $p$  only falls off relatively slowly, demonstrating that the two linear mode structures are still quite similar in the neighborhood of the EP. This implies that computing  $p$  can be an efficient means to detect EPs, i.e., given a set of initial parameters which lead to two instabilities, it is possible to compute the gradient of the scalar product with respect to parameter variations and by iterative parameter changes find a setting with  $p = 1$ . This technique has been used to find the parameter settings of the examples in the last section.

Given that the linear mode structure often exhibits some persistence in nonlinear simulations, another possible implication of the strong correlation between the two microinstabilities in the neighbourhood of an exceptional point is that the character of the resulting turbulence in the neighborhood of an EP might reflect its existence. Although first nonlinear investigations did not show a dramatic influence, a more detailed study could reveal an effect of this correlation, particularly for cases in which  $p$  remains close to unity over a relatively wide range in  $k_y$  space. One such example is shown in the right plot of Fig. 4.6.

## 4.6. Theory and occurrence of non-Hermitian degeneracies

Although a "branch point" was mentioned (and again forgotten) in an early study of linear microinstabilities with simplified equations in [58], the results of this chapter (published in [47]) represent the first systematic study of the nontrivial structures occurring at mode transitions in linear gyrokinetics. Through this study, it has been possible to identify these structures as exceptional points, revealing a connection to a very active research field, with applications in many different physical systems.

Exceptional points are, as the microinstabilities themselves, linked to the non-Hermiticity of the linear operator. The concept and name was first introduced by Kato [59] in a book from 1966 but gained considerable interest only in recent years (for an overview, see, e.g. [60, 61]). Considering the matrix (in Jordan form) representing the non-Hermitian operator, the appearance of an EP corresponds to the formation of a nontrivial Jordan block out of a diagonal part. This means, that besides the degenerate eigenvalues, (at least) two eigenvectors of the matrix become degenerate and form a Jordan chain. These degeneracies are of codimension 2, i.e. only in a two-dimensional parameter space they appear as (zero-dimensional) points, in general they form a hypersurface with two dimensions less than the parameter space under consideration. For this reason, many authors prefer the expression "non-Hermitian degeneracy" instead of "exceptional point". This also explains why it was relatively simple to find the numerous examples for exceptional points presented in Sec. 4.4; if the degeneracies really were points in the multi-dimensional parameter space of gyrokinetics, a fine-tuning of all plasma parameters and scan directions would be necessary and the probability of finding such a point would be reduced dramatically. The dimensionality of the non-Hermitian degeneracies in gyrokinetics has also been verified with GENE computations. By varying an additional parameter with respect to the two-dimensional scans in Sec. 4.4, it was found that the degeneracies form lines in three dimensions, as expected.

Since their two sets of parameters are very close, the multi-dimensionality of the non-Hermitian degeneracy leads to the conjecture that at least the two EPs involving the kinetic ballooning modes shown in Fig. 4.5 are connected; three computations at intermediate parameters also showed EPs with the same basic properties, supporting this conjecture. It could actually be possible that all exceptional points studied above are part of a single multidimensional structure, but a verification of this would require many more simulations and would probably not provide any practical benefit.

While so far, only cases with two eigenvectors merging in an EP at a time have been found with GENE, it is in principle possible to have  $n > 2$  eigenvectors merge, which would increase the number of orbits around the EP necessary to return to the initial mode to  $n$ . In this case, for each turn, there would be a cyclic 'exchange' of the eigenmodes.

It is interesting to note that degeneracies can also arise in the more familiar real symmetric or complex Hermitian cases, but with different properties (see [60]). In the real symmetric case, the degeneracies are also of codimension two, but the eigenvalue surfaces form a double cone instead of the branch-point structure seen in Fig. 4.3 and are therefore also called "diabolical points". Degeneracies of complex Hermitian operators, on the other hand, have codimension

three.

Non-Hermitian degeneracies are of interest for many areas of physics where corresponding operators play a role; one of the areas which contributed most to this subject in recent years being again quantum mechanics (for an overview, see [62] and references therein). Researchers from a different area of plasma physics, namely MHD-based dynamo models, have also reported non-Hermitian degeneracies [63].

The degeneracies described here are not only a theoretical concept, they have also been observed experimentally in a growing number of different systems in the past few years, e.g. in crystals of light [64], propagation of light in dissipative media [65], microwave billiards [66, 67, 68], ionization of atoms by lasers [69], and electronic circuits [70].

## 4.7. Summary

It has been shown that due to the nontrivial topology of the eigenvalue surfaces in the proximity of non-Hermitian degeneracies, different types of microinstabilities (like density and temperature gradient driven TEMs, ETG and ITG modes, and kinetic ballooning modes) can be transformed into each other via continuous variations of the plasma parameters. In the parameter space of the gyrokinetic equation, these degeneracies, which are caused by the non-Hermiticity of the linear operator resulting from the  $\delta f$ -splitting, form hypersurfaces of codimension 2, which implies that the probability of finding such structures close to a given set of parameters is quite substantial.

These findings explain why in some conventional parameter scans, i.e. one-dimensional cuts through the high-dimensional parameter space, dominant and subdominant modes could be distinguished clearly, while in others the two modes hybridized or important properties like the drift direction changed. The finding of non-Hermitian degeneracies implies that while it is surely still useful to label the modes in the usual way in parameter ranges that don't include an exceptional point, one has to be aware that a strict discrimination is not possible. This becomes very obvious close to a non-Hermitian degeneracy, where even a slight change of the direction of the scan axis can lead to a completely different picture, and sometimes even to a reversal of the labelling. In these cases, trying to designate the modes in the usual sense might be more confusing than helpful and should maybe be avoided altogether.

#### *4. Fundamental features of linear gyrokinetics*

# 5. Trapped electron mode turbulence

After the investigations of the microinstabilities related to the linearized system, which were discussed in the previous chapter, in this and the following chapters the full, i.e. nonlinear gyrokinetic equation will be considered.

So far, most theoretical and computational research on anomalous transport in the core of fusion devices has focused on ion temperature gradient (ITG) turbulence in tokamaks [34], adopting the adiabatic electron approximation (see Sec. 2.9.2). This development is, in part, due to the relatively good tractability of this problem. Consequently, the findings from such studies have become standard paradigms in the understanding of plasma microturbulence. The most prominent example for this is the role of zonal flows. As has been discussed extensively in the literature, adiabatic ITG turbulence generates  $\vec{E} \times \vec{B}$  shear flows which are associated with purely radial fluctuations of the electrostatic potential; these zonal flows in turn regulate the turbulence via vortex shearing. This interplay constitutes the dominant saturation mechanism in these systems and therefore determines the level of anomalous transport (see, e.g., Refs. [71, 72, 73, 74]).

It is clear, however, that ITG modes are not the only relevant source of core turbulence. In particular, many present-day (and future) fusion experiments rely on powerful electron heating systems which can turn trapped electron mode (TEM) turbulence into an important, if not dominant agent of cross-field transport.

In this chapter, some basic properties of fully developed, collisionless TEM turbulence driven by electron temperature gradients will be discussed, followed by a more detailed study of the relevant saturation mechanism. As it turns out, the results – which are first of all helpful for a deeper understanding of anomalous transport in tokamak plasmas – can also be used to justify a quasilinear transport model that has already been employed in previous works. The results of this chapter have been published in [75].

## 5.1. Simulation parameters

All GENE simulations in this chapter are performed in  $\hat{s}\text{-}\alpha$  geometry with  $\alpha = 0$  for simplicity. The nominal plasma parameters, unless stated otherwise, are  $R/L_{T_e} = 6$ ,  $R/L_{T_i} = 0$ ,  $R/L_n = 3$ ,  $\beta_e = 10^{-3}$ ,  $T_e/T_i = 3$ ,  $m_e/m_i = 1/400$ ,  $\hat{s} = 0.8$ ,  $q_0 = 1.4$ , and  $\epsilon \equiv r/R = 0.16$ . This parameter set was motivated by experimental studies of plasmas with dominant electron heating [76] and has been used before in [37]. For these nominal parameters, only one mode is linearly unstable at a given perpendicular wave number, corresponding to a pure, electron temperature gradient driven TEM in the conventional nomenclature. Electron temperature gradient (ETG) modes are linearly stable due to the relatively cold ions [77], and there is no ITG drive. The perpendicular box size is given by  $L_x = 165\rho_s$  and  $L_y = 210\rho_s$ , and the numerical resolution is  $96 \times 128 \times 16 \times 32 \times 8 \times 2$  points in the radial, binormal, parallel,

## 5. Trapped electron mode turbulence

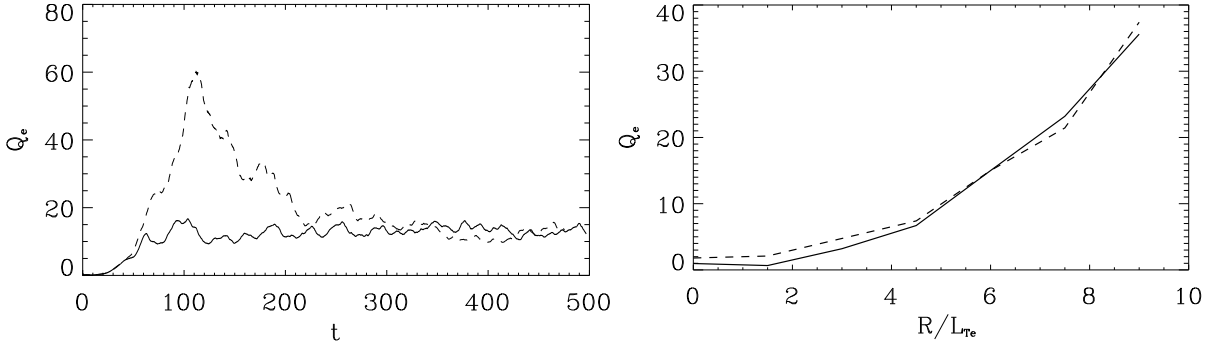


Figure 5.1.: Time evolution (left plot) of the electron heat flux  $Q_e$  (in units of  $\rho_s^2 c_s p_{e0} / L_n^2$ ) for the nominal parameters and dependence on  $R/L_{T_e}$  (right plot) for TEM simulations with (solid line) and without (dashed line) zonal flows. The time is measured in units of  $L_n/c_s$ .

$v_{\parallel}$ ,  $\mu$  and species direction, respectively. For convergence studies concerning velocity space resolution, see Ref. [37].

## 5.2. Zonal flows in TEM turbulence

As mentioned in the introduction of this chapter, it is still widely assumed that zonal flows are the universal saturation mechanism for plasma microturbulence. To determine the role of zonal flows in collisionless TEM turbulence, a set of 'normal' TEM simulations is compared to runs in which the zonal modes have been artificially zeroed out in each time step of the simulation. The left plot of Fig. 5.1 shows the time traces of the electron heat flux for such a pair of simulations for the nominal parameters defined above. Although differences in the transport level are observable in the initial (transient) saturation phase, the physically relevant quasistationary state remains the same if the zonal flows are suppressed. This behavior is very different from the well studied (adiabatic) ITG case, where the suppression of zonal flows typically leads to a significant increase of the heat flux [71, 72, 73], usually by an order of magnitude or more. The result of this test is that zonal flows are not the dominant saturation mechanism for TEM turbulence, at least for the parameters studied here.

The result of a nonlinear scan of the electron temperature gradient is shown in the right plot of Fig. 5.1. Again, the electron heat flux resulting from "normal" simulations is compared to the result from simulations where the zonal flows have been artificially suppressed. As  $R/L_{T_e}$  decreases from the nominal value to zero, the underlying TEM instability changes from an electron temperature gradient driven type to a purely density gradient driven one. As can be seen in the plot, this linear property translates into the absence of a critical electron temperature gradient in the nonlinear runs, although the electron heat flux becomes comparatively small for  $R/L_{T_e} \rightarrow 0$ . More importantly in the present context, the artificial suppression of zonal flows leads to a relative increase of the electron heat flux (although at a low level for the parameters considered here) if the turbulence is sustained by density gradient driven TEMs, in line with the results published in [78]. However, for reasonably large electron temperature

### 5.3. Similarities between linear and nonlinear simulations

gradients, characteristic of the majority of fusion plasmas, the influence of the zonal flows seems to be irrelevant for the transport level. A detailed study of the parameter dependence of the importance of zonal flows, that was inspired by the seemingly contradictory results for the nominal parameters considered here and [37] and the results in [78] has been published recently [79].

Although there are different regimes, for the plasma parameters considered in this chapter, zonal flows have practically no impact on the saturated transport level, implying that the dominant saturation mechanism must be of a different nature. The question what this mechanism is and how it can be described it will be the subject of the remainder of this chapter.

## 5.3. Similarities between linear and nonlinear simulations

Interestingly, the quasistationary state of a TEM turbulence simulation still exhibits many properties of the linear system. As can be seen in Fig. 5.2, the amplitude spectrum of the electrostatic potential  $\phi$  shows the same features as the linear growth rate spectrum. As usual, the nonlinear amplitude spectrum is shifted towards lower perpendicular wave lengths compared to the linear growth rate spectrum, but the maximum remains at  $k_x = 0$  and finite  $k_y$ , reflecting a dominance of radially elongated streamers.

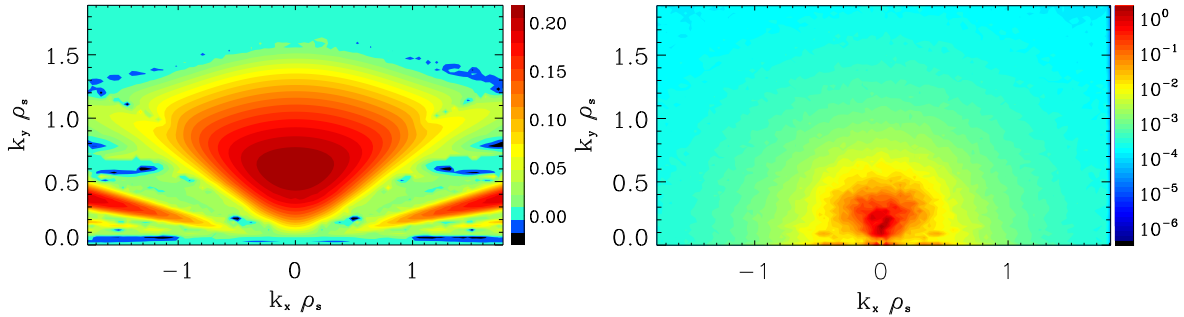


Figure 5.2.: Left plot: Linear growth rates for all modes in the  $(k_x, k_y)$  plane for the nominal parameter defined above. Right plot: The corresponding nonlinear amplitude spectrum for the electrostatic potential.

Also, the phase relations between various pairs of fluctuating quantities [like  $(\phi, n)$  or  $(\phi, T_\perp)$ ] are very close to the values obtained from linear computations, as can be seen in the left plot of Fig. 5.3, where the values for  $k_x = 0$  are shown (the contributions of trapped and passing particles have been considered separately). Note that for  $k_y > 1.6$ , the linear modes are stable (compare the left plot of Fig. 5.2). However, because an initial value solver was used for the computation, it was still possible to compute the linear cross phases of the dominant mode – only that this was the mode with the smallest damping rate in this case, i.e. the mode in the initial condition which decayed the slowest. In the turbulence simulation, the high  $k_y$  contributions are excited nonlinearly, but also here the cross phases are well defined.

## 5. Trapped electron mode turbulence

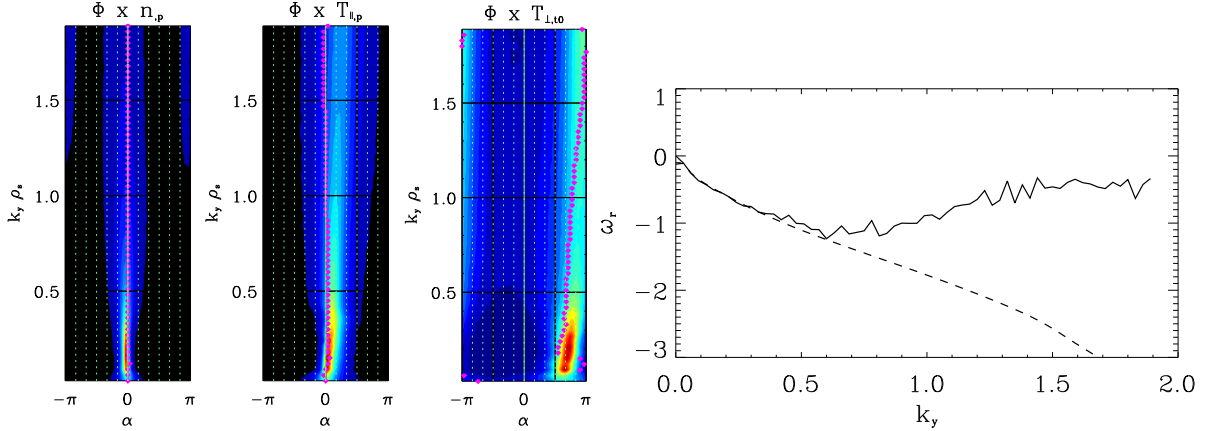


Figure 5.3.: Left: Histograms of the phase angle  $\alpha$  between different fluctuating quantities for a nonlinear TEM simulation at the nominal parameters; the corresponding linear values are given in magenta. Right: Real frequency (in units of  $c_s/R$ ) as a function of  $k_y$  (in units of  $1/\rho_s$ ) for the nonlinear (solid line) and linear (dashed line) simulation.

Another similarity concerns the nonlinear frequency  $\omega_{nl}$ , which can be computed in nonlinear simulations via

$$\omega_{nl} = \left\langle \text{Im} \frac{\ln(\phi_n/\phi_{n-1})}{t_n - t_{n-1}} \right\rangle \quad (5.1)$$

(here, only the  $k_x = 0$  mode is considered,  $\langle \rangle$  corresponds to an average over the available time steps  $n$  and the parallel direction). The right plot of Fig. 5.3 shows that the nonlinear values of the real frequency  $\omega_r$  exactly match the respective linear results in the low  $k_y$  regime; it is only for  $k_y \gtrsim 0.6$  that the results begin to differ. Here, the (time averaged) nonlinear frequency tends to zero for increasing  $k_y$ , whereas  $|\omega_r|$  of the linear modes increases further (the negative sign indicates that the mode drifts in the electron diamagnetic direction).

In order to explain the findings of the last two sections, a nonlinear saturation mechanism is required that leaves the various linear properties intact and is not related to zonal flow shearing.

## 5.4. Statistical properties of the nonlinearity

In an attempt to quantify the statistical properties of the  $\vec{E} \times \vec{B}$  nonlinearity  $\mathcal{N}[g]$ , which is responsible for saturating the linear unstable modes, the ansatz  $\mathcal{N}[g] \propto g$  is made. This implies that the nonlinear gyrokinetic equation (2.38) can be rewritten as an effective linear equation,

$$\frac{\partial g}{\partial t} = \mathcal{L}g + \mathcal{X}g, \quad (5.2)$$

where a model constant " $\mathcal{X} \approx \mathcal{N}[g]/g$ " with the dimension of a frequency has been introduced. In the following, the properties of  $\mathcal{X}$  will be explored by means of nonlinear gyroki-

#### 5.4. Statistical properties of the nonlinearity

netic simulations. The model assumption above is only a statistical relation and the expression for  $\mathcal{X}$  stated above is not well defined, since the perturbed distribution function  $g$  can be zero.

In order to find a value for  $\mathcal{X}$ , the squared error of the model,  $\langle |\mathcal{N}[g] - \mathcal{X}g|^2 \rangle$ , is minimized by calculating the derivative with respect to the real and imaginary part of  $\mathcal{X}$  and setting it to zero. This yields

$$\mathcal{X} = \frac{\langle g^* \mathcal{N}[g] \rangle}{\langle |g|^2 \rangle}.$$

To reduce the amount of data and obtain a manageable model,  $\mathcal{X}$  is considered to only depend on the spatial coordinates and the species label;  $\langle \rangle$  then denotes averaging over time and velocity space. To get a measure for the validity of Eq. (5.2), in a second simulation the normalized error of the real part,

$$\text{err}_{\text{Re}} = \frac{\langle |\text{Re}(\mathcal{N}[g] - \mathcal{X}g)|^2 \rangle^{1/2}}{\langle |g|^2 \rangle^{1/2}},$$

and its counterpart  $\text{err}_{\text{Im}}$  are computed.

The  $k_y$  dependence of  $\mathcal{X}$  for  $k_x = 0$  and  $z = 0$  (low-field side) is displayed in Fig. 5.4. Here, only the electron data is shown, but the ion results are very similar. The solid line depicts the average value, while the bars indicate the model error as defined above. Clearly two  $k_y$  ranges with rather different properties can be distinguished. For  $|k_y| \gtrsim 0.3$ , one finds a more or less constant (and small) real part of  $\mathcal{X}$ , an imaginary part which is roughly proportional to  $k_y$ , as well as large deviations from the model. For the much more important, transport dominating scales with  $|k_y| \lesssim 0.3$ , completely different properties are observed, namely a clearly discernible structure in the average values together with a very low fluctuation level. Because of its practical importance for heat and particle transport, only the low  $k_y$  regime is considered in the following.

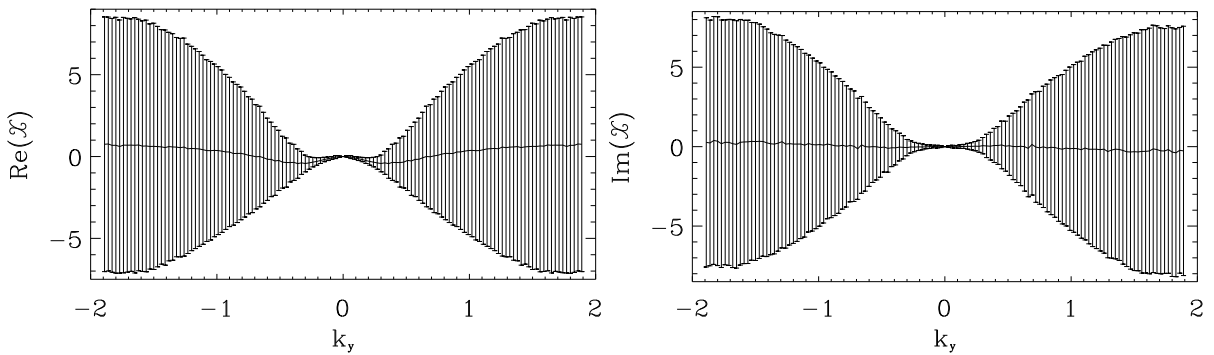


Figure 5.4.: Real and imaginary part of the quantity  $\mathcal{X}$  in units of  $c_s/R$ . The bars indicate the model error as defined in the text.

The  $k_y$  dependence of  $\mathcal{X}$  for  $k_x = 0$ , now averaged over the parallel direction  $z$ , is shown (for a smaller region around  $k_y = 0$ ) in Fig. 5.5. The plots show that the imaginary part of  $\mathcal{X}$  is very close to zero for  $|k_y| \lesssim 0.3$ , meaning that  $g$  and  $\mathcal{N}[g]$  are (almost) in phase. The corresponding real part, in contrast, is not zero, and its  $k_y$  dependence is well represented by a parabola through the origin. Combining these results for the real and imaginary parts, the

## 5. Trapped electron mode turbulence

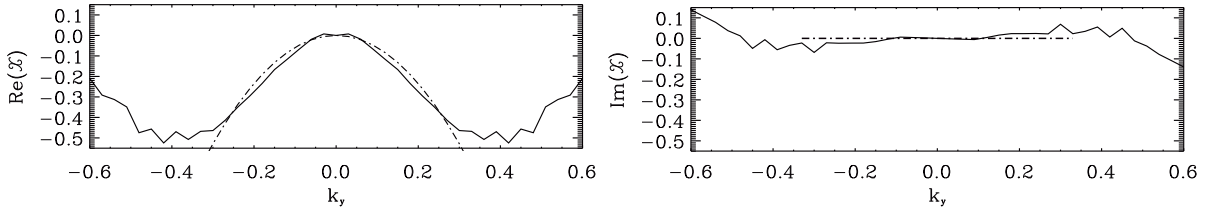


Figure 5.5.: The quantity  $\mathcal{X}$  in units of  $c_s/R$  in the transport dominating region. The real part can be fitted by a parabola, the imaginary part by a constant (zero).

constant  $\mathcal{X}$  can be written as

$$\mathcal{X} \approx -Dk_y^2, \quad (5.3)$$

implying that the overall effect of the  $\vec{E} \times \vec{B}$  nonlinearity on the large, transport dominating scales is well described by perpendicular particle diffusion.

This kind of behavior is in line with analytical results obtained, e.g., in the framework of Dupree's resonance broadening theory [80], and is qualitatively consistent with the nonlinear damping expected in the long-wavelength limit of other renormalized turbulence theories [81]. Modern renormalized theories also include a nonlinear forcing term  $F(t)$ ,

$$\frac{\partial g}{\partial t} = \mathcal{L}g + \mathcal{X}g + F(t),$$

which is a noise term, that is related to the scatter represented by the bars in Fig. 5.4 and turns the quasilinear ansatz into a stochastic differential equation (also see [81]). The behavior found here is moreover consistent with the notion of dressed test modes in a bath of stochastic small-scale fluctuations [82]. However, this is the first time that such phenomena have been observed directly in gyrokinetic simulations of plasma microturbulence, demonstrating their relevance for the nonlinear saturation of (electron temperature gradient driven) TEM turbulence.

It is worth pointing out that the result represented by Eq. (5.3) can nicely explain all the general observations about the similarity of nonlinear and linear runs mentioned above. First, an additional perpendicular diffusion term does not affect the eigenmodes of the linear operator  $\mathcal{L}$  in Eq. (5.2); since  $\mathcal{L}$  is block diagonal in  $k_y$ , the diffusivity only induces a spectral shift of the eigenvalues. This means that although the effective growth rate of the quasilinear equation can approach zero (the nonlinear damping rate is comparable to the linear growth rate for low  $k_y$ ), the cross phases remain at the linear values, as observed in the simulations.

For higher values of  $k_y$ , where the diffusion approximation breaks down, the positive value of  $\text{Re}(\mathcal{X})$  in Fig. 5.4 corresponds to a nonlinear destabilization, but as can be seen from the error bars, effects that are neglected in Eq. (5.2) (in particular the nonlinear forcing term mentioned above) do play an important role in this range. The same applies for the real frequency: The mean value of the nonlinear frequency shift  $\text{Im}(\mathcal{X})$  at larger values of  $k_y$  helps to explain the results in Fig. 5.3, but obviously the frequency spectrum of the nonlinear forcing dominates.

## 5.5. Quasilinear transport model for TEM turbulence

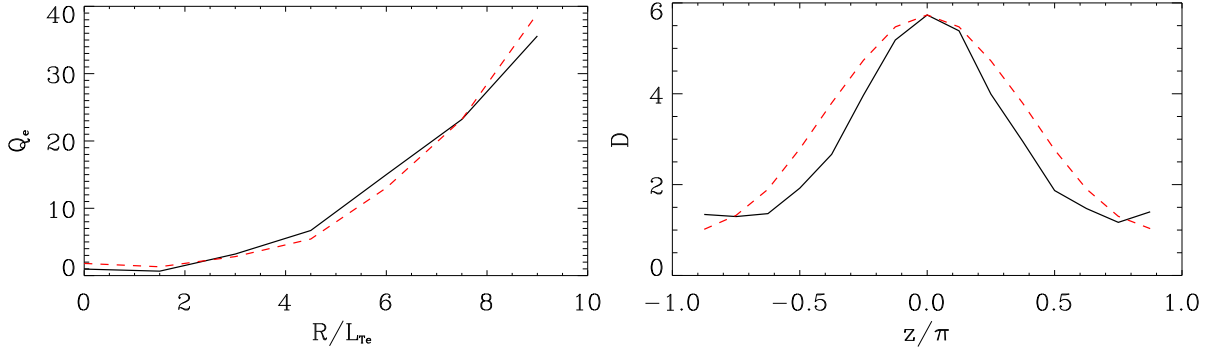


Figure 5.6.: Left: Comparison of the electron heat flux obtained directly from nonlinear simulations (solid line) and from Eq. (5.4) (dashed line) as a function of the electron temperature gradient. Right: Parallel structure of the diffusivity  $D$  (solid line) and of the linear squared amplitude  $|\phi_{k_y}|^2$  (dashed line).

## 5.5. Quasilinear transport model for TEM turbulence

Another important result is related to the dashed curve in the left plot of Fig. 5.6. It shows an estimate for the heat flux,

$$Q_e^{model} = c_0 D(R/L_{T_e}) (R/L_{T_e} + R/L_n) , \quad (5.4)$$

obtained from the diffusivity  $D$ , which has been determined from quadratic fits to the low  $k_y$  range of  $\text{Re}(\mathcal{X})$  in various nonlinear simulations. The scalar fit parameter  $c_0$  has a value of  $c_0 = 0.3$  in this case. The plot clearly exhibits a good quantitative correlation between the heat transport calculated from the diffusivity  $D$  and the heat transport directly obtained from the simulations.

These findings can be used to justify a refined quasilinear transport model which has been described in Refs. [37, 83, 84] and used successfully to reproduce various nonlinear simulation results which are difficult, if not impossible, to capture in more conventional models of this type.

The parallel structure of the diffusivity  $D$  occurring in Eq. (5.3) is shown in the right plot of Fig. 5.6. The diffusion term, corrected for the parallel change of  $k_\perp^2$  due to the metric coefficients of the  $\hat{s} - \alpha$  model, peaks on the low-field side and exhibits a ballooning mode structure which is typical for curvature driven microinstabilities like TEMs. In the model considered here, quasistationarity is reached when the effective growth rate of the right hand side of Eq. (5.2) vanishes. This means that the linear growth rate  $\gamma$  from the  $\mathcal{L}g$  term has to be balanced by the nonlinear contribution. With the averaging procedure  $\|f(z)\| \equiv L_s^{-1} \int_{-L_s/2}^{L_s/2} f(z) dz$  over the parallel coordinate (usually  $L_s > 2\pi$ ), the effective growth rate for a given  $k_y$ , which has to approach zero in the saturated state, can be approximated as

$$\gamma_{\text{eff}} \equiv \gamma(k_y) - k_y^2 \|D(z)(1 + \hat{s}^2 z^2)\|$$

Given the fact that, according to the right plot of Fig. 5.6, the nonlinear  $D(z)$  can be approximated reasonably well by the parallel structure of the linear (squared) electrostatic potential

## 5. Trapped electron mode turbulence

$|\phi_{k_y}|^2(z)$ , one finally obtains the model

$$Q_e \propto \max_{k_y} \left[ \frac{\gamma_l(k_y)}{k_y^2 (1 + \hat{s}^2 \|z^2\|)} \right] \left( \frac{R}{L_{T_e}} + \frac{R}{L_n} \right) \quad (5.5)$$

for the full (advective and diffusive) electron heat flux  $Q_e$ , where the parallel dependence is now captured by the purely linear

$$\|z^2\| \approx \frac{\int z^2 |\phi_{k_y}|^2(z) dz}{\int |\phi_{k_y}|^2(z) dz}.$$

This prescription helps to avoid a divergence as  $k_y \rightarrow 0$  [37, 83]. The subdominant ion heat and particles fluxes,  $Q_i$  and  $\Gamma$ , can then be computed from the quasilinear ratios for the  $k_y$  which maximizes the right-hand side expression in Eq. (5.5). This model is able to capture various key features of TEM turbulence as has been discussed in [37, 83].

## 5.6. Summary

In summary, it has been shown by a careful analysis of gyrokinetic turbulence simulations that in the parameter regime explored here, the nonlinear saturation mechanism for electron temperature gradient driven trapped electron modes is not zonal flow generation (in contrast to the ITG case), but perpendicular particle diffusion. Statistically, the action of the  $\vec{E} \times \vec{B}$  nonlinearity on the long-wavelength, transport dominating modes can be expressed by a simple diffusion term, in line with the notion of dressed test modes in a bath of random small-scale fluctuations. This finding is not only able to explain the observed resemblance between linear and nonlinear modes, but can also help to develop and justify new, improved kinds of quasi-linear transport models which are in very good agreement with fully nonlinear simulations.

## 6. TEM/ITG turbulence in tokamaks

The investigations of plasma microturbulence available in the literature usually focus on studying turbulence in an idealized limit, i.e. pure ion or electron temperature gradient (ITG/ETG) mode driven turbulence or trapped electron mode (TEM) turbulence. For the gyrokinetic simulations of the former two cases (see, e.g., [34, 36]), often the adiabatic electron/ion approximation described in Sec. 2.9 has been used, which reduces the numerical effort considerably, but eliminates several physical aspects. One very important effect that occurs only with a gyrokinetic treatment of all species is the coupling of ITG/ETG turbulence with TEM turbulence; the latter has been discussed in [37, 78, 79] or Chap. 5 with  $\omega_{Ti} = 0$ , i.e. in an equally idealized limit as the ITG and ETG investigations cited above.

While it was important to isolate and study the various effects occurring in these regimes separately in a first step, eventually more realistic scenarios have to be considered, with gyrokinetic effects and gradients taken into account for both electrons and ions. As already mentioned in the last chapter, usually ITG turbulence is considered to be the main cause of anomalous transport in fusion experiments, and if the plasma conditions are chosen appropriately, it is also possible to experimentally investigate "pure" TEM regimes [76]. But in more conventional situations, the application of several heating methods (ECRH plus NBI) and/or a sufficiently high collisionality leads to finite (and often similar) values for the temperature gradients of all species, which usually means that several linear instabilities are present simultaneously.

There has been some work recently on the interplay between ETG and ITG turbulence, which exist on different spatio-temporal scales [85, 86, 87]. However, even in parameter ranges where ETG modes are stable, there is the possibility of a coexistence of different modes, namely TEM and ITG instabilities, which have comparable spatial scales, comparable linear growth rates but in general different real frequencies. The linear and nonlinear coexistence of these different modes in the transition region between the "pure" TEM and ITG regimes will be studied in this chapter. (It was shown in Chapter 4 that a strict classification of the linear instabilities is not possible; however, the parameters used here are sufficiently far from non-Hermitian degeneracies that the traditional naming can be applied.)

As will be shown, the interaction between the different unstable modes produces some new, interesting phenomena, including a suppression mechanism for the particle flux. This is of importance because the particle flux in gyrokinetic simulations using experimentally measured gradients is often too high, which could be explained by a detuning of the suppression mechanism due to the substantial errors in the gradients. Some of these features can be understood at least qualitatively by quasilinear investigations, which offer the possibility for extended parameter scans. This will be exploited to examine the collisionality dependence of the TEM-ITG transition.

## 6.1. Setup for the simulations

As in the previous section, all simulations are performed in  $\hat{s}$ - $\alpha$  geometry with  $\alpha = 0$ ,  $q_0 = 1.4$ ,  $\hat{s} = 0.8$ , and  $\epsilon \equiv r/R = 0.16$ . Other plasma parameters are  $\beta = 10^{-3}$  and  $T_e/T_i = 2$ . Furthermore, again a reduced mass ratio of  $m_e/m_i = 1/400$  is used. Due to the temperature ratio, which can be achieved experimentally with predominant electron heating, the ETG modes are suppressed in a wide region of the  $(\omega_{Te}, \omega_{Ti}, \omega_n)$  parameter space, so that the perpendicular resolution of the following nonlinear simulations can be limited to ion scales. In the nonlinear simulations, collisions are neglected, the remaining instabilities are thus collisionless TEMs (CTEMs) and ITG modes according to the traditional naming. The perpendicular box size for the nonlinear simulations is  $L_x = 150\rho_s$  and  $L_y = 125\rho_s$ , the numerical resolution is  $128 \times 64 \times 24 \times 48 \times 8$  points in the radial, binormal, parallel,  $v_{\parallel}$ , and  $\mu$  direction, respectively, and both electrons and ions are treated gyrokinetically in all computations. For the linear computations, the perpendicular box sizes are adapted in order to obtain the maximum number of poloidal connections, the radial mode number is reduced to five and all other parameters are kept fixed at the values of the nonlinear simulations. As usual, the normalization scales are chose to be  $L_{\text{ref}} = R$ ,  $T_{\text{ref}} = T_e$ ,  $n_{\text{ref}} = n_i = n_e$  and  $m_{\text{ref}} = m_i$ , so that all growth rates and frequencies in this chapter are normalized to  $c_s/R$ , the particle fluxes to  $n_e c_s (\rho_s/R)^2$  and the heat fluxes to  $p_e c_s (\rho_s/R)^2$ .

## 6.2. Nonlinear results and comparison to linear behaviour

To study the transition between the TEM and ITG turbulence regimes, first of all a scan of the ion temperature gradient at a fixed and finite electron temperature gradient  $R/L_{Te} = 4.5$  and density gradient  $R/L_n = 3$  is performed. Fig. 6.1 shows the particle and heat fluxes of the nonlinear simulations, as well as the average squared fluctuation density as a measure of the fluctuation level. While the end points of the scan match the expectations for the fluxes (i.e. clear outward particle transport at both ends, TEM induced electron heat transport for low  $R/L_{Ti}$  and an advective contribution at high  $R/L_{Ti}$ , very strong ion heat transport for the ITG dominated end of the scan), the results exhibit a very clear and unexpected feature, namely a significant minimum at  $R/L_{Ti} = 4.625$ . This is approximately the transition point between TEM and ITG turbulence, which can be seen in Fig. 6.2, where the  $R/L_{Ti}$  dependence of the two linear instabilities at a typical  $k_y$  of 0.25 is depicted. This linear scan shows a critical gradient for the ITG instability of  $R/L_{Ti} \approx 3.3$  and a relatively slow decay of the TEM growth rate with the ion temperature gradient, with TEM subdominantly unstable even for the highest  $R/L_{Ti}$ . As already mentioned above, there is no ambiguity in the labelling of the modes for all parameters used in this chapter, they can be clearly distinguished by their diamagnetic drift direction (i.e. the sign of their frequency), see also Fig. 6.4 on this issue. The minimum in the nonlinear  $R/L_{Ti}$  scan is also visible in the fluctuation amplitude, which can be partly explained by the minimum of the growth rate at the transition point. This effect of course contributes to the minimum in the fluxes but can not explain the drop of the particle flux to

## 6.2. Nonlinear results and comparison to linear behaviour

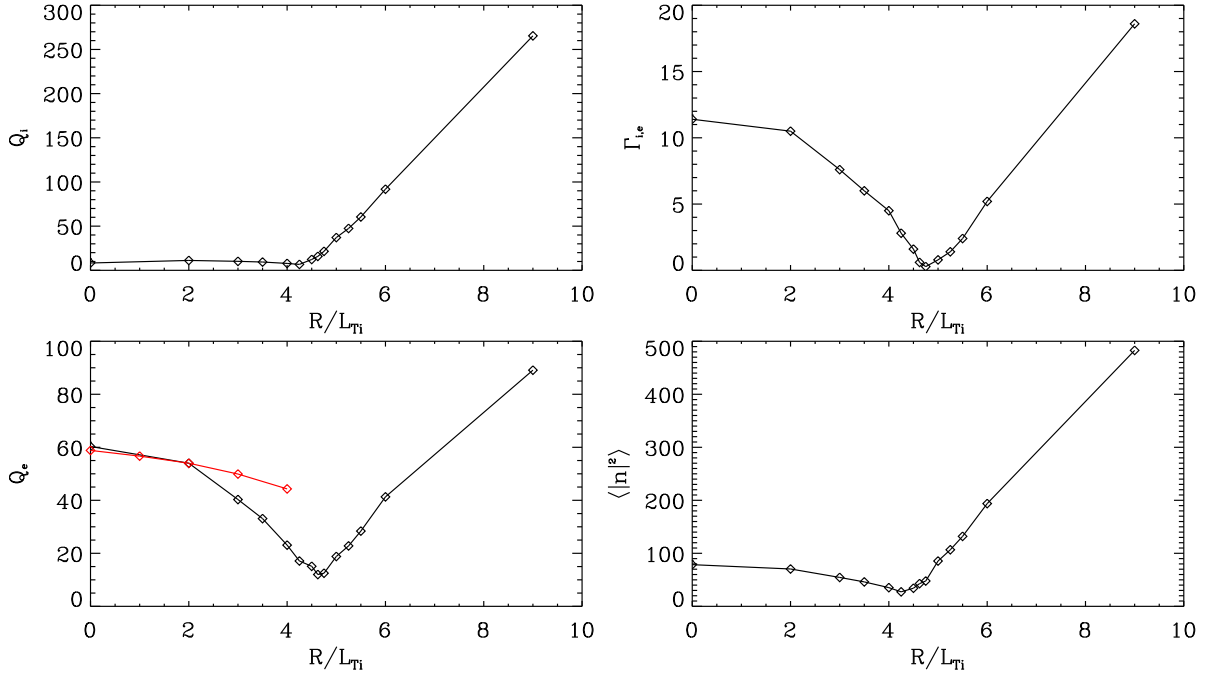


Figure 6.1.: Heat and particle fluxes and the fluctuation level as a function of the ion temperature gradient. The red curve in the plot for the electron heat flux corresponds to the TEM transport model described in the last chapter.

almost zero.

The fact that the TEM/ITG transition occurs very close to the minimum of the fluxes at  $R/L_{Ti} \approx 4.625$  is also confirmed by a rather abrupt change in the relevance of zonal flows. The left plot of Fig. 6.3 shows the shearing rate as a function of  $R/L_{Ti}$ , displaying a sudden increase at  $R/L_{Ti} \approx 4.25$ , i.e. slightly below the TEM/ITG transition, but well above the linear critical gradient for ITG modes. The right plot of Fig. 6.3 shows this even clearer: As already discussed in Chapter 5, zonal flows often don't play a decisive role for the saturation of pure TEM turbulence, the transport levels of the saturated phase stay almost constant even when the zonal flows are artificially suppressed, as has been done for the red curve in the plot. For low values of  $R/L_{Ti}$ , the curves with and without zonal flows are virtually identical, but this changes drastically when the ITG modes start to become the dominant drive of the system – then the zonal flow suppression leads to an increase of the electron heat transport of a factor five or more, as reported in the literature for the pure ITG regime [71, 72, 73].

The transition in the zonal flow dependence coincides with the rise of the ion heat flux. Interestingly, it occurs at a value that is significantly higher than the linear critical  $R/L_{Ti}$  for the onset of ITG instability. As can be observed by comparing the linear results in Fig. 6.2 with the behaviour of the nonlinear fluxes and the zonal flows (Figs. 6.1 and 6.3), the nonlinear critical gradient is shifted from its linear value of  $R/L_{Ti} \approx 3.3$  to  $R/L_{Ti} \approx 4.5$ . This implies that the saturation mechanism that stabilizes the TEM turbulence also works for weakly unstable ITG modes. However, the decrease of the TEM activity with  $R/L_{Ti}$  due to smaller growth rates, combined with a simultaneous increase of ITG growth rates, obviously leads to

## 6. TEM/ITG turbulence in tokamaks

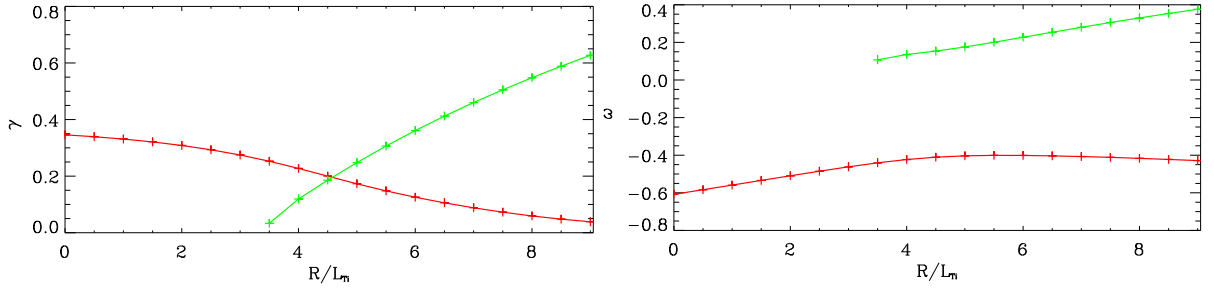


Figure 6.2.: The linear growth rates and frequencies of the TEM (red) and ITG mode (green) for a "characteristic" wave length of  $k_y = 0.25$ . Since the all parameters used in this section are far away from non-Hermitian degeneracies, the modes are clearly distinguishable and the traditional nomenclature can be applied.

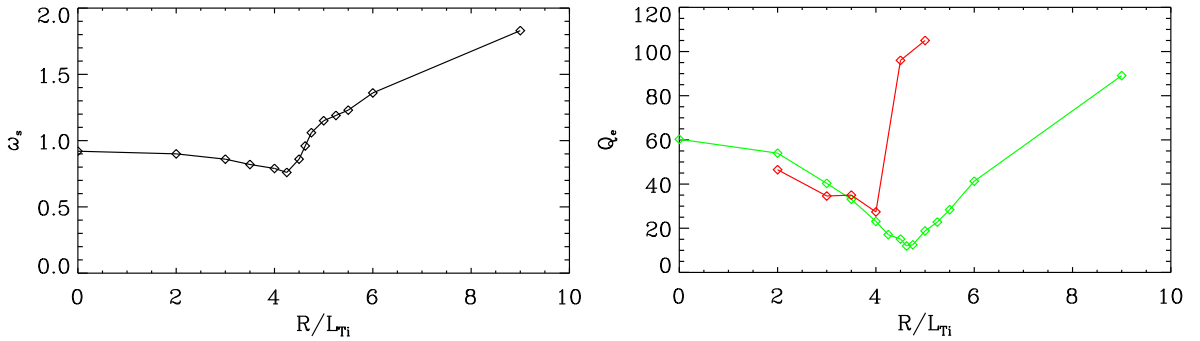


Figure 6.3.: Shearing rate (left) and electron heat flux (right) as a function of  $R/L_{Ti}$ . The green curve corresponds to a full nonlinear simulation, for the red curve, the zonal flows have been artificially suppressed.

a situation where this TEM induced stabilization is not longer possible and the ITG generated zonal flows take over that role.

While these global features of the fluxes demonstrate the presence of nontrivial effects at the transition point between TEM and ITG turbulence, for a deeper understanding, the spectral dependence has to be taken into account. In Fig. 6.4, the linear growth rates and frequencies are shown as functions of the two dimensional parameter space ( $k_y, R/L_{Ti}$ ). The plot shows that for a wide range of parameters, both instabilities are present simultaneously. Furthermore, the intersection of the two planes describing the growth rates of the different modes is not parallel to the  $k_y$  axis (also see the right plot of Fig. 6.7). It rather describes a curved line, with the  $R/L_{Ti}$  of the transition first increasing up to  $k_y = 0.15$  and then decreasing with  $k_y$ , implying that for some rather large range in  $R/L_{Ti}$ , the dominant microinstability is different for different  $k_y$ . This means that at least linearly, the TEM/ITG transition takes place gradually and for a quite extended parameter range, a coexistence between TEM and ITG modes is to be expected.

It is a priori not clear that a higher growth rate leads to a higher amplitude (i.e. dominance) of the mode in the saturated turbulent regime, i.e. whether the linear findings are decisive for the nonlinear simulations on that issue. If the nonlinear damping mechanism is different for

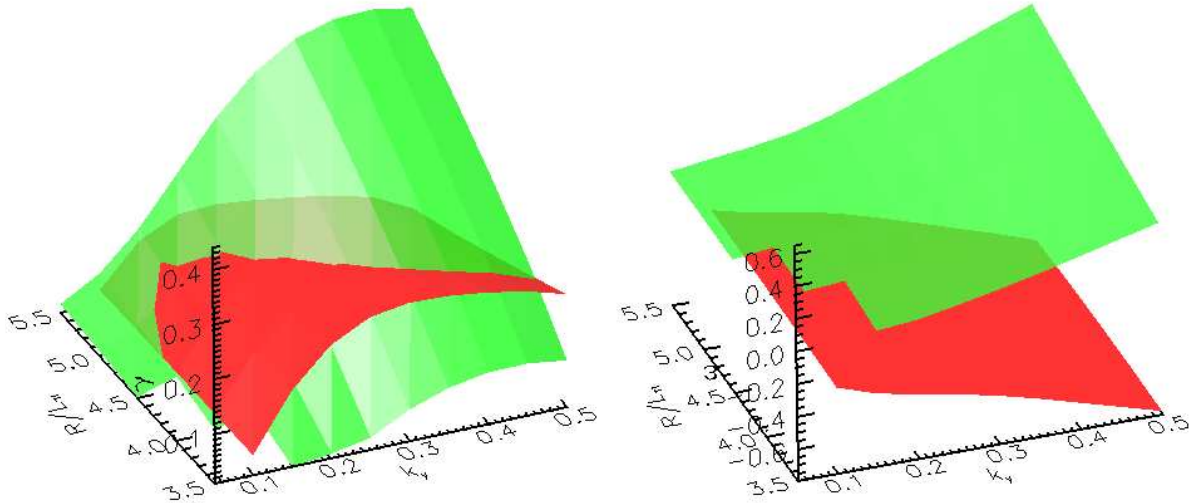


Figure 6.4.: Linear growth rates and frequencies for the TEM (red) and ITG mode (green).

The last plot is a top view of the growth rate plot, showing the dominant mode in the different regions of parameter space. The missing patches correspond to areas where the modes are stable.

the two instabilities (as is strongly suggested by Fig. 6.3), it is well possible that a linearly subdominant mode, although growing slower in the initial phase of the simulation, ends up at a higher saturation level and thus dominates the system.

To determine the role of the different modes for the different perpendicular wavenumbers, a new frequency diagnostic is used. The prescription (5.1) that was used in the last chapter is not applicable here, since it implicitly assumes that only one frequency plus some noise is present. To extract all frequencies in the nonlinear system, a windowed Fourier transform is applied to the time traces of all components of the perturbed density field and the result is averaged over the parallel direction. In plots showing the  $k_y$  dependence of this frequency spectrum, the amplitudes of the frequency components are normalized to the sum of amplitudes at each  $k_y$ , whose variation would otherwise obscure the frequency distribution of interest.

The left plot of Fig. 6.5 shows the  $k_y$  dependence of the resulting distribution of the frequency components for the  $R/L_{Ti} = 4.625$  case. The nonlinear amplitudes are color coded, the red and green lines indicate the frequencies of the linear TEM and ITG modes for comparison. The right plot shows the corresponding growth rates of the two microinstabilities. The nonlinear result reveals that while the TEM contribution dominates for  $0.1 < k_y \leq 0.2$  and the ITG contribution dominates for  $k_y \geq 0.25$  and  $k_y = 0.05$ , TEM and ITG turbulence can coexist not only at different  $k_y$  in the same simulation but even at the same perpendicular wave number, with the remnants of the two microinstabilities interpenetrating and drifting in opposite directions, at a frequency that is practically unaltered with respect to the linear computations. The linear  $k_y$  values where the growth rates of the two instabilities intersect and the nonlinear values where the dominant frequency changes sign are not distinguishable ( $k_y \approx 0.1$  and  $k_y \approx 0.22$  in both cases), implying that the properties of the turbulence are largely set by the linear physics also on this issue. This interesting phenomenon has never been reported

## 6. TEM/ITG turbulence in tokamaks

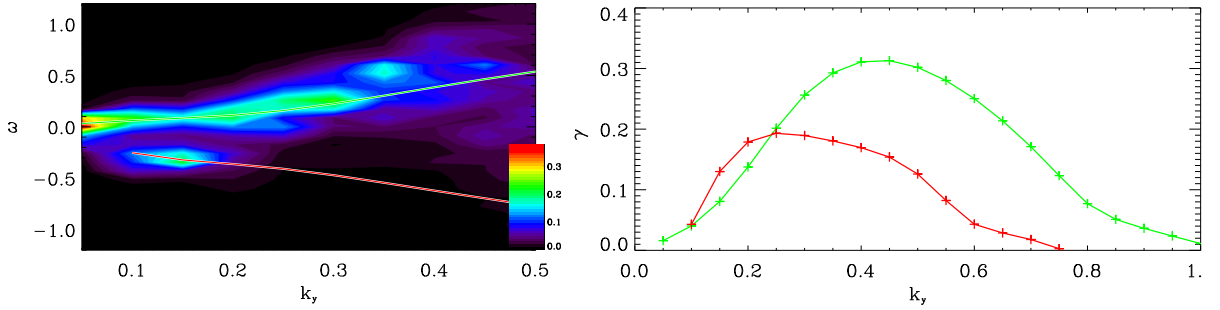


Figure 6.5.: Left: Normalized nonlinear frequency spectrum (color coded) as function of  $k_y$  for  $R/L_{Ti} = 4.625$ ; the red and green lines are the linear frequencies for TEM and ITG modes respectively. Right: The corresponding linear growth rates.

before and might also be accessible experimentally by means of Doppler reflectometry (see, e.g. [88, 89]).

Note that the distribution function of the frequencies becomes broader with increasing  $k_y$  and the peaks at the linear eigenfrequencies become less pronounced, indicating that the linear drive plays a less decisive role for  $k_y \gtrsim 0.5$ , but since TEM and ITG mode driven turbulence does not produce much transport in this  $k_y$  range, this effect is secondary.

It is also interesting to look at the relative change of the amplitudes of the TEM- and ITG-like contributions for a specific  $k_y$  as a function of  $R/L_{Ti}$ . Again, the "representative" wave number  $k_y = 0.25$  is used. Since for this case, the two contributions to the frequency distribution are well separated by a minimum at  $\omega \approx -0.1$ , all contributions with  $\omega \leq -0.1$  /  $\omega > -0.1$  are summed and attributed to the TEM / ITG mode respectively. This criterion is of course not strict, since the tails of the frequency distributions of TEM and ITG turbulence can leak into the other frequency range. The result (normalized to the overall amplitude) is shown in Fig. 6.6. It shows a very clear transition between a regime with  $\approx 90\%$  TEM contribution for  $R/L_{Ti} \leq 3.5$  and  $\approx 85\%$  ITG contribution for  $R/L_{Ti} \geq 4.625$ . However, there is a transition range where both instabilities act at the same perpendicular wavenumber; the two contributions are equal for  $R/L_{Ti} \approx 4.2$ .

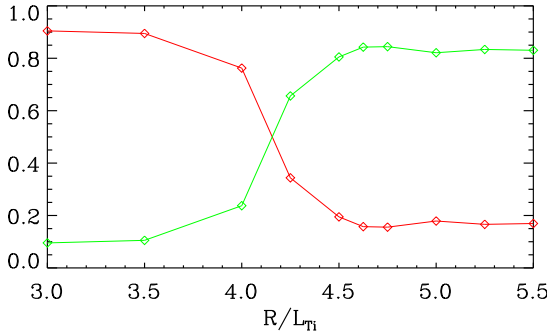


Figure 6.6.: Normalized TEM (red) and ITG (green) contributions to the frequency distribution at  $k_y = 0.25$  as a function of  $R/L_{Ti}$ .

## 6.2. Nonlinear results and comparison to linear behaviour

Since the TEM-ITG transition is reasonably sharp, it is possible to get an indication of which microinstability dominates the turbulence from the first moment of the frequency distribution. Since the ITG and TEM peaks in the frequency distribution are not exactly symmetric with respect to the origin, an expectation value of  $\omega = 0$  does not exactly correspond to equal amplitudes of TEM and ITG contributions, but this criterion can nevertheless be used as a reasonable identification mark for the transition. The result is shown in the left plot of Fig. 6.7, where the average frequency is depicted as a function of  $(k_y, R/L_{Ti})$ . The transition is quite clearly visible in the color coding, additionally the  $\omega = 0$  contour line has been marked in black. Due to the finiteness of the data set for the computation of the frequency distribution and the crudeness of the  $\omega = 0$  criterion, the plot and the line are subject to noise, but the comparison with the right plot of Fig. 6.7 again displays a remarkable similarity of the linear and nonlinear behavior, clearly showing that the coexistence of TEM and ITG mode turbulence at different  $k_y$  is very common if electron and ion temperature gradients are in the same range.

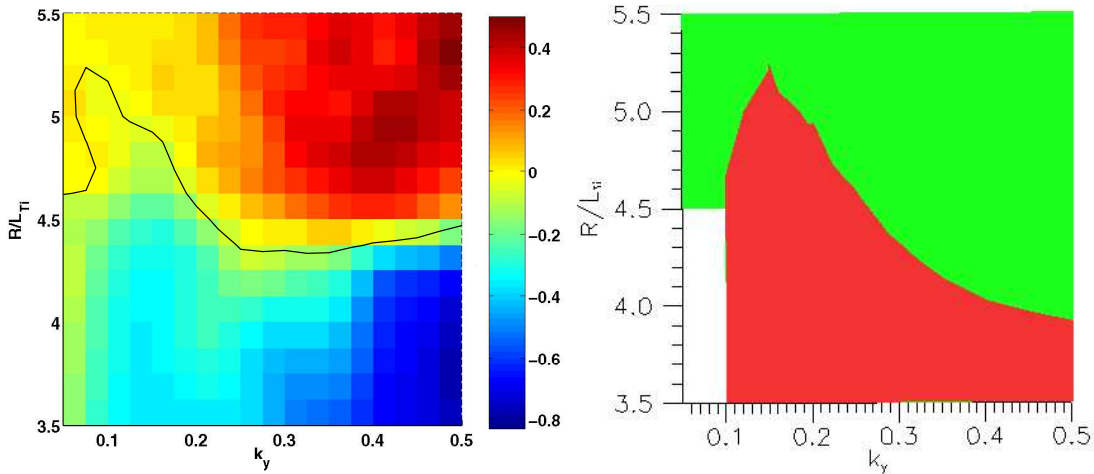


Figure 6.7.: Left: First moment of the nonlinear frequency distribution (color coded), the  $\omega = 0$  contour line (black) may be used to mark the TEM-ITG transition. Right: The areas where the dominant microinstability is TEM/ITG are coloured red/green.

After this discussion of the general features of the TEM-ITG transition, a detailed investigation of the most intriguing feature of Fig. 6.1, namely the clear minima in the transport quantities at the TEM-ITG transition is in order. Of special interest in this context is the particle flux, as will be discussed in more detail in Sec. 6.4. To reveal the mechanism that creates this minimum at  $R/L_{Ti} = 4.625$ , the spectral decomposition of the fluxes is shown in Fig. 6.8. The TEM turbulence, which is predominant at  $0.1 \leq k_y \leq 0.2$ , leads to an outward transport, this transport is balanced by the particle pinch of the ITG turbulence at  $0.2 < k_y < 0.4$ ; the contribution from even higher (or lower)  $k_y$  can be neglected. The particle flux shows a zero crossing very close to the  $k_y$  values where the growth rates of the two underlying microinstabilities intersect and the frequency distribution shows comparable TEM and ITG contributions, implying that the same balancing of inward and outward flux can not only work globally for the whole system, but even for one specific  $k_y$  contribution. Together this implies that the

## 6. TEM/ITG turbulence in tokamaks

phenomenon of approximately zero global particle flux observed in this nonlinear simulation is the result of a fine tuning of the effects of the TEM and ITG contributions at different  $k_y$ .

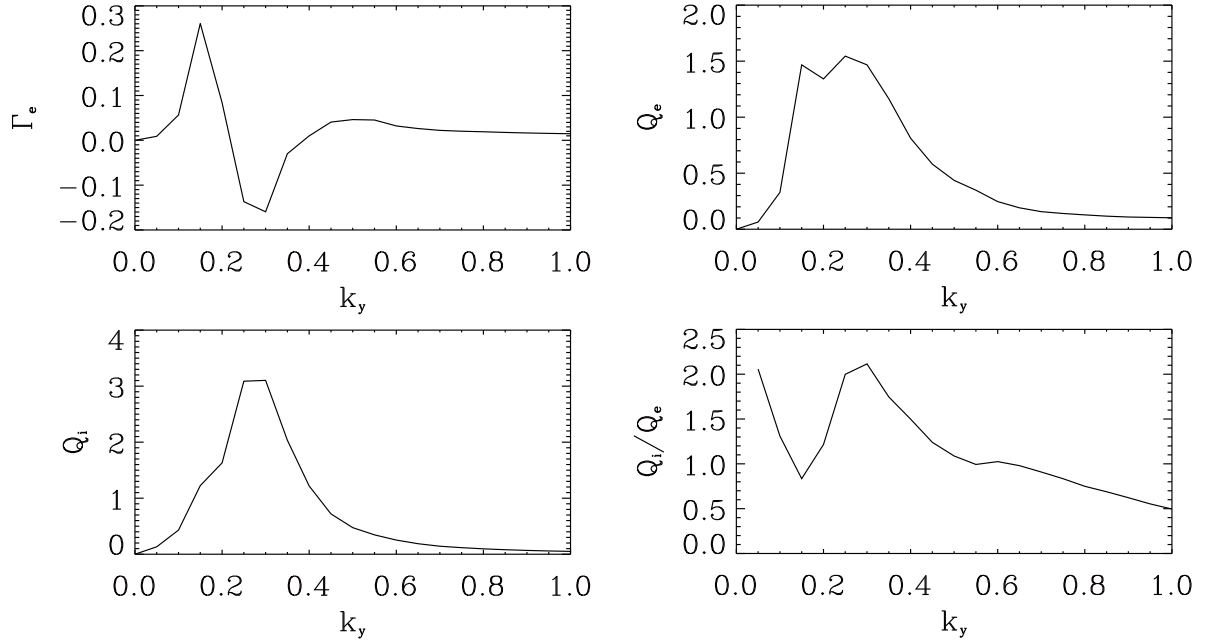


Figure 6.8.: Particle and heat transport and the ratio of the heat transport of the two species as a function of  $k_y$  for  $R/L_{Ti} = 4.625$ .

The other plots of Fig. 6.8 show that the spectral separation of dominant ITG and TEM turbulence also causes a double peak in  $Q_e^*$  and can be confirmed by other characteristic properties like the ratio of ion and electron heat flux, which has typical values for TEM turbulence at  $k_y \approx 0.15$  and typical ITG values at  $k_y \approx 0.3$ .

### 6.3. Construction of a quasilinear model for the flux ratios

The quasilinear transport model described in Sec. 5.5 ignores subdominant contributions and has been tested so far for pure TEM cases only. It is therefore not surprising that it does not capture the effects of the TEM-ITG transition. This is demonstrated by the red line in Fig. 6.1, which describes the nonlinear parameter dependencies of the electron heat flux to a good degree for the pure TEM regime, but deviates from the nonlinear values when ITG contributions start to appear. Nevertheless, it has been shown in the last section that the turbulence inherits many features of the microinstabilities, even in the TEM-ITG transition region, it is therefore conceivable that a quasilinear description is sufficient for some qualitative investigations. The construction and test of such a model will be the topic of the remainder of this chapter.

For the almost electrostatic cases considered here, the heat and particle fluxes are determined by the amplitudes of the corresponding moment of the distribution function and of the

### 6.3. Construction of a quasilinear model for the flux ratios

electrostatic potential and the phase angle between these two quantities. While the saturation amplitude and therefore the absolute value of the heat and particle fluxes can only be determined by nonlinear simulations, an unambiguous value for the sign and the ratio of the different fluxes,  $Q_i/Q_e$ ,  $\Gamma/Q_e$ ,  $\Gamma/Q_i$ , can be determined from linear computations already.

From the last section it is clear that estimating the amplitude ratio of the two coexisting modes at a given  $k_y$  is not completely straightforward, however it seems plausible to make the ansatz that the amplitude of the two modes at a given  $k_y$  is a monotonically increasing function of the respective growth rate. This is of course not exactly true, as can be concluded from the comparison of Figs. 6.2 and 6.6, but it may still serve as an approximation. Another problem is the weighting of the different  $k_y$  contributions in the system. As discussed in the last section, the ratio of the amplitudes / growth rates of the two instabilities is very sensitive to the  $k_y$  value chosen. Since a nonlinear simulation contains many different  $k_y$  contributions with different amplitudes, it is difficult to find an appropriate prescription for the superposition of different linear modes in a quasilinear model.

In order to arrive at a predictive quasilinear model that allows for extensive parameter scans, the problem of the weighting of the different  $k_y$  contributions is solved by using only one, "characteristic"  $k_y$ . This is of course a crude approximation, but as has been discussed in the last section, the same coexistence of modes that influences e.g. the particle transport in the full system also occurs at a single  $k_y$ . If this value of  $k_y$  is chosen carefully, the TEM and ITG contributions at that  $k_y$  value approximately represent the summed contributions from lower and higher  $k_y$ , so that this "central" mode reflects the whole system. A suitable choice for this mode is, as it turns out, again  $k_y = 0.25$ . As mentioned above, a method to combine the contributions from the two microinstabilities has to be prescribed; an obvious starting point for the weighting factors to combine the flux ratios computed from TEM and ITG modes are powers of the respective growth rates:

$$R_m = \frac{\gamma_{\text{TEM}}^p R_{\text{TEM}} + \gamma_{\text{ITG}}^p R_{\text{ITG}}}{\gamma_{\text{TEM}}^p + \gamma_{\text{ITG}}^p} \quad \text{with } R = (Q_i/Q_e, \Gamma/Q_e, \Gamma/Q_i) \quad (6.1)$$

A suitable value for the exponent  $p$  has been determined by comparison of the resulting quasilinear flux ratios to the nonlinear values, the result for  $p = 10$  is shown in Fig. 6.9.

Given the crude approximations, the agreement between the respective curves is quite good. It is obvious that all basic features like the position of the minima, turning points and even the approximate values of the curves are well described by the quasilinear approximation. The most significant deviation is that the value of the minimum of the particle flux is underestimated by the model, predicting a particle pinch instead of a small remaining outward transport. Nevertheless, this quasilinear model seems to be able to describe the basic features correctly and will therefore be used to try to understand some parameter dependencies by simple and fast linear computations. Note that there have been quasilinear gyrokinetic investigations of TEM/ITG turbulence before [90], but because an initial value solver was used for the computations, the subdominant modes have not been accessible, resulting in a discontinuity of the quasilinear predictions at the linear TEM-ITG transition – which is of course unphysical and difficult to interpret. Furthermore, initial value computations become increasingly difficult close to mode transitions, as the amplitudes of the two exponentially growing modes take longer and longer to separate. Since this separation of the amplitudes is the prerequisite for

## 6. TEM/ITG turbulence in tokamaks

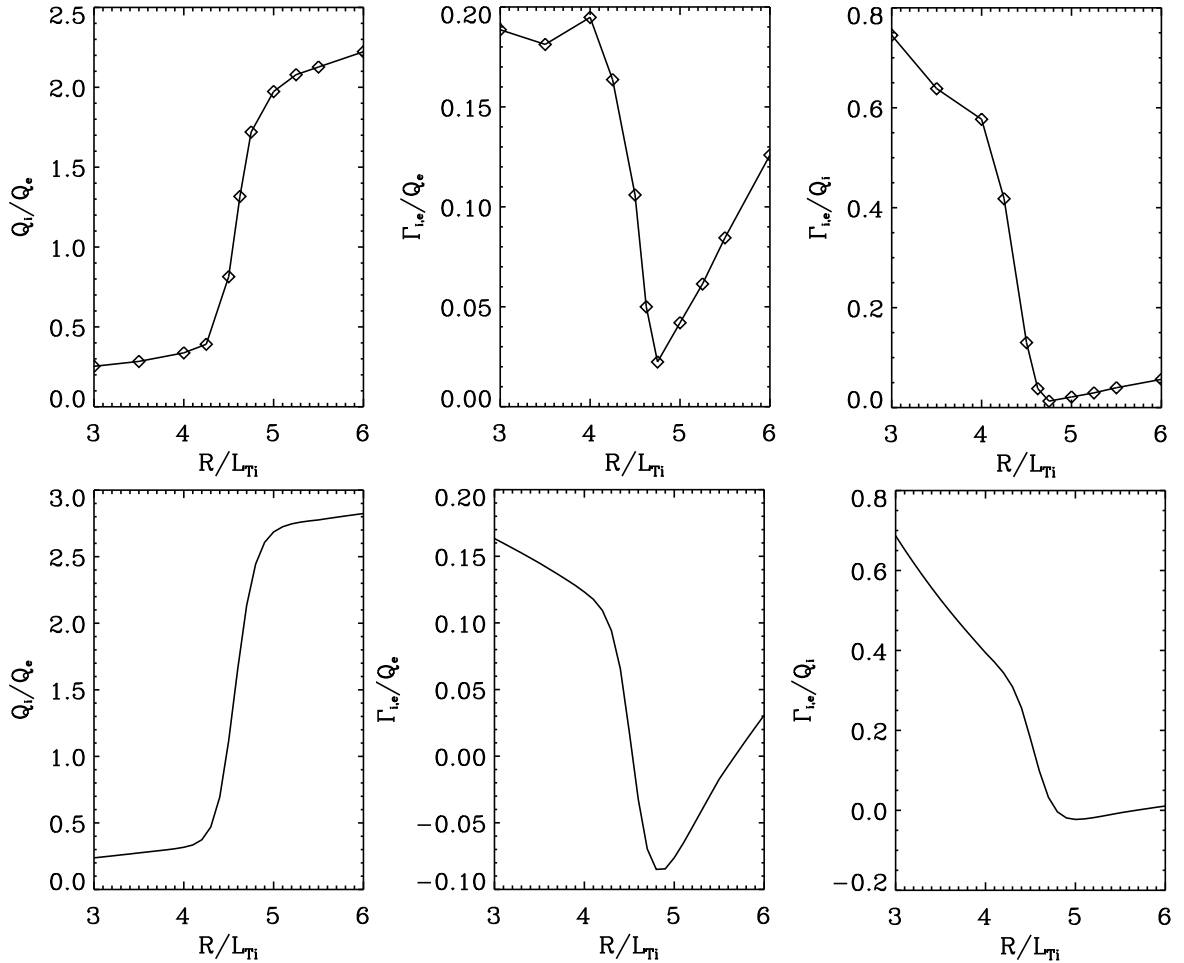


Figure 6.9.: Nonlinear flux ratios (top) vs. quasilinear flux ratios (bottom) as defined by Eq. (6.1).

convergence of the initial value solver, the computation time diverges at the mode transition, showing the superiority of eigenvalue computations for this kind of investigations.

## 6.4. Application and test of the quasilinear model

The model defined in the last section does not predict the values of the transport fluxes, but only their ratios. This may seem not very useful at first glance, but has one very important application, namely the prediction of the zero-crossing of the particle flux.

To realize the relevance of this, it is important to understand that in the local  $\delta f$  approximation used in GENE and most other gyrokinetic codes, the average background gradients ( $\omega_n, \omega_{Te}, \omega_{Ti}$ ) driving the turbulence are held constant throughout a simulation. They are, in particular, independent of the transport fluxes ( $\Gamma, Q_e, Q_i$ ), which constitute the main output of such simulations. In contrast to that, the fluxes in a real fusion experiment are dictated by the output of the heating and refueling systems; the values for the gradients, which adjust more

## 6.4. Application and test of the quasilinear model

or less freely to meet these constraints on the fluxes, are obtained experimentally from a combination of direct experimental measurements and a MHD reconstruction of the equilibrium. This procedure usually leads to quite substantial error bars (a couple of 10%) in the gradients, while the values for the fluxes are much more accurate. There are of course also uncertainties for other parameters like the  $\beta$ ,  $\hat{s}$ , or the temperature ratio, but the simulated fluxes are, in general, much less sensitive to changes of these parameters than of the gradients.

The combination of these two points implies that it can be difficult to directly compare simulations and experiments, especially close to critical gradients, where small variations (or inaccuracies) of the gradients can lead to big variations of the computed fluxes. If the three fluxes in all points of the three dimensional parameter space of the gradients could be computed, this information could be used to match the experimental fluxes and make a prediction for the gradients, allowing for much more robust comparisons to experimental data. Since this is out of scope for nonlinear simulations, it is important to find reliable quasilinear descriptions that at least partially allow for the comparisons described above.

An especially interesting (and accessible) subject for this kind of investigations is the particle flux. While all fusion experiments have strong heating systems which deposit their energy close to the magnetic axis and can therefore sustain significant radial heat fluxes, the possibilities of refueling particles at the plasma center are limited. The pellet injection systems used for that purpose are pulsed and are not able to change the quasi-stationary particle fluxes significantly, and also the neutral beam injection (NBI) systems that are used for heating have no significant impact, so that  $\Gamma \approx 0$  has to be fulfilled for all experimentally accessible situations [90]. This has a very advantageous implication for quasilinear models. While it is difficult to predict the absolute value of the transport, the prediction of the sign of the transport (or transport ratio), and thus its zero-crossing in parameter space is no problem. This even holds for simple models like the one presented in the last section.

If the fluxes vary smoothly with all parameters of the system (as is expected), the  $\Gamma \approx 0$  condition defines a hypersurface with one dimension less than the parameter space under consideration (i.e. it has codimension one). If the parameter space is restricted to the most important parameters for the fluxes, namely the gradient triple  $(\omega_n, \omega_{Te}, \omega_{Ti})$ , the  $\Gamma \approx 0$  condition is fulfilled on a two-dimensional surface in parameter space. In previous quasilinear studies considering only dominant linear contributions [90], only low dimensional cuts of this hypersurface have been shown, but with the model based on eigenvalue computations defined in the last section and the possibility of easy parameter scans in GENE, it is now possible to compute the hypersurface in higher dimensions.

To demonstrate this, a three dimensional linear scan of the gradients  $R/L_{Te}$ ,  $R/L_{Ti}$ ,  $R/L_n$  was used to compute the quasilinear  $\Gamma \approx 0$  surface shown in blue in Fig. 6.10. It shows that the parameter dependencies are far from trivial; the blue surface, which separates the region exhibiting a particle pinch from the region with outward particle transport, is not aligned with any of the axes, so that for a minimization of the particle transport, the dependence on all three gradients really has to be taken into account. The  $\Gamma \approx 0$  surface consists of two "wings". The right one appears in the proximity of and more or less parallel to the yellow surface that represents the linear TEM-ITG transition of the  $k_y = 0.25$  mode; it corresponds to the balance of TEM induced outward and ITG induced inward particle transport that was discussed in Sec. 6.2. For the left wing however, the TEM growth rate is too small to affect the system; the

## 6. TEM/ITG turbulence in tokamaks

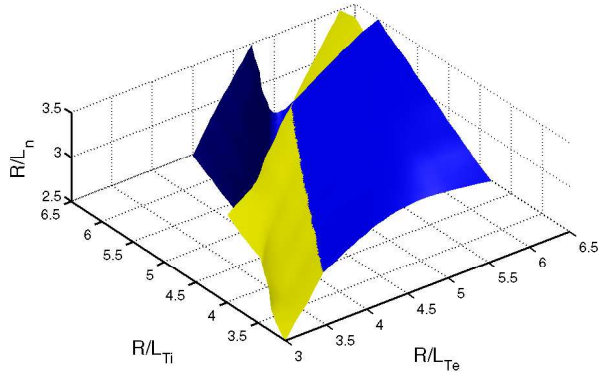


Figure 6.10.: The  $\Gamma \approx 0$  surface (blue) as predicted by the quasilinear model defined in Sec. 6.3, and the ITG-TEM transition surface (yellow) for the "typical"  $k_y = 0.25$  mode. The region with the particle pinch is "behind" the blue surface in this view.

zero particle flux in this case arises due to a change of sign of the ITG contribution itself.

The nonlinear scan presented in Sec. 6.2 corresponds to a line with  $R/L_{Te} = 4.5$  and  $R/L_n = 3.0$  in this three dimensional plot, slightly cutting through the blue surface very close to the TEM-ITG transition. If this line is shifted to a slightly higher electron temperature gradient or slightly lower density gradient, the quasilinear model predicts a particle pinch in a range of  $R/L_{Ti}$  values.

To test this prediction and examine the nature of the second zero-crossing of the particle flux, another nonlinear scan with again  $R/L_{Te} = 4.5$  but  $R/L_n = 2.5$  has been performed. The transport fluxes, which indeed confirm the existence of a particle pinch, are shown in Fig. 6.11. The curves largely resemble the  $R/L_n = 3$  case of Fig. 6.1, except that the electron

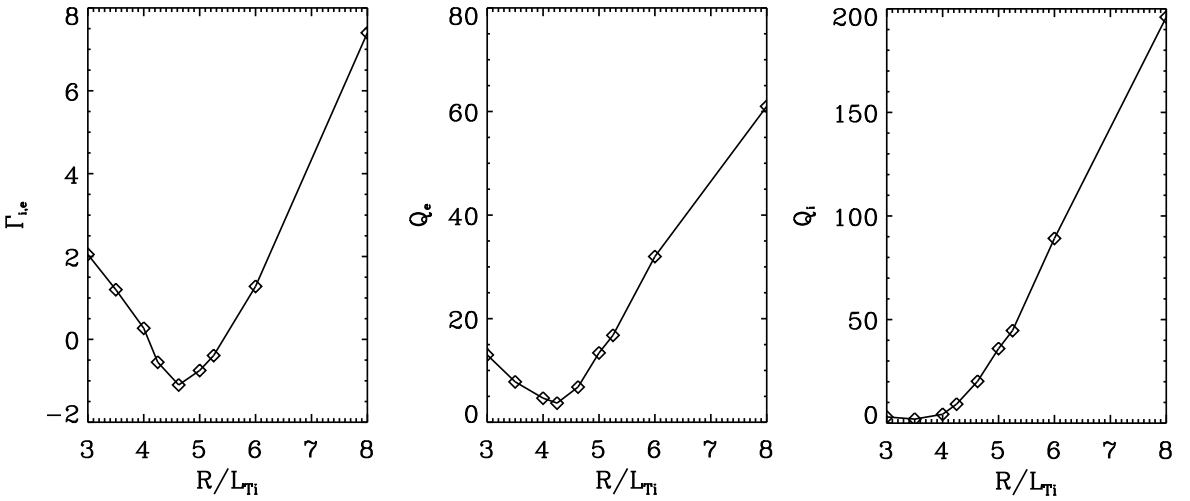


Figure 6.11.: The fluxes for the reduced density gradient  $R/L_n = 2.5$ , showing a particle pinch.

#### 6.4. Application and test of the quasilinear model

heat flux on the TEM dominated low  $R/L_{Te}$  side is significantly lower due to a decrease of the TEM growth rates and the particle flux is generally reduced and shifted to negative values by almost two units.

For a detailed analysis of the predictions of the quasilinear model, Fig. 6.12 shows the nonlinear and quasilinear flux ratios for the  $R/L_n = 2.5$  case (black curves). It is obvious that

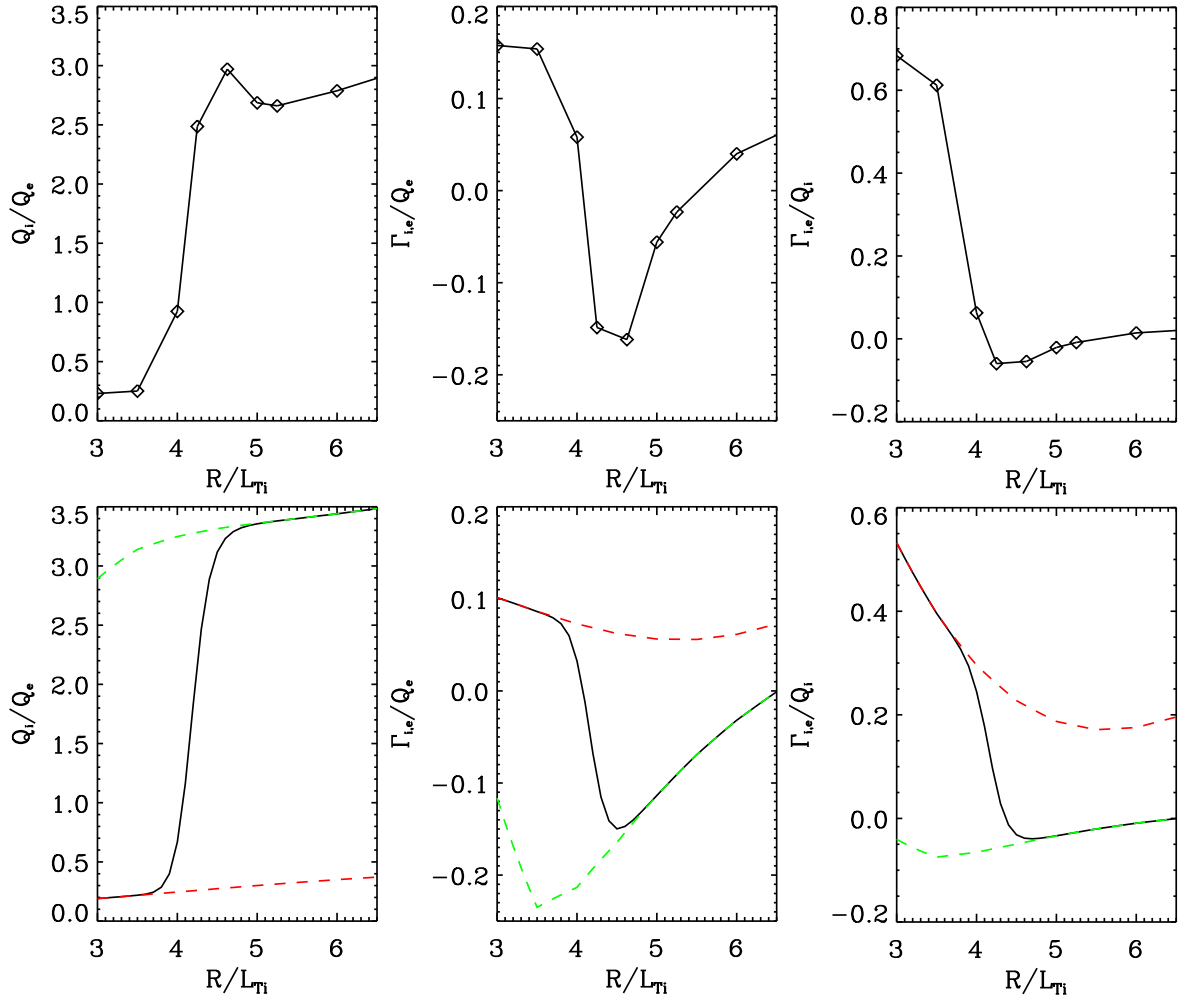


Figure 6.12.: The black curves depict the nonlinear (top) and quasilinear (bottom) ratios of the different fluxes for  $R/L_n = 2.5$ . The red and green curves correspond to the values of the underlying TEM and ITG modes respectively.

the model describes the basic features also in this case, e.g. the position (and its shift in  $R/L_{Ti}$  with respect to the  $R/L_n = 3$  case) of the turning point of the  $Q_i/Q_e$  curve, which might be used as a definition of the TEM/ITG transition, or the positions of the transport minima.

The red and green curves in the quasilinear plots show the values computed from the "pure" TEM and ITG modes respectively. The plots involving the particle flux confirm the above statement on the causes for vanishing particle flux. While the first zero-crossing is caused by the coexistence of TEM and ITG modes with opposite transport directions, the second is

## 6. TEM/ITG turbulence in tokamaks

due to a change of the transport direction of the ITG contribution alone. To confirm this also nonlinearly, the transport spectra for the  $R/L_n = 2.5$ ,  $R/L_{Ti} = 6.0$  case (i.e. slightly above the zero-crossing) are shown in Fig. 6.13. The plots show no sign of a mode transition. All  $k_y$

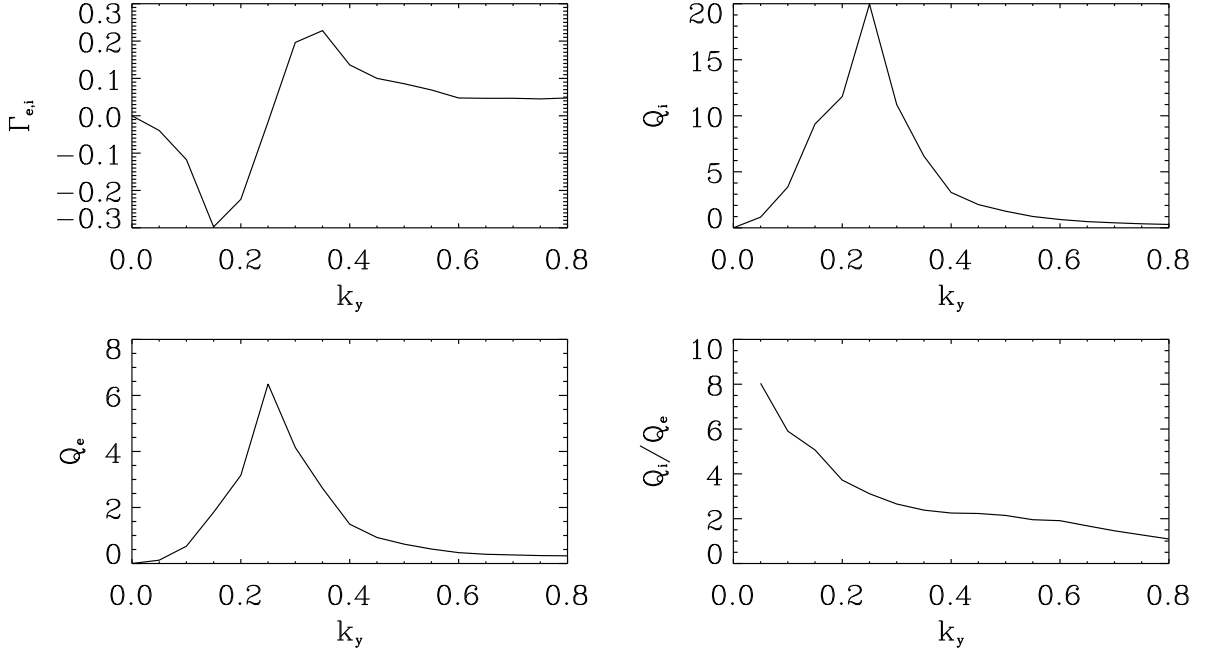


Figure 6.13.: Spectra of the heat and particle fluxes close to the second zero-crossing of the particle flux ( $R/L_{Ti} = 6.0$ ) for the  $R/L_n = 2.5$  case.

contributions are ITG-like, as is especially obvious from the  $Q_i/Q_e$  curve, which is smooth and way above TEM levels for all  $k_y$ . However, the direction of the particle flux changes sign, implying that the second zero-crossing of  $\Gamma$  – as the first – is due to a spectral balance between inward (this time at low  $k_y$ ) and outward fluxes (at high  $k_y$ ), but this time these are both caused by ITG turbulence. As has been shown, this effect is qualitatively captured by the quasilinear model, which relies on only one “representative”  $k_y$ , and although the gradient value of this second zero-crossing in the  $R/L_{Ti}$  scan is overestimated by almost 20%, it is obvious that the quasilinear model can be used to (at least qualitatively) describe also this region of parameter space.

With this example, the applicability of the quasilinear model of Sec. 6.3 for qualitative investigations is demonstrated; as a further application, the influence of collisions on the TEM-ITG transition will be addressed in the next section.

## 6.5. TEM-ITG transitions in the presence of collisions

Collisions are a very interesting topic in the context of TEM-ITG transitions, since they mainly affect the growth rates of TEMs, while leaving the ITG growth rates almost unaltered. This

## 6.5. TEM-ITG transitions in the presence of collisions

is shown in the left plot of Fig. 6.14. The increase of the collision frequency leads to the disintegration of the trapped passing boundary and thus to a stabilization of the TEM, while the growth rate of the ITG mode does not change very much. This stabilization mechanism is well known and can even be used experimentally to provoke TEM/ITG transitions [89].

The decrease of the TEM growth rate at constant ITG growth rate leads to a shift of the intersection between the two microinstabilities to lower ion temperature gradients (or higher electron temperature gradients), which is shown in the right plot of Fig. 6.14. Since one of the

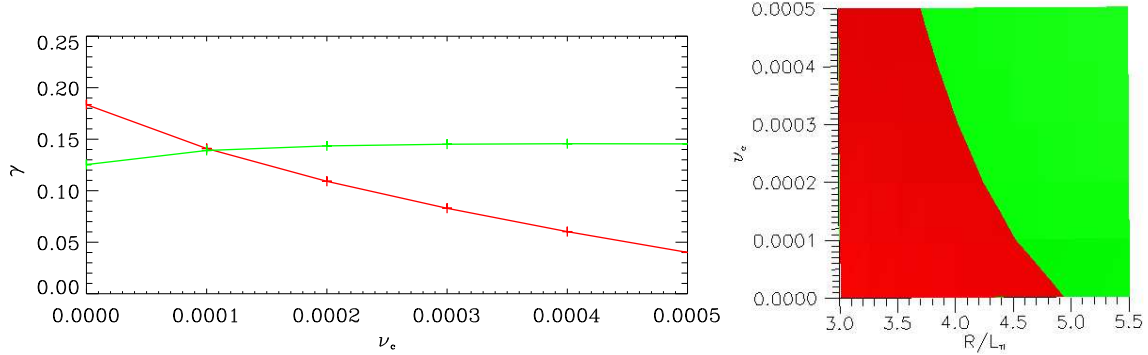


Figure 6.14.: Left: Growth rates of TEM (red) and ITG modes (green). Right: Regions with dominant TEM and ITG instabilities.

mechanisms that lead to zero particle flux relies on a balance of TEM and ITG contributions, it is clear that this shift will also affect the  $\Gamma \approx 0$  surface. To check this explicitly, two scans of the density and temperature gradients – equivalent to the one shown in Fig. 6.10 – have been performed, using the linearized Landau-Boltzmann operator given in Sec. 2.8, with the  $\langle C_{jj'}^\perp \rangle$  contribution neglected since the most important effect of collisions in gyrokinetics is detrapping and not spatial diffusion. The results for  $\nu_c = 0.00025$  and  $\nu_c = 0.0005$  are shown in the first two plots of Fig. 6.15.

As expected, compared to the collisionless case of Fig. 6.10, the yellow surface that indicates the linear TEM-ITG transition of the  $k_y = 0.25$  mode is gradually tilted towards higher values of the electron temperature gradient, reflecting the fact that the TEM growth rate decreases and has to be compensated by a higher drive to equal the (almost unaltered) ITG growth rate. Without collisions, the line of the TEM-ITG transition on a constant  $R/L_n$  surface was roughly at  $R/L_{Ti} \approx R/L_{Te}$ ; with collisions this angle is changed. In contrast to the scan without collisions, parts of the front edge of the yellow surface now lie inside the scanned parameter space, i.e. there are regions (low  $R/L_n$ , low  $R/L_{Te}$ ) where the TEMs are completely stabilized, implying that ITG is always dominant in these regions, independent of the ion temperature gradient.

The wing of the blue  $\Gamma \approx 0$  surface that is connected to the balance of TEM outward transport and ITG pinch more or less follows the yellow surface and is therefore shifted and tilted to larger values of  $R/L_{Te}$ , as expected. What is more surprising is that the other wing, which is solely determined by the ITG mode, also exhibits a shift to higher  $R/L_{Te}$  due to collisions. So although the ITG growth rate is almost unchanged, the collisions affect the phase angle between the density and the potential such that the boundary between inward and

## 6. TEM/ITG turbulence in tokamaks

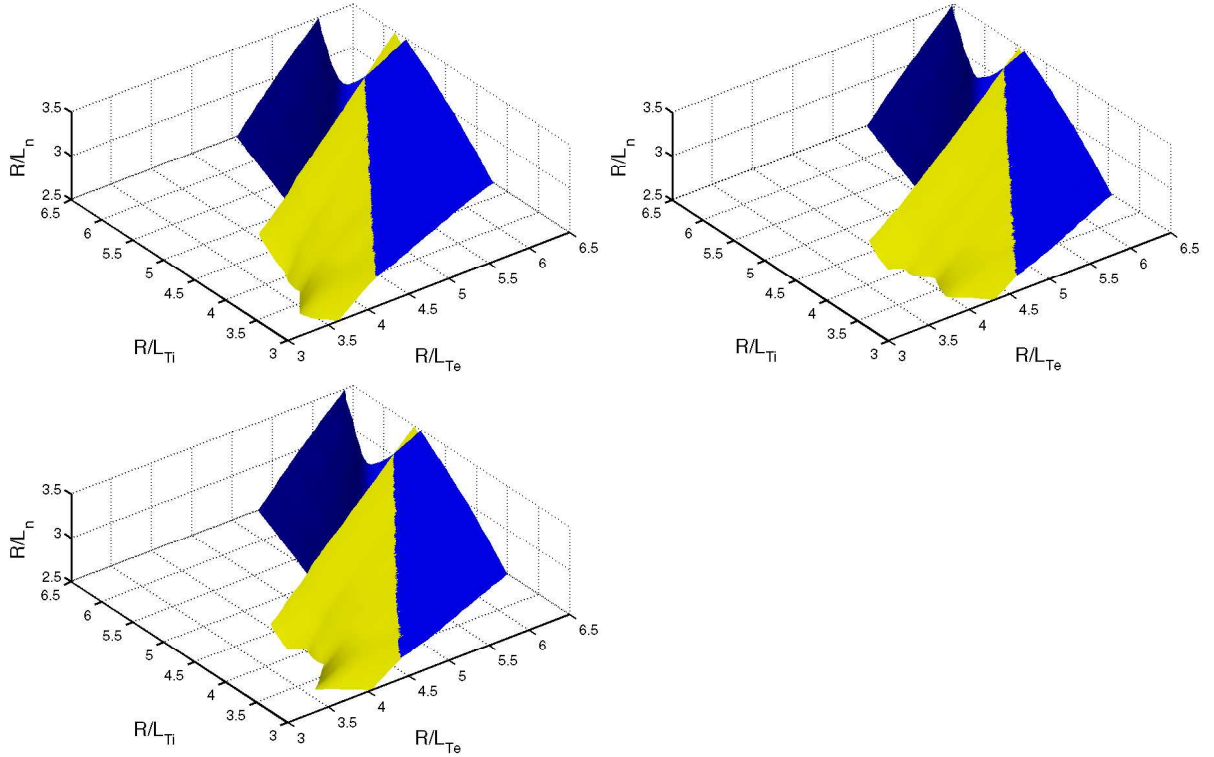


Figure 6.15.: Top: The  $\Gamma \approx 0$  surface as predicted by the quasilinear model defined in Sec. 6.3, for  $\nu_c = 0.00025, 0.0005$  of the Landau-Boltzmann collision operator (velocity space part). Bottom: The corresponding simulation for pitch-angle scattering with  $\nu_c = 0.0005$ .

outward transport is shifted towards higher electron temperature gradients.

The last plot of Fig. 6.15 shows the result of a similar scan, using the the pitch-angle operator (see Sec. 2.9.4) with  $\nu_c = 0.0005$ . The pitch angle operator is widely used in gyrokinetics because of its simplicity, and although some of the assumptions made in its derivation (see discussion in Sec. 2.9.4) can in general not be justified, the discrepancies between the results obtained with the linearized Landau-Boltzmann operator and the pitch-angle operator are very small (at least in this case).

## 6.6. Summary

In this chapter, it has been shown that in situations where TEM and ITG instabilities coexist linearly, features of both microinstabilities can also be found in nonlinear simulations. Due to their  $k_y$  dependence, different microinstabilities can be dominant at different  $k_y$  in the same nonlinear system, leading to a spectral coexistence of the TEM and ITG turbulence. At the transition point, this coexistence can even be present at a single perpendicular wave number, implying that two different frequencies (and even drift directions) are observed for the same spectral mode.

## 6.6. Summary

Two mechanisms for the experimentally important condition of zero particle flux have been identified in the TEM-ITG system: The first is a fine-tuned balance of the TEM-induced outward transport and the ITG-induced particle pinch at different perpendicular wave numbers. The second is the transition between pinch and outward transport within the ITG dominated regime; this transition is also  $k_y$  dependent and thus also allows for a balance between in- and outward transport, similar to the previous case.

It has been shown that the basic phenomena in the nonlinear TEM-ITG system can be described and understood at least qualitatively by a very simple quasilinear model, which only uses the (dominant and subdominant) eigenvalues at a single, "characteristic"  $k_y$ . This model can be used to compute higher dimensional cuts of the  $\Gamma \approx 0$  (or rather  $\Gamma/Q_{e/i} \approx 0$ ) hypersurface, allowing to study its parameter dependence. As an application, the dependence on the collisionality and the details of the collision operator have been studied.

This quasilinear model is also of interest for attempts to compare gyrokinetic simulations to experiments. Since it allows for extensive, multi-dimensional parameter scans, the quasilinear model offers a possibility to tell whether a variation of the nominal experimental gradients within their error bars will lead to an acceptable particle flux (or the experimental flux ratios), and shows how the gradients for more detailed (nonlinear) investigations have to be adapted to produce sensible results.

## *6. TEM/ITG turbulence in tokamaks*

## 7. ITG turbulence in stellarators

In all previous chapters, the analytic  $\hat{s} - \alpha$  model describing a large aspect ratio tokamak has been used for the magnetic equilibrium. While most present day fusion experiments are tokamaks, there are also considerable advances in the field of stellarators, making these devices an interesting topic for theoretical and numerical investigations, too [91].

The main advantage of stellarators is that the twisting of the magnetic field lines, which is necessary to obtain stable plasma confinement, is achieved directly by external coils, without the need for a large plasma current. The latter, which is a key feature of tokamaks, constitutes a major source of free energy for macroscopic plasma instabilities like disruptions, which can cause damage to the plasma vessel due to enormous heat loads. Although the planning and construction of stellarators is much more complicated compared to tokamaks, they might provide a way to obtain fusion plasmas that are much easier to control and retain (macroscopically) stable up to relatively high values of  $\beta$ . Therefore, they are under investigation as an alternative to the tokamak concept.

In stellarators, the axisymmetry, which is inherent to tokamaks, has to be abandoned. This creates many new challenges for the construction and understanding of these devices. For simplicity, stellarators are usually constructed with a discrete rotational symmetry, so that the same magnetic field configuration is repeated several times before the torus closes (the LHD experiment for example has ten identical field periods, W7-X has five). In the first "naively" constructed machines, the complicated orbits of the trapped particles, which are inevitable in a stellarator, lead – in combination with collisions – to huge neoclassical transport. Historically, the main goal of stellarator theory was therefore the understanding and reduction of these neoclassical losses, and a lot of effort has been invested in the characterization and numerical optimization of the possible magnetic equilibria.

There are still several stellarator concepts under investigation, the most important ones being the Heliotron, which is realized in the LHD experiment in Japan, and the Helias configuration with the Wendelstein experiments at IPP.

As already mentioned, stellarator theory focused on neoclassical transport for a long time, since the other transport channels were dwarfed by the neoclassical contribution. An example of an up-to-date experiment is the Wendelstein 7-X (W7-X) stellarator, currently being built in Greifswald, which was designed with high numerical effort to minimize neoclassical transport [92]. With the reduction of the neoclassical contribution, the anomalous transport will become increasingly important, and will have to be taken into account for an overall minimization of heat and particle losses.

This insight and the new possibilities due to ever bigger supercomputers have sparked the interest in gyrokinetic simulations for stellarators. There exist some results from fluid simulations of stellarator edge turbulence [93, 94, 95]. Gyrokinetic results that can be found in the literature are usually limited to linear studies [53, 96, 97]; to date, only one other group is

## 7. ITG turbulence in stellarators

working on gyrokinetic stellarator turbulence, using the adiabatic electron approximation and an analytic model equilibrium for LHD [98, 99].

After extensive preparatory work [17], the development of the TRACER code to extract the relevant information out of magnetic equilibria, and linear investigations [100], all performed by Pavlos Xanthopoulos, GENE was used to produce some of the first results for ITG turbulence with realistic stellarator geometry for W7-X, published in [101]. These results were obtained in the adiabatic electron approximation and will be discussed in this chapter, along with equivalent results for a different W7-X equilibrium. Finally, the first two-species simulations for ITG turbulence in stellarators will be presented, introducing a new level of realism to the still very young field of gyrokinetic stellarator microturbulence.

### 7.1. Flux tube approximation for stellarators

Due to their truly three dimensional magnetic structure, stellarators are much more complicated than tokamaks, with various levels of trapping between the different maxima of the magnetic field and spatially separate populations of trapped particles in the different magnetic wells along a field line. To resolve these structures, the parallel resolution typically has to be increased drastically compared to tokamaks (approximately a factor of five in the case of W7-X), increasing the numerical effort involved in stellarator simulations substantially, since this fivefold increase of the resolution not only leads to five times the numerical effort to compute one time step, but also decreases the maximum time step significantly and thus increases the number of time steps that have to be computed to reach a saturated state and appropriate statistics.

A weak point of the flux tube approach for stellarators that is absent in tokamaks is the fact that different field lines on a given flux surface are not equivalent but give slightly different flux tubes. To obtain a general result for the flux surface, in principle the results from several flux tubes on that flux surface have to be averaged. However, given the enormous computational effort that is needed to obtain results even in this local approximation, it is at present not realistic to drop this simplification.

Another consequence of the absence of axisymmetry is that the magnetic field properties of stellarators are not always periodic after one poloidal turn, a condition that is needed for the parallel boundary condition (2.10). However, if an integer number of poloidal turns (in general greater than one) is used, the discrete stellarator symmetry can be exploited to construct a periodic flux tube for all rational  $q_0$  surfaces, i.e. arbitrarily close to any position inside the separatrix. Although in principle, simulations can be performed for any rational  $q_0$ , the computational effort increases with the number of poloidal turns, so that for practical reasons, flux surfaces with "favourable"  $q_0$  values will be chosen.

Another complication that occurs when the circular concentric flux surfaces used in the previous chapters are replaced by more complicated equilibria, is that it is not obvious that the most unstable mode for a given  $k_y$  is the one with  $k_x = 0$  (with the central point of the flux tube in parallel direction, i.e.  $g^{12} = 0$  at the outboard side). This is not stellarator specific, it already arises in flux tubes of strongly shaped tokamak equilibria, e.g. close to the X-point [102]. For large perpendicular box sizes (i.e. small minimum  $k_x, k_y$ ) and a large number of

radial modes, this does not pose a problem, but such resolutions are often not feasible. A small perpendicular box size leads to a crude discretization in  $k_x$ , and a small resolution to a low maximum  $k_x$ , which means that for practical resolutions, it is possible that the most unstable mode lies somewhere between two  $k_x$  retained in the simulation or even outside, so that the maximum growth rate can not be determined. One way to handle this problem at least for linear investigations are scans in  $k_x$ ; for the computation of the nonlinearity in turbulence simulations however, Fourier transforms have to be performed so that this trick is not possible, leaving an increase of the resolution as the only possibility to obtain correct results.

The TRACER code can read geometric information from all major stellarator (and tokamak) experiments, but for this chapter, only W7-X equilibria are used. The W7-X stellarator is still under construction and no experimental data concerning the achievable  $\beta$  values and the related MHD equilibria are available, therefore only vacuum equilibria (i.e.  $\beta = 0$ ) are used.

## 7.2. Adiabatic ITG turbulence in a standard equilibrium

The first results were obtained with a flux tube of the equilibrium hs5v10u [103], relatively close to the magnetic axis, with  $q_0 = 1$  and a global shear  $\hat{s} \approx 0$ , which means that the flux tube closes after one poloidal turn and is periodic. The details of the properties of this magnetic equilibrium and the geometric and magnetic structure of the flux tube can be found in [100].

For these first attempts to simulate stellarator microturbulence, the adiabatic electron approximation described in Sec. 2.9.2 was used, with the baseline parameters  $\omega_{Ti} = 18$ ,  $\omega_n = 0$ , with  $L_{\text{ref}} = R$  the major radius of the device. The temperatures were chosen to be  $T_e = T_i = T_{\text{ref}}$ , the perpendicular box size  $L_x = L_y = 64\rho_{\text{ref}}$  (with  $m_{\text{ref}} = m_i$ ). The numerical resolution was  $48 \times 32 \times 96$  points in direct space coordinates  $x$ ,  $y$  and  $z$ , and  $32 \times 8$  in  $v_{\parallel}$  and  $\mu$  direction.

As already indicated above, the linear physics of stellarators is much more complicated compared to the tokamak equilibria considered so far, with several spatially separated trapped fractions and various levels of trapping. This is reflected in a way more complicated parallel mode structures of the linear modes [100], but also in the increased number of unstable modes (for investigations in a drift wave model, see [104, 105]) and the related abundance of mode transitions. Fig. 7.1 shows the  $k_y$  spectrum of the growth rate and frequency of the most unstable mode and the ion heat flux spectrum of the corresponding nonlinear simulation. As observed in the tokamak cases considered previously, the maximum of the heat flux exhibits a spectral downshift with respect to the growth rate maximum. Furthermore, the figure shows a mode transition between different ion microinstabilities, which can be seen clearly in the linear plot by the sudden jump of the frequency, but also appears in the nonlinear heat flux spectrum in the form of a double peak, similar to the observations in the last chapter.

In the adiabatic electron approximation, the particle flux vanishes, leaving the (ion) heat flux (or heat diffusivity) as the most important integral quantity that can be accessed with the simulations. To explore its dependence on the temperature gradient, a nonlinear parameter

## 7. ITG turbulence in stellarators

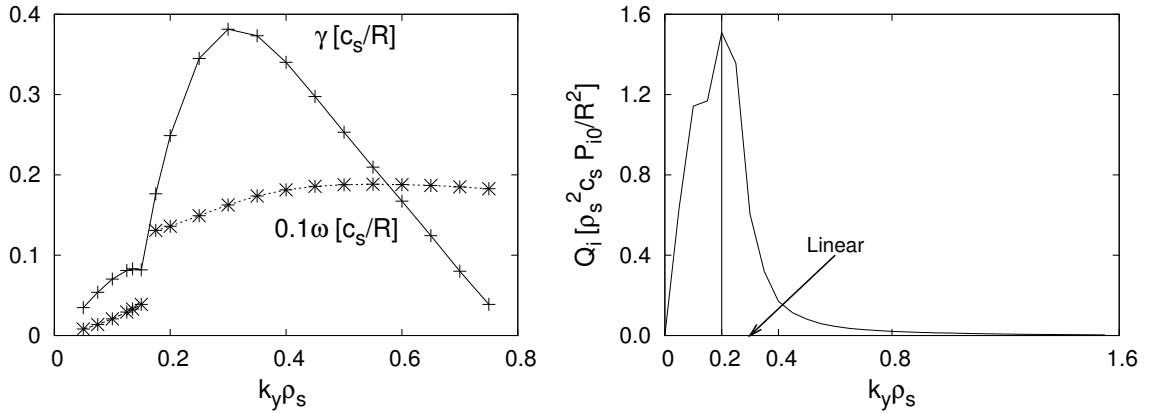


Figure 7.1.: Left: Dominant linear mode as function of  $k_y$ , showing a mode transition at 0.18. Right: Flux spectrum of the nonlinear simulation showing a discontinuity at the same position and indicating the position of the maximum growth rate.

scan has been performed; the thermal diffusivity is shown in left plot of Fig. 7.2 for a wide range of  $\omega_{Ti}$ . Given the threshold for linear instability, which is also marked in the plot, the scan reveals a nonlinear upshift of the critical gradient of about 25%, which, together with the observation of a significant zonal component in the electrostatic potential shown in the right plot of Fig. 7.2, can be identified as the Dimits shift [34] already known from tokamaks. This can be confirmed also by the zonal flow test, where the zonal flows are removed artificially, resulting in an increase of the ion heat flux of an order of magnitude (see [101]). An interesting

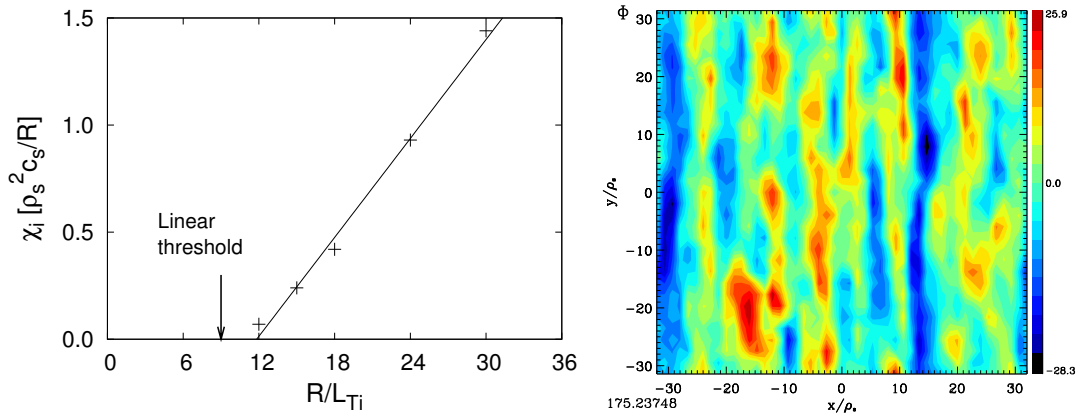


Figure 7.2.: Left: Scan of the heat diffusivity over the ion temperature gradient. Right: Contour plot of the electrostatic potential showing a significant zonal component.

difference with respect to equivalent tokamak simulations, which can be observed in Fig. 7.2 is that the heat diffusivity shows an offset-linear dependence on  $\omega_{Ti}$ , in contrast to the  $\hat{s} - \alpha$  tokamak case considered in [34] where the heat transport is offset-linear. This difference and the lack of experimental values for the achievable temperature gradients make a direct comparison between this W7-X configuration and tokamaks and general comments on the

anomalous transport in stellarators rather difficult. However, the parameters of the linear fit

$$\chi_i \approx C(\omega_{Ti} - \kappa_c) \frac{\rho^2 c_s}{R}, \quad (7.1)$$

are  $\kappa_c \approx 12$  and  $C \approx 0.08$ , implying that the transport level is well below typical tokamak levels for a relatively wide range in  $\omega_{Ti}$ .

The results of this section have been published in [101].

## 7.3. Adiabatic ITG turbulence in the high mirror configuration

The W7-X design features additional field coils to allow for the testing of different magnetic field configurations within the experimental constraints. Since the anomalous transport is sensitive, e.g., to shifts of the location of trapped particles with respect to regions with bad curvature, it is important to probe different magnetic configurations to understand the relevance of anomalous transport in this device. For the remainder of this chapter, a flux tube of the W7-X high mirror vacuum configuration with a mirror ratio of 10% will be used, i.e. a different configuration than the one used in the last section. The safety factor  $q_0$  for this configuration varies from  $q_0 \approx 1$  close to the magnetic axis to  $q_0 \approx 1.2$  close to last closed flux surface. With its discrete fivefold toroidal symmetry, the quasiperiodic boundary conditions in the parallel direction used in the flux tube approach would allow for treating just a single poloidal turn for both limits. However, the most interesting region is between these two values, at moderate values of the normalized minor radius, where the magnetic field structure is more pronounced and trapping and transport is expected to be bigger than close to the axis, but complications like magnetic islands and ergodic regions that occur close to the edge can be safely avoided. To limit the number of poloidal turns needed to have periodicity in the magnetic field, a  $q_0 = 1.1$  flux tube is chosen. Details of the magnetic geometry and the position of the flux tube are shown in Fig. 7.3, the geometric coefficients for the flux tube are shown in Fig. 7.4.

As in the previous section, the density gradient is fixed to zero, and in a first step, the electrons are again assumed to be adiabatic. The value of the magnetic shear  $\hat{s} = -0.11$  is prescribed by the W7-X high mirror equilibrium; the safety factor  $q_0 = 1.1$  together with the fivefold symmetry of W7-X requires that the simulation domain covers two poloidal (i.e. 2.2 toroidal) turns before the parallel boundary condition (2.10) can be applied. The other parameters that are used are  $T_e = T_i = T_{\text{ref}}$ ,  $L_x = 184\rho_s$ ,  $L_y = 125\rho_s$  ( $m_{\text{ref}} = m_i$ ). The macroscopic normalization length  $L_{\text{ref}}$  is now chosen to be  $a$ , the minor radius of the device. For a comparison to the last section, factors of the aspect ratio  $R/a \approx 12$  have to be taken into account. The numerical resolution used for the nonlinear simulations is  $96 \times 64 \times 256$  points in direct space  $x$ ,  $y$  and  $z$  directions (note that two poloidal turns have to be resolved in parallel direction), and  $48 \times 8$  points in  $v_{\parallel}$  and  $\mu$  directions, for linear runs the number of  $k_x$  can be reduced to three (corresponding to six poloidal turns) or even one (i.e. two poloidal turns).

## 7. ITG turbulence in stellarators

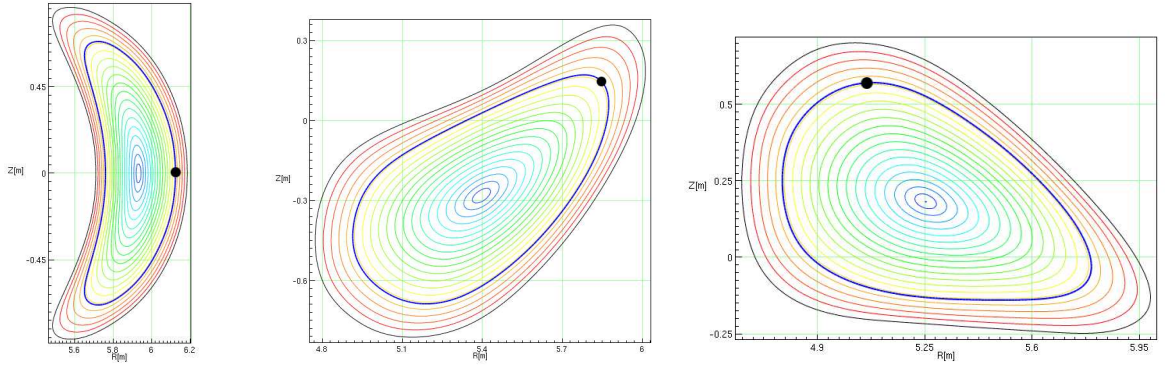


Figure 7.3.: Cross sections of the magnetic flux surfaces of the W7-X high mirror equilibrium for  $z = 0, \pi/4$  and  $\pi/2$ . The blue line marks the flux surface under consideration, the black dot denotes the position of the flux tube.

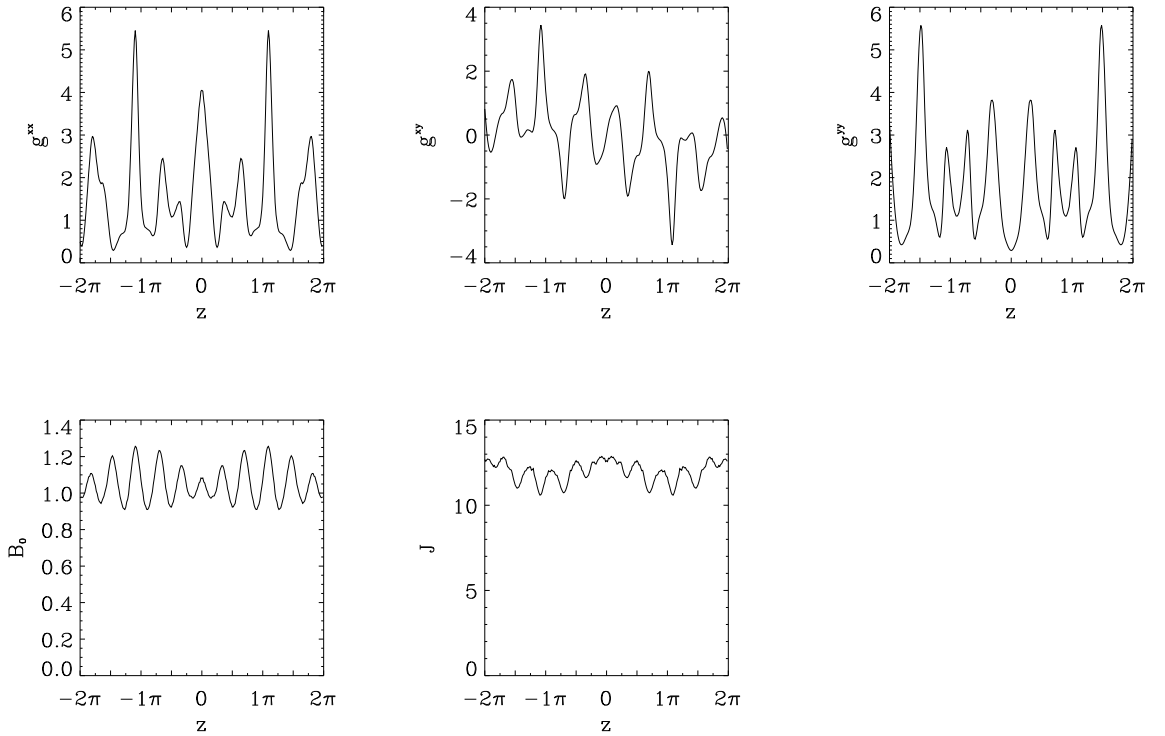


Figure 7.4.: Some geometric and magnetic characteristics for the flux tube of the high mirror equilibrium.

A scan with the eigenvalue solver reveals that even in this adiabatic case, many modes are destabilized simultaneously. The left plot of Fig. 7.5 shows a  $k_y$  scan of the most unstable modes for an example with temperature gradient  $\omega_{Ti} = 3$ . In order to limit the computation time to reasonable values, the eigenvalue solver was set to compute only the ten most unstable

### 7.3. Adiabatic ITG turbulence in the high mirror configuration

modes, but it is obvious that there are even more. Since a proper identification and tracking of the different subdominant eigenmodes is very difficult and would provide probably only little insight, the coloring of the eigenvalues only shows their ordering with respect to the growth rate. The complexity of this spectrum is significantly higher than that of tokamaks, where (as seen in Chap. 6) usually only one or two modes are unstable at a time.

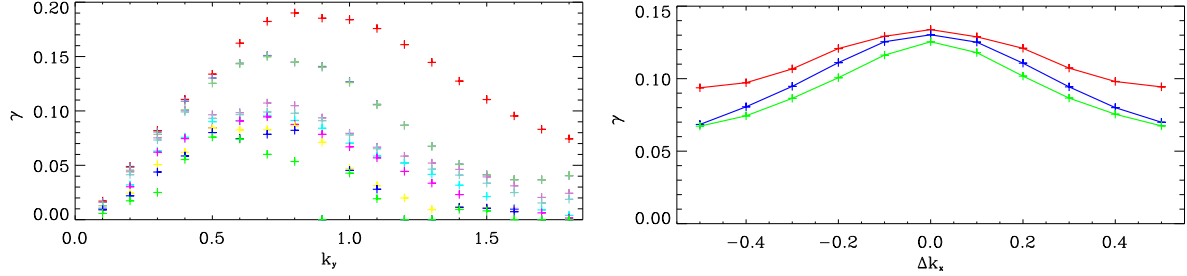


Figure 7.5.: Growth rates and frequencies of the most unstable modes for  $\omega_{Ti} = 3$  and adiabatic electrons. The  $k_y$  scan is performed with  $k_x = 0$ , the  $k_x$  scan with  $k_y = 0.5$ .

As mentioned above, given the freedom of choice for the parallel center of the flux tube and the finite resolution, it is not clear that the most unstable mode has  $k_x = 0$ . This has to be tested explicitly, which has been done in the right plot of Fig. 7.5. The plot shows that due to the symmetry of the geometric coefficients with respect to  $z = 0$  (see Fig. 7.4), the growth rate spectrum is symmetric with respect to  $k_x = 0$ . Fortunately, the maximum is at  $k_x = 0$ , indicating an advantageous choice for the center of the flux tube. Since  $k_x = 0$  is established as the most unstable mode, the following linear investigations will focus on that mode; this finding also implies that the maximum is always contained in the nonlinear simulations, independent of  $L_x$ .

In order to understand how such a complicated spectrum evolves with increasing drive, the same  $k_y$  scan was performed for different values of  $\omega_{Ti}$ . Fig. 7.6 shows the  $k_y$  spectra of the growth rates and frequencies of the ten most unstable modes for ion temperature gradients  $\omega_{Ti} = 1, 2, 3, 4$ . It is obvious that the total number of unstable modes increases with increasing  $\omega_{Ti}$  and becomes significantly larger than ten.

For  $\omega_{Ti} = 1$ , the number of unstable modes is such that an identification of the modes by their frequencies would still be possible. For larger gradients, however, more and more modes (or better families of modes) appear, with different frequency ranges and  $k_y$  dependencies in the growth rate spectrum. For these cases, a labelling of the modes would be very difficult or even impossible (see Chap.4), since it can be seen from the plot that in several cases the growth rates and frequencies of pairs of eigenvalues come very close, possibly indicating the presence of exceptional points in the  $(k_y, \omega_{Ti})$  plane. Since a verification of the existence non-Hermitian degeneracies in the parameter range considered here will probably not lead to relevant insights, this conjecture is not pursued further – given the abundance of linear microinstabilities, it is not expected that the merging of two (subdominant) modes would lead to significant effects.

One peculiarity for the spectra with  $\omega_{Ti} \geq 2$  is that below the dominant mode (red), the two modes with the second and third biggest growth rates have almost identical properties, to the

## 7. ITG turbulence in stellarators

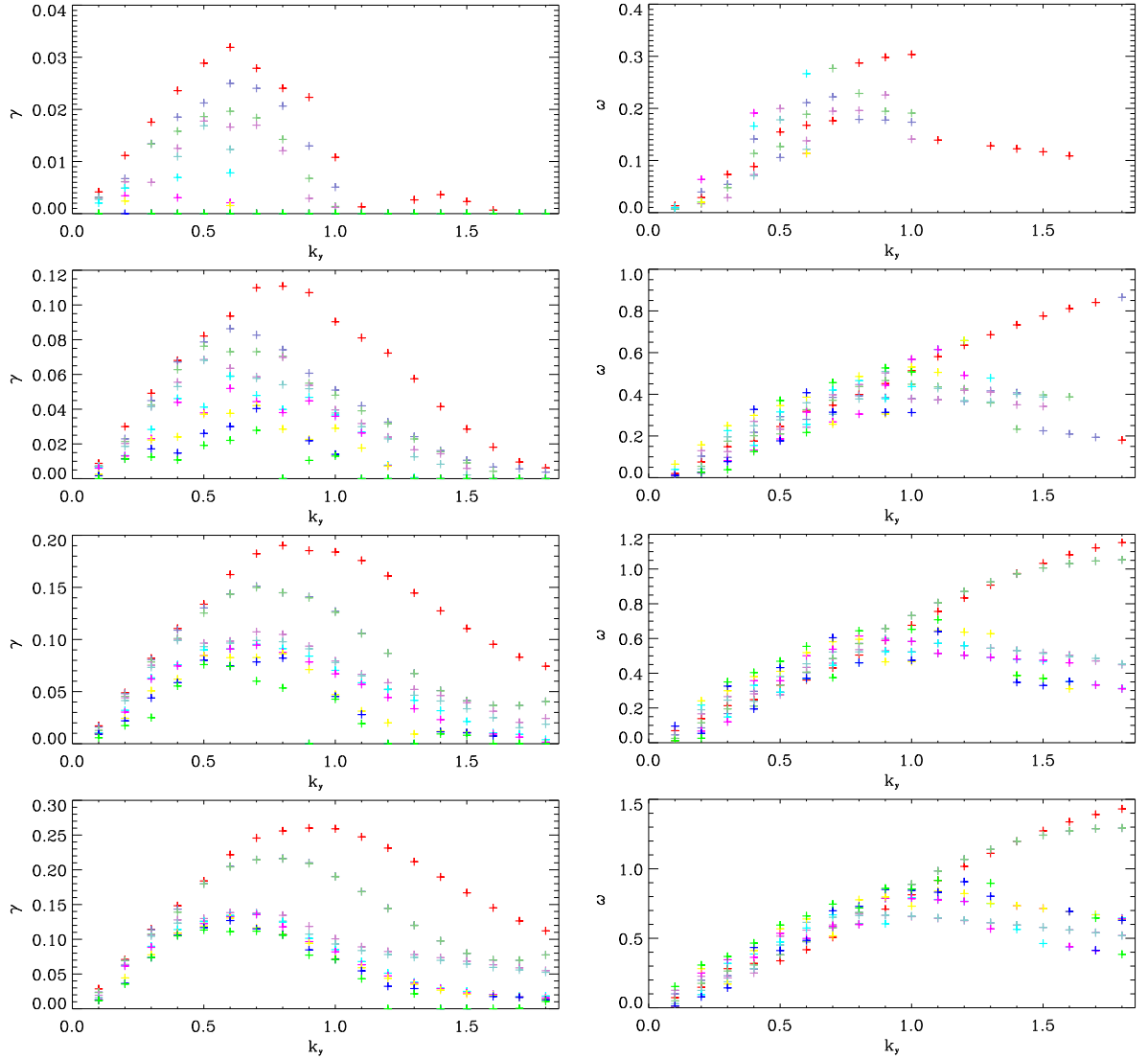


Figure 7.6.: Growth rates and corresponding frequencies of the most unstable modes for  $\omega_{Ti} = 1, 2, 3, 4$  (from top). The colors show the ordering with respect to the growth rate.

extent that they can hardly be distinguished in Fig. 7.6. The parallel structure of the quasilinear radial heat transport computed from the four most unstable modes for  $\omega_{Ti} = 3$  is shown in Fig. 7.7. The most unstable mode has one clear peak at the outboard side; the second and third most unstable modes, which both have two clear peaks close to the ends of the flux tube (i.e. almost outboard side) again exhibit striking similarities, but are mirrored with respect to  $z = 0$ . The fourth most unstable and even more subdominant modes have less pronounced global structures, but show a multitude of peaks of almost equal height along the field line. Although Fig. 7.7 only shows the values for  $\omega_{Ti} = 3$  and  $k_y = 0.6$ , the parallel mode structures of corresponding modes stay virtually the same also for other  $k_y$  and  $\omega_{Ti}$ ; in cases where the identification of "corresponding" modes due to the eigenvalue becomes difficult (e.g. for low

### 7.3. Adiabatic ITG turbulence in the high mirror configuration

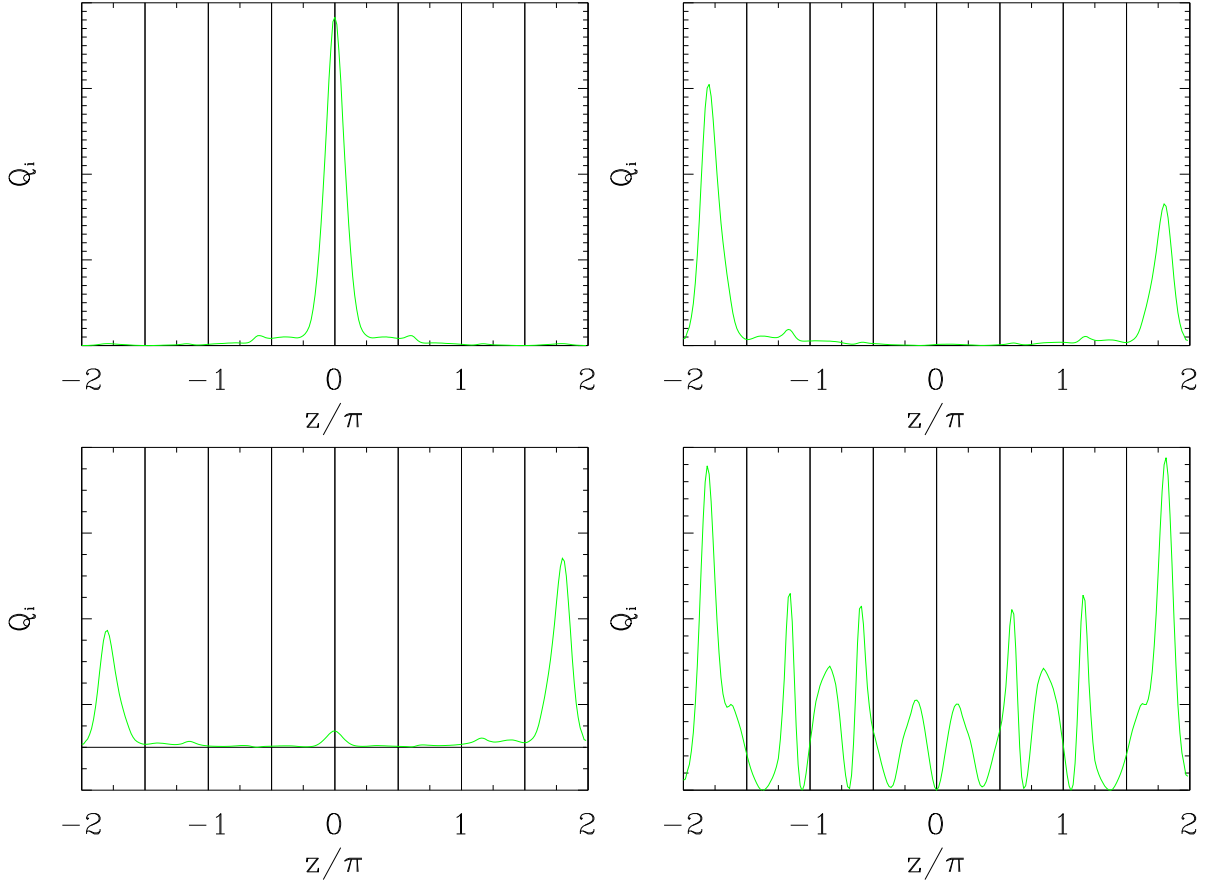


Figure 7.7.: Parallel mode structure of the four most unstable modes (decreasing growth rate from left to right and top to bottom) for  $\omega_{Ti} = 3$  and  $k_y = 0.6$  (compare Fig. 7.6).

$k_y$ ), the parallel mode structure can even be used to identify corresponding modes that belong together.

A nonlinear scan of the  $\omega_{Ti}$  values considered above is shown in the left plot of Fig. 7.8. Again, the ion heat diffusivity scales approximately linear with the ion temperature gradient. However, the values for the diffusivity are considerably higher than in the last section, the fit parameters of the model (7.1) in the corresponding  $R$  normalization are  $\kappa_c = 12 * 0.79 = 9.5$  for the critical gradient and  $C = 1.87$  for the slope. This shows that the profile stiffness due to anomalous transport, which is related  $C$ , is quite sensitive to the specific magnetic configuration and the exact position of the flux tube, making general statements about the confinement properties W7-X stellarator difficult, but indicating that the level of anomalous transport can be manipulated significantly by changing the magnetic configuration. The linear scan of the growth rate at the approximate wavenumber of the maximum,  $k_y = 0.6$ , is depicted in the left plot of Fig. 7.8. The computation of the linear critical gradient of  $\omega_{Ti} = 0.47$  (compared to the nonlinear value of 0.79) reveals the presence of a nonlinear upshift, which can be attributed to a zonal flow induced Dimits shift, as in the last section.

## 7. ITG turbulence in stellarators

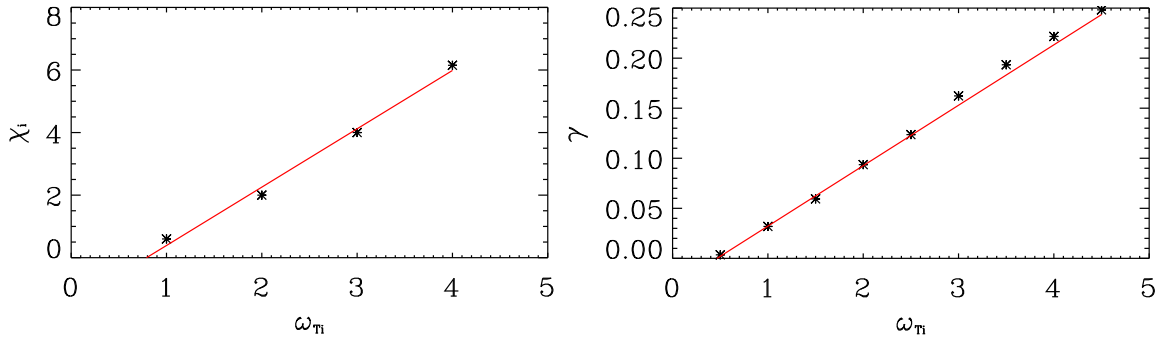


Figure 7.8.: Left: Ion heat diffusivity (in  $\rho_s^2 c_s/a$ ) as a function of the ion temperature gradient.  
Right: Linear growth rate for the dominant  $k_y = 0.6$  mode.

## 7.4. Stellarator turbulence with kinetic electrons

Finally, the adiabatic electron approximation is dropped and the first two species turbulence simulations in a realistic stellarator geometry are presented. This new level of realism increases the numerical effort significantly with respect to the adiabatic case, with each nonlinear simulation presented in this section consuming about 70,000 CPU hours on a BlueGene/P. The numerical parameters are the same as in the previous section, except that the electrons are now treated gyrokinetically with vanishing temperature gradient,  $\omega_{Te} = 0$ , and a reduced mass ratio  $m_i = m_{\text{ref}} = 400m_e$ . Although a vacuum magnetic equilibrium is used,  $\beta$  is set to a small but finite value of 0.1% to avoid (unphysical) electrostatic shear Alfvén waves, which due to their high eigenfrequency would reduce the (already strict) linear time step limit even further.

A  $k_y$  spectrum of eigenvalues of the ten most unstable modes is shown in Fig. 7.9. As in the adiabatic case, the number of unstable modes is very large, making the tracking of the modes over the full  $k_y$  range is very difficult. The maximum growth rates for the different gradients and the range of frequencies is also quite similar compared to the one species case. The most obvious change is that the spectrum of the dominant mode in the medium  $k_y$  range for  $\omega_{Ti} \geq 2$ , which can be identified with the equivalent mode of Fig. 7.9 by their parallel structure, is compressed and the maximum is shifted to lower  $k_y$ . For higher ion temperature gradients, there seem to be two families of modes, one which is stabilized at  $k_y \approx 1$ , and a second one extending (at low growth rates) up to the highest  $k_y$ . All modes of Fig. 7.7 can also be identified in the nonlinear spectra, the second and third most unstable mode with almost equal growth rates reappearing for  $\omega_{Ti} = 4$ .

The results of a nonlinear scan similar to the one in the last section are shown in Fig. 7.10. The ion heat diffusivity is increased considerably by the full gyrokinetic treatment of the electrons. The nonlinear critical gradient is in this case 0.63 (7.6) in  $a$  ( $R$ ) units and the slope in Eq. (7.1) is 3.44, predicting a significantly stiffer ion temperature profile than the simulations with adiabatic electrons. Another important difference is the absence of a Dimits shift. The linear results shown in the right plot of Fig. 7.10 indicate a linear critical gradient of 0.64, almost identical to the nonlinear result.

The ratio of the electron and ion heat flux is shown in Fig. 7.11. As is expected because

#### 7.4. Stellarator turbulence with kinetic electrons

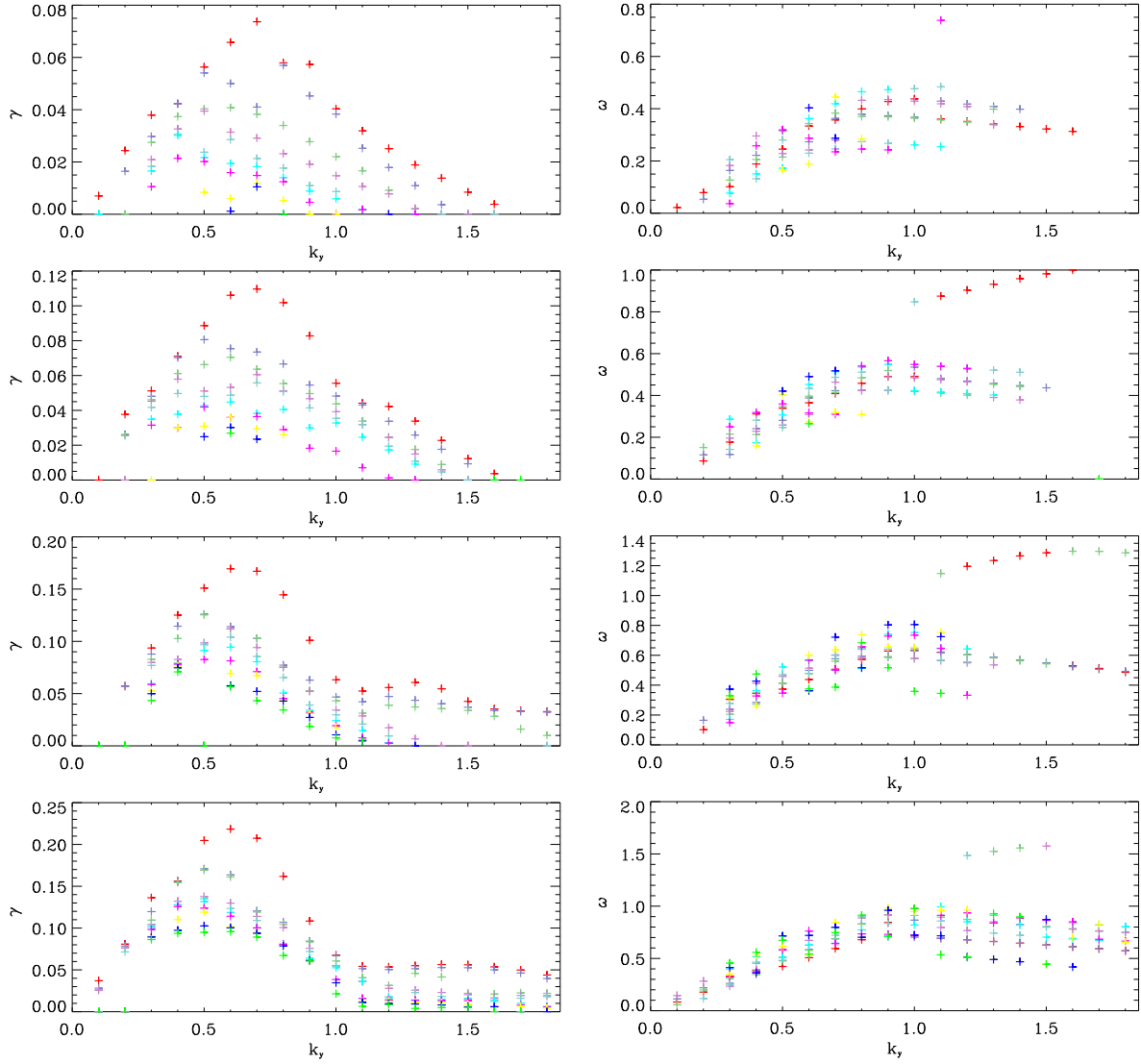


Figure 7.9.: Growth rates and corresponding frequencies of the most unstable modes for  $\omega_{Ti} = 1.5, 2, 3, 4$  (from top) for the two species case. Again, the colors show the ordering with respect to the growth rate.

of the vanishing electron temperature gradient, the heat flux caused by the electrons is very small compared to the ion contribution. The ratio is almost independent of the ion temperature gradient, with an average of  $\langle Q_e/Q_i \rangle = 0.047$ . The particle flux shows a very similar behaviour to the electron heat flux, the average ratio of particle and ion heat transport being  $\langle \Gamma/Q_i \rangle = 0.041$ .

Finally, some of the features of the simulations with adiabatic and gyrokinetic electrons are compared, on the basis of the  $\omega_{Ti} = 3$  case. The parallel structure of the ion heat flux of the two simulations is shown in the left plot of Fig. 7.12. The positions of the peaks along the field line are the same for both cases, as was already indicated by the linear results. The three peaks in the nonlinear simulations reflect in both cases the contributions from the

## 7. ITG turbulence in stellarators

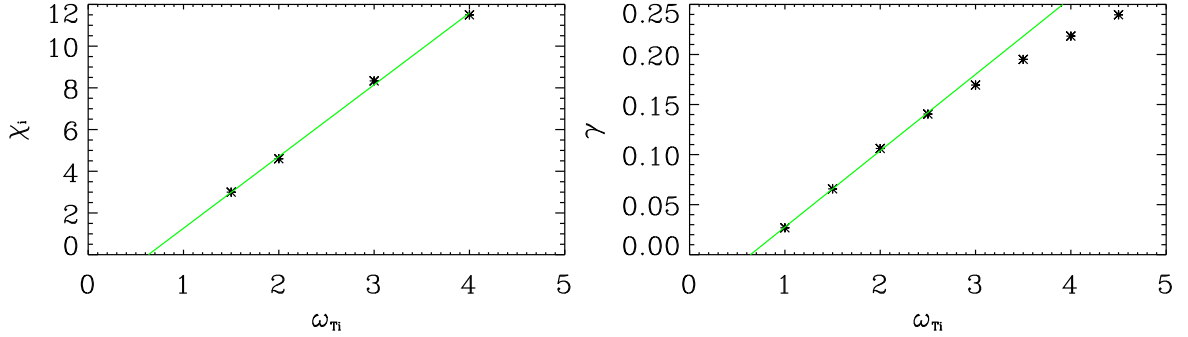


Figure 7.10.: Left: Ion heat diffusivity as a function of the ion temperature gradient. Right: Linear growth rate for the  $k_y = 0.6$  mode.

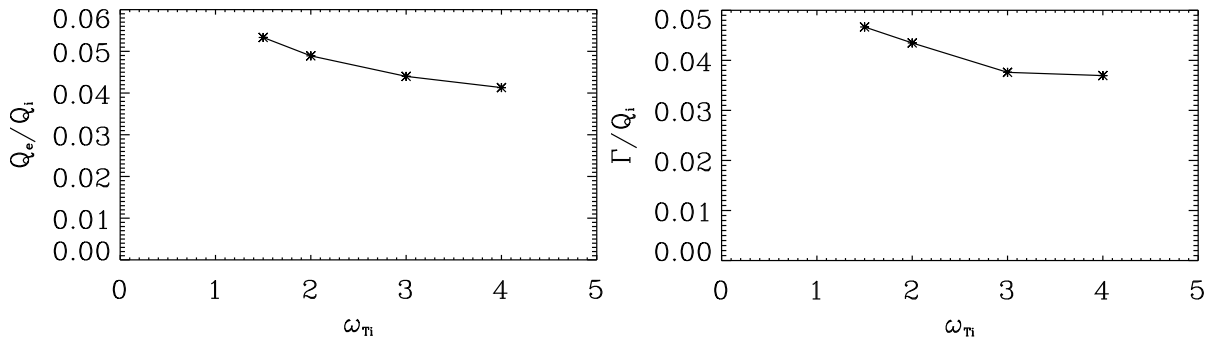


Figure 7.11.: Ratio of the heat fluxes of the two species (left) and of the particle and ion heat flux (right) as a function of the ion temperature gradient.

three most unstable modes displayed in Fig. 7.7. For the adiabatic case (red), the peaks are very pronounced and the regions between the peaks have a very low value of transport. With gyrokinetic electrons (green), the peaks are still clearly discernible but the area between the peaks also contributes significantly, so that the overall transport is higher. The right plot of Fig. 7.12 shows the  $k_y$  spectra of the ion heat transport of the two simulations. As usual, the maxima of the transport spectra are at significantly lower  $k_y$  than the maxima of the linear growth rate spectra. Nevertheless, linear result that the spectrum of the adiabatic case peaks at higher  $k_y$  and is broader than the spectrum for the fully gyrokinetic case, also holds for the nonlinear transport spectra.

Fig. 7.13 shows contour plots of the electrostatic potential and the perturbed density at  $z = 0$ , i.e. the transport maximum. In line with the observations concerning the Dimits shift, the simulation with adiabatic electrons shows a considerable zonal component in the electrostatic potential, in contrast to the two species simulation. Furthermore, it is obvious that the turbulent structures are significantly bigger in the simulation with gyrokinetic electrons, confirming the results of the transport spectra.

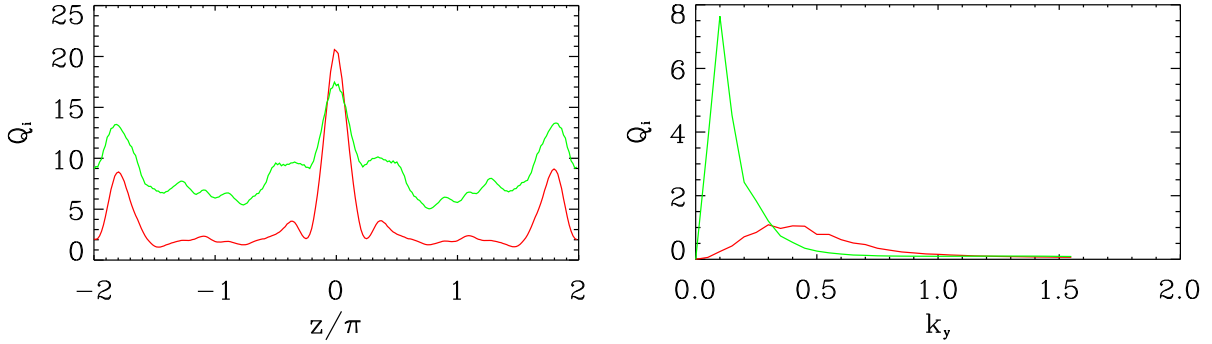


Figure 7.12.: Left: Parallel distribution of the ion heat flux for simulations with adiabatic (red) and fully gyrokinetic (green) electrons at  $a/L_{Ti} = 3$ . Right: The corresponding transport spectra.

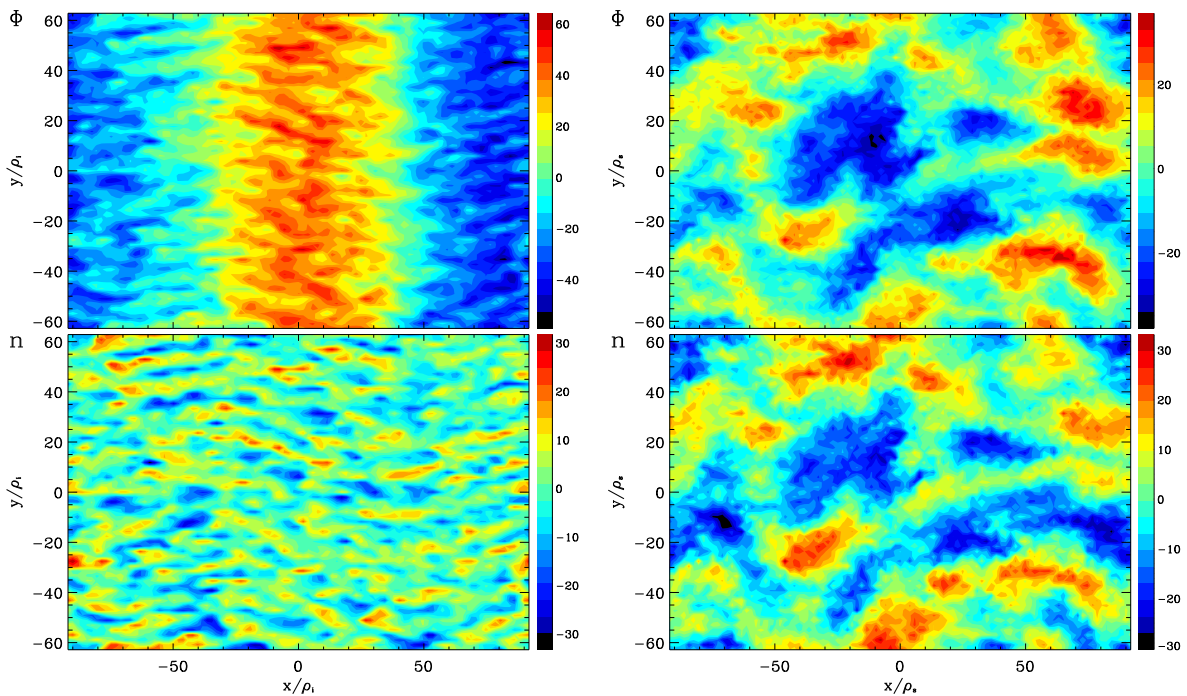


Figure 7.13.: Left: Contour of the electrostatic potential and perturbed density at  $z = 0$  and for  $a/L_{Ti} = 3$ . Right: The corresponding plots for the simulation with gyrokinetic electrons.

## 7.5. Summary

In this chapter, it has been demonstrated that with the interface to the TRACER code, the improvements on the hardware side and the generalization and optimization efforts of the last few years, GENE is now capable of performing gyrokinetic simulations of stellarator microturbulence in realistic geometry, as one of very few codes in the world. With recent improvements of the SLEPc library, it is possible to compute the numerous microinstabilities

## *7. ITG turbulence in stellarators*

that occur in a stellarator, improving the understanding of the linear physics of stellarators. Simulations of stellarator microturbulence in the adiabatic electron approximation can now be performed with reasonable effort, but even two species simulations are possible, as has been shown in the last section.

The results for pure ITG turbulence in the W7-X stellarator showed that the more complex geometry increases the number of microinstabilities and mode transitions compared to conventional tokamak cases. As expected, the mode structure and also the parallel dependency of the transport fluxes reflect the more complicated geometric properties of the corresponding flux tube. The two different magnetic configurations of W7-X, that were analyzed in the adiabatic electron approximation in this chapter, showed significant variations in the level of anomalous heat transport, which implies that it might be possible to significantly influence the anomalous transport by a variation of the magnetic configuration. The comparison of the one and two species simulations for the high mirror configuration showed that while some linear and nonlinear properties are well represented in the adiabatic electron approximation, zonal flows are much more pronounced compared to the two species case and the profile stiffness is underestimated significantly.

# 8. Conclusions

In the course of this PhD project, the gyrokinetic plasma turbulence code GENE has been extended by important physical and numerical features. A fundamental modification of the representation together with significant optimization and parallelization efforts improved the robustness and performance and helped to make GENE one of the most advanced codes in this field worldwide. This enhanced simulation code was used for the numerical investigations of gyrokinetic microinstabilities and anomalous transport in fusion plasmas presented in this work, contributing to an understanding of several aspects of this very important topic in magnetic confinement fusion.

Below, only a short overview of the main results of this thesis is given – more detailed summaries can be found at the ends of the respective chapters.

## 8.1. Summary

### Code development

The gyrokinetic equations in the local  $\delta f$  approximation have been presented in a form that is suitable for a numerical treatment. Compared to previous versions, the equations have been extended by a linearized Landau-Boltzmann collision operator, are formulated in general geometry and include additional physical effects like the dependence on the pressure gradient, compiling different aspects in a single coherent presentation. Furthermore, the normalization has been generalized to allow for an arbitrary number of species. The extensions and generalizations of the equations have been implemented in the GENE code, including a transition from a direct space to a Fourier space representation of the radial coordinate. Together with improved numerical schemes (e.g. for the time stepping), which allow for faster, more robust computations, completely new features like an interface to an eigenvalue solver have been implemented. Many of these developments, like the more sophisticated collision operator or the eigenvalue solver, are in this form presently only available in GENE, allowing for completely new numerical investigations of plasma microturbulence and the underlying microinstabilities.

### Linear physics

The application of the newly implemented eigenvalue solver lead to the discovery of non-Hermitian degeneracies in linear gyrokinetics. These degeneracies, which correspond to non-trivial topological structures of the eigenvalue surfaces in parameter space, connect microinstabilities that were previously considered to be independent. This result explains the different regimes that are found in the usual one dimensional parameter scans of linear mode transitions; furthermore, it reveals fundamental shortcomings in the traditional nomenclature of microinstabilities, since pairs of all major types of microinstabilities have been found to be connected.

## 8. Conclusions

The structure of the linear operator and the sources of non-Hemiticity have been discussed in detail, and analogies to quantum mechanics and other fields, where non-Hermitian degeneracies occur, have been pointed out.

### Plasma microturbulence in tokamaks

By means of nonlinear investigations of pure, i.e. idealized, TEM turbulence, it was shown that zonal flows, which are crucial for the saturation of the well studied ITG turbulence, are often not essential in the TEM case. Instead, a detailed and rather fundamental investigation of the statistical properties of the  $\vec{E} \times \vec{B}$  nonlinearity suggests that the latter can be approximated by a simple diffusion term, which explains the resemblance of linear and nonlinear results and numerically confirms, for the first time, longstanding predictions obtained in the context of Dupree's resonance broadening theory and renormalized turbulence theories. These results were also used to justify a quasilinear transport model that has been applied successfully to pure TEM turbulence in previous works.

In addition, the more realistic scenario of similar temperature gradients for electrons and ions was considered. The transitions between TEM and ITG turbulence in a parameter range where the two underlying microinstabilities are clearly distinguishable were studied in detail, revealing that for a wide range of parameters, the two kinds of turbulence coexist on different spatial scales and are in some cases even observable at the same wavenumber. The nonlinear TEM-ITG transitions were shown to largely match the linear predictions about the dominant mode, allowing for a simple quasilinear description based on eigenvalue computations with a single, "typical"  $k_y$ . This description is (in contrast to previous models based on initial value calculations) free of discontinuities and was shown to reliably describe the basic features of the transition, in particular the mechanisms that lead to zero particle transport. Because the model allows for high dimensional parameter scans, it offers a way to understand the parameter dependencies of the experimentally relevant hypersurface of zero particle transport, which has often been probed only pointwise in previous works. As an example, the dependence of the TEM-ITG system on the collision frequency was studied.

### Plasma microturbulence in the W7-X stellarator

The GENE code was used to perform some of the first simulations of ITG turbulence with adiabatic electrons in the W7-X stellarator and the first simulations with a full gyrokinetic treatment of electrons and ions for any stellarator, demonstrating the advances in computational gyrokinetics. For these simulations, realistic geometric information extracted from MHD equilibria was used, in contrast to comparable studies for other stellarators based on analytic model equilibria. Several results like the gradient dependence of the ion heat transport have been discussed, suggesting a significant potential of non-axisymmetric devices for a systematic control of turbulent transport.

All in all, the results demonstrate how – supported by the increasing computation power available – extensions and improvements of the simulation code have been used to significantly push the limits of numerical investigations of plasma turbulence, leading to progress

in the understanding of basic features, but also opening the possibilities for more realistic simulations and comparisons to experiments.

## 8.2. Outlook

As more effects are included in the simulations and the understanding of the various effects increases, it will become more and more feasible to not only explain the phenomena that occur in plasma microturbulence, but to compute realistic experimental scenarios including all relevant effects, thus turning to truly predictive simulations.

A major step to overcome the difficulties of comparing simulations and experiments that have been discussed in Sec. 6.4 would be the transition from a gradient driven to a flux driven simulation code. A first step in this direction is to drop the assumption of locality and to allow for radial variations of the equilibrium quantities. With increasing computation power, it will eventually even become possible to drop the locality assumption in the binormal direction, which will remove the limitations of the flux tube approach for three dimensional equilibria, facilitating predictions especially for stellarators.

At present, many different aspects of the fusion plasma are treated with different numerical codes and descriptions. There are, e.g., MHD codes for the analysis of the macroscopic plasma stability and the reconstruction of magnetic equilibria, gyrofluid codes to describe the plasma edge, particle codes for the computation of neoclassical transport, and gyrokinetic codes for core turbulence.

There are, however, physical phenomena that do not fit in these categories and are not described by any of the models or codes described above. One such phenomenon is the experimentally observed transition between the low (L) and high confinement (H) regime, a bifurcation related to the dynamics at the plasma edge. Despite its significance for confinement, the L-H transition (or the generation of radial transport barriers in general) has not yet been reproduced in simulations, and it is assumed that a more general description, e.g. taking into account the interaction between MHD and microturbulence, is necessary to achieve this – and thus to provide a basis for detailed studies and eventually an understanding of this important effect.

The long term goal of computational fusion research is a complete numerical description of all relevant processes in a fusion device (i.e., a "numerical tokamak" or a "numerical stellarator"), which allows for an optimization of all parameters – including the ones that are hard or impossible to access experimentally, like the size and shape of the fusion device. To achieve this kind of universality, it is necessary to combine the different aspects described above and to extend, integrate or couple several of the existing developments.

With constant effort and progress on different levels, theoretical and computational plasma physics will be able to make important contributions to design and finally build a working fusion power plant, which could help to satisfy the energy requirements of the future.

## *8. Conclusions*

# A. Integrals for the field equations

The gyroaverage of a scalar field can be written as

$$\begin{aligned}\langle A(X) \rangle &= \frac{1}{2\pi} \int_0^{2\pi} A(\vec{X} + \vec{r}) d\theta = \frac{1}{2\pi} \int_0^{2\pi} \sum_{k_x, k_y} A(k_x, k_y) e^{i\vec{k}_\perp \cdot (\vec{X} + \vec{r})} d\theta \\ &= \sum_{k_x, k_y} A(k_x, k_y) e^{i\vec{k}_\perp \cdot \vec{X}} \frac{1}{2\pi} \int_0^{2\pi} e^{i\vec{k}_\perp \cdot \vec{r}} d\theta.\end{aligned}$$

With the expressions from Sec. 2.2.2, the scalar product of  $\vec{r}$  and  $\vec{k}$  is  $\vec{k}_\perp \cdot \vec{r} = k_\perp \rho \cos(\theta - \theta_0)$  (with  $k_\perp = \sqrt{\vec{k}_\perp \cdot \vec{k}_\perp}$ ) where  $\theta_0$  is the angle between  $\vec{k}_\perp$  and  $\vec{r}(\theta = 0) = \vec{e}_x$ . Since the whole ( $2\pi$  periodic) expression is integrated over one period, the integral boundaries can be shifted and the integral transformed

$$\frac{1}{2\pi} \int_0^{2\pi} \vec{a}(\theta) e^{i\vec{k}_\perp \cdot \vec{r}(\theta)} d\theta = \frac{1}{2\pi} \int_0^{2\pi} \vec{a}(\theta + \theta_0) e^{ik_\perp \rho \cos(\theta')} d\theta'. \quad (\text{A.1})$$

For  $a(\theta) = 1$ , this is simply

$$\frac{1}{2\pi} \int_0^{2\pi} e^{ik_\perp \rho \cos(\theta')} d\theta' = J_0(k_\perp \rho) \quad \text{with} \quad J_n(z) = \frac{i^{-n}}{\pi} \int_0^\pi e^{iz \cos \theta} \cos(n\theta) d\theta$$

the definition for the Bessel functions and  $J_0(-z) = J_0(z)$ . The gyroaverage can therefore be written

$$\bar{A}(X) = \sum_{k_x, k_y} A(k_x, k_y) e^{i\vec{k}_\perp \cdot \vec{X}} J_0(\rho k_\perp),$$

i.e. if the perpendicular directions are represented in Fourier space, the gyroaveraging is a mere multiplication with the zeroth order Bessel function  $J_0$ . Similarly

$$\begin{aligned}\langle \bar{A}(\vec{x} - \vec{r}) \rangle &= \frac{1}{2\pi} \int_0^{2\pi} \frac{1}{2\pi} \int_0^{2\pi} A(\vec{x} - \vec{r} + \vec{r}') d\theta d\theta' \\ &= \frac{1}{4\pi^2} \int_0^{2\pi} \int_0^{2\pi} \sum_{k_x, k_y} A(k_x, k_y) e^{i\vec{k}_\perp \cdot (\vec{X} - \vec{r} + \vec{r}')} d\theta d\theta' \\ &= \sum_{k_x, k_y} A(k_x, k_y) e^{i\vec{k}_\perp \cdot \vec{X}} J_0^2(\rho k_\perp).\end{aligned}$$

### A. Integrals for the field equations

In the calculation of the integrals appearing in the charge density, the fields and  $J_0$  do not depend on  $v_{\parallel}$ , inserting

$$\begin{aligned} \int_{-\infty}^{\infty} F_{0j} dv_{\parallel} &= \left( \frac{m_j}{2\pi T_{0j}} \right)^{\frac{3}{2}} n_{0j} e^{-\frac{\mu B_0}{T_{0j}}} \int_{-\infty}^{\infty} e^{-\frac{m_j v_{\parallel}^2}{2T_{0j}}} dv_{\parallel} = \left( \frac{m_j}{2\pi T_{0j}} \right)^{\frac{3}{2}} n_{0j} e^{-\frac{\mu B_0}{T_{0j}}} \sqrt{\frac{2\pi T_{0j}}{m_j}} \\ &= \frac{m_j}{2\pi T_{0j}} n_{0j} e^{-\frac{\mu B_0}{T_{0j}}} \end{aligned}$$

and taking into account that the fields themselves (after the gyroaveraging has been expressed by  $J_0$  factors) do not depend on the velocity space leaves

$$\begin{aligned} \int 2\pi J_v \langle \bar{\phi}(\vec{x} - \vec{r}) \rangle F_0 dv_{\parallel} d\mu &= \frac{B_0}{T_{0j}} n_{0j} \sum_{k_x, k_y} e^{i\vec{k}_{\perp} \cdot \vec{x}} \phi(k_x, k_y) \int_0^{\infty} e^{-\frac{\mu B_0}{T_{0j}}} J_0^2(\rho k_{\perp}) d\mu \\ &= n_{0j} \sum_{k_x, k_y} e^{i\vec{k}_{\perp} \cdot \vec{x}} \phi(k_x, k_y) \int_0^{\infty} e^{-\mu'} J_0^2(\lambda) d\mu' \\ \int 2\pi J_v \mu \langle \bar{B}_{1\parallel}(\vec{x} - \vec{r}) \rangle F_0 dv_{\parallel} d\mu &= \frac{B_0}{T_{0j}} n_{0j} \sum_{k_x, k_y} e^{i\vec{k}_{\perp} \cdot \vec{x}} B_{1\parallel}(k_x, k_y) \int_0^{\infty} e^{-\frac{\mu B_0}{T_{0j}}} \mu I_1(\rho k_{\perp}) J_0(\rho k_{\perp}) d\mu \\ &= \frac{T_{0j}}{B_0} n_{0j} \sum_{k_x, k_y} e^{i\vec{k}_{\perp} \cdot \vec{x}} B_{1\parallel}(k_x, k_y) \int_0^{\infty} e^{-\mu'} \mu' I_1(\lambda) J_0(\lambda) d\mu' \end{aligned}$$

after the coordinate transformation  $\mu' = \frac{B_0}{T_{0j}} \mu$ , implying  $\lambda = \rho k_{\perp} = \frac{v_{\perp}}{\Omega} k_{\perp} = \sqrt{\frac{2B_0\mu}{m} \frac{k_{\perp}}{\Omega}} = k_{\perp} \frac{v_T}{\Omega} \sqrt{\mu'}$ . The remaining integrals can be solved (e.g. with Mathematica):

$$\begin{aligned} \int_0^{\infty} e^{-\mu'} J_0^2(\lambda) d\mu' &= \Gamma_0(b) \\ \int_0^{\infty} e^{-\mu'} \frac{2\mu'}{\lambda} J_1(\lambda) J_0(\lambda) d\mu' &= \Delta(b) \end{aligned}$$

with  $\Gamma_n(x) = e^{-x} \hat{I}_n(x)$ ,  $\Delta(x) = \Gamma_0(x) - \Gamma_1(x) = \frac{\hat{I}_0(x) - \hat{I}_1(x)}{e^x}$ ,  $\hat{I}_n$  the modified Bessel functions and  $b = k_{\perp}^2 \frac{v_T^2}{2\Omega^2}$ .

For the integrals for  $\vec{j}_{\perp}$ , the relevant gyroaverages are of the form

$$\langle \vec{v}_{\perp} \bar{A}(\vec{x} - \vec{r}) \rangle = \frac{1}{2\pi} \int_0^{2\pi} \vec{v}_{\perp} \bar{A}(\vec{x} - \vec{r}) d\theta = \sum_{k_x, k_y} \bar{A}(k_x, k_y) e^{i\vec{k}_{\perp} \cdot \vec{x}} \frac{1}{2\pi} \int_0^{2\pi} \vec{v}_{\perp} e^{-i\vec{k}_{\perp} \cdot \vec{r}} d\theta.$$

Equation A.1 with now  $\vec{a}(\theta) = \vec{v}_{\perp}$  gives

$$\begin{aligned} \frac{1}{2\pi} \int_0^{2\pi} v_{\perp} (-\sin(\theta' + \theta_0) \vec{e}_x + \cos(\theta' + \theta_0) \vec{e}_y) e^{ik_{\perp} \rho \cos \theta'} d\theta' \\ = v_{\perp} (-\sin \theta_0 \vec{e}_x + \cos \theta_0 \vec{e}_y) \frac{1}{2\pi} \int_0^{2\pi} \cos \theta' e^{ik_{\perp} \rho \cos \theta'} d\theta' \\ - v_{\perp} (\cos \theta_0 \vec{e}_x + \sin \theta_0 \vec{e}_y) \frac{1}{2\pi} \int_0^{2\pi} \sin \theta' e^{ik_{\perp} \rho \cos \theta'} d\theta'. \end{aligned}$$

The second term is  $\propto [e^{ik_{\perp}\rho \cos \theta'}]_0^{2\pi} = 0$  and drops out, the first term gives

$$\begin{aligned} & v_{\perp}(-\sin \theta_0 \vec{e}_x + \cos \theta_0 \vec{e}_y) \frac{1}{2\pi} \left( \int_0^\pi \cos \theta' e^{ik_{\perp}\rho \cos \theta'} d\theta' + \int_0^\pi \cos(\hat{\theta} + \pi) e^{ik_{\perp}\rho \cos(\hat{\theta} + \pi)} d\hat{\theta} \right) \\ &= v_{\perp}(-\sin \theta_0 \vec{e}_x + \cos \theta_0 \vec{e}_y) \frac{1}{2\pi} (-i\pi J_1(k_{\perp}\rho) + i\pi J_1(-k_{\perp}\rho)) \\ &= iv_{\perp}(\sin \theta_0 \vec{e}_x - \cos \theta_0 \vec{e}_y) J_1(k_{\perp}\rho). \end{aligned}$$

The angle between  $\vec{k}$  and the x-axis is determined with  $\sin \theta_0 = \frac{k_y}{k_{\perp}}$ ,  $\cos \theta_0 = \frac{k_x}{k_{\perp}}$ , which gives

$$\langle \vec{v}_{\perp} \bar{A}(\vec{x} - \vec{r}) \rangle = \sum_{k_x, k_y} \bar{A}(k_x, k_y) e^{i\vec{k}_{\perp} \cdot \vec{x}} i \frac{v_{\perp}}{k_{\perp}} (k_y \vec{e}_x - k_x \vec{e}_y) J_1(k_{\perp}\rho)$$

with  $v_{\perp} = \sqrt{\frac{2\mu B_0}{m}}$ , the  $f$ -integral reads

$$\int 2\pi J_v \langle \vec{v}_{\perp} f(\vec{x} - \vec{r}) \rangle dv_{\parallel} d\mu = \pi \left( \frac{2B_0}{m} \right)^{3/2} \sum_{k_x, k_y} e^{i\vec{k}_{\perp} \cdot \vec{x}} i \frac{k_y \vec{e}_x - k_x \vec{e}_y}{k_{\perp}} \int \sqrt{\mu} J_1(\lambda) f(k_x, k_y) dv_{\parallel} d\mu.$$

The  $v_{\parallel}$  integration of the remaining integrals gives

$$\begin{aligned} & \int 2\pi J_v \langle \vec{v}_{\perp} \bar{\phi}(\vec{x} - \vec{r}) \rangle F_0 dv_{\parallel} d\mu \\ &= \frac{B_0}{T_{0j}} n_{0j} \sum_{k_x, k_y} e^{i\vec{k}_{\perp} \cdot \vec{x}} \phi(k_x, k_y) i \frac{k_y \vec{e}_x - k_x \vec{e}_y}{k_{\perp}} \int v_{\perp} e^{-\frac{\mu B_0}{T_{0j}}} J_0(\lambda) J_1(\lambda) d\mu \\ &= n_{0j} v_{Tj} \sum_{k_x, k_y} e^{i\vec{k}_{\perp} \cdot \vec{x}} \phi(k_x, k_y) i \frac{k_y \vec{e}_x - k_x \vec{e}_y}{k_{\perp}} \int \sqrt{\mu} e^{-\mu} J_0(\lambda) J_1(\lambda) d\mu' \end{aligned} \tag{A.2}$$

$$\begin{aligned} & \int 2\pi J_v \mu \langle \vec{v}_{\perp} \bar{B}_{1\parallel}(\vec{x} - \vec{r}) \rangle F_0 dv_{\parallel} d\mu \\ &= \frac{B_0}{T_{0j}} n_{0j} \sum_{k_x, k_y} e^{i\vec{k}_{\perp} \cdot \vec{x}} B_{1\parallel}(k_x, k_y) i \frac{k_y \vec{e}_x - k_x \vec{e}_y}{k_{\perp}} \int \frac{2v_{\perp}\mu}{\lambda} e^{-\frac{\mu B_0}{T_{0j}}} J_1(\lambda)^2 d\mu \\ &= \frac{2\Omega_j n_{0j} T_{0j}}{B_0} \sum_{k_x, k_y} e^{i\vec{k}_{\perp} \cdot \vec{x}} B_{1\parallel}(k_x, k_y) i \frac{k_y \vec{e}_x - k_x \vec{e}_y}{k_{\perp}^2} \int \mu' e^{-\mu'} J_1(\lambda)^2 d\mu' , \end{aligned} \tag{A.3}$$

which can be simplified using

$$\begin{aligned} \int \sqrt{\mu} e^{-\mu} J_0(\lambda) J_1(\lambda) d\mu' &= \frac{k_{\perp} v_{Tj}}{2\Omega_j} \Delta_0(b_j) \\ \int \mu' e^{-\mu'} J_1(\lambda)^2 d\mu' &= k_{\perp}^2 \frac{v_T^2}{2\Omega^2} \Delta(b_j). \end{aligned}$$

*A. Integrals for the field equations*

## B. Finite difference methods

Finite differences are methods to numerically approximate derivatives on a finite grid. They are called finite because the computation of  $\frac{\partial^n}{\partial x^n}g|_i$ , where  $i$  denotes a (discrete)  $x$  position, only involves a finite number of  $g$  values in the neighbourhood of  $g_i$ , as opposed to global schemes, which involve all values of  $g$ . The variable  $x$  in this section does not refer to the radial direction but is a generic variable; in GENE, finite differences are used for the  $z$ ,  $v_{\parallel}$  and in simulations that include collisions, the  $\mu$  direction.

All finite difference schemes can be written as a convolution with a finite stencil  $d$ :

$$\left. \frac{\partial^n}{\partial x^n} g \right|_i = \sum_{j=s_1}^{s_2} d_j g_{i+j}, \quad (\text{B.1})$$

a Taylor expansion of  $g_{i+j}$  around the position  $g_i$  gives

$$\begin{aligned} \left. \frac{\partial^n}{\partial x^n} g \right|_i &= \sum_{j=s_1}^{s_2} d_j \left( g_i + (x_i - x_{i+j}) \frac{\partial g}{\partial x} \Big|_i + \frac{(x_i - x_{i+j})^2}{2} \frac{\partial^2 g}{\partial x^2} \Big|_i + \frac{(x_i - x_{i+j})^3}{3!} \frac{\partial^3 g}{\partial x^3} \Big|_i + \dots \right) \\ &= A_{0j} g_i + A_{1j} \frac{\partial g}{\partial x} \Big|_i + A_{2j} \frac{\partial^2 g}{\partial x^2} \Big|_i + A_{3j} \frac{\partial^3 g}{\partial x^3} \Big|_i + \dots \end{aligned} \quad (\text{B.2})$$

with

$$A_{ki} = \sum_{j=s_1}^{s_2} d_j \frac{(x_i - x_{i+j})^k}{k!}.$$

The stencil  $d$  approximates  $\frac{\partial^n}{\partial x^n} g|_i$  to order  $m$ , if the condition  $A_{ki} = \delta_{kn}$  is fulfilled for all  $i$  and  $k \leq m$ . For an equidistant grid with  $x_i - x_{i-1} = \Delta x$  for all  $i$ , the  $i$  dependence drops out and the condition reduces to

$$\sum_{j=s_1}^{s_2} d_j \frac{(j \Delta x)^k}{k!} = \delta_{kn}.$$

Of special relevance for GENE are centered difference schemes with  $s = s_2 = -s_1$ . For the parallel advection, trapping term, collision operator and the hyperdiffusion, the following stencils, which fulfill the above criteria, are implemented (also see, e.g. [39]):

$n$	$s$	$m$	$d$
1	1	2	$\frac{1}{2\Delta x}[-1 \ 0 \ 1]$
2	1	3	$\frac{1}{\Delta x^2}[1 \ -2 \ 1]$
1	2	4	$\frac{1}{12\Delta x}[1 \ -8 \ 0 \ 8 \ -1]$
2	2	5	$\frac{1}{12\Delta x^2}[-1 \ 16 \ -30 \ 16 \ -1]$
4	2	5	$\frac{1}{\Delta x^4}[1 \ -4 \ 6 \ -4 \ 1]$

## B. Finite difference methods

The locality of the finite difference schemes is an advantage for parallelization via domain decomposition. If the state vector  $g$  is split along the  $x$  dimension and distributed to different processors, on a given processor, only an interval  $g_{i_1} \dots g_{i_2}$  is available. To be able to compute derivatives also at positions close to these artificial interval bounds, the locally stored interval of  $g$  is extended by  $s$  so-called ghost cells at the upper and lower bounds. Before the evaluation of the derivative, the ghost cells are filled with copies of the corresponding values from neighbouring processors, so that now the values  $g_{i_1-s} \dots g_{i_2+s}$  are available, then the derivatives  $g_{i_1}^{(n)} \dots g_{i_2}^{(n)}$  can be computed easily with Eq. (B.1). Even without domain decomposition, ghost cells can be useful to define the boundary conditions for the external bounds of the simulation domain, especially if they are more complicated like for the  $z$  direction (Sec. 2.2.1).

Applying the convolution (B.1) to every point of the discretized state vector  $g$  is equivalent to multiplying  $g$  with a banded matrix. As an example, the spatial discretization of the advection equation

$$\frac{\partial}{\partial t}g = c\frac{\partial}{\partial x}g$$

( $c$  a real velocity) can be written with the 3-point stencil taken from (B.3) as

$$\frac{\partial}{\partial t}g = \frac{c}{2\Delta x} \begin{pmatrix} \ddots & \ddots & \ddots & & \\ & -1 & 0 & 1 & \\ & & -1 & 0 & 1 \\ & & & -1 & 0 & 1 \\ & & & & \ddots & \ddots & \ddots \end{pmatrix} g,$$

with all values outside the band equal zero. The advection equation is hyperbolic, i.e. the operator  $c\frac{\partial}{\partial x}$  has purely imaginary eigenvalues. All centered difference schemes for the first derivative are antisymmetric, which guarantees that this property is retained in the numerical representation. A difficulty arises at the boundaries of the simulation domain, where the boundary conditions have to be chosen carefully not to destroy this antisymmetry, because otherwise artificial unstable modes can be created. Numerical tests showed that the parallel direction  $z$  is especially susceptible to perturbations of this kind.

For the three point scheme, the only two boundary conditions that do not break the anti-symmetry of the operator matrix are zero boundary conditions, which corresponds to simply cutting off the upper right -1 and lower left 1, or periodic boundary conditions, which have an additional -1 / 1 in the upper right / lower left corner of the matrix.

For schemes with bigger stencils, there is some freedom, since by manipulating the ghost cells, the computation of the derivatives that include such cells can be changed arbitrarily, which is equivalent to modifying the corresponding rows of the operator matrix. For a five point scheme, the two upper and lower rows are concerned. Most of the entries are fixed by

the condition of antisymmetry,

$$\begin{pmatrix} 0 & c & -1 & 0 & \cdots & & \\ -c & 0 & 8 & -1 & 0 & \cdots & \\ 1 & -8 & 0 & 8 & -1 & 0 & \cdots \\ 0 & 1 & -8 & 0 & 8 & -1 & 0 & \cdots \\ \cdots & 0 & 1 & -8 & 0 & 8 & -1 & 0 \\ \cdots & 0 & \ddots & \ddots & \ddots & \ddots & \ddots \end{pmatrix}, \quad (\text{B.4})$$

but one arbitrary parameter  $c$  and an equivalent but in principle independent counterpart at the lower right side of the matrix remain; for symmetry reasons, these two parameters are chosen to be equal. Note that if  $g_0$  designates the first value of the simulation domain, this matrix structure can be achieved by assigning the values

$$g_{-1} = (8 - c)g_0, \quad g_{-2} = (8 - c)(8g_0 - g_1)$$

to the left ghost cells (and similar for the right bound) and applying the same stencil to all  $g_i$ . Zero boundary conditions correspond in this notation to  $c=8$ .

If a coupling between the two ends of the simulation domain is permitted, there is more freedom, namely an arbitrary  $(2 \times 2)$  submatrix at the upper right and the negative transpose of it at the lower left corner (together 4 real parameters), however there is no physical justification for such a coupling and at least for the parallel direction numerical tests produced unphysical results.

To preserve the properties of the eigenvalue spectrum, the antisymmetry condition could in principle be extended to antihermiticity, extending the number of free parameters by imaginary entries on the diagonal, but this possibility is dropped for physical reasons.

*B. Finite difference methods*

## C. Runge-Kutta methods

The Runge-Kutta schemes are a family of one step schemes to solve initial value problems,

$$\frac{\partial}{\partial t} g = N(t, g) \quad (\text{C.1})$$

where  $N(t, g)$  is in general a time dependent and nonlinear operator acting on  $g$ . The time advancement  $g_n \rightarrow g_{n+1}$  is computed with  $s$  intermediate stages. All Runge-Kutta schemes are of the form

$$g_{n+1} = g_n + \Delta t \sum_{i=1}^s b_i k_i \quad (\text{C.2})$$

$$k_i = N \left( t_n + c_i \Delta t, g_n + \Delta t \sum_{j=1}^s a_{ij} k_j \right) \quad (\text{C.3})$$

$$c_i = \sum_{j=1}^s a_{ij}. \quad (\text{C.4})$$

The various schemes differ by their sets of coefficients  $a_{ij}$ ,  $b_i$ ,  $c_i$  with  $i, j \in [1, s]$ . To give a full and simple definition of a scheme, its coefficients are usually arranged in a so-called Butcher tableau,

$c_1$	$a_{11}$	$a_{12}$	$\dots$	$a_{1s}$
$c_2$	$a_{21}$	$a_{22}$	$\dots$	$a_{2s}$
$\vdots$	$\vdots$	$\vdots$		$\vdots$
$c_s$	$a_{s1}$	$a_{s2}$	$\dots$	$a_{ss}$

The implicit Euler scheme described in Sec. 3.4.1 can also be accommodated in this notation and is therefore actually just a very simple Runge-Kutta scheme. With only one stage ( $s = 1$ ), it has the very simple Butcher tableau

$$\begin{array}{c|c} 1 & 1 \\ \hline & 1 \end{array}.$$

Easier to compute, because independent of matrix inversions, are fully explicit schemes. For a scheme to fit in this category, the array  $A$  of the elements  $a_{ij}$  must not have nonzero entries on or above the diagonal, because only in this case the  $k_i$  in Eq. (C.3) exclusively depend on  $k_j$  with  $0 < j < i$  and the  $k$  can be computed successively without matrix inversions. If in addition  $A$  only has entries in the first subdiagonal band, each vector  $k_i$  only depends

### C. Runge-Kutta methods

on  $k_{i-1}$ ; this implies that after adding its contribution to (C.2) and calculating the second argument of  $N$  in (C.3),  $k_{i-1}$  can be overwritten, so that this condition defines a low-memory scheme. Due to the condition (C.4), these schemes are completely characterized by only two sets of coefficients,  $b_1, \dots, b_s$  and  $c_2, \dots, c_s$ . All explicit time stepping schemes implemented in GENE are of this form.

The order of the Runge-Kutta schemes is determined by comparison to the Taylor expansion

$$g_{n+1} = g_n + \Delta t \left. \frac{\partial}{\partial t} g \right|_{t_n} + \frac{\Delta t^2}{2!} \left. \frac{\partial^2}{\partial t^2} g \right|_{t_n} + \frac{\Delta t^3}{3!} \left. \frac{\partial^3}{\partial t^3} g \right|_{t_n} + \frac{\Delta t^4}{4!} \left. \frac{\partial^4}{\partial t^4} g \right|_{t_n} + \dots$$

of the time evolution, taking into account Eq. (C.1). For an explicit scheme and linear  $N$ , it can be seen that in a  $\Delta t$  expansion of Eq. (C.2), taking into account Eq. (C.3), the highest power of  $\Delta t$  and therefore the maximum agreement with the Taylor expansion for a scheme with  $s$  stages can only be  $s$ . The requirement that the coefficients of the  $\Delta t$  expansion of (C.2) match those of the Taylor expansion up to the desired order ( $\leq s$ ) poses constraints on the entries of the Butcher tableau.

Two maximum time order schemes are implemented in GENE, a three stages, third order scheme (RK3) with and a four stages, forth order scheme (RK4) with

$$\begin{aligned} \text{RK3:} \quad b &= [1/4, 0, 3/4], & c &= [1/3, 2/3] \\ \text{RK4:} \quad b &= [1/6, 1/3, 1/3, 1/6], & c &= [1/2, 1/2, 1]. \end{aligned}$$

Since these two schemes have a time order equal to their number of stages, all coefficients of their  $\Delta t$  expansion are fixed to the Taylor values and their stability region is completely determined by the number of stages.

If the number of stages is increased without improvements on the time order, the additional degrees of freedom (i.e. the terms in the  $\Delta t$  expansion with higher power than the time order) can be used to change the shape of the stability region. While there is no limit on the extent of the stability region along the negative real axis, there is a strict theoretical limit on the maximum extent along the imaginary axis [106]. Since the eigenspectrum of the linear operator in GENE is mostly hyperbolic, i.e. located on or close to the imaginary axis, this constraint is very significant for GENE. The stability region of any explicit Runge-Kutta scheme can at most include the interval  $[-i(s-1), i(s-1)]$  of the imaginary axis (for  $\Delta t = 1$ ). Since the numerical effort is proportional to the number of stages  $s$ , for optimal schemes, i.e. schemes that (almost) achieve the theoretical limit, the performance scales with  $(s-1)/s$ . This means that incrementing  $s$  improves performance, but the gain for further increase goes down rapidly. Since the expanding stability interval allows for a bigger  $\Delta t$ , numerical errors can increase as well, setting a practical limit on the number of stages. In GENE, the numerically optimized 6 stages, 4th order Runge-Kutta (RK4M) scheme with the coefficients

$$\begin{aligned} b &= [-0.15108370762927, 0.75384683913851, -0.36016595357907, 0.52696773139913, \\ &\quad 0.0, 0.23043509067071], \\ c &= [0.16791846623918, 0.48298439719700, 0.70546072965982, 0.09295870406537, \\ &\quad 0.76210081248836] \end{aligned}$$

proposed in [107] has been implemented.

# Bibliography

- [1] *World Energy Outlook 2006*, International Energy Agency, 2006.
- [2] *Key World Energy Statistics 2007*, International Energy Agency, 2007.
- [3] *Energieverbrauch in Deutschland im Jahr 2007*, Arbeitsgemeinschaft Energiebilanzen e.V., 2008.
- [4] *IPCC Fourth Assessment Report*, Intergovernmental Panel on Climate Change, 2007.
- [5] J. Wesson, *Tokamaks*, Oxford Science Publications, 1997.
- [6] A. Brizard and T. Hahm, *Foundations of nonlinear gyrokinetic theory*, *Reviews of Modern Physics* **79**, 421 (2007).
- [7] N. Krall and A. Trivelpiece, *Principles of Plasma Physics*, San Francisco Press, 1986.
- [8] K. Spatschek, *Theoretische Plasmaphysik*, Teubner, 1990.
- [9] *NRL Plasma Formulary*, Office of Naval Research, 2007.
- [10] R. Hazeltine and F. Waelbroeck, *The Framework of Plasma Physics*, Perseus Books, 1998.
- [11] W. D'Haeseleer and W. Hitchon, *Flux Coordinates and Magnetic Field Structure*, Springer, 1991.
- [12] K. Roberts and J. Taylor, *Gravitational resistive instability of an incompressible plasma in a sheared magnetic field*, *Physics of Fluids* **8**, 315 (1965).
- [13] S. Cowley, R. Kulsrud, and R. Sudan, *Considerations of ion-temperature-gradient-driven turbulence*, *Physics of Fluids B* **3**, 2767 (1991).
- [14] M. Beer, S. Cowley, and G. Hammett, *Field-aligned coordinates for nonlinear simulation of tokamak turbulence*, *Physics of Plasmas* **2**, 2687 (1995).
- [15] H. Grad and H. Rubin, *Hydromagnetic equilibria and force-free fields*, Proceedings of the 2nd United National International Conference on the Peaceful Uses of Atomic Energy **31** (1958).
- [16] V. Shafranov, *On magnetohydrodynamical equilibrium configurations*, Soviet Physics JETP **6**, 545 (1958).

## Bibliography

- [17] P. Xanthopoulos and F. Jenko, *Clebsch-type coordinates for nonlinear gyrokinetics in generic toroidal configurations*, Physics of Plasmas **13**, 092301 (2006).
- [18] B. Scott, *Shifted metric procedure for flux tube treatments of toroidal geometry: Avoiding grid deformation*, Physics of Plasmas **8**, 447 (2001).
- [19] R. Littlejohn, *Guiding center Hamiltonian - new approach*, Journal of Mathematical Physics **20**, 2445 (1979).
- [20] R. Littlejohn, *Hamiltonian formulation of guiding center motion*, Physics of Fluids **24**, 1730 (1981).
- [21] R. Littlejohn, *Hamiltonian perturbation-theory in non-canonical coordinates*, Journal of Mathematical Physics **23**, 742 (1982).
- [22] T. Hahm, *Nonlinear gyrokinetic equations for tokamak microturbulence*, Physics of Fluids **31**, 2670 (1988).
- [23] T. Hahm, W. Lee, and A. Brizard, *Nonlinear gyrokinetic theory for finite-beta plasmas*, Physics of Fluids **31**, 1940 (1988).
- [24] A. Brizard, *Gyrokinetic energy conservation and Poisson-bracket formulation*, Physics of Fluids B **1**, 1381 (1989).
- [25] T. Dannert, *Gyrokinetische Simulation von Plasmaturbulenz mit gefangenen Teilchen und elektromagnetischen Effekten*, PhD thesis, Technische Universität München, 2005.
- [26] R. Balescu, *Transport Processes in Plasmas*, North-Holland, 1988.
- [27] A. Brizard, *A guiding-center Fokker-Planck collision operator for nonuniform magnetic fields*, Physics of Plasmas **11**, 4429 (2004).
- [28] J. Candy, R. Waltz, S. Parker, and Y. Chen, *Relevance of the parallel nonlinearity in gyrokinetic simulations of tokamak plasmas*, Physics of Plasmas **13**, 074501 (2006).
- [29] Y. Idomura et al., *New conservative gyrokinetic full-f Vlasov code and its comparison to gyrokinetic delta f particle-in-cell code*, Journal of Computational Physics **226**, 244 (2007).
- [30] P. Catto and K. Tsang, *Linearized gyro-kinetic equation with collisions*, Physics of Fluids **20**, 396 (1977).
- [31] X. Xu and M. Rosenbluth, *Numerical simulation of ion-temperature-gradient-driven modes*, Physics of Fluids B **3**, 627 (1991).
- [32] J. Connor, R. Hastie, and J. Taylor, *Shear, periodicity, and plasma ballooning modes*, Physical Review Letters **40**, 396 (1978).

- [33] X. Lapillonne et al., *Clarifications to the limitations of the  $s - \alpha$  equilibrium model for gyrokinetic computations of turbulence*, to be published in Physics of Plasmas (2008).
- [34] A. Dimits et al., *Comparisons and physics basis of tokamak transport models and turbulence simulations*, Physics of Plasmas **7**, 969 (2000).
- [35] W. Nevins et al., *Verification of gyrokinetic delta f simulations of electron temperature gradient turbulence*, Physics of Plasmas **14**, 084501 (2007).
- [36] F. Jenko, B. Dorland, M. Kotschenreuther, and B. Rogers, *Electron temperature gradient driven turbulence*, Physics of Plasmas **7**, 1904 (2000).
- [37] T. Dannert and F. Jenko, *Gyrokinetic simulation of collisionless trapped-electron mode turbulence*, Physics of Plasmas **12**, 072309 (2005).
- [38] H. Lederer et al., *Application enabling in DEISA: Petascaling of plasma turbulence codes*, Advances in Parallel Computing **15**, 713 (2008).
- [39] M. Abramovitz and I. Segun, *Handbook of Mathematical Functions*, Dover Publications, 1965.
- [40] V. Hernandez, J. Roman, and V. Vidal, *SLEPc: Scalable Library for Eigenvalue Problem Computations*, Lecture Notes in Computer Science **2565**, 377 (2003).
- [41] V. Hernandez, J. Roman, and V. Vidal, *SLEPc: A scalable and flexible toolkit for the solution of eigenvalue problems*, ACM Transactions on Mathematical Software **31**, 351 (2005).
- [42] S. Balay et al., *PETSc web page*, 2001, <http://www.mcs.anl.gov/petsc>.
- [43] S. Balay, W. Gropp, L. C. McInnes, and B. Smith, *Efficient management of parallelism in object oriented numerical software libraries*, in *Modern Software Tools in Scientific Computing*, pages 163–202, Birkhäuser Press, 1997.
- [44] S. Balay et al., *PETSc users manual*, Technical Report ANL-95/11 - Revision 2.1.5, Argonne National Laboratory, 2004.
- [45] M. Kammerer, *Betrachtung linearer Mikroinstabilitäten des gyrokinetischen Eigenwertproblems mit GENE*, Master's thesis, Universität Ulm, 2008.
- [46] J. Roman, M. Kammerer, F. Merz, and F. Jenko, *Fast eigenvalue calculations in a massively parallel plasma turbulence code*, to be published in the 5th Special Issue of Parallel Computing (Elsevier) on Parallel Matrix Algorithms and Applications (2008).
- [47] M. Kammerer, F. Merz, and F. Jenko, *Exceptional points in linear gyrokinetics*, Physics of Plasmas **15**, 052102 (2008).
- [48] C. Bender and S. Boettcher, *Real spectra in non-Hermitian Hamiltonians having PT symmetry*, Physical Review Letters **80**, 5243 (1998).

## Bibliography

- [49] A. Mostafazadeh, *Pseudo-Hermiticity versus PT-symmetry. II. A complete characterization of non-Hermitian Hamiltonians with a real spectrum*, Journal of Mathematical Physics **43**, 2814 (2002).
- [50] Z. Ahmed, *Pseudo-Hermiticity of Hamiltonians under gauge-like transformation: Real spectrum of non-Hermitian Hamiltonians*, Physics Letters A **294**, 287 (2002).
- [51] C. Bender, *Making sense of non-Hermitian Hamiltonians*, Reports on Progress in Physics **70**, 947 (2007).
- [52] G. Rewoldt, W. Tang, and M. Chance, *Electromagnetic kinetic toroidal eigenmodes for general magneto-hydrodynamic*, Physics of Fluids **25**, 480 (1982).
- [53] O. Yamagishi, M. Yokoyama, N. Nakajima, and K. Tanaka, *On the particle fluxes and density profiles in helical systems*, Physics of Plasmas **14**, 012505 (2007).
- [54] G. Rewoldt, R. Budny, and W. Tang, *Multispecies density and temperature gradient dependence of quasilinear particle and energy fluxes*, Physics of Plasmas **12**, 042506 (2005).
- [55] G. Rewoldt, *Toroidal microinstability studies of high-temperature tokamaks*, Physics of Fluids B **2**, 318 (1990).
- [56] B. Coppi and F. Pegoraro, *Theory of ubiquitous mode*, Nuclear Fusion **17**, 969 (1977).
- [57] B. Coppi and G. Rewoldt, *New trapped-electron instability*, Physical Review Letters **33**, 1329 (1974).
- [58] C. Cheng, *Kinetic-theory of collisionless ballooning modes*, Physics of Fluids **25**, 1020 (1982).
- [59] T. Kato, *Perturbation theory of linear operators*, Springer, 1966.
- [60] M. Berry, *Physics of nonhermitian degeneracies*, Czechoslovak Journal of Physics **54**, 1039 (2004).
- [61] W. Heiss, *Exceptional points of non-Hermitian operators*, Journal of Physics A **37**, 2455 (2004).
- [62] U. Gunther, I. Rotter, and B. Samsonov, *Projective Hilbert space structures at exceptional points*, Journal of Physics A **40**, 8815 (2007).
- [63] F. Stefani and G. Gerbeth, *Asymmetric polarity reversals, bimodal field distribution, and coherence resonance in a spherically symmetric mean-field dynamo model*, Physical Review Letters **94**, 184506 (2005).
- [64] M. Oberthaler et al., *Atom waves in crystals of light*, Physical Review Letters **77**, 4980 (1996).

- [65] M. Berry and M. Dennis, *The optical singularities of birefringent dichroic chiral crystals*, Proceedings of the Royal Society A **459**, 1261 (2003).
- [66] C. Dembowski et al., *Observation of a chiral state in a microwave cavity*, Physical Review Letters **90**, 034101 (2003).
- [67] C. Dembowski et al., *Encircling an exceptional point*, Physical Review E **69**, 056216 (2004).
- [68] C. Dembowski et al., *Experimental observation of the topological structure of exceptional points*, Physical Review Letters **86**, 787 (2001).
- [69] O. Latinne et al., *Laser-induced degeneracies involving autoionizing states in complex atoms*, Physical Review Letters **74**, 46 (1995).
- [70] T. Stehmann and H. von Bergmann, *IGBT lifetime in all-solid-state pulsers for CO<sub>2</sub> TEA lasers*, Proceedings of SPIE – the International Society for Optical Engineering **5777**, 495 (2005).
- [71] G. Hammett et al., *Developments in the gyrofluid approach to tokamak turbulence simulations*, Plasma Physics and Controlled Fusion **35**, 973 (1993).
- [72] B. Cohen, T. Williams, A. Dimits, and J. Byers, *Gyrokinetic simulation of EXB velocity-shear effects on ion-temperature-gradient modes*, Physics of Fluids B **5**, 2967 (1993).
- [73] A. Dimits, T. Williams, J. Byers, and B. Cohen, *Scalings of ion-temperature-gradient-driven anomalous transport in tokamaks*, Physical Review Letters **77**, 71 (1996).
- [74] P. Diamond, S. Itoh, K. Itoh, and T. Hahm, *Zonal flows in plasma - a review*, Plasma Physics and Controlled Fusion **47**, R35 (2005).
- [75] F. Merz and F. Jenko, *Nonlinear saturation of trapped electron modes via perpendicular particle diffusion*, Physical Review Letters **1**, 035005 (2008).
- [76] F. Ryter et al., *Experimental study of trapped-electron-mode properties in tokamaks: Threshold and stabilization by collisions*, Physical Review Letters **95**, 085001 (2005).
- [77] F. Jenko, W. Dorland, and G. Hammett, *Critical gradient formula for toroidal electron temperature gradient modes*, Physics of Plasmas **8**, 4096 (2001).
- [78] D. Ernst et al., *Role of trapped electron mode turbulence in internal transport barrier control in the Alcator C-Mod tokamak*, Physics of Plasmas **11**, 2637 (2004).
- [79] J. Lang, S. Parker, and Y. Chen, *Gyrokinetic delta f particle simulation of trapped electron mode driven turbulence*, Physics of Plasmas **14**, 082315 (2007).
- [80] T. Dupree, *Nonlinear theory of drift-wave turbulence and enhanced diffusion*, Physics of Fluids **10**, 1049 (1967).

## Bibliography

- [81] J. Krommes, *Fundamental statistical descriptions of plasma turbulence in magnetic fields*, Physics Reports **360**, 1 (2002).
- [82] K. Itoh, S. Itoh, and A. Fukuyama, *Transport and Structural Formation in Plasmas*, IoP, 1999.
- [83] F. Jenko, T. Dannert, and C. Angioni, *Heat and particle transport in a tokamak: Advances in nonlinear gyrokinetics*, Plasma Physics and Controlled Fusion **47**, B195 (2005).
- [84] M. Kotschenreuther, *Quantitative predictions of tokamak energy confinement from first-principles simulations with kinetic effects*, Physics of Plasmas **2**, 2381 (1995).
- [85] F. Jenko, *On the nature of ETG turbulence and cross-scale coupling*, Journal of Plasma and Fusion Research SERIES (2004).
- [86] J. Candy, R. Waltz, M. Fahey, and C. Holland, *The effect of ion-scale dynamics on electron-temperature-gradient turbulence*, Plasma Physics and Controlled Fusion **49**, 1209 (2007).
- [87] T. Görler and F. Jenko, *Scale separation between electron and ion thermal transport*, Physical Review Letters **100**, 185002 (2008).
- [88] G. Conway et al., *Plasma rotation profile measurements using Doppler reflectometry*, Plasma Physics and Controlled Fusion **46**, 951 (2004).
- [89] G. Conway et al., *Observations on core turbulence transitions in ASDEX Upgrade using Doppler reflectometry*, Nuclear Fusion **46**, S799 (2006).
- [90] C. Angioni, A. Peeters, F. Jenko, and T. Dannert, *Collisionality dependence of density peaking in quasilinear gyrokinetic calculations*, Physics of Plasmas **12**, 112310 (2005).
- [91] M. Wakatani, *Stellarator and Heliotron Devices*, Oxford Univ. Press, 1998.
- [92] J. Nührenberg and R. Zille, *Stable stellarators with medium-beta and aspect ratio*, Physics Letters A **114**, 129 (1986).
- [93] R. Kleiber and B. Scott, *Fluid simulations of edge turbulence for stellarators and axisymmetric configurations*, Physics of Plasmas **12**, 102507 (2005).
- [94] A. Kendl, B. Scott, Ball, and R. Dewar, *Turbulent edge structure formation in complex configurations*, Physics of Plasmas **10**, 3684 (2003).
- [95] A. Kendl, B. Scott, and H. Wobig, *Transition from tokamak to stellarator turbulence*, Plasma Physics and Controlled Fusion **42**, L23 (2000).
- [96] A. Kendl, *Gyrokinetic analysis of microinstabilities in a stellarator reactor*, Plasma Physics and Controlled Fusion **43**, 1559 (2001).

- [97] G. Rewoldt, L. Ku, and W. Tang, *Comparison of microinstability properties for stellarator magnetic geometries*, Physics of Plasmas **12**, 102512 (2005).
- [98] T. Watanabe, H. Sugama, and S. Ferrando-Margaret, *Gyrokinetic simulation of zonal flows and ion temperature gradient turbulence in helical systems*, Nuclear Fusion **47**, 1383 (2007).
- [99] T. Watanabe, H. Sugama, and S. Ferrando-Margaret, *Reduction of turbulent transport with zonal flows enhanced in helical systems*, Physical Review Letters **100**, 195002 (2008).
- [100] P. Xanthopoulos and F. Jenko, *Gyrokinetic analysis of linear microinstabilities for the stellarator Wendelstein 7-X*, Physics of Plasmas **14**, 042501 (2007).
- [101] P. Xanthopoulos, F. Merz, T. Goerler, and F. Jenko, *Nonlinear gyrokinetic simulations of ion-temperature-gradient turbulence for the optimized Wendelstein 7-X stellarator*, Physical Review Letters **99**, 035002 (2007).
- [102] D. Told et al., *Gyrokinetic microinstabilities in ASDEX Upgrade edge plasmas*, Physics of Plasmas **15**, 102306 (2008).
- [103] X. Bonnin, *Calculation of magnetic coordinates for stellarator fields including islands and the scrape-off layer*, Nuclear Fusion **45**, 22 (2005).
- [104] A. Kendl and H. Wobig, *Geometric effects on drift wave stability in advanced stellarators*, Physics of Plasmas **6**, 4714 (1999).
- [105] T. Rafiq, R. Kleiber, M. Nadeem, and M. Persson, *Unstable ion-temperature-gradient modes in the Wendelstein 7-X stellarator configuration*, Physics of Plasmas **9**, 4929 (2002).
- [106] R. Vichnevetsky, *New stability theorems concerning one-step numerical methods for ordinary differential equations*, Mathematics and Computers in Simulation **25**, 199 (1983).
- [107] J. Mead and R. Renaut, *Optimal Runge-Kutta methods for first order pseudospectral operators*, Journal of Computational Physics **152**, 404 (1999).

*Bibliography*

*Bibliography*

*Bibliography*

# Danksagung

Zuallererst möchte ich mich bei Prof. Frank Jenko für die Betreuung dieser Arbeit bedanken. Er nahm sich immer Zeit für alle Fragen und Anliegen, war in den vielen Diskussionen für alle Ideen offen und sorgte so für ein sehr angenehmes, kreatives und freundschaftliches Arbeitsumfeld. Durch seine ständige Unterstützung und Förderung, sowie die Besuche von internationalen Konferenzen, Summer Schools und Forschungseinrichtungen, die er ermöglichte, waren die vergangenen drei Jahre sehr lehrreich und motivierend.

Ich möchte auch Prof. Rudolf Friedrich für die Übernahme der Betreuung an der Uni Münster danken. Die interessanten und inspirierenden Treffen mit ihm und seiner Arbeitsgruppe, die immer in einem angenehmen Rahmen stattfanden, waren sehr hilfreich.

Außerdem möchte ich mich bei allen Mitgliedern der Arbeitsgruppe für die vielen hilfreichen physikalischen (und unphysikalischen) Diskussionen und die nette Arbeitsatmosphäre in den letzten drei Jahren bedanken. Besonderer Dank geht an Tilman Dannert, der mir beim Einstieg in das parallele Programmieren und den GENE Code eine große Hilfe war; Tobias Görler für seine Hilfe bei IDL-, Script- und sonstigen Computerproblemen und das teilweise Probelesen dieser Arbeit; Pavlos Xanthopoulos für die langjährige Kollaboration bezüglich des TRACER Codes und der Stellaratorsimulationen und Matthias Kammerer für die gute Zusammenarbeit bezüglich der Verbesserung des Eigenwertlösers und der nichthermiteschen Entartungen.

Stephan Eule möchte ich für die vielen Informationen und die Hilfe bei der Organisation der Abgabe der Doktorarbeit an der Uni Münster danken, außerdem David Coster für seine Hilfe bei einigen Computerproblemen und Reinhard Tisma vom Rechenzentrum Garching für die Hilfe bei der Parallelisierung und Portierung des GENE-Codes.

Zuletzt möchte ich mich noch herzlich bei meiner Familie und allen Freunden bedanken, die mich in den letzten Jahren unterstützt haben.